Long-lived discs in T associations: Pre-main-sequence ages for low-mass stars

Jon Morgan Rees

Submitted by Jon Morgan Rees to the University of Exeter as a thesis for the degree of Doctor of Philosophy in Physics, August, 2016.

I certify that all material in this thesis which is not my own work has been identified and that no material has previously been submitted and approved for the award of a degree by this or any other University.

Signed: . . . . . .

Jon Morgan Rees

Date: . . . . . .

Abstract

In this thesis, ages have been derived for 4 young clusters by fitting the pre-main-sequence stars with semi-empirical models in colour-magnitude diagrams. Combining these ages with the (consistent) set presented in previous work, the first robust evidence of increased circumstellar disc lifetimes in low-mass, low-density regions is obtained. To obtain this result, the following steps were necessary:

- Semi-empirical model isochrones have been constructed in a number of *rizJHK* photometric systems. These models overcome the issues typically seen in purely theoretical models in which the blue flux of low-mass stars is overestimated. These models are presented in a number of widely used filter sets for the first time, allowing for wider use with new clusters. Additionally the models constructed in previous filter sets have been refined using new observations.

- To support the construction of these models, upper-main-sequence fitting is performed for 2 fiducial clusters, and it is demonstrated that the resulting age and distance measurements are consistent with other measures.

- A new reduction process for data in the Blanco-DECam system is presented, and it is shown that the DECam photometric system is well characterised.

- A photometric method for dereddening stars individually in regions of spatially variable extinction is presented, and applied to the young regions in this study. This method of photometric dereddening can be applied to large numbers of stars, greatly decreasing the time investment needed compared to spectroscopic methods.

The ages derived for the young clusters using the semi-empirical models are around a factor 2 older than typically assumed in the literature, which is in-line with that seen for the ages derived for other clusters using the same technique. By considering the disc fraction in these clusters as a function of age, it is shown that Taurus and Chamaeleon show a significant excess of discs compared to a set of massive, dense clusters of similar age. This is clear evidence that discs seem to survive longer in this low-mass, low-density region, giving crucial hints at different disc evolution in these regions. ρ-Oph is a low-mass region with a high stellar density, and so could be used to identify the dominant mechanism leading to these long-lived discs. However the presence of a similar disc excess in ρ-Oph is dependent on the assumed distance, which is currently poorly constrained, and so the dominant mechanism is still unclear.

Contents

List of Figures

List of Tables

Declaration

The work presented in Chapter 4 was taken from a paper published in the Monthly Notices of the Royal Astronomical Society by Cameron P. M. Bell, Jon M. Rees, Tim Naylor, N. J. Mayne, R. D. Jeffries, Eric E. Mamajek and John Rowe, entitled Pre-main-sequence isochrones - III. The Cluster Collaboration Isochrone Server (2014, MNRAS, 445, 3496). All of the text in this chapter was written by myself. The work presented in Chapters 3, 5 and 6 was taken from a paper submitted to the Monthly Notices of the Royal Astronomical Society by Jon M. Rees, T. Wilson, Cameron P. M. Bell, Simon P. Goodwin, R. D. Jeffries and Tim Naylor. Chapters 7, 8 and 9 contain work that will be published in the near future.

The observations taken with the Wide-Field Camera on the Isaac Newton Telescope (Chapter 2) were obtained by Tim Naylor, Darryl Sergison and myself. The observations taken with the Dark Energy Camera on the Blanco 4m telescope were obtained by David James, based on my own observing plan. The reduction of these data was performed by myself, with input from Tim Naylor.

The rest of the work presented in this thesis is my own.

Acknowledgements

First and foremost I would like to thank Tim Naylor for his support throughout my PhD. None of this would have been possible without his guidance. Major thanks must also go to Cameron Bell who has always been willing to help point me in the right direction, and to David James, who obtained a lot of the data that made this thesis possible. I also offer my gratitude to Darryl, Nathan and Rob who have helped shape my work and given me useful insight.

On a more personal note my thanks go to all those people that have helped me stay (somewhat) sane these past four years! In particular to Tom and Liz, who have somehow put up with sharing an office with me (though both wisely left the country while this thesis was being written), and to Hannah who always knows when fluffy things are required (bring on America!). To Andrew and Ben, whose knowledge of obscure and bizarre facts was always welcome relief, to David who never shied away from the endless Sanderson discussions, and to Felix for distracting me when the thesis was being difficult. My sincerest appreciation to Alex and Michael, who ensured that I had something of a life outside of the office. Finally to my family, especially my Mum and Nan for their unwavering belief in me.

Jon Rees

August 2016

1

Introduction

1.1 The Birth of Low-Mass Stars

1.1.1 The Interstellar Medium and Molecular Clouds

The interstellar medium (ISM) is the relatively sparse material found throughout the Galaxy. The average density of the ISM is $\simeq 1$ hydrogen atom cm^{-3} (Ferrière 2001), but is (largely) composed of three major components. The first is the dense, cold gas (densities above 10 cm^{-3}, temperatures below 100 K). The second is the warm inter-cloud component (densities between 0.1 to 1 cm^{-3}, temperatures of several thousand K) and the third is the hot, low-density coronal component (densities < 0.01 cm^3, temperatures $> 10^5$ K) (see e.g. Cox 2005; McKee & Ostriker 1977).

Within the Galaxy we find giant molecular clouds (GMCs), large clouds composed mostly of molecular hydrogen, such as the Orion Molecular Cloud (Mass 10^5 $M_\odot$ and size $\simeq 100\times50$ pc, see e.g. Maddalena et al. 1986; Genzel & Stutzki 1989). Within the GMCs the density rises to 10^2-10^6 atoms cm^{-3} and the temperatures are 10-20 K (Williams et al. 2000). For stars to form

from this material, some regions must collapse under gravity to form dense pre-stellar clumps (Andre et al. 1993). This collapse can be triggered by turbulence (e.g. Ballesteros-Paredes et al. 2007), collisions with other clouds (e.g. Sato et al. 2000) or shocks from supernovae (e.g. Vanhala & Cameron 1998).

The minimum initial mass above which a spherical cloud will be unstable to collapse (termed the Jeans mass, M_J) or the minimum initial radius (the Jeans radius) can be derived by comparing the internal energy of the gas to its gravitational energy. The internal energy, E_{thermal}, of an ideal gas is given by

$$E_{\text{thermal}} = \frac{3}{2}NkT \tag{1.1}$$

where N is the number of gas molecules, T its temperature and k is the Boltzmann constant. Assuming a single composition medium the number of molecules is simply the mass, M divided by the mean mass of a particle, μ,

$$E_{\text{thermal}} = \frac{3}{2}\frac{MkT}{\mu}. \tag{1.2}$$

Assuming a spherical uniform density cloud the gravitational energy is given by

$$U = -\frac{3}{5}\frac{GM^2}{R}, \tag{1.3}$$

where G is the gravitational constant and R is the cloud radius. The virial theorem gives the condition for stability as

$$U + 2E_{\text{thermal}} = 0 \tag{1.4}$$

$$\therefore 3\frac{MkT}{\mu} = \frac{3}{5}\frac{GM^2}{R} \tag{1.5}$$

and given that the density, ρ, is simply the ratio of the cloud's mass to its volume the Jeans radius is given by

$$R_J = \sqrt{\frac{15kT}{4\pi\rho G\mu}} \tag{1.6}$$

and the Jeans mass is given by

$$M_J = \left(\frac{3}{4\pi\rho}\right)^{\frac{1}{2}}\left(\frac{5kT}{G\mu}\right)^{\frac{3}{2}}. \tag{1.7}$$

From Equation 1.7 it can be seen that either increasing the density or decreasing the temperature of the gas will lead to a smaller Jeans mass (i.e. less mass is required for collapse), from which

it is clear why the cool and dense GMCs are ideal locations for star formation. Taking the typical values for a GMC from above ($\rho = 10^6$ H atoms $cm^{-3} = 10^{12}$ m^{-3}, $\mu = 2 \times m_H$, $T = 20K$) and inserting them into equation 1.7 gives a Jeans mass of 3 $M_\odot$. Alternatively adopting $\rho = 10^8$ H atoms m^{-3} yields a Jeans mass of 300 $M_\odot$. This does not mean that the cloud would form a single massive star, however. As a cloud collapses the rising density will cause the Jeans mass to fall, leading to fragmentation and the formation of several smaller cores from the initial cloud (e.g. Zinnecker 1984; Bate et al. 2003).

If the pre-stellar core exceeds the Jeans mass it will collapse isothermally until the core becomes optically thick ($\rho = 10^{-13} gcm^{-3}$, Larson 1969) at which point the radiation will be unable to escape and the gas will begin to heat up. This halts the collapse and the resulting object is referred to as the first hydrostatic core, with a predicted radius of 4 AU (e.g. Bate 1998). The continuing infall of new material will continue to heat the core until it reaches 2000 K, at which point the energy from the collapse is used to dissociate and ionise H_2 rather than increasing the thermal pressure. This stagnation of thermal pressure causes the collapse to continue (Larson 1969). When all of the H_2 has been ionised the temperature rises again until the gas becomes hot enough for thermal pressure to counter the collapse and the core reaches hydrostatic equilibrium. At this point, with the gravitational collapse halted by the thermal pressure, the core is stable and is referred to as a protostar.

Of course this description of cloud collapse ignores sources of cloud support beyond thermal pressure such as magnetic fields or turbulence, which may serve to increase timescales of collapse (Klessen et al. 2000; Crutcher et al. 2009).

The free-fall time (see Hunter 1962) is the time taken for a spherical cloud to collapse purely under gravity, neglecting all other forces and methods of support and is given by

$$t_{\rm ff} = \left(\frac{3\pi}{32G\rho}\right)^{\frac{1}{2}}. \tag{1.8}$$

This free-fall time is short for the GMCs, with a value $t_{\rm ff} \simeq 0.1$ Myr. Although this argument ignores the methods of support it gives an estimate for the time it would take a core with at least a Jeans mass to collapse to a protostar.

1.1.2 Protostellar Evolution

After a cloud collapses to form a protostar it will continue to evolve, slowly contracting and radiating the energy away. This evolution is broadly divided into four classes of young stellar objects (YSOs). Class 0 objects are still embedded in the cloud of gas and dust from which they formed and have not yet reached their final mass (Andre et al. 1993). The envelope of surrounding material heavily obscures any optical emission (and, in fact, most emission shortwards of 10 microns, see Figure 1.1) from the protostar but it can be detected in the sub-mm. The Class I, II and III stages of YSO evolution were first described by Lada (1987), based on the earlier observations of three distinct populations in Rho Ophiuchi in Lada & Wilking (1984). To summarise, as the envelope around the protostar collapses conservation of angular momentum leads to the formation of a disc (see e.g. Yorke et al. 1993; Williams & Cieza 2011). Material from this disc slowly accretes onto the protostar. As the envelope clears the central protostar becomes visible at infrared and optical wavelengths, albeit with emission still dominated by the envelope, and is referred to as a Class I object. The protostar will have obtained most of its mass by the end of this phase. When the envelope is fully dissipated the remaining object is largely dominated by flux directly from the stellar photosphere, with a significant excess emission at infrared wavelengths compared to what would be expected for a blackbody alone. This excess infrared emission comes from the circumstellar disc, the distinguishing characteristic of the Class II phase. Dust in the disc attenuates the flux from the star, re-radiating it at longer wavelengths. The disc continues to accrete onto the central object and eventually becomes optically thin. The YSO is now referred to as a Class III object. The infrared excess is almost entirely absent in Class III YSOs and the spectral energy distribution (SED) closely resembles a simple stellar SED, with some excess emission at long wavelengths ($> 10\,\mu m$). The SEDs of both Class II and Class III objects are dominated by the stellar photosphere, and their properties are largely determined by the evolution of the central star towards the main-sequence. Together, these Class II and Class III objects are referred to as pre-main-sequence stars (see Section 1.2). In the low mass ($< 2\,M_{\odot}$) regime Class II and Class III sources are often referred to as T-Tauri stars, after the prototype star of this classification scheme, T-Tau (Joy 1945). Based on the strength of the $H\alpha$ emission line T-Tauri stars are further subdivided into classical T-Tauri stars (CTTS) ($H\alpha >$ 10å) and weak-line T-Tauri stars (WTTS) ($H\alpha <$ 10å). The $H\alpha$ emission is believed to arise from accretion from a circumstellar disc (CTTS; see e.g. Bertout et al. 1988) or chromospheric activity (WTTS; see e.g. Calvet et al. 1984; Walter et al. 1988). CTTS and WTTS

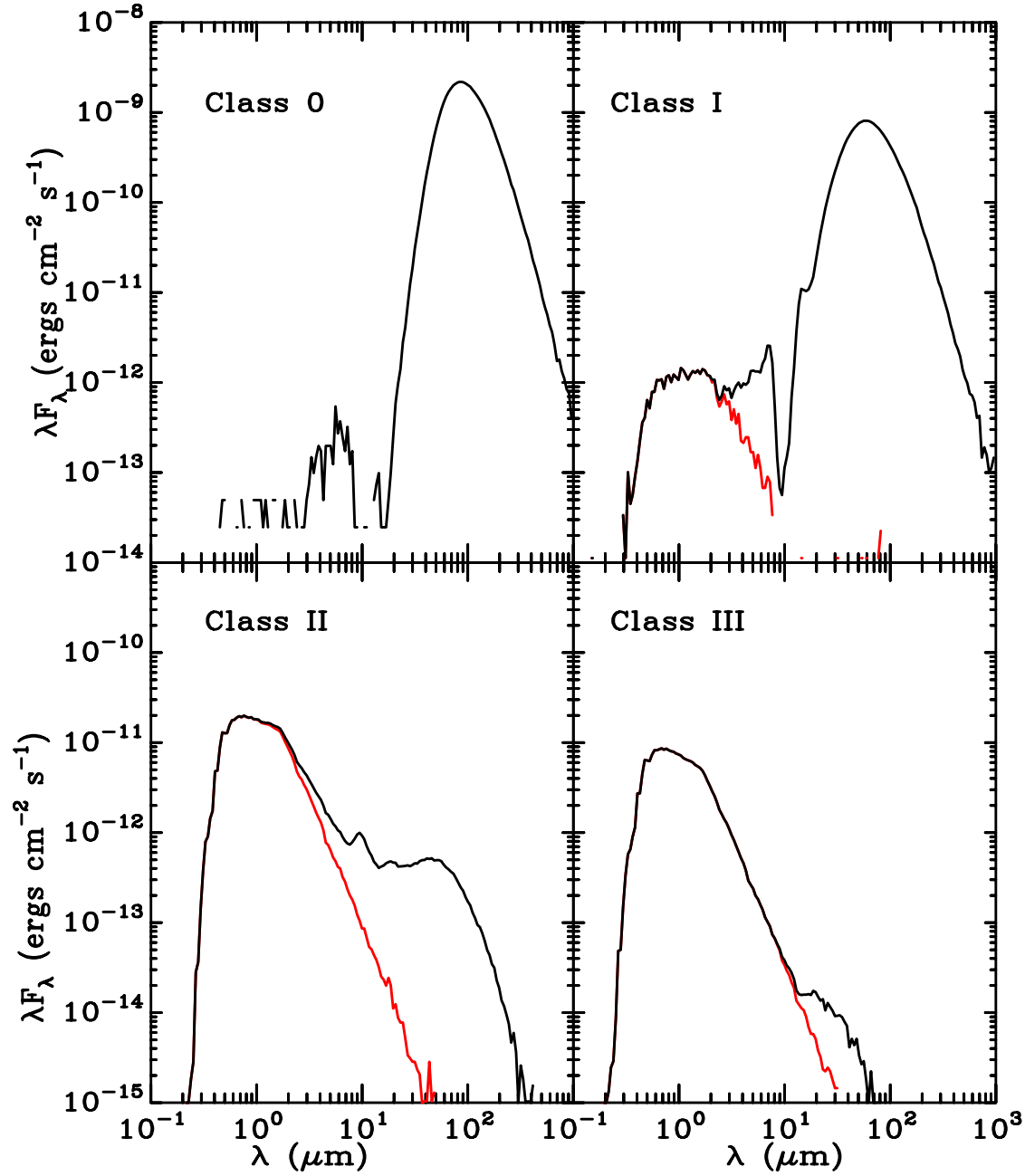

Figure 1.1: Spectral energy distributions for 2 $M_{\odot}$ YSOs at different evolutionary stages, taken from the models of Robitaille et al. (2006). The predicted flux is calculated assuming a distance of 1 kpc. The black line is the total predicted flux and for the Class I, II and III YSOs the red line shows the stellar flux without contribution from the disc or envelope. The Class 0 source is dominated by cold blackbody emission from the envelope. The Class I source is still dominated by emission from the cold envelope, but the protostar and disc begin to become visible in the infrared. In the Class II source the central star becomes visible as the envelope is dissipated, but there is still significant infrared excess from the circumstellar disc. Finally the Class III source is almost entirely dominated by the stellar flux, with only a small, optically thin component present at long wavelengths (> 10 μm).

broadly correspond to Class II and Class III objects respectively (e.g. Appenzeller & Mundt 1989; White et al. 2007).

Classifying a YSO is largely performed using spectral indices (see e.g. Lada 1987; Greene et al. 1994; Luhman et al. 2008). The spectral index, α, is defined as

$$\alpha = \frac{\mathrm{dlog}\,(\lambda F_\lambda)}{\mathrm{dlog}\,(\lambda)} \tag{1.9}$$

where λ is the wavelength and F_λ is the flux at this wavelength. The spectral index is usually calculated using pairs of fluxes between 2.2 μm and 25 μm. Class 0 objects are unobservable at these wavelengths, and so cannot be classified using the spectral index. Class I objects have $\alpha > 0.3$ (i.e. their flux rises towards longer wavelengths). Class II objects have -1.6 < α < -0.3 (flux falls at longer wavelengths). Class III objects have $\alpha \lesssim$ -1.6 (their flux falls sharply at longer wavelengths), but this limit has a slight dependence on spectral type as objects of later spectral type naturally have redder spectra (see Figure 12 of Luhman et al. 2008). There also exists an intermediate class of flat-spectrum sources, classified with -0.3 < α < 0.3. These are generally believed to be a midpoint of the Class I to Class II evolution, in which the envelope is largely cleared and the stellar flux is revealed but with significant veiling in the infrared due to circumstellar dust (Greene & Lada 2000).

1.1.3 YSO Lifetimes

Understanding the timescales of protostellar evolution is a critical component to our understanding of star formation theory. The lifetime of Class II objects (i.e. how long discs survive) can be estimated from observations of clusters. There is a large literature on the subject of disc lifetime, which typically finds lifetimes in the range 2-3 Myr. These studies can broadly be divided into those based on stars of different ages within clusters and those based on differing ages between different clusters. The first method involves determining an age for each individual star (usually within a cluster) and deriving a mean disc lifetime based on the distribution of ages of disc-bearing stars. Examples of this method include Strom et al. (1989) studying stars in Taurus, Zuckerman et al. (1995) using a selection of young stars across the sky, Hernández et al. (2007) in Orion, Spezzi et al. (2008) in Chamaeleon, Evans et al. (2009) in IC348 and Galli et al. (2015) in Lupus. However it is still unclear whether the observed luminosity spread seen in young clusters

corresponds to an age spread, or if it arises from other physical processes (see Section 1.3). Thus assigning ages to individual stars may be erroneous.

In the alternative method the disc fractions in different clusters are compared, assuming a single age for every star in a given cluster. Examples include Haisch et al. (2001) using a survey of NGC 1960, NGC 2264 and NGC 2362, Hillenbrand (2005) using a sample of $\sim$ 30 clusters, Bell et al. (2013) with a sample of 13 young clusters and Ribas et al. (2014) with a sample of 22 young associations. This method has the benefit of avoiding assumptions as to the cause of the luminosity spread within clusters (instead adopting mean ages), but is vulnerable to factors other than age affecting disc evolution e.g. environmental impact, which will be shown in later chapters to be a legitimate effect.

By assuming a constant rate of star formation Class 0/I lifetimes can be estimated by comparing the ratio of number of these objects to the number of Class II objects. Typical estimates are 0.03 Myr for Class 0 objects (Andre et al. 2000) and 0.5 Myr for Class I objects (Hatchell et al. 2007). These estimates depend on the assumed lifetime of Class II objects. For example, Bell et al. (2013) revised the PMS age scale (see Section 1.5) and showed that Class II lifetimes are likely a factor of 2 longer than previously thought, and thus Class I lifetimes are likely closer to 1 Myr. Pfalzner et al. (2014) argue that the disc lifetimes derived previously are subject to selection effects, and stars may retain the discs beyond 10 Myr. Beyond the impact on Class 0/I lifetimes, Class II lifetimes are also used to test estimates of galactic star formation rates (Robitaille & Whitney 2010) and to place a limit on planet formation timescales (planets must form before the disc is depleted, e.g. Ayliffe & Bate 2009). Given the importance of assumed Class II lifetimes it is critical to identify other impacts on Class II lifetimes.

A potential effect on disc lifetimes comes from the local environment. Circumstellar discs may be ablated by highly-ionising UV photons and stellar winds from massive stars (e.g. Johnstone et al. 1998; Störzer & Hollenbach 1999; Matsuyama et al. 2003; Alexander et al. 2006; Gorti & Hollenbach 2009). They may also be tidally disturbed by interactions with other stars (e.g. Clarke & Pringle 1993; Larson 2002; Olczak et al. 2006; Vincke et al. 2015). In "low-mass regions" i.e. star-formation complexes with fewer massive stars, the ablation of discs will be decreased compared to regions containing many massive stars, and in areas of low stellar-density there will be fewer tidal interactions (see e.g. Olczak et al. 2010; Rosotti et al. 2014). We may therefore expect that discs around stars in T-associations (low-density, low-mass regions) would

survive longer than those in massive, dense clusters.

Evidence of environmental impact on disc lifetime is still unclear. Recently Galli et al. (2015) suggested that disc lifetimes in Lupus may be shorter than in Taurus. Lupus contains four main clouds, with the majority of members lying in the Lupus 3 cloud. Lupus 3 is a dense region, with a stellar density of around 500 pc^{-3} (Nakajima et al. 2000), much larger than that seen in Taurus. The reduced disc lifetime in Lupus may well be evidence of environmental effects. However this study is based on adopting individual ages for stars within the clusters.

1.2 The Pre-Main-Sequence

The pre-main-sequence (PMS) phase of stellar evolution can be considered to be the time between the star emerging from its natal envelope to when it begins hydrogen fusion in its core and enters hydrostatic equilibrium, reaching the zero-age main sequence (ZAMS). In contrast to high mass stars ($> 8\ M_{\odot}$), which have very short lifetimes ($\simeq 10^6$ Myr) and emerge from their parent cloud already at the ZAMS (Palla & Stahler 1990), low mass stars ($M \leq 2\ M_{\odot}$) spend a significant amount of time on the PMS. As a PMS star has by definition not yet started the nuclear fusion which powers main-sequence stars, instead the luminosity of a PMS star arises from gravitational potential energy liberated from contraction. The radius of a PMS star is larger than a MS star of the same mass and it also has a larger luminosity. For example the evolutionary models of (Baraffe et al. 1998) predict a 1 $M_{\odot}$ star to have a radius of 2.3 $R_{\odot}$ and luminosity of 1.7 $L_{\odot}$ at an age of 1 Myr. The fact that the luminosity is powered by contraction places a fundamental limit on the lifetime of this stage of stellar evolution (i.e. the phase must end before the star has radiated away the entirety of its gravitational energy). This timescale is referred to as the Kelvin-Helmholtz timescale, and is given by the ratio of the total gravitational energy to the stars luminosity

$$t_{KH} = \frac{GM^2}{RL_{\rm bol}} \tag{1.10}$$

where $L_{\rm bol}$ is the bolometric luminosity. For the previously mentioned 1 $M_{\odot}$ star this timescale is $\simeq 8$ Myr (c.f 30 Myr for the present-day Sun). Of course these values are a simplification, as they assume that the luminosity and radius of the star do not evolve with time.

1.2.1 Pre-main-sequence Evolution in the Hertzsprung-Russell Diagram

The Hertzsprung-Russell (HR) diagram is one of the most powerful tools in astronomy. The HR diagram is a plot of luminosity against effective temperature, $T_{\rm eff}$, which first arose from the work of Russell (1910) and Hertzsprung (1911). Russell (1910) measured parallaxes for 52 stars and noticed a relationship between the absolute magnitude (a proxy for luminosity) and the spectral type (a proxy for $T_{\rm eff}$) of these stars. Hertzsprung (1911) described a relationship between the absolute magnitude and peak flux wavelength (another proxy for $T_{\rm eff}$) observed in a handful of clusters.

The HR diagram is ideally suited to illustrating stellar evolution. A PMS star is initially fully convective throughout and contracts isothermally, and so in the HR diagram it follows an almost vertical path (see Figure 1.2) towards lower luminosity (due to the decrease in radius) along Hayashi tracks (Hayashi 1961). As the contraction continues the core temperature increases and the dominant opacity source becomes the opacity due to bound-free and free-free transitions. This opacity decreases as the core temperature increases. For stars more massive than 0.4 $M_{\odot}$ eventually radiation becomes the dominant method of energy transport and the core becomes radiative. The effective temperature begins to increase and the star moves almost horizontally towards the left of the HR diagram along Henyey tracks (Henyey et al. 1955). Stars less massive than this limit remain fully convective throughout their lifetime and follow the Hayashi track until they reach the ZAMS. Figure 1.2 shows the evolution of PMS stars in the HR diagram. As the luminosity and temperature of a star change drastically over its PMS evolution the HR diagram can be used to determine the age of PMS stars, by comparison to stellar evolutionary models (see Section 1.2.2 for a discussion of these models). Figure 1.2 illustrates this with the positions of stars at 1 Myr, 9 Myr and the ZAMS. These lines of constant age are referred to as isochrones. It can be seen that higher-mass stars evolve faster than lower-mass stars (at 9 Myr the 2 $M_{\odot}$ star has almost reached the ZAMS, while the lowest mass stars still have significant evolution remaining).

To compare PMS stars with the evolutionary models using an HR diagram requires knowledge of the $L_{\rm bol}$ and $T_{\rm eff}$ of the stars. However these are not directly observable quantities. One possible strategy would be to transform the data from the observable plane into the theoretical plane. Assuming one has a good knowledge of the distance of a given star it may seem trivial to then move from observed magnitude to $L_{\rm bol}$. However for young PMS stars the effect of the disc must be considered. Excess emission arises in the IR due to emission from the disc (e.g. Myers

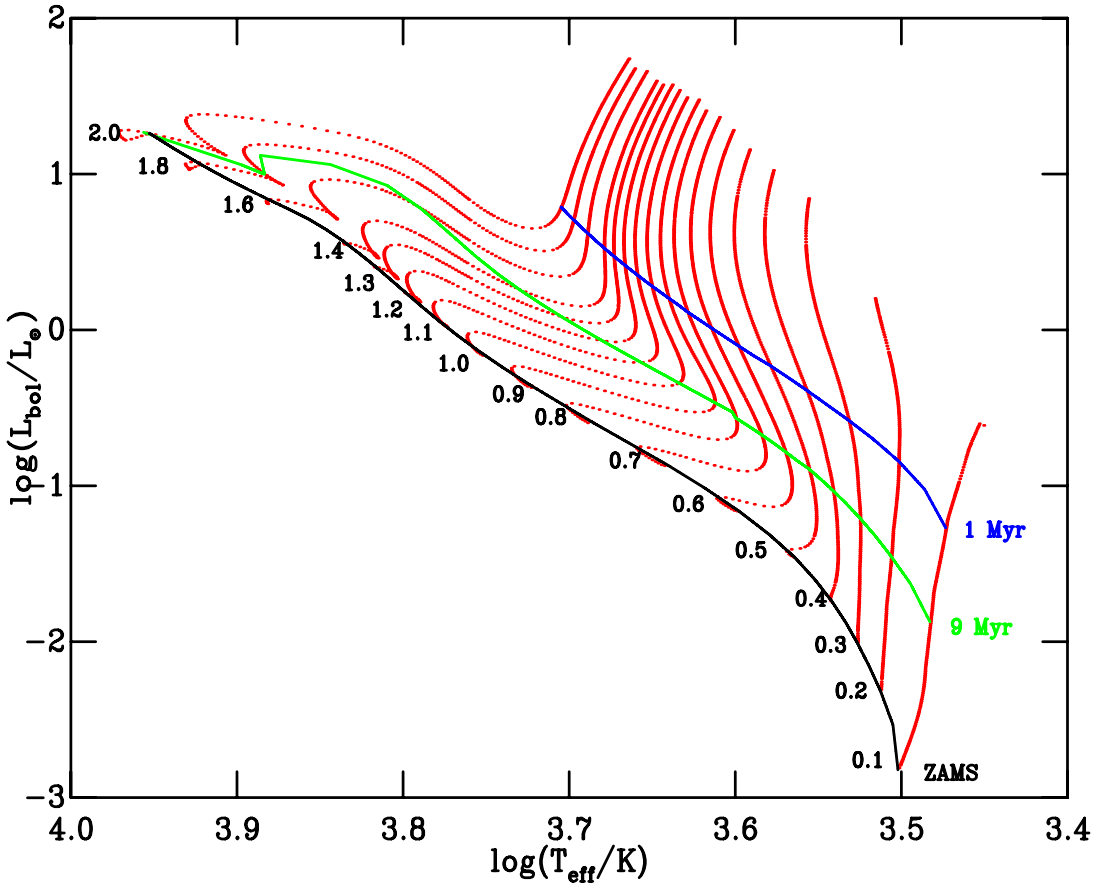

Figure 1.2: HR diagram showing PMS evolution for stars between 0.1 and 2.0 $M_{\odot}$. The red lines are the evolution tracks from the evolutionary models of Dotter et al. (2008) (i.e. how the $L_{\rm bol}$ and $T_{\rm eff}$ of a star of a given mass evolve with time). The mass of each star is given on the left hand side. The blue, green and black solid lines are the positions of the stars at 1 Myr, 9 Myr and at the ZAMS, also from the Dotter et al. (2008) models.

et al. 1987; Strom et al. 1989) and in the UV due to accretion from the disc onto the star (e.g. Hartigan et al. 1991; Hillenbrand et al. 1998), and so $L_{\rm bol}$ cannot be obtained by simply integrating the observed flux over the filters. Typically a bolometric correction (BC) is used to transform from the measured magnitude in a band that is not affected by these issues to the bolometric magnitude (e.g. Kenyon & Hartmann 1995; Pecaut & Mamajek 2013). These bolometric corrections are a function of spectral type as the flux distribution of a star changes with $T_{\rm eff}$.

Measuring $T_{\rm eff}$ is also difficult. Using spectroscopic observations the stellar temperature can be estimated using temperature sensitive spectral lines or, more commonly, spectra can be compared to model atmospheres of differing $T_{\rm eff}$ to find the best match. Spectra can also be used to determine the spectral type of the star, and from this spectral type-$T_{\rm eff}$ relationships can be defined. Spectral type-$T_{\rm eff}$ relationships can then be used to estimate the $T_{\rm eff}$ of any star given a spectral type (see e.g. Cohen & Kuhi 1979; Herczeg & Hillenbrand 2014), but spectral type-$T_{\rm eff}$ relationships can depend on whether spectral types are measured in the optical or in the infrared (see e.g. Herczeg & Hillenbrand 2014). Using broadband photometric observations alone colour-$T_{\rm eff}$ relationships can be used to estimate the $T_{\rm eff}$ based on the observed colour (e.g. Kenyon & Hartmann 1995; Scandariato et al. 2012; Pecaut & Mamajek 2013), but this necessitates using the same photometric system as that in which the relationship was derived.

There is a further issue with both the BC and spectral type-colour-$T_{\rm eff}$ relationships, relating to the stars used to derive them. Most studies use MS dwarf stars to define the relationships (e.g. Cohen & Kuhi 1979; Kenyon & Hartmann 1995; Hillenbrand 1997), but PMS stars have lower surface gravity than MS stars of the same spectral type and the spectral type-$T_{\rm eff}$ relationship differs between the two (see e.g. Figure 8 of Luhman et al. 2003). It is therefore inaccurate to take relationships derived from MS dwarfs and apply them to PMS stars. Doing so can introduce large errors into the placement of PMS stars in the HR diagram, typically of order 200 K in $T_{\rm eff}$ and 0.1 mag on the bolometric magnitude (Soderblom et al. 2014).

Alternatively, to avoid transforming the observed stars the data can be left in the observational (colour-magnitude) plane and the evolutionary models transformed. This involves the use of stellar atmosphere models to transform the evolutionary models, and is the method that I will follow in this work (see Section 1.3).

1.2.2 Stellar Evolutionary Models

Before discussing how the evolutionary models can be transformed into the observational plane it is necessary to introduce some background on the models themselves. The evolutionary models mentioned previously in Section 1.2.1 model the interior stellar structure and its evolution with time (and will be referred to henceforth as the interior models). These models predict $L_{\rm bol}$, $T_{\rm eff}$ and surface gravity, $\log(g)$, for a star of a given age and mass. The interior models are usually 1-dimensional due to the extreme computational cost of higher dimensional models, though recently advances have been made in this area (e.g. Geroux et al. 2016; Pratt et al. 2016). There are a number of interior models available, each using different input physics. These models can differ greatly from one another, and so care must be taken when choosing which models to use. The choice of models will be addressed further in Section 1.5 but to summarise, in this thesis the PMS interior models used are those of Baraffe et al. (1998), Dotter et al. (2008) and Tognelli et al. (2011) with some updated calculations described below (hereafter BCAH98, DCJ08 and Pisa respectively). The interior models solve the equations for conservation of mass, hydrostatic equilibrium, conservation of energy, and energy transport (see e.g. Clayton 1983; Guzik 2011). The models also include considerations of the equation of state (EOS), which yields internal energy and pressure given density, radiative and conductive opacities (although conductive opacities are negligible the interior models still treat them), nuclear reaction rates, a treatment of convection (which is a 3-d process and thus must be parameterised in some way), and some surface boundary condition (which can be improved by using an atmosphere model to provide a more physically realistic boundary).

The major features of the models mentioned previously are as follows. The DCJ08 models cover a mass range of 0.1 - 5.0 $M_{\odot}$. The models use high-temperature opacities from OPAL (Iglesias & Rogers 1996) and low-temperature opacities from Ferguson et al. (2005). The EOS for $M \geq 0.8\ M_{\odot}$ is an ideal gas EOS (Chaboyer & Kim 1995), and for $M < 0.8\ M_{\odot}$ is the FreeEOS (see Irwin 2012). Convection is treated using mixing length theory, which characterises convection with an average length that a packet of material travels before mixing with the background material (usually expressed in terms of the pressure scale height). DCJ08 adopt a solar-calibrated mixing length of 1.938 and the solar abundance of Grevesse & Sauval (1998). The surface boundary condition was derived using the PHOENIX model atmospheres (Hauschildt et al. 1999) for $T_{\rm eff} \leq$ 10,000 K and the Castelli & Kurucz (2004) models atmospheres for $T_{\rm eff} >$ 10,000 K. Note that

this surface boundary refers to the top of the stellar interior not the surface of the star itself. The DCJ08 models also include convective core overshoot (convective flows overshooting beyond the convective region into the radiative zone).

The BCAH98 models cover a smaller mass range than the DCJ08, but extend to lower masses (0.02 - 1.4 $M_{\odot}$). These models also use high-temperature opacities from OPAL. Low-temperature opacities are taken from Alexander & Ferguson (1994). The adopted EOS is that of Saumon et al. (1995). Convection is again treated using mixing length theory, and the BCAH98 models are available with both a mixing legth of 1.0 and 1.9. Only the 1.9 models are used in this thesis (see Section 1.5 for details). The BCAH98 models adopt the solar abundance of Grevesse et al. (1993) and a surface boundary condition derived from the PHOENIX model atmopsheres. The BCAH98 models do not include convective overshooting.

The Pisa models as presented in Tognelli et al. (2011) cover 0.2 - 9.0 $M_{\odot}$ and use the 2006 update to the OPAL EOS (Rogers & Nayfonov 2002). A comparison between this EOS and FreeEOS is presented in Tognelli et al. (2011), showing that they differ by at most 60 K at a given luminosity. The adopted radiative opacities are from Iglesias & Rogers (1996) for high-temperature, and low-temperature opacities are from Ferguson et al. (2005), (i.e. the same as those used in the DCJ08 models). The outer boundary condition is derived from the atmosphere models of Brott & Hauschildt (2005) (computed with the PHOENIX code) for 2,000 $K < T_{\rm eff} \leq$ 10,000 K and the Castelli & Kurucz (2004) models atmospheres for $T_{\rm eff} >$ 10,000 K. An updated version of the Pisa models was provided to Bell et al. (2014) for use in their work, extending to lower masses. These models cover 0.08 - 9.0 $M_{\odot}$ and also updated several inputs. As the models extend to lower mass, the EOS of Saumon et al. (1995) is adopted for $M < 0.2 M_{\odot}$. The outer boundary conditions for these low-mass stars are calculated from the atmosphere models of Allard et al. (2011), and boundary conditions for all masses are calculated using the updated solar abundances of Asplund et al. (2009). The mixing length parameter is a solar-calibrated value of 1.74, and convective core overshooting is included.

The interior models predict $L_{\rm bol}$ and $T_{\rm eff}$, and so can be used to fit the parameters of observed stars in the HR diagram. In Section 1.2.1 the difficulty of placing observations in the HR diagram was discussed. Instead it is desirable to leave the observations in colour-magnitude space and transform the interior models into this space. To accomplish this stellar atmosphere models can be used. The atmosphere models predict the distribution of the stellar flux as a function of

wavelength (F_λ) for stars of a given $T_{\rm eff}$ and $\log(g)$. The atmosphere models used in this thesis are those of Castelli & Kurucz (2004) (Kurucz ATLAS9 models) for $T_{\rm eff} > 8000\ K$ and those of Allard et al. (2011) (BT-Settl models) for $T_{\rm eff} \leq 8000\ K$.

The Kurucz ATLAS9 models are an evolution of those of Kurucz (1992). They are based on the propagation of flux through plane-parallel layers under local thermodynamic equilibrium. The 2004 models use the mixing length theory to treat convection, with a mixing length of 1.25 and a turbulent velocity of 2 km s^{-1}. The solar abundances of Grevesse & Sauval (1998) are adopted and opacities are calculated using opacity distribution functions, which average the contribution of atomic and molecular atmospheric species at each wavelength (see Kurucz 1979).

The BT-Settl models are computed using the PHOENIX atmospheric code and utilise spherical radiative transfer instead of assuming plane-parallel geometry. As opposed to opacity distribution functions, the BT-Settl models handle opacity using a library of $\sim 10^8$ lines for both atomic and molecular species. In particular the BT-Settl models include an updated methane line list (Homeier et al. 2003) and H_2O line list (Barber et al. 2006) which improves the prediction of the infrared flux distribution in cool stars. The models also include a cloud and dust model to account for the formation of condensates in low-temperature atmospheres, based on the formation models of Freytag et al. (2010). Convection is treated using the mixing length theory, adopting a mixing length value of 2.0 and turbulent velocity of 2 km s^{-1}.

1.2.3 Creating Bolometric Corrections From the Model Atmospheres

To transform a theoretical star into colour-magnitude space using the atmosphere models requires the derivations of bolometric corrections. Bolometric corrections relate the star's bolometric magnitude to the magnitude in a given filter by

$$BC_\lambda = M_{\rm bol} - M_\lambda \tag{1.11}$$

where BC_λ is the bolometric correction for a given bandpass, $M_{\rm bol}$ is the absolute bolometric magnitude and M_λ is the absolute magnitude in the given bandpass. These bolometric corrections can be derived by folding the flux distributions from the atmosphere models through the response

function for the given filter. The apparent magnitude of a star in a given band is given by

$$m_\lambda = -2.5 \log\left(\frac{I_\lambda}{I_{\lambda,\mathrm{ref}}}\right) + m_{\lambda,\mathrm{ref}} \tag{1.12}$$

where m_λ is the apparent magnitude in a given filter, I_λ the observed flux in that filter and $m_{\lambda,\mathrm{ref}}$ and $I_{\lambda,\mathrm{ref}}$ are the equivalent for a reference magnitude and flux. I_λ depends on the response function of the observing system (i.e. a combination of the filter response, telescope optics and Earth's atmosphere), and is given by

$$I_\lambda(R_\lambda) = \int_\lambda \lambda f_\lambda R_\lambda \mathrm{d}\lambda \tag{1.13}$$

where f_λ is the flux at a given wavelength and R_λ is the response function at that wavelength. Note that this equation is specifically applicable to CCD detectors (which are photon counting systems), and hence the extra factor of λ which gives the number of photons instead of energy. For energy integrating systems (e.g. photomultiplier tubes) the integral is simply $\int_\lambda f_\lambda R_\lambda \mathrm{d}\lambda$. The apparent magnitude of a star is then

$$m_\lambda = -2.5 \log\left(\frac{\int_\lambda \lambda f_\lambda R_\lambda \mathrm{d}\lambda}{\int_\lambda \lambda f_{\lambda,\mathrm{ref}} R_\lambda \mathrm{d}\lambda}\right) + m_{\lambda,\mathrm{ref}} \tag{1.14}$$

The flux predicted by the atmosphere models is the flux at the stellar surface, F_λ, and the observed flux in terms of this predicted flux is

$$f_\lambda = \left(\frac{r}{d}\right)^2 F_\lambda \tag{1.15}$$

where r is the stellar radius and d is the distance to the star. Equation 1.14 then becomes

$$m_\lambda = -2.5 \log\left(\frac{r^2}{d^2}\frac{\int_\lambda \lambda F_\lambda R_\lambda \mathrm{d}\lambda}{\int_\lambda \lambda F_{\lambda,\mathrm{ref}} R_\lambda \mathrm{d}\lambda}\right) + m_{\lambda,\mathrm{ref}}. \tag{1.16}$$

It is sensible at this point to switch to absolute magnitude, which gives $d = 10$ pc. Additionally using the Stefan-Boltzmann law

$$L = 4\pi r^2 \sigma T_{\mathrm{eff}}^4 \tag{1.17}$$

the radius term can be replaced with luminosity and temperature, both of which are included in the atmosphere models. The bolometric correction is thus given by

$$BC_\lambda = M_{\mathrm{bol}} + 2.5 \log\left(\frac{L}{4\pi\sigma T_{\mathrm{eff}}^4 . 10\mathrm{pc}^2}\frac{\int_\lambda \lambda F_\lambda R_\lambda \mathrm{d}\lambda}{\int_\lambda \lambda F_{\lambda,\mathrm{ref}} R_\lambda \mathrm{d}\lambda}\right) - m_{\lambda,\mathrm{ref}}. \tag{1.18}$$

In this manner sets of bolometric corrections can be derived from the model atmospheres and used to transform the outputs of the interior models to the observational plane. From Equation 1.11 it follows that the colour-$T_{\rm eff}$-BC relationship is given simply by the difference in two bolometric corrections. For example, to determine the $(g-i)$ colour

$$\begin{aligned}(g-i) &= M_g - M_i \\ \therefore (g-i) &= (M_{\rm bol} - BC_g(T_{\rm eff}, \log g)) - (M_{\rm bol} - BC_i(T_{\rm eff}, \log g)) \\ &= BC_i(T_{\rm eff}, \log g) - BC_g(T_{\rm eff}, \log g)\end{aligned} \tag{1.19}$$

Note that the order of the bolometric corrections is the reverse of the colour, as the bolometric corrections are subtractive ($M_\lambda = M_{\rm bol} - BC_\lambda$).

1.3 The Colour-Magnitude Diagram

The colour-magnitude diagram (CMD) is the observational equivalent of the HR diagram and can be used to derive ages by comparing observations of stars to the transformed evolutionary models. While this may at first seem to be a simple proposition, several factors serve to complicate the derivation of ages from the CMD. The derivation of ages for single stars is extremely difficult. Targeting clusters or associations improves the situation, as the group of stars will presumably be of similar age, metallicity and at a similar distance. From this point in this thesis the focus will be on young clusters instead of single stars, and the techniques below are discussed with this in mind.

After transformation to the observational plane, the predicted magnitudes from the evolutionary models are given in absolute magnitude (i.e. at a distance of 10 pc). The effect of distance in a CMD is purely on the magnitude (the effect is independent of bandpass, and thus cancels when constructing the colour). Therefore to compare the models to observations a crucial piece of information is the distance to the cluster. Parallax measurements provide a model-independent estimate of distance and are thus one of the most robust estimates of stellar distances. The *Hipparcos* mission measured parallaxes for $\sim$ 120,000 bright ($V < 12.4$) stars (Perryman et al. 1997), and is an excellent source for distance measurements of nearby clusters (see van Leeuwen 2009). However the *Hipparcos* limiting magnitude translates to a limiting distance of $\sim$ 200 pc. Beyond this limit other distance measurements are required (see e.g. Soderblom et al. 2005; Torres et al. 2007, for parallax measurements from other sources).

Section 1.2.1 introduced the large change in luminosity and temperature observed over the PMS lifetime. Equivalently in the CMD PMS stars will exhibit large changes in colour and magnitude as they evolve. This evolution is highly degenerate with distance (i.e. it can be unclear if a given sequence is older or merely further away). In comparison to the relatively rapid PMS evolution, once a star has reached the main-sequence its colour and magnitude change very little with time until it reaches the terminal-age main sequence (TAMS), and the post-MS evolution begins. MS stars are therefore poorly suited to age determinations, but ideal for distance fitting (e.g. Johnson 1957; An et al. 2007). The typical method involves overlaying a MS isochrone on the data and shifting the position vertically (purely in the magnitude direction) until the model fits the data, and is generally performed by-eye.

Another complication is interstellar extinction. Dust in the ISM and leftover material from the natal cloud for young stars can attenuate light from stars. Unlike the effect of distance, extinction is wavelength dependent and thus is not only evident in magnitude, but also in colour. Typically the term "extinction" is used to refer to the effect on magnitude and "reddening" to refer to the effect on colour (as it makes stars appear redder). The relationship between the effect in colour and magnitude can be quantified using reddening vectors. Extinction values are typically quoted in terms of $E(B-V)$, defined as

$$E(B-V) \equiv (B-V) - (B-V)_{\text{intrinsic}} = A_B - A_V \tag{1.20}$$

where A_B is the extinction in the B-band and A_V is the extinction in the V-band. There are a number of methods used to measure extinctions. Often the pair method is used, in which the spectrum of a reddened star is compared with an unreddened star of the same spectral type, but alternative photometric methods include fitting isochrones to a CMD, using a colour-colour diagram (CCD) to eliminate the effect of distance, or the Q-method (Johnson & Morgan 1953). See Chapter 5 for a further discussion of the effect of extinction, in which a new method of measuring extinction is introduced.

A further complication in fitting CMDs arises from the effect of unresolved binaries. If a binary star pair is unresolved it will be detected as a single object. The maximum this effect will have is equal-mass binaries, in which both component stars have the same mass and thus the same flux. Comparing an unresolved equal-mass binary, with observed flux F, to a single-star of the

same mass with observed flux $f = F/2$, gives a magnitude of

$$\begin{aligned} m_{\text{binary}} &= -2.5\log(F) = -2.5\log(2f) \\ &= -2.5\log(f) - 2.5\log(2) \\ &= -2.5\log(f) - 0.75 \\ \therefore m_{\text{binary}} &= m_{\text{single}} - 0.75. \end{aligned} \tag{1.21}$$

As with distance, this effect will cancel when constructing colours. The equal-mass binaries will therefore sit 0.75 mag brighter than the single-star sequence. Unequal-mass binaries lie between these two extremes, and will also have a small colour effect. Unresolved binaries thus serve to spread the sequence, and this must be considered when fitting models to observations.

Finally, young clusters ($\lesssim 10$ Myr) show intrinsic spread in their sequences in the CMD (see e.g. Bell et al. 2013; Soderblom et al. 2014). The source of the luminosity spread in these young clusters is still unclear, but is often attributed to a spread in stellar ages and used as evidence of protracted periods of star formation over $\simeq 10$ Myr. Hartmann (2001) identified several potential sources that could potentially explain the luminosity spread, both astrophysical and observational. These include the uncertainties in the observations themselves, uncertainties in the distance to the cluster (and any spread in distance within the cluster), extinction, photometric variability, unresolved binaries and accretion. Given that these potential sources will likely all play some role in creating a luminosity spread it may be unwise to ascribe it entirely to an age spread. Burningham et al. (2005) simulated PMS populations including the effects of observational uncertainties, unresolved binaries and variability (on few-year timescales) and showed that they were unable to account for the entirety of the observed spread. Using Monte Carlo simulations combined with observations of Upper Sco, Slesnick et al. (2008) found that after accounting for a combination of observational uncertainties the luminosity spread in Upper Sco is consistent with a single burst of star formation. Da Rio et al. (2010) used a maximum-likelihood technique to show that, after taking account of variability, accretion and differential reddening, the remaining spread in LH 95 was still too large to be explained by other sources of uncertainty and thus represented an age spread. Jeffries et al. (2011) compared the Class II and Class III population in the Orion Nebula Cluster and found that any age spread must be smaller than the median disc lifetime. Using other age determinations Jeffries (2012) further argued that the observed luminosity spreads are likely

dominated by non-age related effects. Whatever the source of the spread in young clusters, it is clear that it can complicate age determinations.

1.3.1 τ^2 Fitting

As mentioned in Section 1.3, most CMD or HR diagram fitting is performed by-eye. Naylor & Jeffries (2006) introduced a statistical method of fitting CMDs with model isochrones, τ^2 fitting (later updated by Naylor 2009). The technique has been used by several groups to determine ages in a number of regions (e.g. Jeffries et al. 2007; Joshi et al. 2008; Cargile et al. 2010; Curtis et al. 2013; Bell et al. 2013, 2015). The τ^2 statistic can be viewed as an evolution of the χ^2 statistic to allow for the 2-d distributions of both the model and the data, the correlated uncertainties in the colour and magnitude data and the effects of unresolved binaries on the sequence. The best-fitting age and distance can be determined by comparing a grid of models over a range of age and distance to the observations.

Each model is a simulated population of 10^6 stars drawn from the evolutionary models at a given age using a Monte Carlo method and adopting the broken power law IMF of Kroupa (2001). The stellar interior models predict $L_{\rm bol}$, $T_{\rm eff}$ and $\log(g)$, and are transformed to CMD space using the atmosphere models as discussed in Section 1.2.3. Binaries are included in the simulated population. A binary fraction of 50% is assumed with a uniform companion mass ratio distribution, which well describes observations for solar-type stars (e.g. Raghavan et al. 2010). For O-stars there is evidence that the binary fraction is higher than for later spectral types (e.g. Chini et al. 2012) and so a binary fraction of 75% is assumed for O-stars. The model is then turned into a pseudo-continuous distribution by binning the model stars into pixels in CMD space.

An intuitive description of the fitting statistic is given here. For a rigorous derivation see Naylor & Jeffries (2006). Given a set of observations of a cluster and a grid of models the best fit will be given by the model that has the strongest overlap with the data. For a single point (star) this overlap is calculated by taking the function representing its position in the CMD (a 2-dimensional Gaussian based on the uncertainties in the observation), multiplying it by the model pseudo-continuous distribution on a pixel-by-pixel basis and then summing the resulting values. For example, denoting the model distribution by $\rho(c, m)$, where c and m are the colour and magnitude coordinates respectively and the distribution for the data point and its uncertainties

$U_i(c - c_i, m - m_i)$ (where c_i and m_i are the measured coordinates), the overlap is

$$\int\int U_i(c - c_i, m - m_i)\rho(c, m)\mathrm{d}c\mathrm{d}m. \tag{1.22}$$

Expanding this to the case of N stars the probability that the set of stars originate from the model then becomes the product of these individual overlaps

$$P = \prod_{i=1}^{N} \int\int U_i(c - c_i, m - m_i)\rho(c, m)\mathrm{d}c\mathrm{d}m. \tag{1.23}$$

τ^2 is defined as $-2\ln P$, mirroring the relationship between χ^2 and probability ($\chi^2 = -2\ln P$). This then gives

$$\tau^2 = -2\sum_{i=1}^{N} \ln \int\int U_i(c - c_i, m - m_i)\rho(c, m)\mathrm{d}c\mathrm{d}m. \tag{1.24}$$

The most likely model to fit the data is found by minimising τ^2 over the entire grid of age and distance, and statistically meaningful uncertainties on the derived age and distance are defined using the 68% confidence limits.

1.3.2 The Lithium Depletion Boundary

Although the focus in this introduction has been on the use of CMDs to derive ages (and indeed this focus will continue throughout this thesis), there are a number of other techniques that can be used to derive stellar ages. One of the more important techniques, lithium depletion boundary fitting, is discussed below as it serves as a validation of ages from other techniques. For a more in-depth review of other techniques as applicable to young stars see Soderblom et al. (2014). The lithium depletion boundary (LDB) technique relies on the highly convective nature of low-mass PMS stars. When the core temperature reaches 3×10^6 K lithium fusion begins and rapidly depletes the available lithium (see e.g. Jeffries 2006). In low-mass PMS stars convection brings material from the photosphere to the core, ensuring that lithium is depleted throughout the entire star. The age at which lithium is depleted in a given star is mass dependent, as the cores of high-mass stars reach the lithium burning temperature sooner than those of low-mass stars. Thus by taking spectra of a number of stars of different masses in a cluster the age can be determined based on the boundary between the stars that have burned lithium and those which retain lithium (see Figure 1.3). Note that the high-mass group of stars that retain lithium are those in which a radiative core

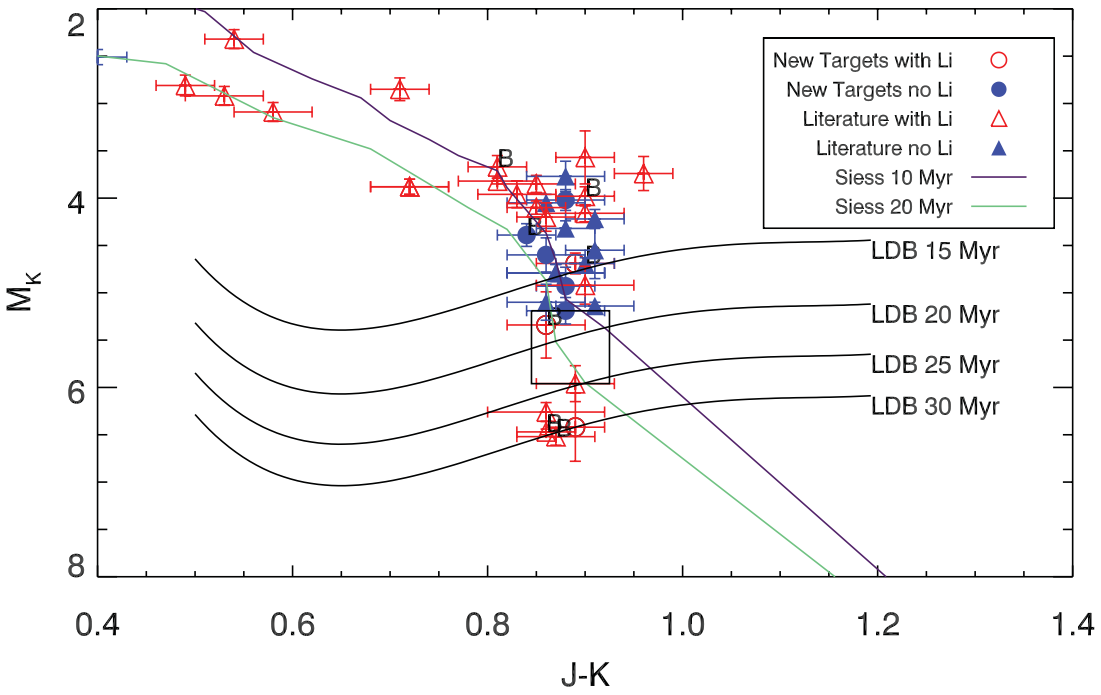

Figure 1.3: CMD for members of the Beta Pic moving group showing stars with lithium (red points) and those in which lithium is depleted (blue points). The black lines show the predicted boundary between the two groups at different ages, based on the models of Chabrier & Baraffe (1997). The black rectangle shows the location of the LDB based on these observations, giving an LDB age of 21±4 Myr. Reproduced from Binks & Jeffries (2014), Figure 2.

has formed, and thus convection is unable to bring lithium from the photosphere to the core. In these stars lithium is burned in the core but is not depleted throughout the photosphere. There is excellent agreement between models for the LDB ages, and thus the LDB offers one of the most robust age estimates (Burke et al. 2004). It is very observationally intensive however, requiring moderate-resolution ($R \geq 3000$) spectra for a large number of members over a range of masses. To date, only 9 clusters have LDB age determinations (see Table 1.1), and these are valuable as tests of other age determination techniques (e.g. Bell et al. 2013).

1.4 Identifying Pre-Main-Sequence stars

In the previous section the use of the CMD to determine ages for groups of young stars was introduced. This obviously hinges on accurately identifying PMS stars. Due to their youth PMS stars exhibit numerous observational indicators which can be used to discriminate between field stars and the young PMS stars.

Table 1.1: A list of the clusters for which an age has been determined from the lithium depletion boundary.

Cluster	LDB Age (Myr)	Reference
Beta Pic moving group	21 ± 4	Binks & Jeffries (2014)
NGC 1960	22 ± 4	Jeffries et al. (2013)
IC 4665	28 ± 5	Manzi et al. (2008)
NGC 2547	35 ± 3	Jeffries & Oliveira (2005)
IC 2602	46^{+6}_{-5}	Dobbie et al. (2010)
IC 2391	50 ± 5	Barrado y Navascués et al. (2004)
Alpha Per	90 ± 10	Stauffer et al. (1999)
Blanco 1	126^{+13}_{-14}	Juarez et al. (2014)
Pleiades	130 ± 20	Barrado y Navascués et al. (2004)

Young PMS stars are more luminous and redder than their ZAMS counterparts. If any of the cloud material remains this can also serve to redden the PMS stars compared to the foreground field population. A group of PMS stars will thus often be separated from the field stars in a CMD, and so photometric cuts in the CMD offer an obvious method of identifying PMS stars (see e.g. de Epstein & Epstein 1985; Kenyon & Hartmann 1995; Sung et al. 2004; Kenyon et al. 2005). The advantage with this method is the ease and low observing cost (i.e. only a single epoch of photometry is required), but the major disadvantage is that such a method can suffer from high levels of contamination from foreground or background field stars.

In Figure 1.1 the effect of a circumstellar disc on YSO SEDs was shown. The large infrared excess introduced by the circumstellar disc can be used to identify young stars. Colour-colour diagrams can be used to differentiate between infrared excess arising from discs or interstellar reddening (e.g. Lada & Adams 1992; Allen et al. 2004; Luhman et al. 2008). As mentioned in Section 1.1.2, for Class II objects accretion from the disc can lead to strong Hα emission lines. Thus Hα emission is also often used as an indicator of youth for identifying PMS stars (see e.g. Sung et al. 1997; Barentsen et al. 2011)

PMS stars exhibit high levels of X-ray activity compared to stars on the MS (Montmerle et al. 1983; Feigelson 1984; Gagne et al. 1995; Stassun et al. 2004). The enhanced X-ray activity primarily arises from the stellar corona and is likely a consequence of the high levels of magnetic activity in PMS stars, although some may be due to accretion (Preibisch & Feigelson 2005; Stassun et al. 2006). X-ray surveys covering the area of young clusters thus offer an additional method of identifying young stars (e.g. Naylor & Fabian 1999; Pillitteri et al. 2004; Güdel et al. 2007). The major benefit of X-ray surveys over the infrared excess identifications is the ability to identify stars

both with and without circumstellar discs (see e.g. Feigelson et al. 2003). However Preibisch et al. (2005) found that X-ray luminsity decreased by a factor 2-3 for accreting vs non-accreting stars, suggesting that basing memberships on X-ray surveys alone may be biased towards non-accreting stars.

One of the strongest indicators of youth (and thus PMS status) is the presence of strong lithium absorption in the stellar spectrum (e.g. Herbig 1962; D'Antona & Mazzitelli 1994; Preibisch et al. 1998). As discussed in Section 1.3.2 lithium burning is very rapid (Jeffries 2006), and thus evidence of strong lithium absorption is a very robust indicator of youth, but only works well for low-mass stars, which remain fully convective.

Another method of identifying potential PMS stars is the identification of common proper motion with already known PMS stars. This is a common technique used for assigning memberships in clusters and associations. Large proper motion surveys are an excellent method of identifying members of young clusters (see e.g. de Zeeuw et al. 1999; Lodieu et al. 2012). By combining modern wide-field surveys with older photographic plate surveys large temporal baselines can be established to more accurately measure proper motions (e.g. Høg et al. 2000; Deacon et al. 2009; Roeser et al. 2010). It should be noted that the identification of common proper motion with a young group is not on its own a definitive indicator of youth. It is however an excellent method of choosing targets for follow up observations to confirm membership when combined with the other measures outlined above. Of course proper motion only accounts for velocity in two dimensions. To measure motion in the third dimension requires spectroscopically measuring the radial velocity of a given star. Although this can be measured in a single observing visit (as opposed to proper motion which requires photometry in at least 2 epochs), obtaining spectra for a large number of stars over wide areas (i.e. in clusters) is still time consuming. Although this is improving with the commissioning of modern multi-object spectrographs (e.g. WEAVE; Dalton et al. 2012, DESI; Levi et al. 2013) radial velocities can be confused by binarity. Combining radial velocities with proper motion to measure the full 3-d velocity can greatly aid the identification of candidate cluster members (Gagné et al. 2015).

1.5 Previous Work

To investigate the effect of environment on circumstellar discs requires robust age determinations for a number of young clusters of differing environments. The work in this thesis will build on previous work aimed at robust age determinations for young stars. It is a well known problem that the stellar evolutionary models fail to match observations at low $T_{\rm eff}$ (see e.g. Bell et al. 2012; Herczeg & Hillenbrand 2015). The source of this discrepancy is still unclear, but suggestions include missing sources of opacity in the model atmospheres (Chabrier et al. 2000; Stauffer et al. 2007) and magnetic activity inhibiting convection (Feiden 2016). Naylor (2009) showed that ages derived from fitting the upper-main-sequence (UMS) are systematically older than those derived from fitting the PMS by roughly a factor 2. The UMS ages agree with other age determinations, including the LDB technique (Jeffries et al. 2013) and therefore the problem was ascribed to the PMS fitting. In an attempt to mitigate this problem Bell et al. (2013, 2014) presented a set of semi-empirical models, and showed that they can be used to derive robust PMS ages which agree with those derived using other age techniques. The semi-empirical models were constructed by taking the interior models of Baraffe et al. (1998), Dotter et al. (2008) and Tognelli et al. (2011), applying the model atmospheres of Allard et al. (2011) and introducing an empirical correction to the BCs at low $T_{\rm eff}$ ($\lesssim$ 4500 K) to ensure the models match observations of a fiducial cluster (effectively adopting an empirical colour-$T_{\rm eff}$ relationship at low $T_{\rm eff}$). The fiducial cluster must have a well constrained age and distance derived from a method independent of fitting the PMS, thus Bell et al. (2013) used the Pleiades, which has a distance determined from main-sequence fitting and parallax, and an age determined from fitting the lithium depletion boundary.

The resulting semi-empirical models are only valid for use in the same photometric system as the observations of the fiducial cluster, which for Bell et al. (2013) is the Isaac Newton Telescope (INT) Wide-Field Camera (WFC) system. In Chapter 3 these semi-empirical models are extended to lower $T_{\rm eff}$ in the WFC system. In Chapter 4 the semi-empirical models are constructed in several other photometric systems.

1.6 Summary

This introduction has laid out how CMDs can be used to derive the ages of young clusters using theoretical model isochrones. The models themselves have been described in Section 1.2.2, and

the transformation of the models into the observational plane has been described in Section 1.2.3. τ^2 fitting, a statistical method for determining age based on the comparison of the isochrones to the data, was described in Section 1.3.1, and potential problems in age determinations from the PMS were described in Section 1.3. These techniques will be used to determine the ages of young, sparse T-Associations.

The aim of this thesis is to determine the effect of environment on circumstellar discs. To robustly determine the effect of environment on disc lifetimes requires robust age determinations for a sample of clusters with differing environments. Bell et al. (2013) measured ages for a sample of massive clusters. The next step is to investigate a set of low-mass, low-density regions.

In Chapter 2 observations in the INT-WFC system are presented and the data reduction process is described. In Chapter 3 observations of a fiducial cluster are used to construct semi-empirical model isochrones in the INT-WFC photometric system, and these models are then used to derive the age of the young cluster NGC 2264. Semi-empirical model isochrones are then constructed in several other photometric systems in Chapter 4. In Chapter 5 a method of photometric dereddening using $iZJH$-band photometry is described, and this is then used to account for the variable extinction in the Taurus star-forming region in Chapter 6. Also in Chapter 6 an age is derived for Taurus, and it is shown that the region shows an excess of discs compared to more massive, dense regions. Chapter 7 presents observations obtained in the Blanco-DECam system, and describes the new reduction process created for these data. In Chapter 8 the open cluster Blanco 1 is introduced, and used as a fiducial cluster to construct semi-empirical models for the Blanco-DECam system. These models are then used in Chapter 9 to determine the ages of the Chamaeleon I and ρ-Ophiuchus regions, and it is shown that Chamaeleon I also shows an excess of discs. Finally, Chapter 10 summarises the main results from this thesis.

2

Photometry in the *Isaac Newton* Telescope Wide-Field Camera System

2.1 Motivation

The ultimate aim of this thesis is to determine the effect of environment on circumstellar disc lifetimes. In Section 1.5 the work of Bell et al. (2013) was introduced. With robust ages for a set of young, massive (and dense) clusters the work of Bell et al. (2013) represents an excellent platform to begin the study of environmental impact on discs.

In later chapters ages will be derived for low-mass, low-density regions, allowing for a comparison to the massive dense clusters in Bell et al. (2013). In this chapter the observations, reduction and calibration of photometric observations in the *Isaac Newton* Telescope Wide-Field Camera system will be discussed. Section 2.2 introduces the observations. In Section 2.3 the data reduction process is outlined including the derivation of linearity coefficients (Section 2.3.1) and the construction of fringe frames (Section 2.3.3). Optimal photometry is discussed in Section

2.3.5 and the photometric calibration procedure is outlined in Section 2.3.6. Finally Section 2.3.7 presents the astrometric calibration procedure.

2.2 Observations

Observations were taken of a number of clusters, including the Pleiades, Praesepe and Taurus. The observations were obtained over two runs with the 2.5 m *Isaac Newton* Telescope (INT) at the Observatorio del Roque de los Muchachos, La Palma. The first set were obtained on the nights of the 3^{rd}, 4^{th} and 5^{th} December 2012 and the second set on 11^{th} November 2013. The nights of the 3^{rd} December 2012 and 11^{th} November 2013 were photometric throughout. For the Pleiades the observations were combined with those presented by Bell et al. (2012) obtained in 2007/2008. The instrumentation and filter set used for all runs was almost identical. All used the Wide-Field Camera (WFC), an instrument made up of a mosaic of four EEV 2048×4096 pixel CCDs arranged in an L-shape, operating in the fast readout mode. The field-of-view of the WFC is 34' $\times$ 34', with a cut-out of 11' $\times$ 11' in the North-East corner due to the mosaic layout. The inter-CCD gaps are equivalent to $27''$ at most and together result in approximately 2% of the total field-of-view being unobserved. The December 2012 and Bell et al. runs made use of the $(UgriZ)_{\rm WFC}$ filter set and the November 2013 run used $(gri)_{\rm WFC}$. The $(gri)_{\rm WFC}$ filters are based on the Sloan Digital Sky Survey (SDSS) filter, although there are some noticeable differences particularly at the blue end of the g filter (see Figure 2.1). The $U_{\rm WFC}$ and $Z_{\rm WFC}$ filters are from the Royal Greenwich Observatory system, as no $u_{\rm SDSS}$ or $z_{\rm SDSS}$ filters are available for the INT-WFC. The observations also covered five fields used as standards. The observed fields and exposure times are given in Tables A.1, A.2 and A.3. Additionally the fields observed in the Pleiades can be seen in Figure 3.1 and those in Taurus can be seen in Figure 6.1

2.3 Data Reduction

First a master bias frame was constructed for each run by median-stacking a set of bias frames. These master bias frames were subtracted from the data frames to debias the data.

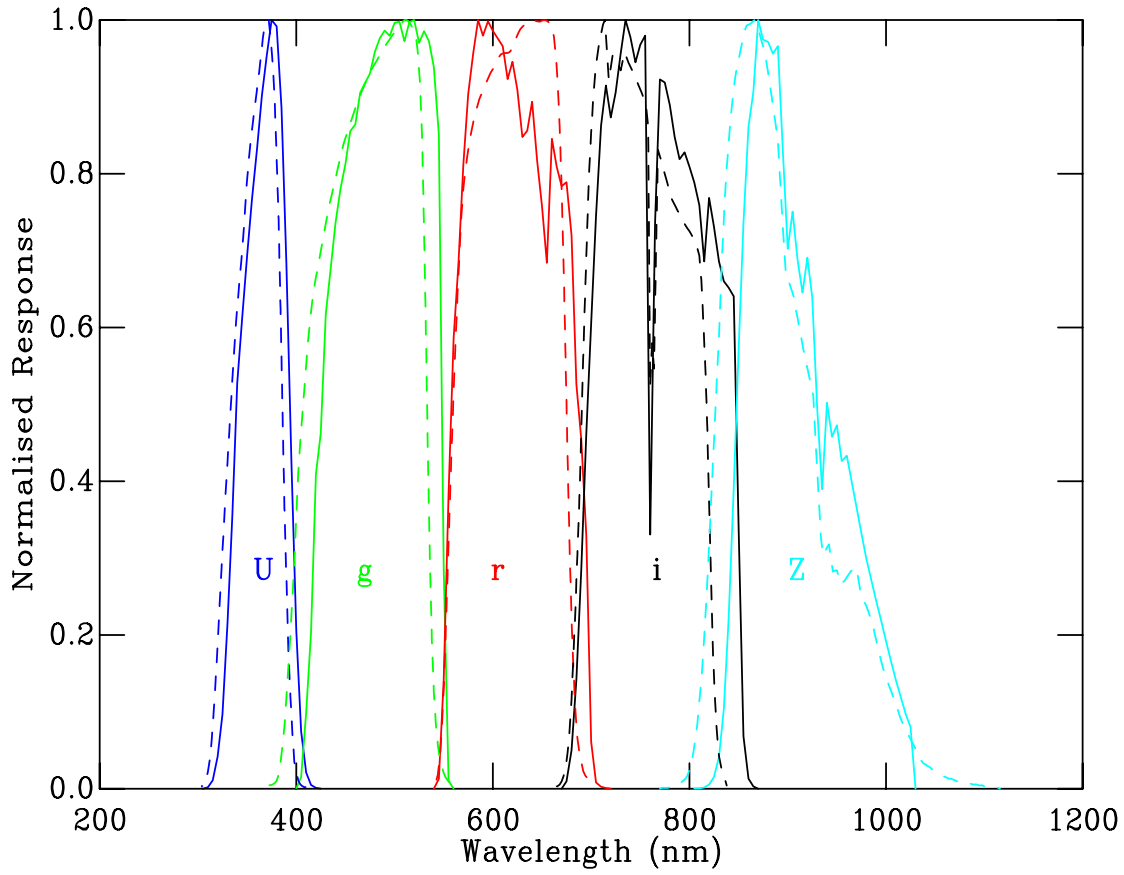

Figure 2.1: System responses for both the INT-WFC (solid lines) and SDSS (dashed lines) photometric systems. The WFC responses are those calculated by Bell et al. (2012) and the SDSS responses are from Doi et al. (2010)

2.3.1 Deriving Linearity Coefficients

CCDs convert incident photons to electrons which are then read out by an analog-to-digital converter as a digital count (in analogue-to-digital units, ADU). This is usually not a perfectly linear system (i.e. doubling the number of photons may not double the ADU), especially when approaching the saturation limit. The non-linearity of the INT-WFC is between 1-2% but changes with time (González-Solares et al. 2008). We tested the linearity of the INT-WFC to better quantify the non-linearity in the data. The North-West corner of CCD 3 suffers from vignetting resulting in lower counts than in the unvignetted regions. This means that when most of the CCDs reach the non-linear regime and approach saturation the corner of CCD 3 continues to respond linearly. The vignetted corner can thus be used as a measure of the actual level of light the WFC is being exposed to, allowing the non-linearity in the rest of the WFC to be quantified (credit to Mike Irwin for this technique). Observations were taken of the dome lights with exposure times of between 2 and 34 seconds. The counts in the vignetted region were compared with the counts in the unvignetted regions to derive linearity curves for each CCD. The linearity curves for both 2012 and 2013 are shown in Figure 2.2. The non-linearity is below 1% for CCDs 1 and 3 in both runs. CCD 4 is noticeably worse with non-linearity of 2% at worse for the 2012 run (although this is significantly improved in the 2013 run, at sub-1%). CCD 2 suffers the worst non-linearity, approaching 2% in 2013 and 3% in 2012. Note that all counts $\geq$ 50,000 were flagged as non-linear during the data reduction process. To derive linearisation coefficients linear functions were fit to the data, with the exception of CCD 4 which required a quadratic function, and these were used to correct for non-linearity in the data. The linearisation coefficients are presented in Table 2.1. The residual non-linearity of the four CCDs is shown in Figure 2.3. The residual non-linearity is below 1% in all cases, except for CCD 4 on the 2013 run, which shows some non-linearity at the 2.5% level at high counts, although this will only affect the brightest sources with counts above 40,000 ADU.

2.3.2 Flat Fields

Flatfielding corrects for variations in pixel sensitivity across the chip and also corrects for vignetting (of particular concern here given the previously mentioned vignetting on CCD 3). To flatfield the data a master flat file was constructed for each run in each filter. These were created by median-stacking sets of twilight sky flats taken over the observing run and then normalising the stacked image. The individual exposures were "nodded" to ensure if stars appeared in individual

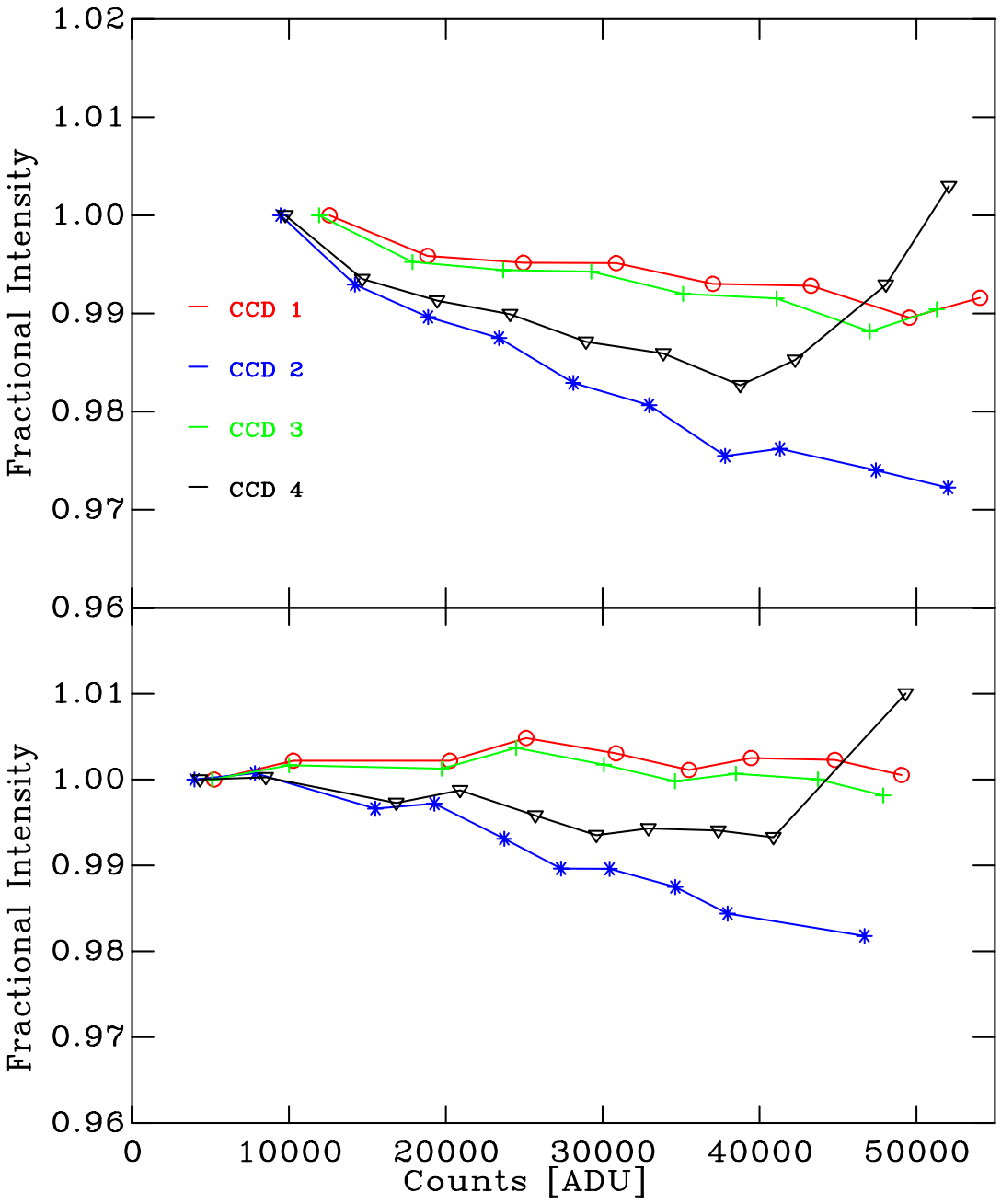

Figure 2.2: Initial linearity curves for the four INT-WFC CCDs for the December 2012 run (top) and November 2013 run (bottom).

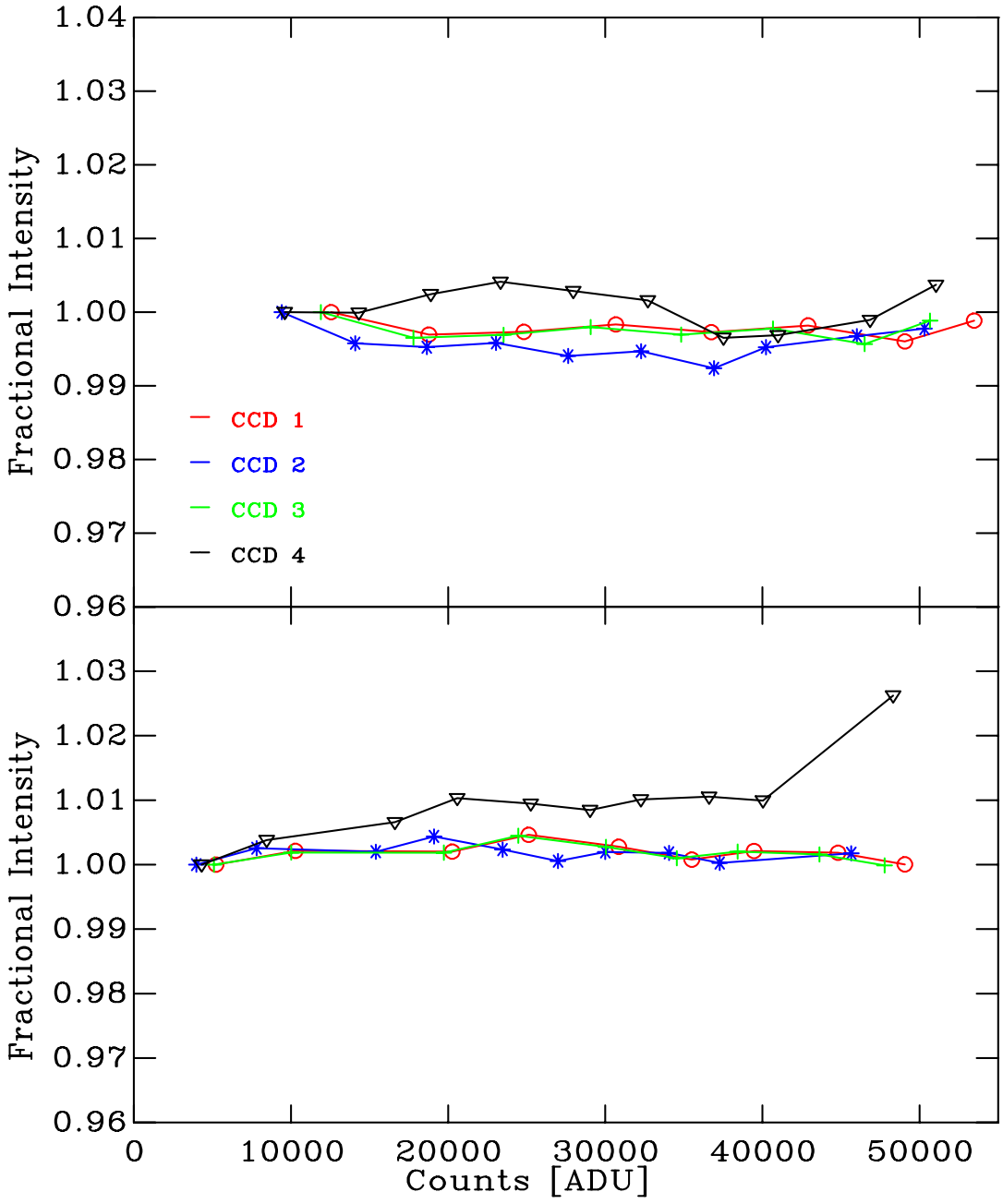

Figure 2.3: Residual linearity curves for the four INT-WFC CCDs for the December 2012 run (top) and November 2013 run (bottom).

Table 2.1: The linearity coefficients derived for each CCD on the 2012 and 2013 INT-WFC runs. The linearity corrections are of the form $y = ax^2 + bx + c$ where x is the measured count and y is the corrected count.

Year	CCD No.	a	b	c
2012	1	0.0	-1.98×10^{-7}	1.0
	2	0.0	-6.27×10^{-7}	1.0
	3	0.0	-2.38×10^{-7}	1.0
	4	3.4×10^{-11}	-2.15×10^{-6}	1.0
2013	1	0.0	4.33×10^{-9}	1.0
	2	0.0	-4.75×10^{-7}	1.0
	3	0.0	-4.75×10^{-8}	1.0
	4	1.19×10^{-11}	-9.95×10^{-7}	1.0

frames they would be removed in the median stack.

2.3.3 Fringe Frames

"Fringing" refers to the interference pattern that can occur on CCD images taken at long optical wavelengths. It is produced when photons reflect within a CCD leading to constructive or destructive interference. This usually occurs longwards of 700 nm, at which wavelengths the light can be internally reflected several times before being absorbed (Lesser 1990). An example of the fringing in the $Z_{\rm WFC}$-band is shown in Figure 2.4. In broadband and narrowband imaging fringing typically occurs due bright night-sky emission lines from atmospheric OH molecules (Howell 2012) and cannot be corrected using dome flats (which are illuminated using polychromatic lights) or twilight sky flats (in which the scattered sunlight will dominate over the sky emission). Instead correcting for fringing is accomplished by use of a "fringe frame" which is typically created by median-stacking sets of deep (long exposure) images together, hence removing stars from the image and leaving behind the fringe pattern. Library fringe frames are available for the INT-WFC, but these date from December 1998. Given that the instrument setup has changed in that time I created my own fringe frame from the long observations taken over the December 2012 run. For the $Z_{\rm WFC}$ frame there were 6×500 second exposures (only one exposure per pointing can be used to ensure stars are removed). To give an odd number of frames for the median stacking two 250 second exposures of the Pleiades were added together to give a 7^{th} frame. For the $i_{\rm WFC}$ frame it was found that combining the 500 second exposures still left stars in the fringe frame, possibly due to saturation in these long exposures. Instead the $i_{\rm WFC}$ fringe frame was constructed by combining 31

Figure 2.4: An example fringe frame for the $Z_{\rm WFC}$-band. A single CCD (CCD4) is shown here for illustration of the fringing effect.

$\times$ 100 s exposures. After median stacking, the fringe frames were then scaled to an exposure time of 1 s to ease calculation of the scaling factor between the fringe frame and data frame. When applying the fringe frame it was scaled to the exposure time of the data frame, the magnitude of the fringing in the data frame was then compared to that in the scaled fringe frame and the scaling factor was refined before subtracting the final scaled fringe frame from the data frame (fringing is an additive process).

2.3.4 Reduction Process

The data were reduced using the CLUSTER package following the method described in Naylor et al. (2002), detailed below. A stacked image was created in the $i_{\rm WFC}$-band by calculating spatial transformations between the long exposures and combining them. The $i_{\rm WFC}$-band was used on the basis of it being the deepest imaging. The sky background was determined by dividing the

CCD into a series of sky boxes. The sky value for any given pixel can then be determined by interpolating between the skyboxes. The interpolated sky was subtracted from each pixel in the image. The histogram of sky values in each skybox was fitted with a skewed Gaussian to determine the standard deviation (σ), used for source detection. The stacked image was then searched to detect objects. Stars are identified as pixels with counts some (user defined) significance above the sky background. These pixels are grouped into stars by applying a simple north-south-east-west connectivity condition (See e.g. Irwin 1997). The search algorithm is iterative, moving from high significance events to the low significance limit ($5 \times \sigma$ for this reduction which ensured we were complete to a signal-to-noise of 10). This iterative process allows for the detection of faint stars in the wings of bright stars, which would be identified as a single object by the connectivity condition in a single low significance pass. New stars on each pass are added to the source list only if they do not include the central pixel of a previously detected star. Duplicates were identified, and removed, by examining whether a star lies within a distance equal to twice the seeing (with the seeing estimated as the full width half maximum of the point spread function) of another star. Some quality flags are introduced at this point in the reduction process (see Table 2.2 for the full list of flags). Stars containing saturated pixels are flagged "S", stars with pixels above the linearity limit are flagged "L" and a non-stellar flag,"N", is also introduced. The non-stellar flag is determined by comparing the flux in a large aperture around the star to that in a small aperture. The large aperture size is taken to be the same as the seeing and the small aperture is taken as half this value. If the ratio of the flux in the large aperture to that in the small aperture is larger than 3σ of the median (where σ here is the sum in quadrature of the uncertainty in each measurement and the RMS about the median) the source was flagged non-stellar.

Table 2.2: A list of the photometric flags applied to the catalogues during the reduction process. The flags in the catalogues are given as two-character strings. For colours (e.g. $(g-i)_{\rm WFC}$) one character comes from each of the two filters which make up the colour. The order of the flags is the same as the order of the colour, e.g. for $(g-i)_{\rm WFC}$ the $g_{\rm WFC}$ flag comes first and the $i_{\rm WFC}$ flag second. For magnitudes (e.g. $g_{\rm WFC}$) in the natural system (and which therefore have been constructed without using colour terms) the first character is always "O", and the second is the flag for that filter.

Flag	Flag Name	Flag Information
O	O.K.	Clean detection.
S	Saturated pixel	At least one pixel within star is saturated.
L	Linearity	Counts above detector linearity limit.
F	Bad (Flagged) pixel	Star lies on known bad pixel(s).
R	Uncalibrated Region	Star lies in a region known to have poor flatfielding.
W	CroWding Test	"Star" is an inserted point used to test for effects of crowding.
N	Non-stellar	Object has non-stellar flux distribution, determined by comparing flux in a small aperture to that in a large aperture
B	Background fit failed	Unable to fit the sky background.
I	Ill-determined background	Sky background fit is highly skewed.
P	Position fit failed	Unable to accurately determine star position.
E	Edge	Star is too close to detector edge
M	Negative (Minus) counts	Object has negative counts after sky subtraction
A	Absent input data	No input data present in this band
H	Poor profile correction	Profile correction for frame is poorly determined.
T	AperTure photometry	Magnitude determined from aperture photometry instead of optimal photometry
V	Variable	Determined by comparing multiple frames. Object has high χ^2 (usually > 10)
C	Cloudy	Frame has large relative transparency correction
G	Poor seeing	Frame has large seeing value (usually defined as > 3.3").
Z	No photometric calibration	Magnitudes are raw instrumental values

The shorter images were then searched to identify the stars which were flagged saturated or non-linear in the deep stack. If the saturated/non-linear stars were not flagged in the short images the flags are removed from the master star list, as the photometry from the short frames will be reliable.

2.3.5 Optimal Photometry

Having established a list of target sources from the deep stack I then used the optimal extraction method detailed in (Naylor 1998; Naylor et al. 2002) to perform photometry. In optimal photometry each pixel in a star is taken as an independent estimate of the total flux such that, assuming the profile of the star is well estimated, the total flux can be recovered by comparing the flux in the pixel with the fraction of the total flux expected in that pixel based on the stellar profile. The extraction of total flux is then optimised by weighting the estimate of total flux from each pixel by the inverse of the square of its uncertainty before combining them. The sky level is determined for each target star in a similar manner to that discussed previously, taking a skybox around the star and fitting the histogram of values with a skewed Gaussian. The sky boxes are chosen to be large enough that, when the sky determination is subtracted from a star, the uncertainty due to sky measurement is small (See Naylor et al. 2002, for a discussion on required sky box sizes).

The profile to be used for the optimal extraction (extraction mask) can be estimated with the PSF. To determine the PSF the 49 brightest, unflagged stars in the image were taken as potential PSF stars. These stars are fitted with elliptical Gaussians and the parameters are adopted for the star with the median value of the geometric mean FWHM. This PSF together with the variance in the pixels is used to construct the extraction mask. To prevent it extending out to infinity this extraction mask is "clipped" at some value, beyond which the mask value is set to zero. For this reduction the clipping radius was set at twice the FWHM which is a conservative estimate to maximise the signal-to-noise in a low-crowding environment (See King et al. 2013, for a discussion of the clipping radius for crowded regions). Photometry was performed on each image individually rather than on the stack. The advantage here is one can avoid compromising the signal-to-noise ratio of good images by combining them with images with poor seeing or high sky background.

After performing the optimal photometry the next stage was to derive and apply the profile corrections. Profile corrections are analogous to the aperture corrections used in traditional aperture photometry. In this case the profile correction can be best imagined as the difference between

the extraction mask and the true stellar profile. Thus if the mask were perfect the profile corrections would be zero but this is unlikely to be the case. The profile corrections were derived by comparing the magnitude derived from the optimal extraction to that derived from aperture photometry using a sufficiently large aperture. The CCD was divided into boxes, with the brightest star in each box being used to determine the profile correction. The profile corrections were fit with a low-order polynomial which allowed the corrections to be defined as a function of CCD position. These profile corrections were then applied to all stars in the frame. An example of the derived profile corrections is shown in Figure 2.5.

2.3.6 Photometric Calibration

At this point in the reduction process profile-corrected magnitudes had been derived for stars in each individual frame. Each image was then corrected to the mean airmass of the group of images using extinction coefficients derived from the standard star observations (See Section 2.3.6). The difference in transparency between the images was then corrected by calculating relative transparency corrections. These relative transparency corrections represent a measure of how accurate the profile corrections were, and how photometric the observing conditions had been. One image for each filter was arbitrarily chosen as the "master" frame. For each other image in that filter a list of stars in common with the master frame was created. The non-flagged common stars were used to calculate the weighted mean of the difference between the image and the master frame. To pull all of the images (including the master) to the mean transparency for the group, each image was corrected by its relative transparency correction (zero for the master frame) minus the average relative correction.

The transparency-corrected magnitudes for repeated measurements of each star in a given filter were combined by taking a weighted mean (in flux space). The reduced-χ^2 was calculated for each star and the distribution of χ^2 vs signal-to-noise used to test the estimation of the uncertainties. If the uncertainties were underestimated the distribution would rise to high χ^2 at high signal-to-noise and conversely if the uncertainties were overestimated the distribution would fall at high signal-to-noise. An additional, magnitude-independent uncertainty was added to the statistical uncertainties at this point to ensure the χ^2 distribution was flat (See Figure 2.6. This added uncertainty was $\simeq$0.01 mag for both runs. These magnitudes were combined to yield colours. The colours and magnitudes were corrected to an airmass of 1.0, again using the extinction coefficients

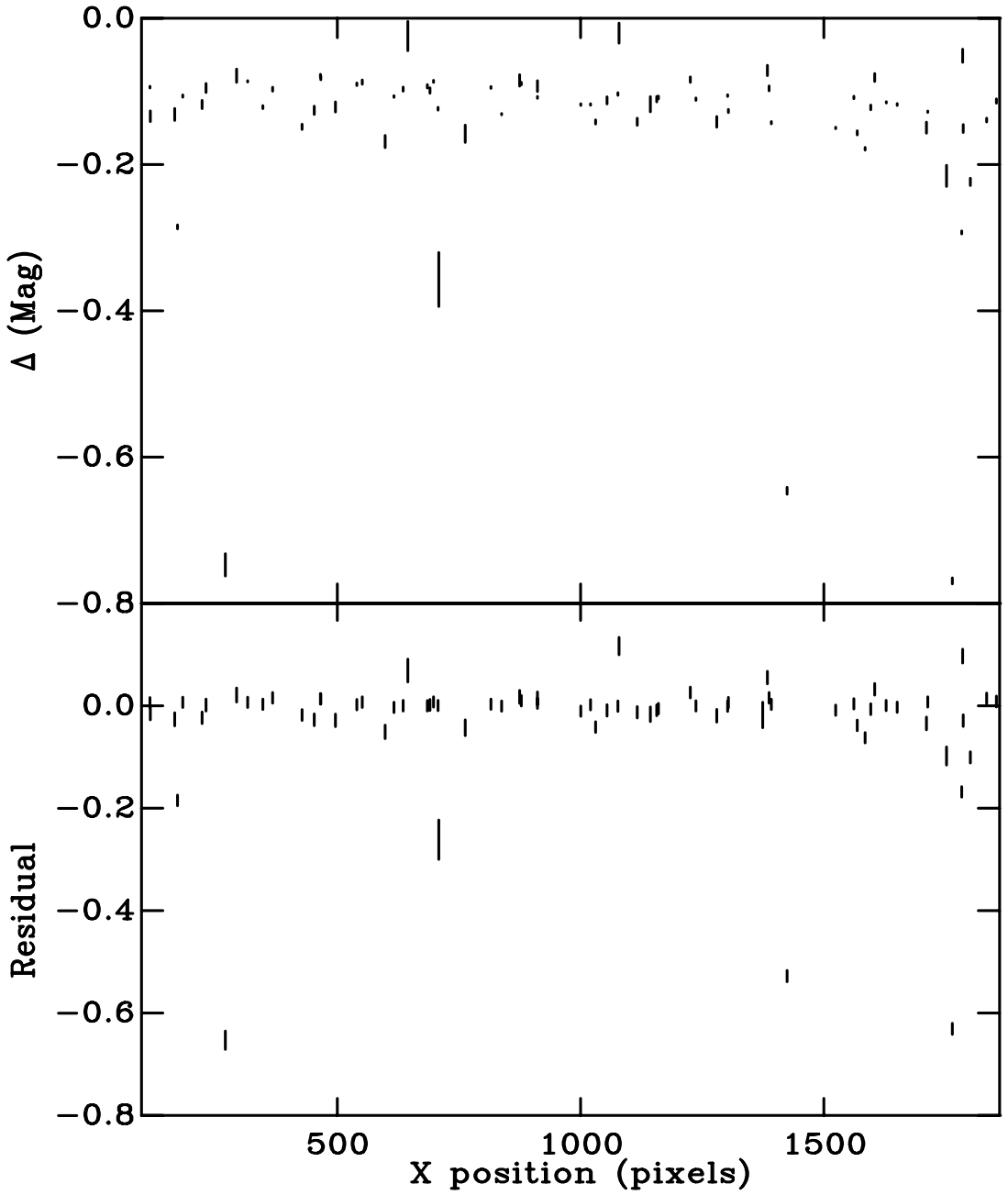

Figure 2.5: (Top): An example of the typical profile corrections as a function of X position on the CCD showing the spatial variation. (Bottom): The residuals of the profile corrections from the polynomial fit. The vertical size of the symbols indicates the uncertainty on each.

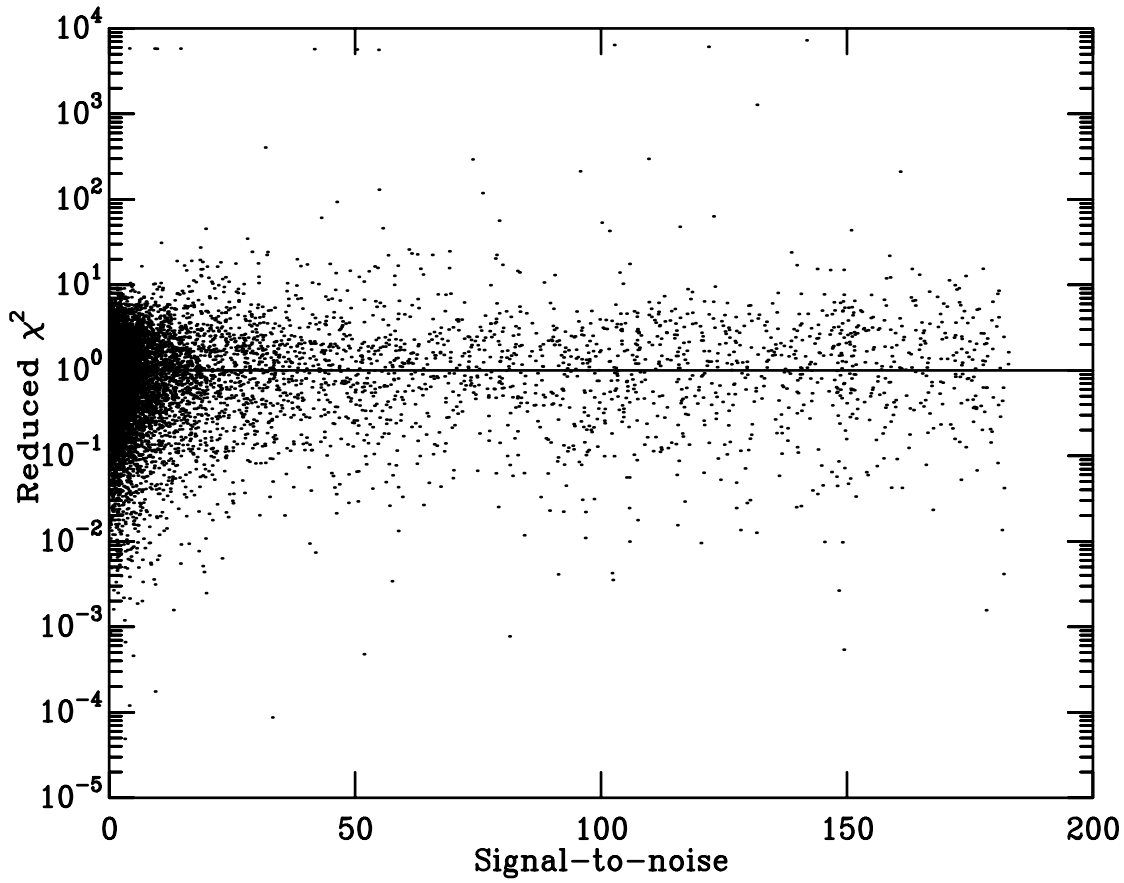

Figure 2.6: A plot of reduced-χ^2 vs signal-to-noise for the stars in one of the Pleiades fields (Field K). The solid line denotes a reduced-χ^2 of 1.

derived from the standard stars.

Standard Star Fields

Standard star observations were made of the same Sloan Digital Sky Survey (SDSS) Stripe 82 fields presented in Bell et al. (2012). For the December 2012 observations a further field was required, which would be at low airmass at the end of the night (when the existing standard fields were setting). The existing fields (referred to as Sloan 1-4) were at RAs of 20.8h, 23h, 1.5h and 4h. The new field, Sloan 6, was chosen at an RA 7.7h. The SDSS Stripe 82 does not extend to this RA and so the field was drawn from the full SDSS catalogue.

Bell et al. (2012) presented an estimate of the INT-WFC system responses, which were used to calculate transformations between the WFC and standard SDSS photometric systems. For an example of how these transformations were calculated in a different photometric system see Chapter 7. In traditional photometry the data are transformed from instrumental magnitudes and

colours to a standard system using observations of standard stars. This is accomplished using equations of the form:

$$g_{\text{standard}} = \phi_g(g-i)_{\text{instrumental}} - K_g\chi + Z_g, \tag{2.1}$$

$$(g-i)_{\text{standard}} = \phi_{g-i}(g-i)_{\text{instrumental}} - K_{g-i}\chi + Z_{g-i}, \tag{2.2}$$

where ϕ is the colour term, K is the extinction coefficient, χ is the airmass and Z the zeropoint.

However if the system responses of the observing system and the standard system are not exactly matched the photometric transformations will no longer be valid (see e.g. Sung & Bessell 2000). Bell et al. (2012) showed that there is no simple linear transformation between the INT-WFC system and the SDSS system, which is unsurprising given the differences in the filter bands. Bell et al. also showed that no single transformation exists that can transform INT-WFC observations of both MS and PMS red ($(g-i)_{\text{SDSS}} \geq 1.8$) stars into the SDSS photometric system. This is due to the differences in spectra between MS and PMS stars of the same colour. Thus applying MS-derived transformations to the photometric catalogue would result in PMS stars lying in the incorrect place in the CMD. Instead the data must be left in the natural photometric system. The traditional photometric calibration method (Equations 2.1 and 2.2) can still be used to derive the frame zeropoints and atmospheric extinctions with the colour terms set to zero. To calibrate the WFC data the observed standard star fields were reduced in the manner discussed in the above sections. An astrometric solution was applied (see Section 2.3.7). Data for the same field were then downloaded from the SDSS. The MS stars were isolated by applying a series of color-colour cuts to the SDSS data (see Section 7 for details on the colour cuts). The SDSS MS catalogue was then transformed into the WFC system using the transformations defined in Bell et al. (2012). The stars common between the WFC and transformed SDSS catalogues were then used to define the zeropoints and atmospheric extinction terms.

2.3.7 Astrometric Calibration

An astrometric solution was calculated using by matching stars in the catalogue to a reference catalogue of the same field from the Two-Micron All-Sky Survey (2MASS, Cutri et al. 2003). A six-coefficient model was used to transform from pixel coordinates to J2000.0 coordinates.

For regions covered by a mosaic of multiple fields-of-view the individual fields were reduced separately. The astrometric solution was used to identify common stars in the overlap re-

gions. These were used to calculate mean inter-field shifts. The zeropoints of the non-photometric fields were then allowed to float and adjusted to minimise the differences. The zeropoint shifts are an indicator of the internal consistency of the photometry, and suggested an accuracy of $\simeq$2%.

3

Constructing and Using Semi-empirical Models in the INT-WFC System

3.1 Motivation

It is a well known problem that the evolutionary models of PMS stars fail to match observations at low $T_{\rm eff}$ (see e.g. Bell et al. 2012; Herczeg & Hillenbrand 2015). The source of this discrepancy is still unclear, but suggestions include missing sources of opacity in the model atmospheres (Chabrier et al. 2000; Stauffer et al. 2007), and magnetic activity inhibiting convection (Feiden 2016). In an attempt to mitigate this problem Bell et al. (2013, 2014) presented a set of semi-empirical models, and showed that they can be used to derive robust PMS ages which agree with those derived using other age techniques. The semi-empirical models were constructed by taking the interior models of Baraffe et al. (1998), Dotter et al. (2008) and Tognelli et al. (2011), applying the model atmospheres of Allard et al. (2011) and introducing an empirical correction to the BCs at low $T_{\rm eff}(\lesssim 4500$ K) to ensure the models match observations of a fiducial cluster (effectively

adopting an empirical colour-$T_{\rm eff}$ relationship at low $T_{\rm eff}$). The fiducial cluster must have a well constrained age and distance derived from a method independent of fitting the PMS, thus Bell et al. (2013) used the Pleiades. The resulting semi-empirical models are only valid for use in the same photometric system as the observations of the fiducial cluster, which for Bell et al. (2013) is the INT-WFC system. In this Chapter I will present an extension to the INT-WFC semi-empirical models using the previously discussed INT-WFC observervations. These models will then be used to derive the age of one of the young clusters observed with the WFC, NGC2264. In Section 3.2 the observations used in this chapter are introduced. The evolutionary models and reddening laws used are discussed in Section 3.3. The process of creating the semi-empirical models is outlined in Section 3.4 and in Section 3.5 these models are used to derive the age of NGC 2264.

3.2 The Data

The $(griZ)_{\rm WFC}$ data used for this analysis were a combination of the Pleiades observations discussed in Bell et al. (2012) and new INT-WFC observations. The new data were obtained as part of the December 2012 INT-WFC run (see Section 2.2). The data included 5 newly observed fields in the Pleiades adjoining the Bell fields. Additionally the new data included a set of deep observations in $(riZ)_{\rm WFC}$ of the previously observed Pleiades A field. The observed fields, including the Bell observations, are shown in Figure 3.1. The additional fields were chosen based on those known to include low-mass members to allow the shape of the lower PMS locus to be better constrained. The addition of extra fields shifts the photometric normalisation of the original Bell data by less than 0.04 mags in all filters. The K-band data used for calculating the empirical corrections were taken from 2MASS and the UKIRT Infrared Deep Sky Survey (UKIDSS; Lawrence et al. 2007) Galactic Cluster Survey (GCS).

The catalogue of Pleiades members was created by cross-matching the photometry catalogue with the combined membership lists of Stauffer et al. (2007) and Lodieu et al. (2012). The Stauffer catalogue is a made up from a combination of surveys combined with proper motion data to calculate membership probabilities (see Appendix A1 of Stauffer et al. 2007, for a discussion of the catalogues used). The Stauffer catalogue does not extend faint enough for our own Pleiades survey, and so the Lodieu catalogue is used to provide a low-mass member list. The Lodieu catalogue is based on the UKIDSS GCS. The GCS included multiple epochs of K-band data, allowing

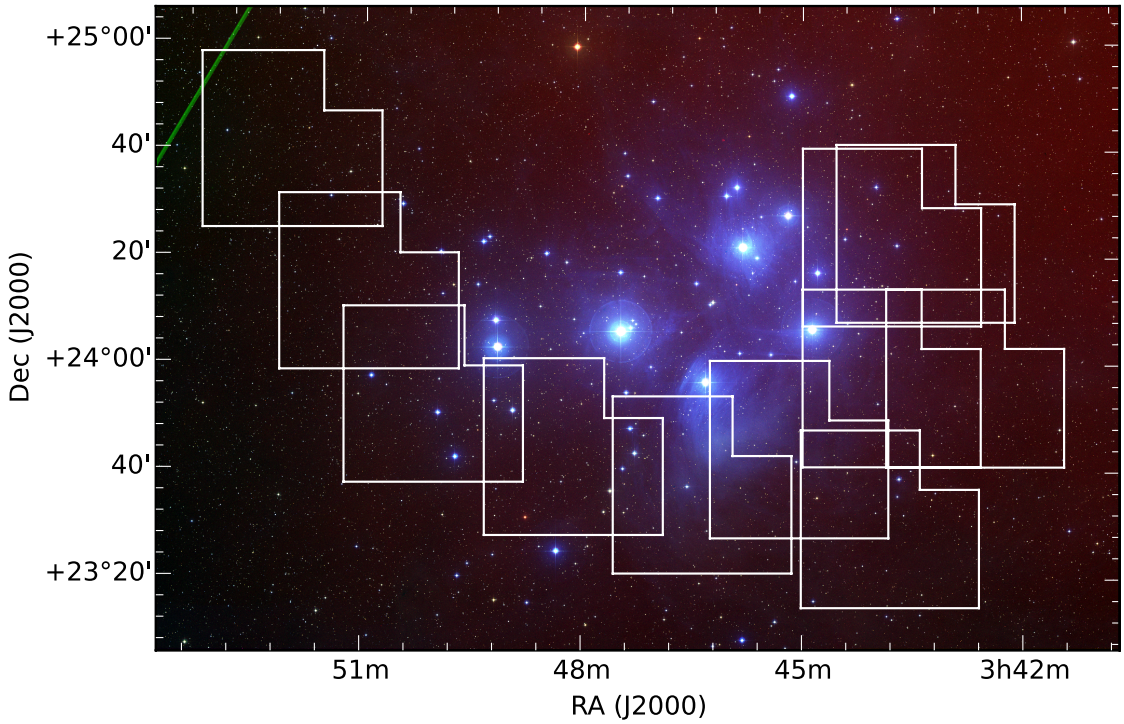

Figure 3.1: Observed INT-WFC fields in the Pleiades overlayed on a three-colour mosaic image of the Pleiades from the Digitised Sky Survey. Fields A-F are those from Bell et al. (2012). Fields H-L are new data from the December 2012 observing run.

for the inclusion of proper motions, which were used to define the Lodieu membership list.

3.3 The Models

The models are created from a combination of interior and atmospheric models. The PMS interior models used were the same as those adopted in Bell et al. (2012, 2013), namely the Baraffe et al. (1998) using the solar calibrated mixing length ($\alpha = 1.9$) and the Dotter et al. (2008) models (hereafter the BCAH98 and DCJ08 models respectively). The atmospheric models used here are again those used in Bell et al. (2012, 2013), the PHOENIX BT-Settl models (Allard et al. 2011)[1]. We note that there are now updated theoretical models from Baraffe et al. (2015), however we do not use them in this chapter. The Baraffe et al. (2015) models and the BCAH98/Allard2011 combination after tuning appear similar (see Bell et al. 2015), but by continuing to use the BCAH98 models we can ensure consistency with the ages derived in Bell et al. (2013).

[1] http://phoenix.ens-lyon.fr/Grids/BT-Settl/

3.3.1 Reddening vectors

It is well known that the effective wavelength of a filter varies depending on how the flux distribution across the filter varies. The effective filter wavelength will therefore vary with the flux distribution of a star. We see the same effect in reddening i.e. a given amount of dust obscuration will produce a larger $E(B-V)$ value for OB stars than for GK stars (Bessell et al. 1998). Equivalently, for a nominal $E(B-V)$ the resultant extinction in a given filter will vary with temperature. Therefore before discussing reddening, it is necessary to define what is meant by $E(B-V)$. I will adopt the notation $E^{\rm Hot}_{B-V}$, i.e. the $E(B-V)$ that would be measured for a hot ($T_{\rm eff}$ = 10,000K) star.

The reddening law used was that of Fitzpatrick (1999) (hereafter F99), adopting $R_{\rm V}$=3.1. To take account of the effect of $T_{\rm eff}$ on the reddening vectors, extinction tables were created. To do this the atmospheric models were reddened in steps of 0.5 from $E^{\rm Hot}_{B-V}$=0.0 to 2.0 mag and folded through the system responses to calculate the extinction in the given filter (A_λ) as a function of $T_{\rm eff}$ and $\log(g)$. To apply the extinction tables when reddening an isochrone the values were interpolated to the required $E^{\rm Hot}_{B-V}$, $T_{\rm eff}$ and $\log(g)$ values for each theoretical star in the isochrone.

Bell et al. (2012, 2013) used the reddening law of Cardelli et al. (1989) (hereafter CCM). The CCM law has been derived using a set of assumed filter wavelengths. In the near-IR these adopted wavelengths are not consistent with the now-ubiquitous 2MASS filters, in particular the H-band. Cardelli et al. adopted values of λ of 1.25, 1.59 and 2.17 μm for the J, H and K filters respectively, compared to the values from (Cohen et al. 2003) of 1.235, 1.662, and 2.159 μm. The F99 reddening law will be compared to the reddening law of CCM in Section 5.1.5 to ensure consistency with the Bell age scale.

3.4 Constructing the Semi-Empirical Models

The models were constructed using the Pleiades as the fiducial cluster. Bell et al. (2012) used main-sequence binaries (which have dynamical masses) to show that the models predict K-band luminosities well, but the discrepancies between the models and data grow as one moves towards blue wavelengths. It is therefore possible to use the K-band luminosity of a star to determine its mass and quantify the difference between the model-predicted and observed magnitude in other filters. In practice the best method of achieving this is plotting the fiducial cluster in a K, $K-m_\lambda$ CMD. The sequence can then be used to define the observed single-star sequence (remembering

that binaries manifest themselves as a spread above the single-star sequence). The models should match the K-band, and so the observed mismatch between the model and the data can be entirely ascribed to the m_λ filter. Thus by working through a variety of CMDs it is possible to quantify the discrepancy as a function of filter, and empirically correct the BC for that filter.

As an example, taking the $K_{\rm 2MASS}$, ($g_{\rm WFC}$-$K_{\rm 2MASS}$) CMD the Pleiades members were plotted and a spline was fit by eye to the single-star sequence. The model isochrone was overlaid, adopting model parameters of age=130 Myr (Barrado y Navascués et al. 2004), distance modulus dm=5.63 (Soderblom et al. 2005) and $E^{\rm Hot}_{B-V}$=0.04 (Stauffer et al. 1998). It should be noted that an alternative space-based parallax distance for the Pleiades was calculated by the *Hipparcos* mission. In this work the *Hipparcos* parallax was disregarded. The Soderblom et al. (2005) parallax measurement agrees, within uncertainties, with other distance measurements (e.g. Pinsonneault et al. 1998; Gatewood et al. 2000; Pan et al. 2004) suggesting that the *Hipparcos* distance suffers from undiagnosed errors. Even the revised *Hipparcos* measurement of (van Leeuwen 2009) is more than 0.2 mag smaller than other estimates.

The difference between the observed spline and the model isochrone was then calculated as a function of $T_{\rm eff}$. This difference was then applied as a correction (ΔBC) to the $g_{\rm WFC}$-band bolometric corrections. Working through a number of CMDs, the ΔBCs were calculated for the set of $(griZ)_{\rm WFC}$ filters. The calculated ΔBCs are shown in Figure 3.3. The $g_{\rm WFC}$and $r_{\rm WFC}$$\Delta$BCs were fundamentally unchanged from those presented in Bell et al. (2012) as the extra fields served only to fill in and better define the observed sequence. However in $i_{\rm WFC}$and $Z_{\rm WFC}$the 2012 data were significantly deeper than those in 2007/2008. It was therefore possible to define the observed spline to much lower $T_{\rm eff}$than that presented in Bell et al. (2012). In fact the lowest mass $(iZ)_{\rm WFC}$ members were too faint to have reliable 2MASS data, and therefore required an alternative source for the K-band data.

UKIDSS was the ideal choice for deep K-band data. UKIDSS uses a similar filter set to 2MASS, but focussed on deeper photometry at the cost of limited sky coverage. Bell et al. used main-sequence binary stars to show that the models reproduce K-band magnitudes well, down to a mass of 0.1 $M_\odot$. With the UKIDSS data it was possible to tune the models below this limit, and so it was necessary to test whether the models were still able to reproduce the K-band magnitudes of stars at these lower masses. Due to a lack of binary stars of sufficiently low mass, a different diagnostic was used. As mentioned previously the data-model discrepancies decrease as

one moves to longer wavelengths. In the K-band the effect is minimal down to 0.1 $M_{\odot}$. The effect would be expected to be even smaller at longer wavelengths, such as the *S pitzer* IRAC bands (3.6-8.0 μm). *S pitzer* photometry was therefore used to construct CMDs to test the $K_{\rm UKIDSS}$-band to lower masses.

The Pleiades membership list was matched against Spitzer photometry of the region and the UKIDSS Pleiades GCS catalogue, and a $K_{\rm UKIDSS}$ vs $K_{\rm UKIDSS} - [3.6]$ CMD was plotted (Figure 3.2). The BCAH98/Allard2011 and Pisa/Allard2011 isochrones were overlaid. The DCJ08 models have a lower mass limit of $0.1 M_{\odot}$, and so were unsuitable for this test. Figure 3.2 show that the models predicted the observed $K_{\rm UKIDSS}$ magnitudes well at low masses, down to the limiting mass of the theoretical models ($0.03 M_{\odot}$for BCAH98, 0.08 for Pisa). Although the fit seems to be poor at high masses, this is likely an issue with residual saturation in the UKIDSS sample, as it has already been demonstrated by Bell et al. (2012) that the models well reproduce observations at this mass. The ΔBCs were calculated for the $i_{\rm WFC}$and $Z_{\rm WFC}$bands using the $K_{\rm UKIDSS}$-band. The ΔBCs calculated for the BCAH98 models are shown in Figure 3.3 and are consistent with those found in (Bell et al. 2012). The resulting tuned $i_{\rm WFC}$, $(i-Z)_{\rm WFC}$CMD is shown in Figure 3.4.

Given that the semi-empirical models are created with reference to the Pleiades, which has an age of 130 Myr, one might question the validity of the models to cluster of a much younger age especially given that the younger stars will have a very different $\log(g)$ to that of the older Pleiades. However the underlying atmospheric models already include corrections for surface gravity and other age effects. In fact the only assumption that is made for the semi-empirical models is that the discrepancies, whatever the source may be, are independent of age. Given that Bell et al. (2013) show good agreement between the UMS and PMS ages using these models, it seems this assumption is valid.

3.5 Determining the Age of NGC 2264

3.5.1 Introduction to NGC 2264

NGC 2264 is a well-studied young cluster (see Dahm 2008, for a review). Typical age estimates are around 3 Myr (Walker 1956; Sung et al. 2004), although recently Turner (2012) derived an age of 5.5 Myr from the PMS and a single UMS star. The combination of low reddening ($E^{\rm Hot}_{B-V}$=0.075; e.g. Turner 2012) and relatively low distance (738 pc Kamezaki et al. 2014) have made it a popular

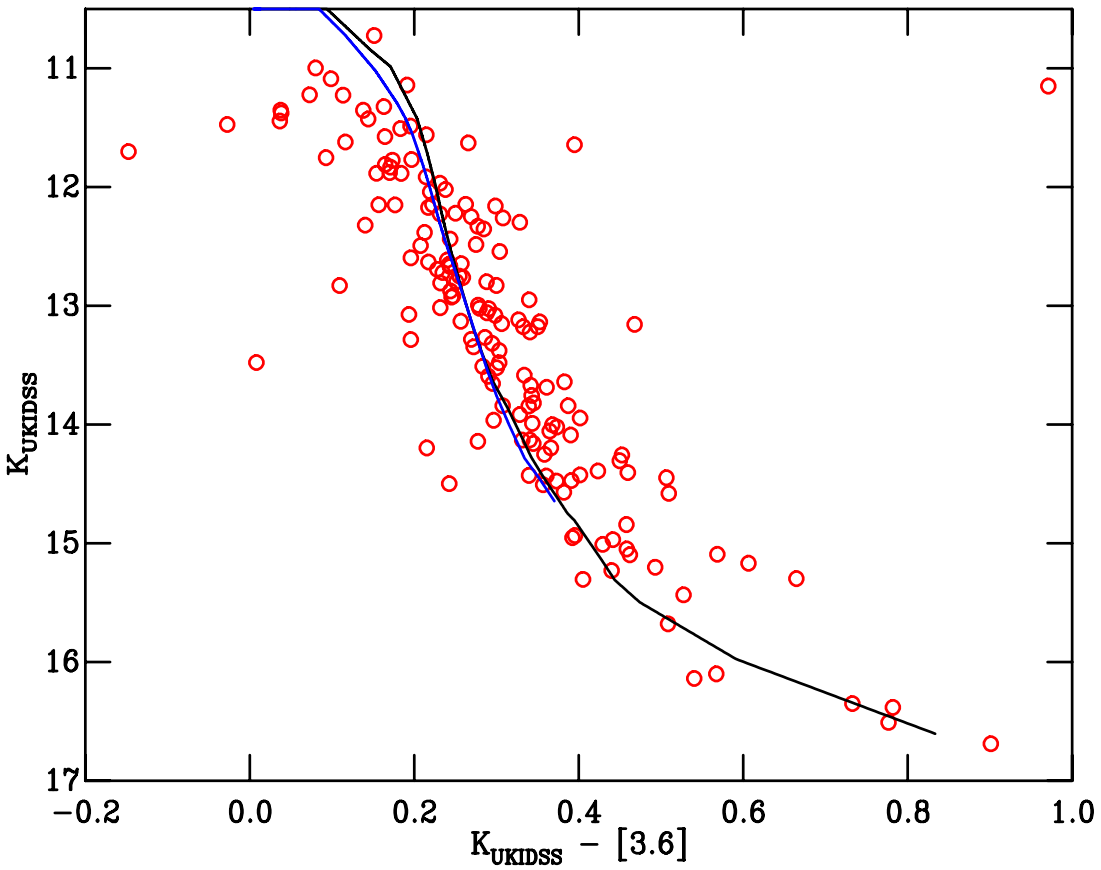

Figure 3.2: K_{UKIDSS}, K_{UKIDSS} - [3.6] CMD for Pleiades members. Overlaid are BCAH98 (black) and Pisa (blue) isochrones, both using the Allard2011 atmospheres.

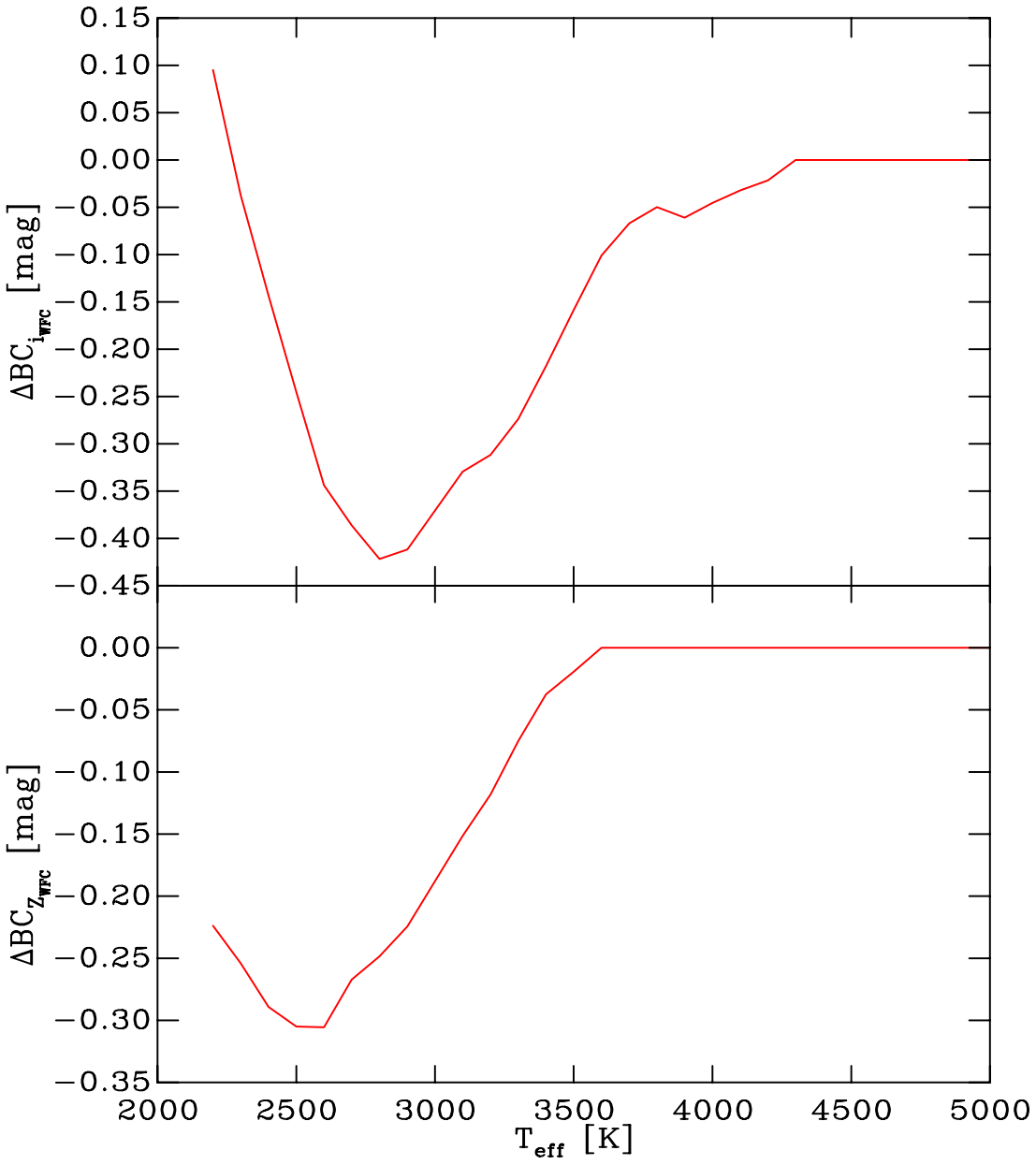

Figure 3.3: ΔBCs calculated in the $i_{\rm WFC}$ and $Z_{\rm WFC}$ bands as a function of $T_{\rm eff}$ for the BCAH98 models.

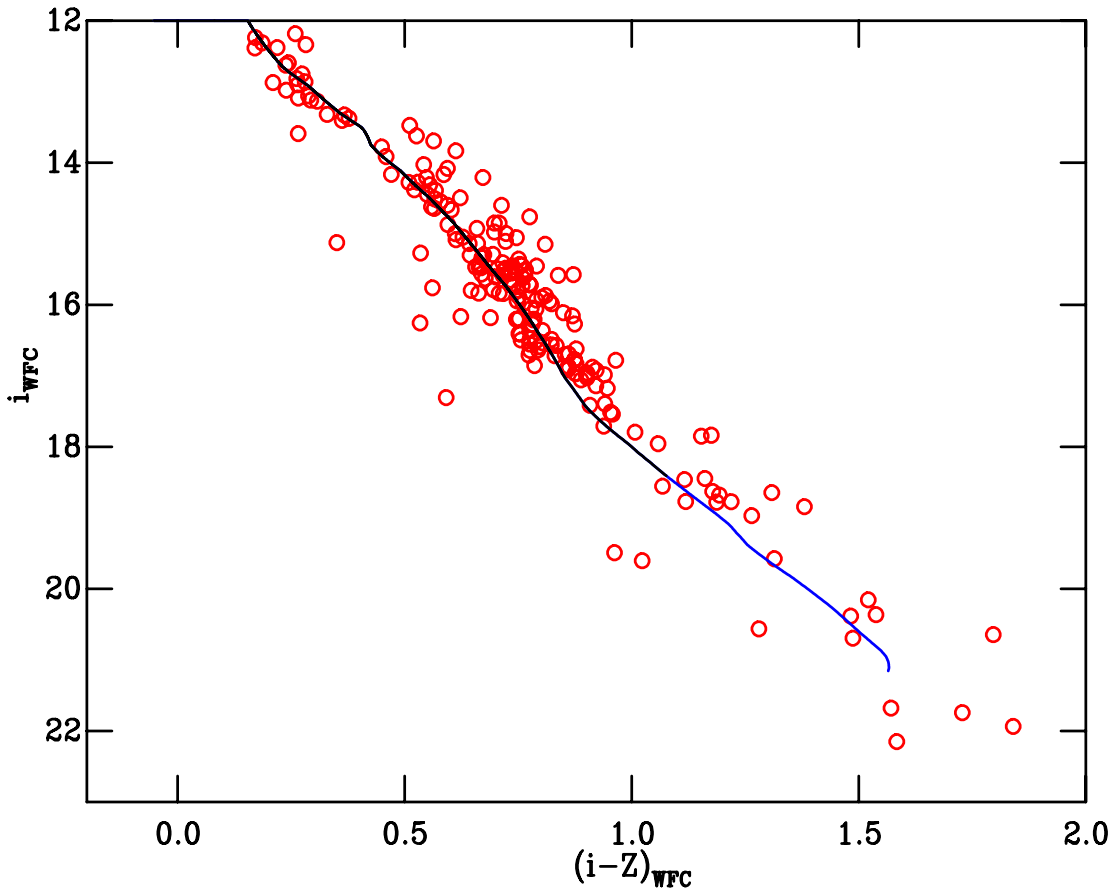

Figure 3.4: $i_{\rm WFC}$, $(i-Z)_{\rm WFC}$CMD for Pleiades members with extended semi-empirical BCAH98 and Pisa isochrones overlaid. Note that the DCJ08 isochrones have a lower mass limit of 0.1 $M_{\odot}$ and so no extension was added.

target for studies across a range of wavelengths (e.g. Margulis et al. 1989; Rebull et al. 2002; Sung et al. 2008, 2009; Buckle & Richer 2015; Stauffer et al. 2016). Determining a robust age for NGC 2264 is therefore of great interest.

3.5.2 The Data

The $(griZ)_{\rm WFC}$data were obtained over the December 2012 observing run, with the reduction performed as described in Chapter 2. The observed fields and exposure times are given in Table A.3.

3.5.3 Membership, Extinction and Distance of NGC 2264

Cluster member identifications were taken from Jackson et al. (2016). Jackson et al. used spectra from the Gaia-ESO Survey to determine probabilistic cluster memberships. Target stars were chosen from CMDs, but utilising a broad region in CMD space so as to avoid excluding potential members. To derive the membership probabilities the RV distribution of the potential member stars was fit with of a pair of quasi-Gaussian distributions, one describing the cluster members and the second, broader distribution, describing a background population. Jackson et al. presented a set of 226 high-confidence cluster members with literature rotation periods, and these were the members adopted in this work.

Turner (2012) used UBV data combined with isochrone fitting to measure the extinction to NGC 2264, deriving a value $E^{\rm Hot}_{B-V}$= 0.075. Turner et al. also determined the distance of NGC 2264 to be 777±12 pc from the same fitting. This distance is consistent with other measurements of the distance to NGC 2264 including those of Kamezaki et al. (2014), who used parallax measurements to derive a value of 738±45 pc, and Sung et al. (1997), who measured a distance of 760±49 from ZAMS fitting.

3.5.4 Determining an Age

To ensure that the derived age is consistent with those in Bell et al. (2013) the age of NGC 2264 was derived in the same manner. Bell used τ^2 fitting (see Section 4.3.3 for an example) to determine the ages of older (>10 Myr) clusters. For the younger clusters Bell determined "nominal ages" because at young ages (<10 Myr) the PMS sequence exhibits a pronounced spread. This luminosity spread was discussed in Section 1.3. For these young clusters τ^2 fitting is not a valid approach because the

source of the luminosity spread is not well understood. Instead the cluster sequence was compared by-eye to the single-star models. Due to the differing extinctions and distances of the sample of clusters in Bell et al. (2013) (which results in effectively probing different mass ranges in each cluster), Bell adopted their nominal ages by using the position of a 0.75 $M_{\odot}$ theoretical star as the measurement location. To ensure consistency with the Bell age scale the same process was adopted here.

The $g_{\rm WFC}$, $(g-i)_{\rm WFC}$CMD with the model isochrones overlaid is shown in Figure 3.5, using the members from Jackson et al. The isochrones were reddened by an $E^{\rm Hot}_{B-V}$of 0.075 (Turner 2012), and dm=9.45 was added to transform the isochrone from absolute to apparent magnitude. Comparing the location of the 0.75 $M_{\odot}$ point to the middle of the sequences yields a best-fit of 3-4 Myr from each of the models.

3.5.5 Disc Fraction

Bell et al. (2013) presented a plot of disc fraction against age for the clusters in their sample. As the age derived for NGC 2264 is in the same system as those in Bell et al. it was possible to place NGC 2264 on this disc diagram.

Bell et al. adopted the disc fraction determined from late-type stars, with spectral types of late-K to early-M, to account for the known variation of disc fraction with spectral type or mass (see e.g. Luhman et al. 2008; Kennedy & Kenyon 2009). Sung et al. (2009) used *Spitzer* data to determine the disc fraction in NGC 2264. For the low mass (i.e. late type) population they found a disc fraction of 0.37±0.05. Figure 3.6 shows NGC 2264 added to the disc fraction plot of Bell et al, from which it is clear that NGC 2264 is consistent with the Bell et al. clusters in terms of the declining disc fraction with age.

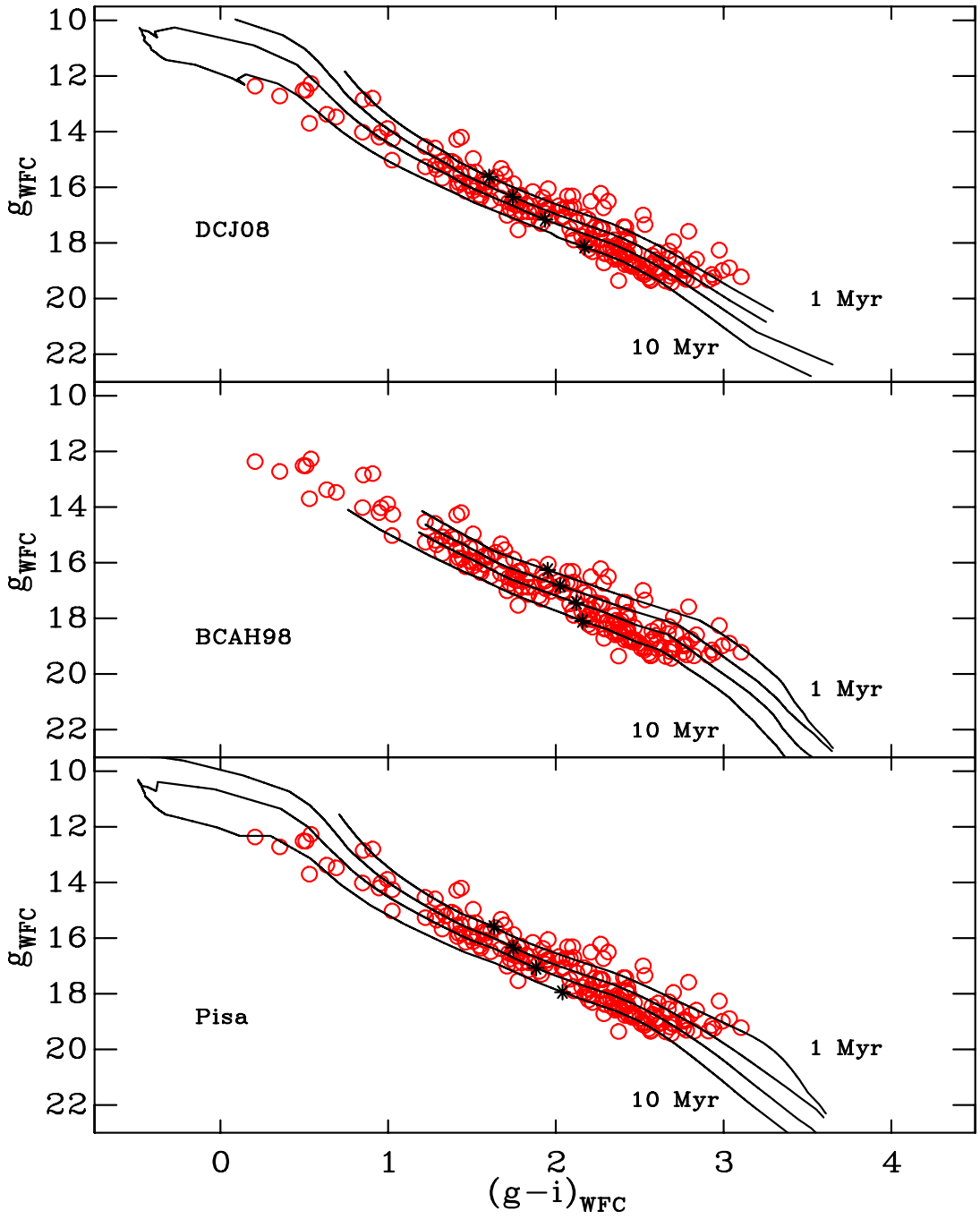

Figure 3.5: $g_{\rm WFC}$, $(g-i)_{\rm WFC}$CMDs for NGC2264 adopting the memberships from Jackson et al. (2016). Overlaid are isochrones for ages of 1, 2, 4 and 10 Myr according to the DCJ08 (top), BCAH98 (middle) and Pisa (bottom) models, after applying the empirical correction described in Section 3.4. The asterisks indicate the position of a theoretical 0.75 $M_{\odot}$ star.

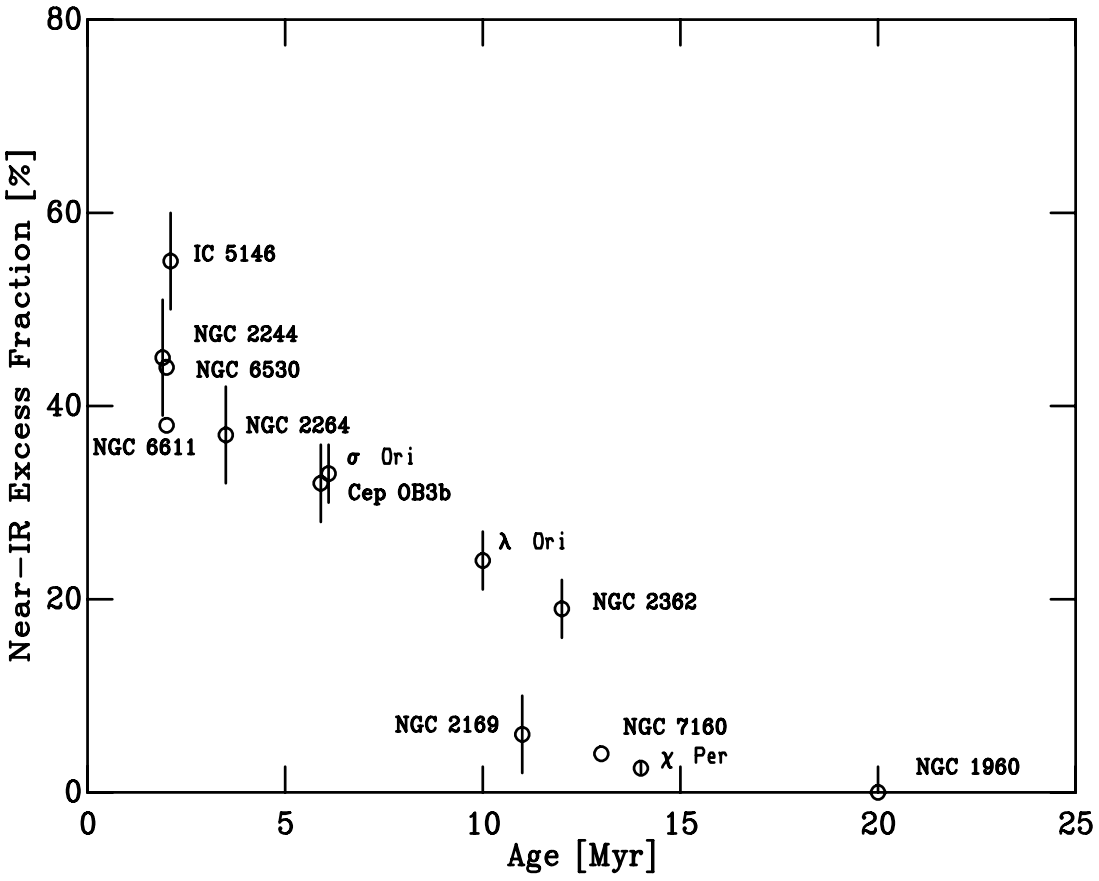

Figure 3.6: Disc fraction (based on near-infrared excess) vs age for the clusters from Bell et al. (2013) and NGC 2264. Note that the ages for IC5146, NGC2244, σ Ori, and CepOB3b have been shifted slightly to better display the uncertainties in the disc fractions.

4

Semi-empirical Models in the SDSS, 2MASS and UKIDSS Systems

4.1 Motivation

Chapter 3 presented the construction of semi-empirical ("tuned") model isochrones in the INT-WFC system. These isochrones are only valid in the photometric system of the INT-WFC which would require observations of target clusters taken in the same system. This is a limiting factor in the usefulness of the semi-empirical models. In this chapter a set of tuned models are constructed in the SDSS, 2MASS and UKIDSS photometric systems, widely used systems with a large quantity of data readily available. The data are introduced in Section 4.2. Upper-main-sequence fitting is performed for Praesepe to determine the age and distance and allow for its use as a fiducial cluster in Section 4.3. UMS fitting is also performed on the Pleiades to demonstrate the consistency of ages and distances derived from UMS fitting and other methods. The tuned models are constructed in the SDSS system in Section 4.4 and the suitability of Praesepe as a fiducial cluster

is discussed in Section 4.5. The effect of (small) metallicity shifts on the theoretical models and empirical corrections is discussed in Section 4.5.3. Tuned models are constructed in the UKIDSS system in Section 4.6 and the extension of the empirical colour-$T_{\rm eff}$ relationship in the 2MASS system using the UKIDSS relationship is discussed in Section 4.7.

4.2 The Data

4.2.1 SDSS

The photometric part of SDSS (York et al. 2000) is a large optical survey covering 14555 deg^2 in the $(ugriz)_{\rm SDSS}$-bands. Although spectroscopic data releases are still ongoing (DR12 as of 2015) the imaging data and catalogues were completed in DR9 (Ahn et al. 2012). The SDSS data used in this chapter were downloaded from the SDSS DR9 archive and clean data were selected by applying quality flags. Specifically, objects were defined as clean if the "BLENDED" (whether the object is a composite), "EDGE" (whether the object was too close to the edge of the frame) and "SATURATED" (whether the object contains any saturated pixels) flags were false, as suggested in the SDSS handbook. Only objects classified as a star ("Type"= 6) were used, and photometry in a given band was only utilised if the star was unflagged in that band and the uncertainty on the magnitude in that band was ≤ 0.1 mag. The SDSS catalogues attempt to reconstruct the magnitudes of saturated stars using the electron bleed trails, however these measurements were not used in this work. A comparison was made between the magnitudes measured by the SDSS and the Carlsberg Meridian Catalogue (Copenhagen University et al. 2006). There was found to be excellent agreement between the two catalogues for non-saturated stars in the SDSS, but those stars which were saturated in the SDSS showed an offset of $\simeq$0.1 mag. The reconstructed saturated magnitudes in the SDSS were thus deemed unreliable and excluded. Note that the Carlsberg Meridian Catalogue uses a single filter (a Sloan *r* filter) and thus could not be used for constructing the semi-empirical models or CMD construction.

4.2.2 2MASS

2MASS (Skrutskie et al. 2006) is an all-sky survey in the $JHK_{\rm 2MASS}$ bands. Data were retrieved from the 2MASS 6X point source catalogue (see Cutri et al. 2012). The 6X observations were taken towards the end of the 2MASS survey with exposures six times longer than those used for

the primary survey and included observations of the Pleiades (the primary fiducial cluster for the tuning process). Data flagging was performed following the suggestions in the 2MASS user guide[1] specifically a "good" detection was defined as having a photometric quality flag ("ph_qual") that was not E,F,U or X, having contamination flags ("cc_flg" and "gal_contam") of 0 and a blend flag ("bl_flg") of 1, indicating a non-blended object.

4.2.3 UKIDSS

UKIDSS (Lawrence et al. 2007) is a combination of 5 wide-field surveys in the $(ZYJHK)_{\rm UKIDSS}$ bands, including 2 epochs of K-band observations. One of these surveys is the Galactic Clusters Survey (GCS), covering $\sim$ 1000 deg^2 in 10 star-forming regions and open clusters (Boudreault et al. 2012). Although not all-sky, UKIDSS aims for much deeper photometry than 2MASS, and so provides an excellent compliment to 2MASS data in the regions in which they overlap. The GCS catalogue includes coverage of the Pleiades. The data were downloaded from the UKIDSS archive and flagged following the recommendations in Appendix A3 of Lucas et al. (2008), specifically requiring pstar (probability that the source is a star) >0.99 and the "ppErrbits" flags for each band to be < 256. Again photometry in a given band was only used if it was unflagged with an uncertainty ≤ 0.1 mag.

4.2.4 INT-WFC Observations of Praesepe

Two fields in Praesepe were observed with the INT-WFC (see Table A.1) on the nights of 5$^{\rm th}$ December 2012 and 11$^{\rm th}$ November 2013. See Section 2.3 for a description of the reduction process. Only the 2013 data were taken in photometric conditions. To create the final optical catalogue the 2012 and 2013 data were reduced separately and the normalisation process (see Section 2.3) performed on the two separate catalogues using overlap stars.

4.3 Praesepe - An Alternative Fiducial Cluster

The Pleiades cluster was not observed as part of the SDSS and therefore an alternative fiducial cluster was required. Comparing the Dias et al. (2002) open cluster catalogue with the SDSS coverage revealed two suitable cluster candidates: IC 4665 and Praesepe. IC 4665 seemed an

[1] http://www.ipac.caltech.edu/2mass/releases/allsky/doc/sec2_2b.html

ideal candidate as it has an LDB age (Manzi et al. 2008). However the sequence in the CMD, defined using the Jeffries et al. (2009) members, was found to be extremely sparse and did not provide a well-sampled population of stars across a significant colour range. Praesepe offered an excellent alternative as it is a rich, nearby ($\sim$ 190 pc Gatewood & de Jonge 1994) cluster with very low (and uniform) reddening (Taylor 2006) thereby allowing the sequence to be well defined to low masses. It is typically quoted to be of similar age to the Hyades ($\sim$ 600 Myr), and to have slightly supersolar metallicity.

The SDSS photometry was crossmatched with the Praesepe memberships from Kraus & Hillenbrand (2007), limited to those stars with membership probabilities of $\geq$ 95 per cent. There were two specific issues which were necessary to address when adopting Praesepe as an alternative fiducial cluster. First the issue of increased magnetic activity at younger ages (see e.g Stauffer et al. 2003) and what effect this may have on the observed colours of stars. Given that the Pleiades, the other fiducial cluster used in this work, is much younger (and therefore more active), and magnetic activity has been suggested as a source of the model-data discrepancy (e.g. Feiden 2016) this was a potential concern. Secondly there was the matter of metallicity and the possible systematic error introduced by using a non-solar composition locus to tune solar metallicity pre-MS model isochrones. In Section 4.5 these issues are discussed and it is demonstrated that, when compared to the observed discrepancy between the models and the data, these effects were not significant.

4.3.1 The Age and Distance of Praesepe

The tuning process requires a robust age and distance determination for the fiducial cluster. In the Pleiades this was the LDB age and distance determination from parallax. Praesepe is a much more evolved cluster and therefore it was not possible to use the LDB to calculate an age (the luminosity at which the LDB would exist at $\sim$ 650 Myr is simply too faint). In addition, although the revised *Hipparcos* distance modulus of $dm = 6.30$ mag (van Leeuwen 2009) is in good agreement with other determinations (e.g. Gatewood & de Jonge 1994; An et al. 2007), the uncertainty in this distance modulus (almost 0.1 mag) is too large for the purposes of calculating empirical BCs at low $T_{\rm eff}$. Hence a consistent age and distance for Praesepe was derived by fitting photometry of MS members in the $V, B-V$ CMD using MS evolutionary models.

Age and distance estimates will be affected by both reddening and metallicity. As Praesepe is significantly older than the Pleiades the higher mass members have already evolved off the MS

and entered the post-MS evolutionary phase. Hence, we are unable to derive a reddening using these members in the $U-B, B-V$ colour-colour diagram (see e.g. Mayne & Naylor 2008). Instead the mean value of $E^{\rm Hot}_{B-V}$=0.027 mag, derived using a combination of polarisation measurements, comparison of β and $(R-I)_{\rm c}$ for F stars, and Strömgren β analysis of A stars by Taylor (2006) was adopted.

An additional consideration is the chemical composition of Praesepe. The Pleiades is, within uncertainties, solar metallicity ([Fe/H] = +0.03±0.02±0.05 dex [statistical and systematic]; see Soderblom et al. 2009). The metallicity of Praesepe is supersolar, with literature values for the absolute difference between the metallicity of the Pleiades and Praesepe from Δ[Fe/H] = 0.07 − 0.09 dex (see An et al. 2007 and Boesgaard et al. 2013 respectively). The mean value was adopted (0.08 dex) which translates to $Z_{\rm Praesepe} = 1.2 Z_{\rm Pleiades}$.

4.3.2 The Models

MS models were required to derive the cluster parameters for Praesepe. For the interior models, to ensure consistency with the MS ages derived in Bell et al. (2013) the same resampled grid of Lejeune & Schaerer (2001) was adopted (specifically the basic "c" grid of Schaller et al. 1992). As the grid of interior models is much coarser in age than was required, intermediate-age models were created by interpolating the grid. The rate of change of $L_{\rm bol}$ and $T_{\rm eff}$ with age changes discontinuously at the TAMS however, and so a simple interpolation scheme could introduce large errors. To avoid this an interpolation routine provided by the Geneva group was used to create the interpolated grid, with spacing in log(age) of 0.02 dex. The atmospheric models used for the MS fitting were the Kurucz ATLAS9/ODFnew models (Castelli & Kurucz 2004).

The interior and atmospheric models were not provided at values of $1.2Z_{\odot}$ and so the models were also interpolated in metallicity. A quadratic interpolation was used for both the interior and atmospheric models to produce grids of each with a metallicity equal to $1.2Z_{\odot}$. At this metallicity the choice of interpolation scheme did not significantly affect the derived best-fit values for the age and distance i.e. adopting a linear interpolation affected the values of parameters at the $\sim 1\sigma$ level. To transform the theoretical models into CMD space, the atmospheric models were reddened by a nominal $E^{\rm Hot}_{B-V}$=0.027 mag using the Galactic reddening law of Fitzpatrick (1999) with $R_V = 3.1$. The BCs were calculated using the Bessell & Murphy (2012) system responses and the CALSPEC

Vega reference spectrum alpha_lyr_stis_005[1] with $V_{Vega} = 0.03$ and all colours equal to zero.

For the tuning process (see Section 4.4) the models used are the same as those in Chapter 3. The atmospheric models and DCJ08 interior models were interpolated to Praesepe metallicity. The BCAH98 and Pisa models were not available at supersolar metallicities and so the solar models were used (see Section 4.5.3 for an estimate of the effect this had)

4.3.3 τ^2 Fitting in Praesepe

The τ^2 fitting statistic (Naylor & Jeffries 2006; Naylor 2009) was used to fit the grid of MS evolutionary models to the UBV photometric data of Praesepe from Johnson (1952). See Section 1.3.1 for an introduction to this process or Bell et al. (2013) for a complete description. Instead of the simple power law distribution used in e.g. Bell et al. (2013) and Naylor (2009) (which yields an even distribution of stars as a function of magnitude), the broken power law IMF of Kroupa (2001) was used. It should be noted that the choice of mass function does not have a significant effect on the parameters derived from the τ^2 fitting (see Naylor 2009). When constructing the binary population, if the assigned secondary mass is below the lower mass limit of the interior models the binary population is lost before the single-star sequence, resulting in a "binary wedge" (see e.g. Jeffries et al. 2007). This is a particular issue when using the Lejeune & Schaerer (2001) models due to the relatively high low-mass limit of 0.8 $M_\odot$. To avoid this affecting the fitting process the Lejeune & Schaerer (2001) models were combined with those of DCJ08, which extend down to masses of 0.1 $M_\odot$. Between 1 $M_\odot$ and 0.8 $M_\odot$ the two showed excellent agreement, and so the Lejeune & Schaerer (2001) models were used down to 1 $M_\odot$ and the DCJ08 models were appended from 1 $M_\odot$to 0.1 $M_\odot$.

The best-fitting $V, B-V$ CMD for Praesepe is shown in Figure 4.1. Four stars which were defined as giants in Johnson (1952) were removed before fitting as these would impact the derived age and distance values. One star which appeared to have evolved off the MS was also removed. Furthermore, four additional stars which lay blueward of the MS locus were removed due to a combination of their positions in the V, B-V CMD and their associated τ^2 values. From the remaining stars an age of 665^{+14}_{-7} Myr and a distance modulus $dm = 6.32 \pm 0.02$ mag were derived, with an associated $\Pr(\tau^2)$=0.87.

The derived age and distance of Praesepe is consistent with, yet more precise than, previous

[1] http://www.stsci.edu/hst/observatory/cdbs/calspec.html

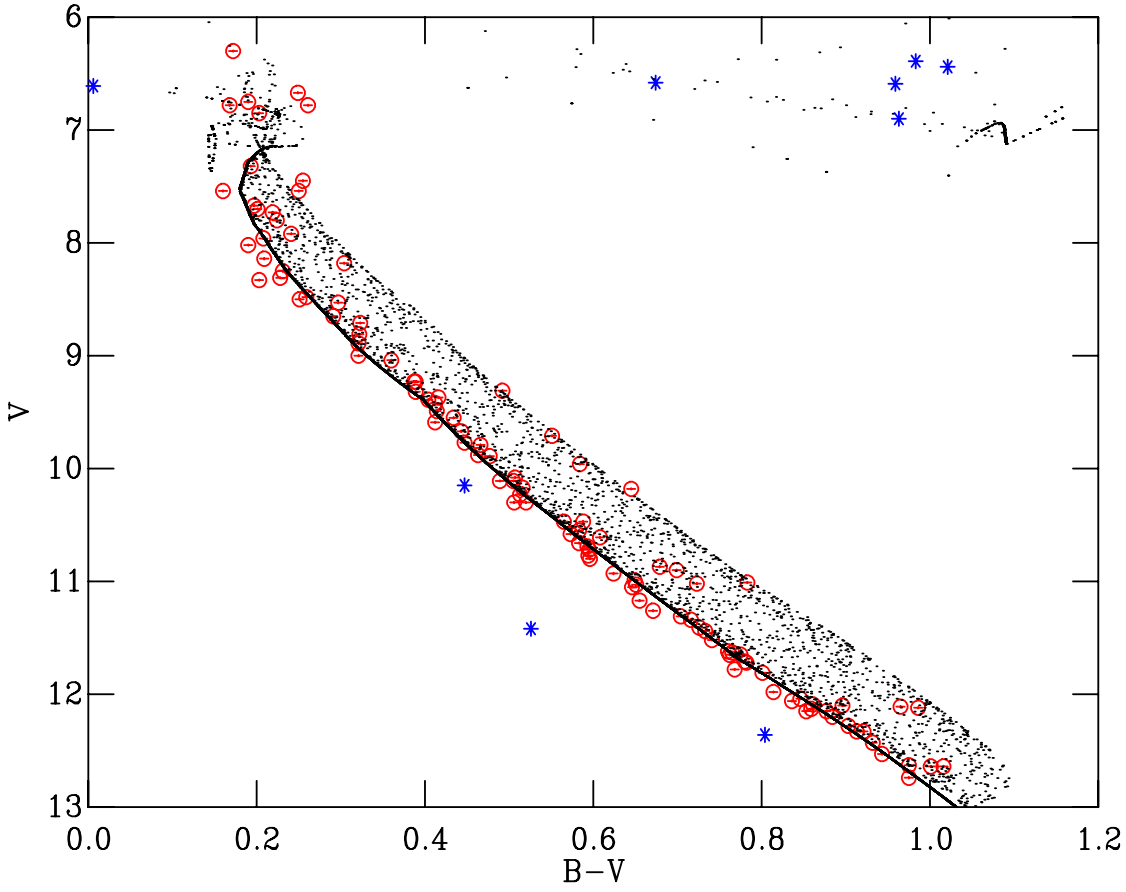

Figure 4.1: Best-fitting CMD of Praesepe with a derived age of 665^{+14}_{-7} Myr and derived distance modulus dm=6.32 ± 0.02 mag. The red circles show the data from Johnson (1952), with the associated uncertainties shown as bars. The blue asterisks show stars that were clipped before deriving the best-fit. The black points show 10,000 stars drawn from the theoretical model.

estimates e.g. 700 ± 100 Myr (Salaris et al. 2004), 590^{+150}_{-120} Myr (Fossati et al. 2008) and dm = 6.30 ± 0.07 (van Leeuwen 2009). It should be noted, however, that the derived age is significantly younger than that of (Brandt & Huang 2015), who found an age of 800 Myr using isochrone fitting with models including the effect of stellar rotation. The non-rotating models show good agreement with the LDB derived ages however (see Section 4.3.4) and consistency with the LDB age is the primary concern here.

4.3.4 τ^2 Fitting in the Pleiades

At this point both the Pleiades and Praesepe have been used as fiducial clusters. Different techniques had been used to derive the adopted ages and distances for Praesepe (UMS fitting, this work) and the Pleiades (LDB & parallax, Barrado y Navascués et al. 2004; Soderblom et al. 2005) which may be systematically different. As a check the Pleiades parameters were determined using the same technique used for Praesepe. Starting with the photometric data of Johnson & Morgan (1953), dereddened by Cameron Bell (priv. comm.). The stars were dereddened on a star by star basis using the revised Q-method (see Mayne & Naylor 2008; Bell et al. 2013). The dereddened members were then fitted using the same τ^2 fitting technique used for Praesepe deriving an age of 135^{+20}_{-11} Myr and distance modulus of $5.61^{+0.03}_{-0.02}$ mag with an associated $\Pr(\tau^2) = 0.23$. The best fit is shown in Figure 4.2. The two brightest stars were removed from the sample before fitting (blue points in Figure 4.2) due to poor τ^2 values. The poor fit to these two stars was likely simply due to the lack of stars in the simulated distribution to get enough density in that region of the CMD. The τ^2-derived age and distance are consistent with those adopted in 3.4 (130 Myr, 5.63 mag), giving confidence that the adopted parameters for both the SDSS and WFC fiducial clusters are on a consistent age and distance scale.

4.4 Tuning the Models in the SDSS Photometric System

The semi-empirical models were constructed in the SDSS system in the same manner as used for the WFC system (see Section 3.4). A spline was fit (by eye) to the single-star sequence in Praesepe in a number of CMDs, and model isochrones overlaid. The $K_{2\mathrm{MASS}}$-band magnitudes were used to quantify the correction in the other bands.

As previously mentioned both the BCAH98 and Pisa interior models are only available in

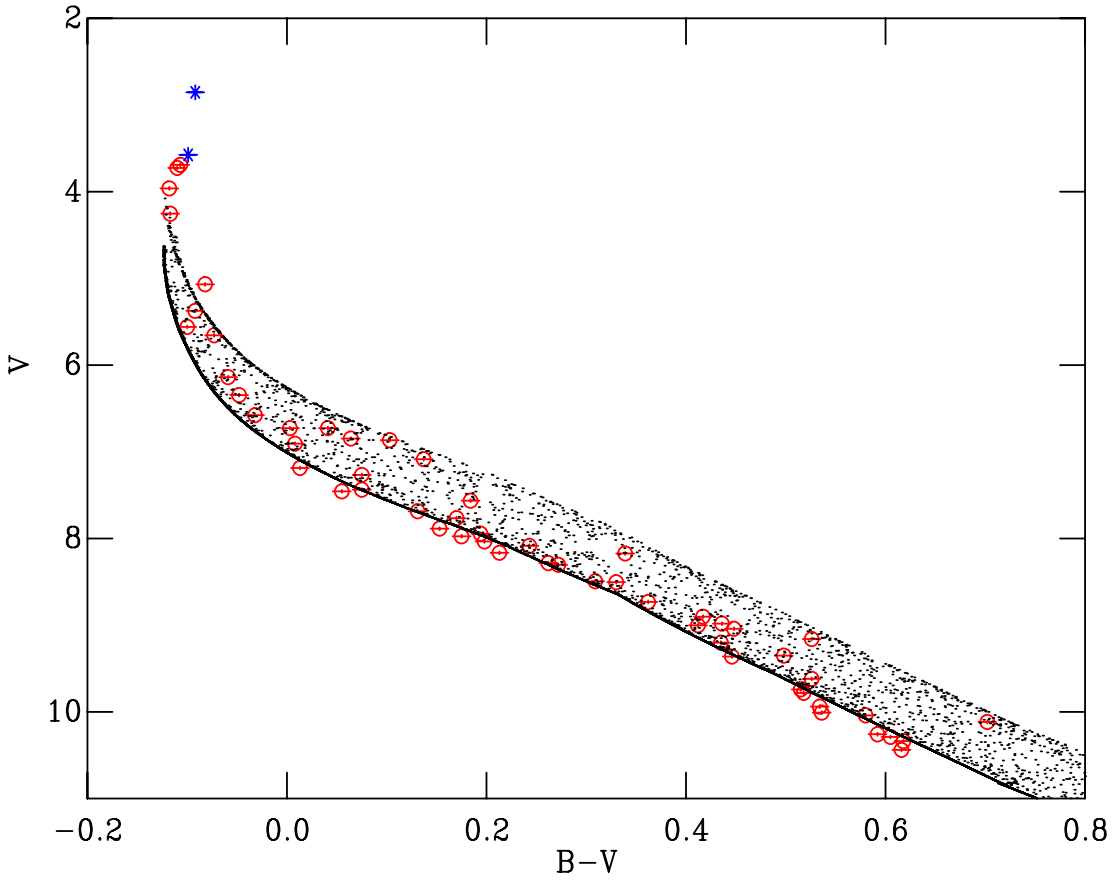

Figure 4.2: Best-fitting V, $B-V$ CMD of the Pleiades with a derived age of 135^{+20}_{-11} Myr and distance modulus$5.61^{+0.03}_{-0.02}$ mag. The red circles show the data from Johnson & Morgan (1953), with the associated uncertainties shown as bars. The blue asterisks show stars that were clipped before deriving the best-fit.

Solar metallicities. For these models the (interpolated) supersolar atmospheres ($1.2Z_{\odot}$) were used to transform the solar composition interior models to the observational plane (see Section 4.5.3 for a discussion on the effect this has). The DCJ08 interior models are available in supersolar metallicities, albeit not at values of $1.2Z_{\odot}$, and for these quadratic interpolation was used to create a grid of $1.2Z_{\odot}$ interior models. The interpolated $1.2Z_{\odot}$ atmospheric models were again used to transform these into CMD space.

Due to the limiting magnitude of the SDSS the Praesepe sequence only allowed the semi-empirical models to extend to a limit of $g - i \simeq 3.5$. In comparison, the Pleiades sequence in the INT-WFC system extends to $(g - i)_{\rm WFC} \simeq 4.0$ (i.e. the tuning extends to cooler $T_{\rm eff}$ in the WFC system than in the SDSS system). Given that the WFC and SDSS photometric systems are similar it was possible that the ΔBCs derived in each system would also be similar. If this were the case, the WFC-derived ΔBCs would offer a convenient method of extending the SDSS tuning to lower $T_{\rm eff}$. The ΔBCs in the two systems are shown for the g- and i-bands in Figure 4.3. The Δ-BCs in the two systems are extremely similar. Thus beyond the limit of the SDSS tuning (3100K) the WFC ΔBCs were adopted and applied to the atmospheric models after folding through the SDSS system responses. Although this was not an ideal solution, it did allow the semi-empirical SDSS isochrones to extend to $T_{\rm eff} \simeq 3100\,{\rm K}$, which was a significant advantage. Additionally, given the large difference between the untuned models and the observed spline, any error introduced by adopting the WFC-derived ΔBCs was small compared to the improvement. Figure 4.4 shows the tuned SDSS model overlaid on Praesepe.

4.5 Factors affecting the use of Praesepe in place of the Pleiades

In Section 4.3 two possible factors with using Praesepe as an alternative fiducial cluster were highlighted. First was the question of enhanced magnetic activity at younger ages and the potential impact on the observed stellar locus in CMD space. Second, what systematic errors were introduced by using a stellar sequence with a supersolar metallicity to recalibrate the solar composition PMS models?

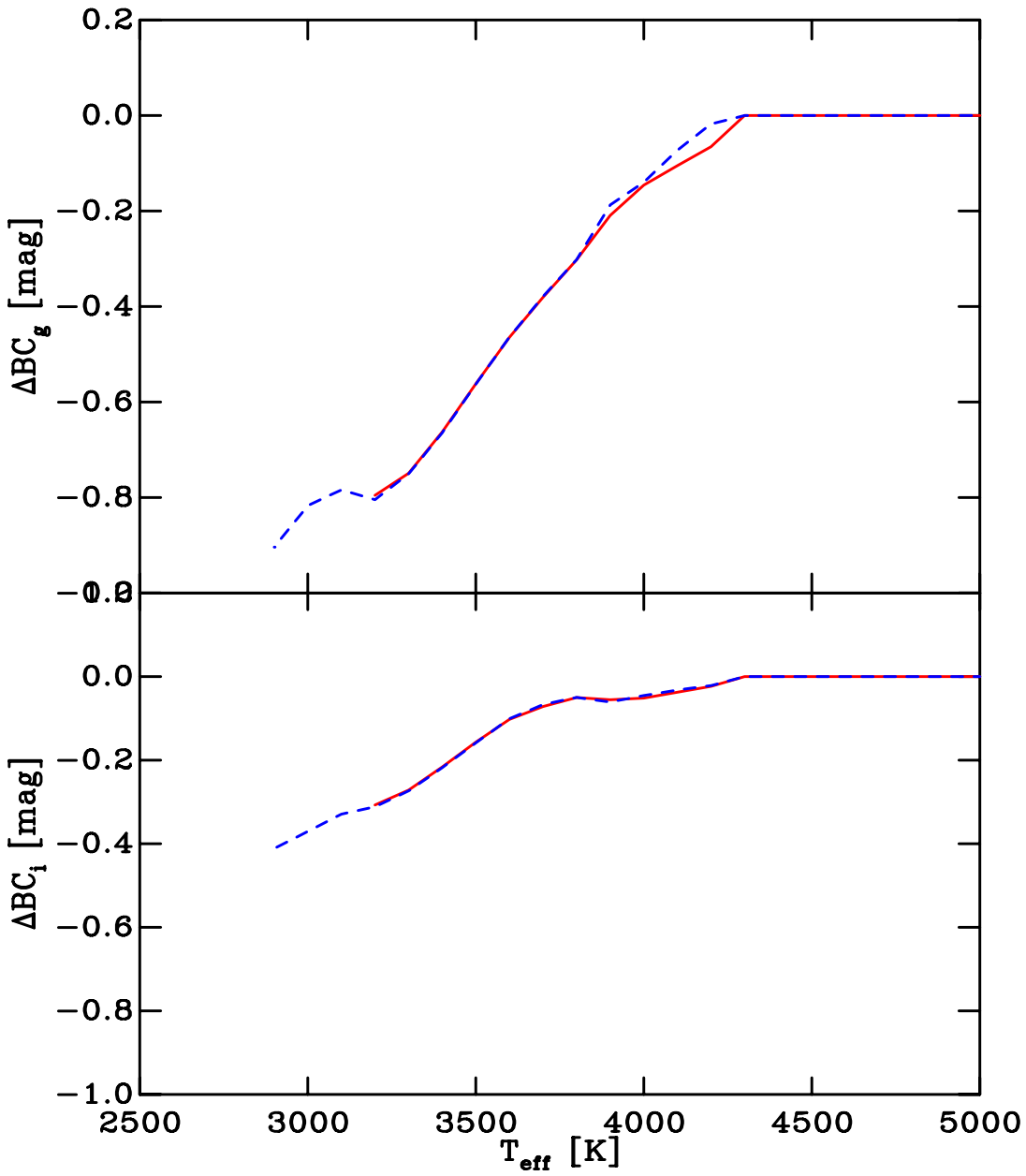

Figure 4.3: Comparison of the ΔBCs in the *g*-band (top) and *i*-band (bottom) for the INT-WFC and SDSS systems. The red solid lines show the ΔBCs in the SDSS system and the blue dashed lines show the ΔBCs in the WFC system.

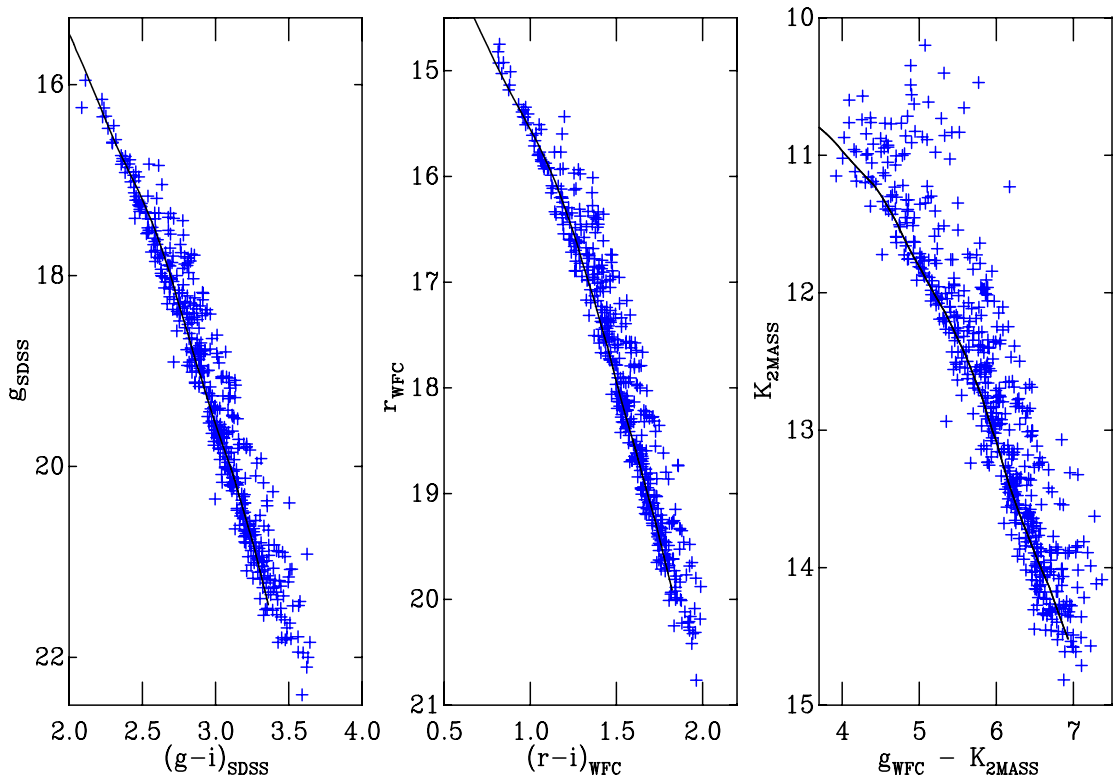

Figure 4.4: Praesepe CMDs in the SDSS system. Overlaid are the Praesepe-tuned $1.2Z_{\odot}$ DCJ08 models adopting an age of 665 Myr and distance modulus6.32 mag.

4.5.1 Effects of enhanced magnetic activity

Any difference in the positions of the Praesepe and Pleiades locus due to enhanced magnetic activity of the Pleiades stars would introduce biases into the calculated empirical corrections. High magnetic activity in younger stars can inhibit the convective flows to the stellar surface and result in star spots covering a large fraction of the photosphere (e.g. Strassmeier 2009). High coverage of star spots can alter the colour of young stars compared to older stars of the same $T_{\rm eff}$. Additionally the convective inhibition can cool the stellar surface and result in a slower contraction rate (Feiden 2016). The result of this is that, at a given age, a star that was magnetically inhibited would have a larger radius and luminosity compared to one without magnetic inhibition of convection. In terms of the CMD, a combination of cooler $T_{\rm eff}$ (redder colour) and larger $L_{\rm bol}$(brighter magnitude) would effectively make a star appear younger.

Stauffer et al. (2003) noted that K dwarfs in the Pleiades were too blue compared to a MS locus, a feature also noted by e.g. Kamai et al. (2014). Stauffer et al. noted that the issue in the $V, B-V$ and $V, V-K$ CMDs, but not in the $V, V-I$ CMD. These differences were well correlated with known highly-spotted stars, and thus were attributed the difference to the presence of star spots on the stellar surface. The presence of spots is observed to become less pronounced with age, and in fact Stauffer et al. (2003) demonstrated that Praesepe does not suffer from the issue they observed with the Pleiades K dwarfs. Given that Praesepe has been adopted as a fiducial cluster in the SDSS photometric system, the question becomes are the effects noted by Stauffer et al. (2003) still observed in the $g, g-i$ and $g, g-K_{\rm s}$ CMDs, and to what level?

4.5.2 CMD comparison of the Pleiades and Praesepe

As previously mentioned the Pleiades were not observed as part of the SDSS. Therefore the comparison between the sequences of the Pleiades and Praesepe in CMD space had to be performed in the INT-WFC photometric system, for which both Pleiades and Praesepe observations were obtained. There are differences between the SDSS and INT-WFC responses (see Figure 2.1) but these are small, and thus any conclusions based on comparing the Pleiades and Praesepe in the INT-WFC system should also be valid in the SDSS system.

For Praesepe the Kraus & Hillenbrand (2007) membership list (adopting those stars with a membership probability ≥95%) was crossmatched with the INT-WFC photometry. For the Pleiades, the same combination of Stauffer et al. (2007) and Lodieu et al. (2012) discussed in

Table 4.1: Extinction values adopted to deredden the Pleiades and Praesepe CMDs. Extinctions were taken from extinction tables using a $T_{\rm eff}$of 5000 K and a log(g) of 4.0.

Pleiades						
$E^{\rm Hot}_{B-V}$	$A_{g_{\rm WFC}}$	$A_{g-i_{\rm WFC}}$	$A_{r_{\rm WFC}}$	$A_{r-i_{\rm WFC}}$	$A_{K_{\rm 2MASS}}$	$A_{g_{\rm WFC}-K_{\rm 2MASS}}$
0.04	0.141	0.068	0.102	0.028	0.014	0.127
Praesepe						
$E^{\rm Hot}_{B-V}$	$A_{g_{\rm WFC}}$	$A_{g-i_{\rm WFC}}$	$A_{r_{\rm WFC}}$	$A_{r-i_{\rm WFC}}$	$A_{K_{\rm 2MASS}}$	$A_{g_{\rm WFC}-K_{\rm 2MASS}}$
0.027	0.095	0.046	0.069	0.019	0.009	0.086

Secion 3.2 was used. The Pleiades and Praesepe data were corrected for distance and extinction using the parameters given in Sections 3.4 and 4.3.3 respectively. Given the $E^{\rm Hot}_{B-V}$values, extinctions in each bandpass were derived using the extinction grids as discussed in Section 3.3.1. Due to the low reddening in both clusters the derived extinction values are effectively insensitive to the effect of $T_{\rm eff}$ variation (the effect is of the order 10^{-3} mags), and so a single extinction value was calculated for each filter in each cluster. The extinction values for each cluster were calculated by taking the value of $A_\lambda/E^{\rm Hot}_{B-V}$ from the extinction tables at a $T_{\rm eff}$of 5000 K and a log(g) of 4.0. The derived values are given in Table 4.1.

The sequences of both the Pleiades and Praesepe are shown in Figure 4.6. Figure 4.6 includes the $g_{\rm WFC}(g-i)_{\rm WFC}$, $r_{\rm WFC}(r-i)_{\rm WFC}$and $g_{\rm WFC}(g_{\rm WFC}$-$K_{\rm 2MASS})$ CMDs. There was no evidence of the difference observed by Stauffer et al. (2003) between the two sequences. Stauffer et al. (2003) saw a difference in the $V, B-V$ CMD. Given that the $g_{\rm WFC}$-band has significant overlap with the Johnson B-band (see Figure 4.5) the lack of a difference in the $g_{\rm WFC}$, $(g-i)_{\rm WFC}$CMD was surprising. Stauffer et al. (2003) noted that the bluer K dwarfs may be due to an enhanced blue continuum (especially at wavelengths $\lesssim$ 4200Å). The B-band cut-off wavelength is $\simeq$ 3600Å, compared to $\simeq$ 4000Å for the $g_{\rm WFC}$-band and is also skewed towards the blue. Thus the presence of bright spots which could appear in the B-band photometry may not be observed in $g_{\rm WFC}$-band. Tentative evidence of small differences can be seen in the $r_{\rm WFC}$, $(r-i)_{\rm WFC}$(at an $(r-i)_{\rm WFC}\simeq$0.5) and $g_{\rm WFC}$, ($g_{\rm WFC}$- $K_{\rm 2MASS}$ (at a $g_{\rm WFC}$- $K_{\rm 2MASS}$ $\simeq$3.0) CMDs. These differences are much smaller than those discussed in Stauffer et al. (2003) and are associated with regions in the sequence with a low number of members (i.e. sparse sections) and may simply be a manifestation of this sparsity. Additional observations of both clusters to fill in these sparse regions of the CMD would be required to ascertain whether these differences were actually due to variations between the two sequences. Thus, in the CMDs used for deriving the semi-empirical corrections, the Pleiades and

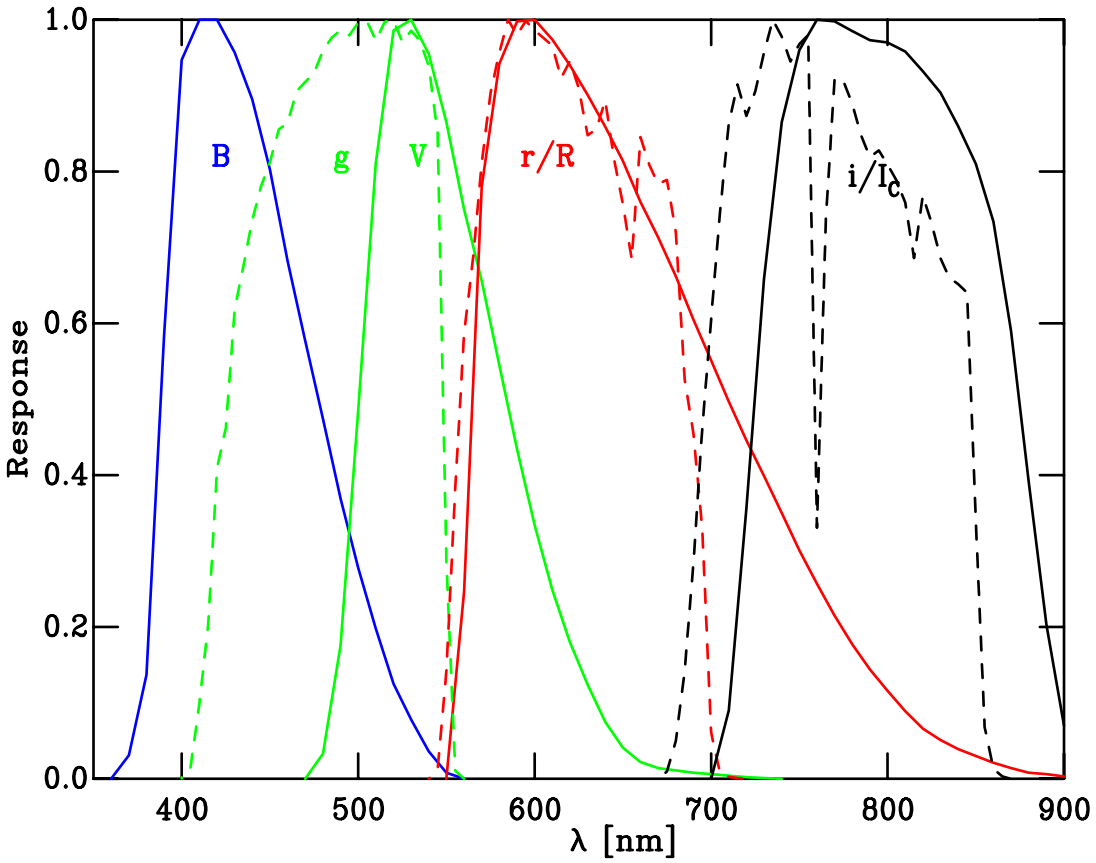

Figure 4.5: Filter responses for the Johnson $BVRI_c$ (solid lines, from Bessell & Murphy 2012) and INT-WFC *gri* filters (dashed lines).

Praesepe loci should give in consistent results.

4.5.3 Effects of metallicity on semi-empirical BC-$T_{\rm eff}$ relations

One of the suggested explanations for the observed model-data discrepancy for M-stars is missing sources of opacity in the atmospheric models (see e.g. Soderblom et al. 2014). Metallicity will effect the sources of opacity in the atmosphere, and so another point of concern with using Praesepe as a fiducial cluster was its slight supersolar metallicity. As the metallicity increases an isochrone of a given age will be fainter and redder when compared to an isochrone with a lower metallicity (see e.g. VandenBerg et al. 2006; Kotoneva et al. 2002).

Praesepe is roughly 20 per cent supersolar compared to the Pleiades. An important point to test was whether the process that causes the observed discrepancy in the CMD is strongly dependent on metallicity (i.e. what level of error had been introduced into the SDSS tuning by deriving ΔBCs from a supersolar fiducial cluster) Both the BCAH98 α = 1.9 and the Pisa models

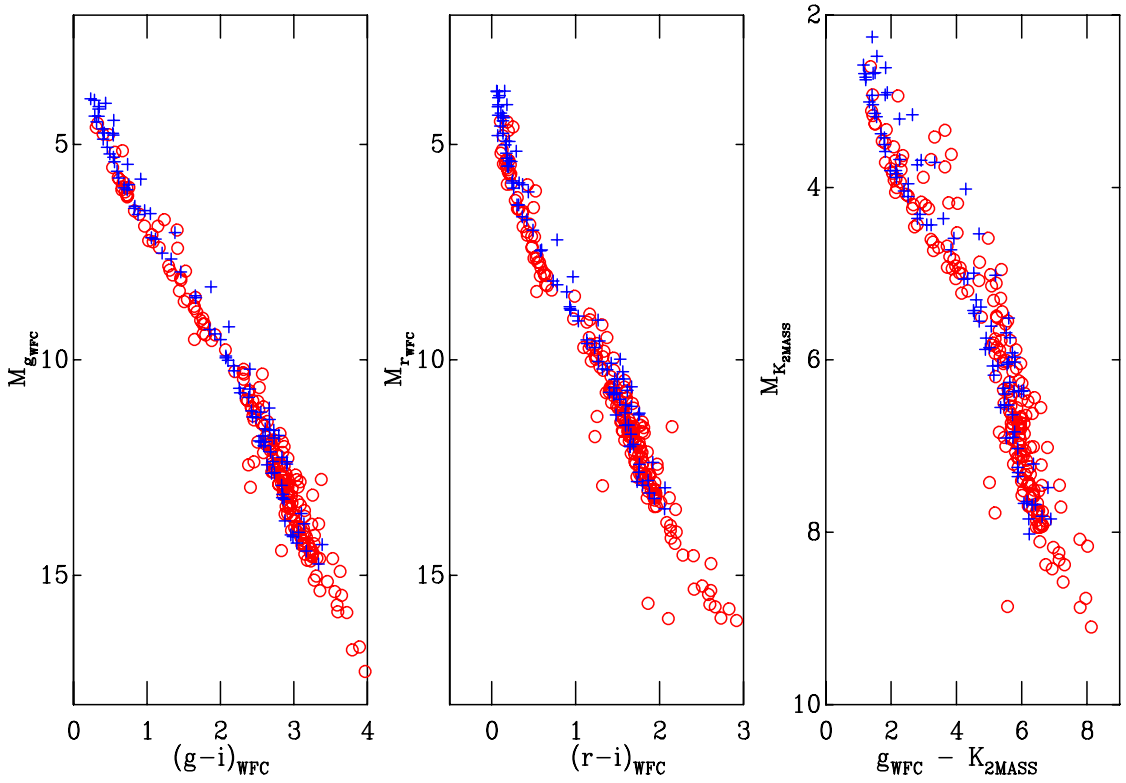

Figure 4.6: Pleiades and Praesepe members plotted in $g_{\rm WFC}$, $(g-i)_{\rm WFC}$(left), $r_{\rm WFC}$, $(r-i)_{\rm WFC}$(middle) and $g_{\rm WFC}$, ($g_{\rm WFC}$- $K_{\rm 2MASS}$) CMDs. Blue crosses show Praesepe members, red circles show the Pleiades members. Note that they have been shifted to absolute magnitudes using the distances given in Sections 4.3.3 and 4.3.4.

were not available in supersolar compositions. This limited the tuning process to using solar metallicity interiors for these models. The DCJ08 models are available in supersolar compositions, and so were used to estimate the effect that using supersolar versus solar interiors would have on the derived ΔBCs.

4.5.4 Effects of metallicity on stellar interior models

Figure 4.7 shows the Praesepe members as defined by Kraus & Hillenbrand (2007) in the $K_{2\mathrm{MASS}}, g-K_{2\mathrm{MASS}}$ CMD. Also plotted in the CMD are 665 Myr DCJ08 model isochrones, one with a solar interior model and one with a supersolar ($1.2Z_{\odot}$) interior model. Both were transformed into CMD space using supersolar ($1.2Z_{\odot}$) atmospheric models. The difference in the predicted colour between the two models was calculated as a function of $K_{2\mathrm{MASS}}$. In the T_{eff} range where empirical BCs were calculated (see Section 4.4) the maximum difference in the colour was $[g - K_{2\mathrm{MASS}}]_{1.2Z_{\odot}} - [g - K_{2\mathrm{MASS}}]_{Z_{\odot}} \simeq 0.05$ mag. Although seemingly large, this difference is small in comparison to observed discrepancy of $\simeq 0.8$ mag in g-$K_{2\mathrm{MASS}}$ (see the empirical spline c.f. the model isochrones in Figure 4.7) The difference was also quantified in other colour indices to investigate whether the difference is wavelength dependent. The difference was ≤ 0.05 mag in all cases. Thus despite having to adopt solar metallicity interior models to create the ΔBCs for the BCAH98 and Pisa models, the resultant semi-empirical model isochrones have a residual uncertainty of $\lesssim 0.05$ mag in magnitude and $\lesssim 0.07$ mag in colour. Note that for the DCJ08 models the ΔBCs were calculated using supersolar ($1.2Z_{\odot}$) interior and atmospheric models and thus the uncertainties in the colour and magnitude would be less than the BCAH98 and Pisa models.

4.5.5 Effects of metallicity on ΔBC

As INT-WFC observations were obtained for both the Pleiades and Praesepe these offered a simple test to investigate the metallicity dependence of the ΔBCs. The semi-empirical models derived using the Pleiades in the INT-WFC system were used to construct a Praesepe-age isochrone which, after adopting the appropriate reddening and distance modulus, was overlaid on the Praesepe WFC data. Figure 4.8 shows Praesepe with two 665 Myr DCJ08 model isochrones overlaid. One is a solar composition semi-empirical model isochrone (derived from the Pleiades; Bell et al. 2013) and the second is a theoretical supersolar ($1.2Z_{\odot}$) metallicity model isochrone without empirical corrections. The solar composition DCJ08 model isochrone presented a good fit to the observed

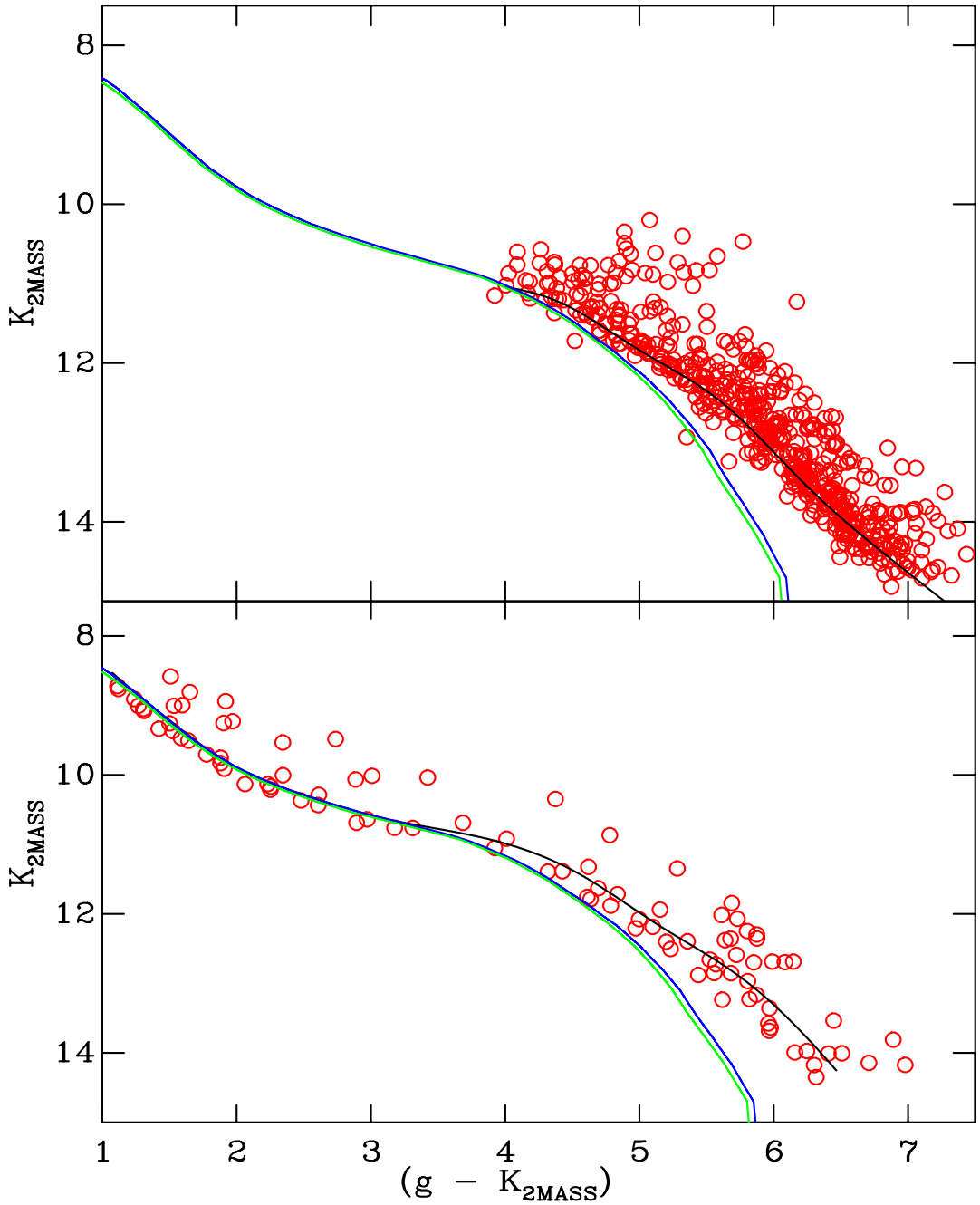

Figure 4.7: $K_s, g - K_s$ CMD of Praesepe members in the SDSS (top) and WFC (bottom) system. Overlaid are two 665 Myr DCJ08 model isochrones adopting a distance modulus of 6.32 mag and a reddening $E^{\rm Hot}_{B-V}$=0.027 mag. The interior models are solar metallicity ($Z_\odot$, green) and supersolar ($1.2Z_\odot$, blue). Both model isochrones have been transformed into CMD space using supersolar $1.2Z_\odot$ atmospheric models. Note that these are untuned models. The black line represents the spline fit by eye to the single-star sequence.

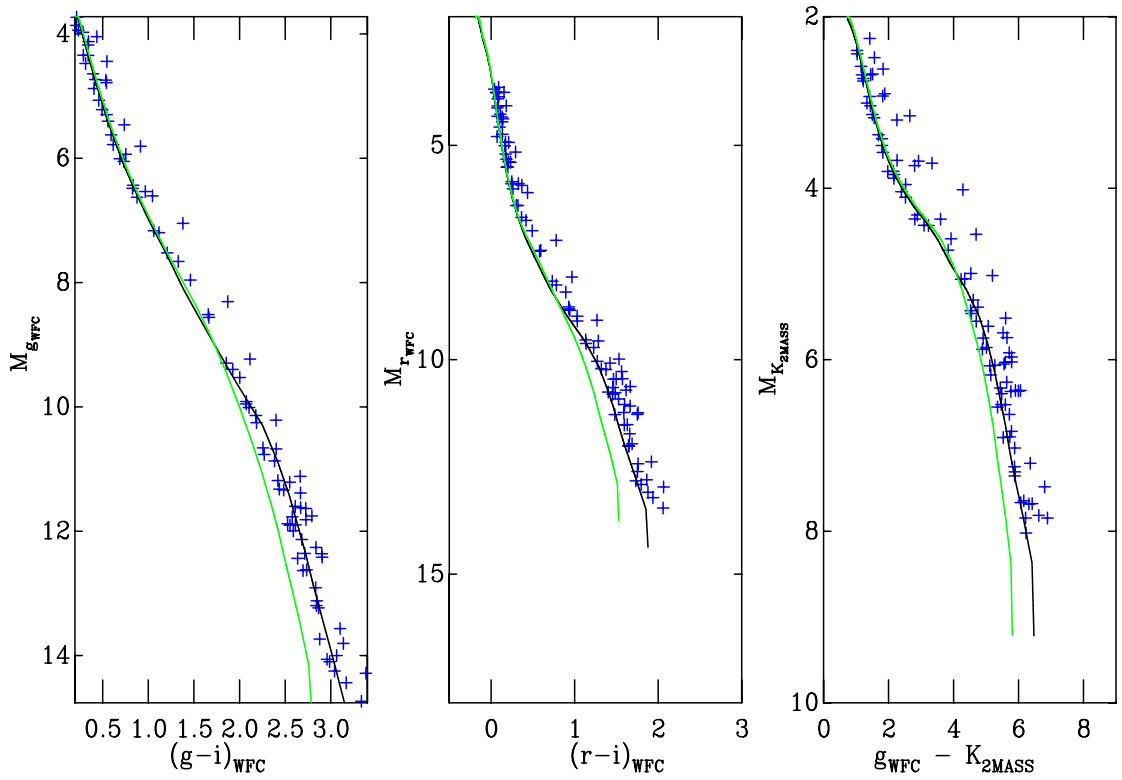

Figure 4.8: Praesepe members plotted in $g_{\rm WFC}$, $(g-i)_{\rm WFC}$(left), $r_{\rm WFC}$, $(r-i)_{\rm WFC}$(middle) and $g_{\rm WFC}$, ($g_{\rm WFC}$- $K_{\rm 2MASS}$) CMDs. Blue crosses show Praesepe members. The black line in each panel is a 665Myr solar composition semi-empirical DCJ08 model isochrone (derived from the Pleiades). The green line is a theoretical (without the empirical corrections) supersolar ($1.2Z_{\odot}$) metallicity DCJ08 model isochrone. The good agreement between the semi-empirical model and the observed sequence shows that there is no strong dependence of ΔBC on metallicity.

Praesepe sequence in all colour combinations. Thus despite the fact that the SDSS ΔBCs were derived from the supersolar Praesepe, these could be applied to the solar metallicity models without introducing significant systematic effects on the ages derived from using these isochrones in CMDs.

4.6 Semi-Empirical Models in the UKIDSS System

It will be shown in Chapter 5 that the $(i-Z),(J-H)$ diagram can be used to photometrically deredden stars. This technique is only useful if the theoretical models match the data. It was therefore necessary to construct semi-empirical models in the J- and H-bands. Bell et al. (2014) created semi-empirical models in the 2MASS bandpasses. The same procedure was followed to construct the semi-empirical models in the UKIDSS J and H bands. Figure 4.9 shows the $K_{\rm UKIDSS}$, $(J-K)_{\rm UKIDSS}$ and $J_{\rm UKIDSS}$, $(J-H)_{\rm UKIDSS}$ CMDs used to calculate the empirical correction, with the resulting tuned isochrones overlaid. The UKIDSS tuning extends to a $T_{\rm eff}$ of 2000 K, compared to a $T_{\rm eff}$ of 2900K for the 2MASS tuning presented in Bell et al. (2014)

4.7 Semi-Empirical Models in the 2MASS System

In Chapter 6 the $(i-Z),(J-H)$ technique (see Chapter 5) will be used to deredden stars in the Taurus star-forming region. As Taurus is younger than the Pleiades a star of a given $T_{\rm eff}$ in Taurus will be brighter than in the Pleiades, despite them being at a similar distance. The limiting magnitude in 2MASS thus corresponds to a cooler $T_{\rm eff}$ in Taurus than in the Pleiades, which means that the Bell et al. (2014) 2MASS tuning did not extend to cool enough temperatures to cover all of the Taurus members. Additionally, although Taurus was covered in the UKIDSS survey, there were no $H_{\rm UKIDSS}$ observations. Thus the $(i-Z),(J-H)$ dereddening had to be performed in the 2MASS system and the 2MASS semi-empirical models had to be extended to lower $T_{\rm eff}$using the ΔBCs derived from the UKIDSS tuning. The UKIDSS and 2MASS bandpasses are very similar in J and H, therefore the data-model discrepancies should be similar in these bands and, if this was the case, the UKIDSS-derived ΔBCs could be applied to the 2MASS models. To test this the UKIDSS derived ΔBCs were applied to Pleiades-age models in the 2MASS photometric system. These models were then overlaid on the Pleiades sequence, shown in Figure 4.10. The resulting tuned isochrones are consistent within the uncertainties in the 2MASS Pleiades data. In practice

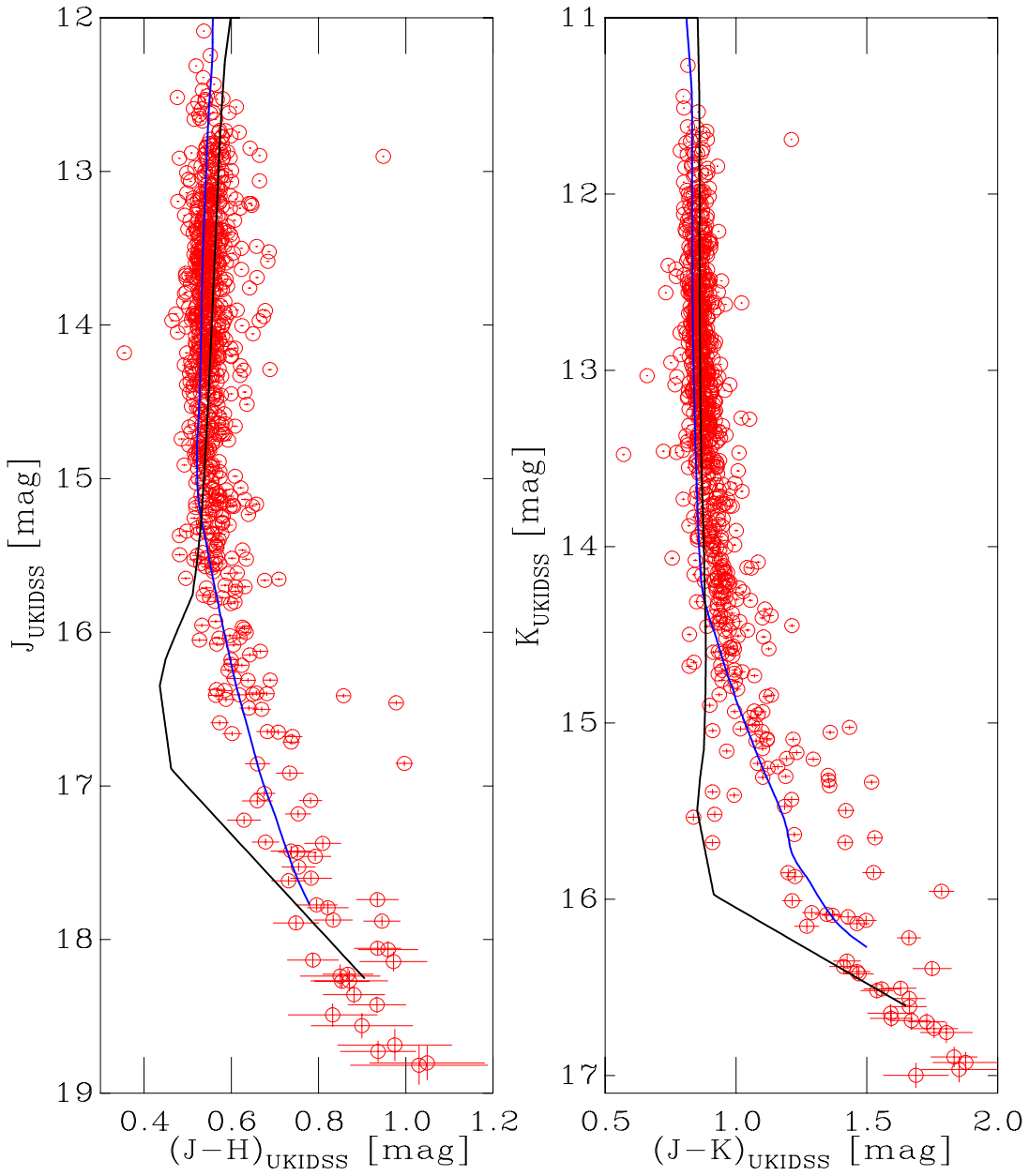

Figure 4.9: Pleiades members plotted in $J_{\rm UKIDSS}$, $(J-H)_{\rm UKIDSS}$ (left) and $K_{\rm UKIDSS}$, $(J-K)_{\rm UKIDSS}$ (right) CMDs. Red circles show the Pleiades members. The solid blue line is a DCJ08 isochrone with the empirical correction, adopting an age of 130 Myr and dm=5.63 mag. The solid black line is the equivalent untuned model (i.e. without the derived empirical correction).

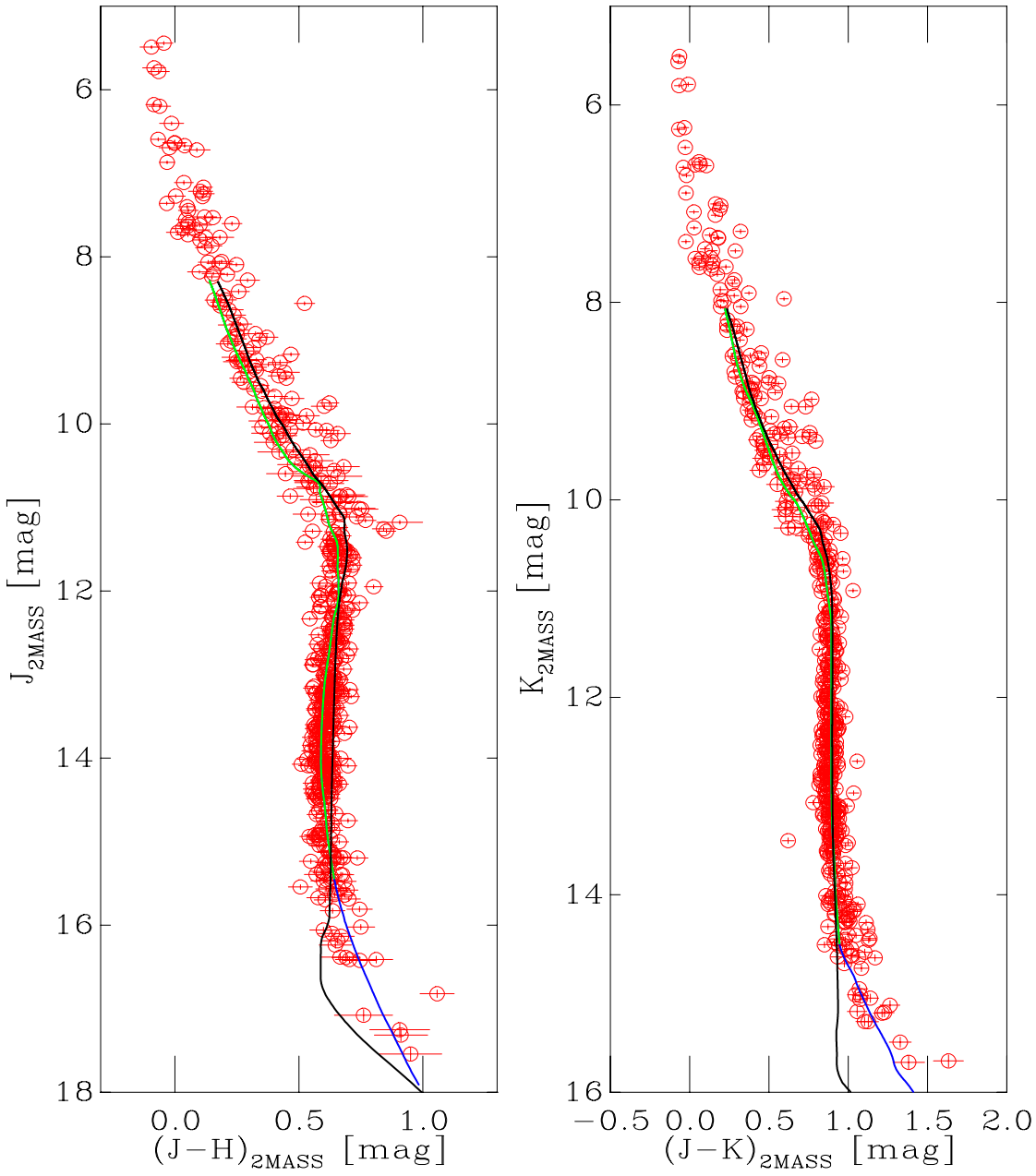

Figure 4.10: Pleiades members plotted in J_{2MASS}, $(J-H)_{2MASS}$ (left) and K_{2MASS}, $(J-K)_{2MASS}$ (right) CMDs. Red circles show the Pleiades members with associated uncertainties plotted as bars. The solid green line is a DCJ08 isochrone adopting an age of 130 Myr and dm=5.63 mag, with the Bell et al. (2014) tuning. The blue line is the extension achieved by adopting the empirical correction derived from the UKIDSS system. The solid black line is the equivalent untuned model (i.e. without the derived empirical correction).

the Bell et al. (2014) tuning (derived from 2MASS data) was adopted down to the limit of 2900 K. Between 2900 K > $T_{\rm eff}$ ≥ 2000K the ΔBCs derived from the UKIDSS data were applied to the 2MASS models. Although one could argue that adopting the UKIDSS-derived ΔBCs may have introduced some error into the models this was still an improvement compared to the untuned models. Additionally the ΔBCs in J and H are small (see Figure 11 in Bell et al. 2012), so any errors introduced here would also be small.

5

A Method of Photometric Dereddening from *iZJH* Data

5.1 Dereddenning - The *i*-*Z*, *J*-*H* diagram

Stellar extinctions for the young regions studied in this thesis have been estimated in a number of surveys (see the individual chapters for details). These surveys, however, do not cover the entirety of our member samples. Additionally, the method and bandpasses used to determine the extinction towards a star can affect the derived value (Herczeg & Hillenbrand 2014). To avoid introducing additional uncertainty into the derived reddening, and hence position in the de-reddened colour-magnitude diagram, values are needed for the extinction for each of our sample of member stars, ensuring consistency across the sample. There are a number of methods for determining cluster reddenings. Typically the pair method is used, in which the spectrum of a reddened star is compared with an unreddened star of the same spectral type, but alternative photometric methods include fitting isochrones to a CMD, using a colour-colour diagram to eliminate the effect of

distance, or the Q-method (Johnson & Morgan 1953).

In very young SFRs stars are often affected by differential reddening, which limits the usefulness of simple isochrone fitting. Instead, when dealing with variable extinction stars must be dereddened on a star-by-star basis. A method of photometric dereddening is required that can be applied to very young stars both with and without discs, allowing us to derive consistent extinction values for both. A multitude of CMDs and colour-colour diagrams were examined in an attempt to identify one that would be useful for dereddening purposes. In most CMDs and colour-colour diagrams the reddening vector runs parallel to, or almost parallel to, the stellar sequence. However Wilson (2013) found that an $i-Z$, $J-H$ colour-colour diagram has a portion that is not parallel to the reddening vector (see Figure 5.1). The reason for this is that at $T_{\rm eff} \simeq 4000\,{\rm K}$ H_2O opacity leads to flux redistribution into the H and K filters (Allard & Hauschildt 1995; see also King et al. 2013). This causes the J-H colours to become degenerate, which can be seen in a J, J-H CMD when the models become almost vertical. This diagram also has the advantage that the i, Z, J and H bands should be minimally affected by accretion flux which is beneficial when dealing with young accreting objects. These bands will also minimise the impact of infrared excess from circumstellar discs, although there will be some small contribution to the J and H flux. Finally, these bands are close to the colours to which the dereddening will be applied (r,i) and so this will minimise the effect of, for example, a non-standard $R_{\rm V}$ value. In this chapter I will develop this method of dereddening using a Bayesian technique, which allows the colour-colour diagram to be used in a quantitative way, taking account of binarity and age effects.

5.1.1 Reddening vectors

Before discussing the dereddening technique it is necessary to consider the reddening law. The $T_{\rm eff}$ dependence discussed in Section 3.3.1 also means that simple reddening vectors cannot be used. Instead to relate $E^{\rm Hot}_{B-V}$ to extinction in individual filters the reddening law of Fitzpatrick (1999) (hereafter F99) is used. To derive $T_{\rm eff}$-dependent reddening vectors the F99 law adopting $R_{\rm V}$=3.1 and $E^{\rm Hot}_{B-V}$=0.5 was applied to the atmospheric models and the results folded through the sets of filter responses to derive a set of reddened colours and magnitudes in each photometric system used in this work (INT-WFC, SDSS, 2MASS and UKIDSS). For any value of $E^{\rm Hot}_{B-V}$ I then linearly interpolated between the unreddened models and the $E^{\rm Hot}_{B-V}$=0.5 models to calculate $T_{\rm eff}$-dependent reddening coefficients (for larger $E^{\rm Hot}_{B-V}$ values, extrapolation was used). Most objects

in Taurus (Chapter 6) and Chamaeleon (Chapter 9) are expected to be at modest extinctions, so this approach gives confidence in the interpolated extinction values around the expected values. Bell et al. (2012) and Bell et al. (2013) used the reddening law of Cardelli et al. (1989) (hereafter CCM). The CCM law has been derived using a set of assumed filter wavelengths. In the near-IR these adopted wavelengths are not consistent with the now-ubiquitous 2MASS filters, in particular the H-band. Cardelli et al. adopted values of λ of 1.25, 1.59 and 2.17 μm for the J, H and K filters respectively, compared to the values from (Cohen et al. 2003) of 1.235, 1.662, and 2.159 μm. Bell et al. (2013) thus switched to the F99 law. To ensure that the work presented in this thesis is on a consistent system to that of Bell et al. (2013) the F99 reddening law is compared to the CCM law in Section 5.1.5.

5.1.2 *iZJH* Dereddening Methodology

We start by considering the *i*-*Z*, *J*-*H* colour-colour diagram for Taurus members. For $(i-Z)_{\rm intrinsic} \geq 0.4$ the reddening vectors derived in Section 5.1.1 cross a single point on the isochrone (see Figure 5.1). This allowed each star above this limit to be dereddened to a unique point on the model isochrone. However unlike MS isochrones which are largely insensitive to age changes, the young cluster work uses PMS models, and so the effect of age on the model $(i-Z),(J-H)$ sequence must be considered. It can be seen in Figure 5.1 that the position of the PMS in the $(i-Z),(J-H)$ diagram is largely insensitive to age changes of a factor 2. For $(i-Z)_{\rm intrinsic} < 0.4$ there can be multiple solutions, leaving us unable to differentiate between a low-mass lightly-extincted star and a high-mass highly-extincted star. Instead I turned to a Bayesian method, based on the foundation of the (*i*-*Z*), (*J*-*H*) diagram, to allow the most likely extinction to be determined.

5.1.3 Bayesian fitting

In Section 5.1.2 the dereddening method was described in terms of dereddening in a colour-colour diagram, it can be generalised to allow it to take account of factors such as stellar age or unresolved binaries using a Bayesian method. For example in the colour-colour diagram method unresolved binaries would be incorrectly dereddened onto the single-star sequence.

A grid of model isochrones was constructed over a range of log(age) (τ) and companion mass-ratios ($q = M_2/M_1$, where M_1 is the primary mass and M_2 is the companion mass). Note that in this chapter τ is used to denote log(age), rather than referring to the τ^2 technique used in

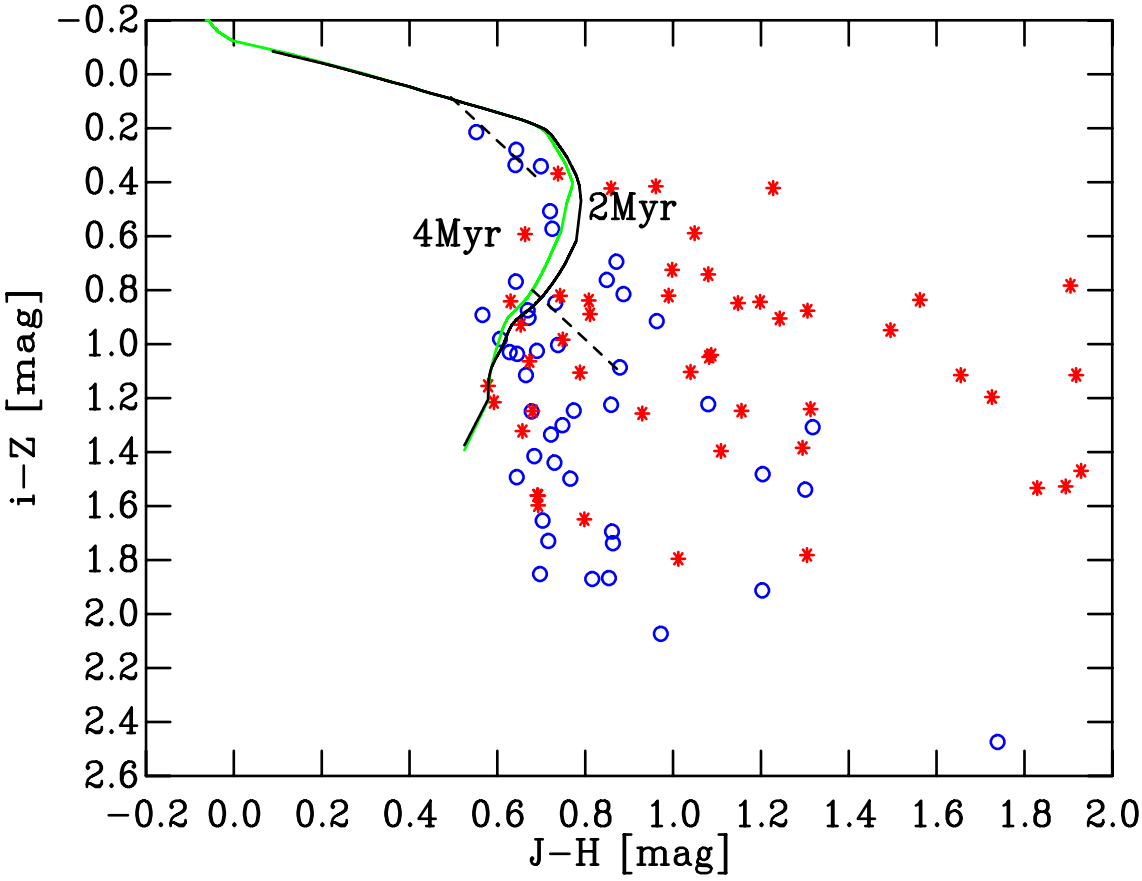

Figure 5.1: An $(i-Z)_{\mathrm{WFC}}$, $(J-H)_{2MASS}$ colour-colour diagram. Red open circles are Class II Taurus members, blue open circles are Class III members. The black and green line are a 2Myr and 4Myr tuned BCAH98 isochrone respectively, showing the insensitivity to age along the majority of the sequence. The black dashed lines are the reddening vectors obtained from the Fitzpatrick (1999) reddening law, showing that stars will deredden to a single position on the isochrone.

Chapter 4. For each model in the grid the $T_{\rm eff}$-dependent reddening vectors derived in Section 5.1.1 were used to redden the models over a range of $E^{\rm Hot}_{B-V}$. The distance modulus is not fitted and is instead adopted from the literature, as the fitting process is already attempting to constrain 4 parameters (q, $T_{\rm eff}$, τ and $E^{\rm Hot}_{B-V}$) with 4 filters. The fitting statistic is defined as

$$\chi^2 \equiv \sum_{\lambda} \frac{(m^{\rm model}_{\lambda} - m^{\rm data}_{\lambda} + D_m + a_{\lambda})^2}{\sigma^2_{\lambda}} \tag{5.1}$$

where $m^{\rm model}_{\lambda}$, $m^{\rm data}_{\lambda}$, a_{λ} and σ_{λ} are the intrinsic model magnitudes, observed magnitudes, extinction and uncertainties in a given filter, and D_m is the distance modulus. The results is a 4-D grid with χ^2 values for each combination of q, $T_{\rm eff}$, τ and $E^{\rm Hot}_{B-V}$.

Given Bayes' theorem:

$$p(M|D) = \frac{p(D|M)p(M)}{p(D)}, \tag{5.2}$$

where $p(M|D)$, the posterior probability, is the probability of the model given the data (i.e the probability of the model being the correct one given our data), $p(D|M)$, the conditional probability, is the likelihood of the data being drawn from the model, $p(M)$, is the prior on M and $p(D)$ is the sum of the probability over all possible datasets. I can then write $p(E^{\rm Hot}_{B-V}|D)$, the probability of a star having extinction $E^{\rm Hot}_{B-V}$ given the data as

$$p(E^{\rm Hot}_{B-V}|D) = \frac{p(D|E^{\rm Hot}_{B-V})p(E^{\rm Hot}_{B-V})}{p(D)}, \tag{5.3}$$

with $p(D|E^{\rm Hot}_{B-V})$ given by

$$p(D|E^{\rm Hot}_{B-V}) = Ae^{-\chi^2/2}. \tag{5.4}$$

The model SEDs are also a function of age, $T_{\rm eff}$ and mass ratio (for a binary), and so this gives

$$p(E^{\rm Hot}_{B-V}, q, T_{\rm eff},\tau|D) = \frac{p(D|E^{\rm Hot}_{B-V}, q, T_{\rm eff}, \tau)p(E^{\rm Hot}_{B-V}, q, T_{\rm eff}, \tau)}{p(D)}. \tag{5.5}$$

I then considered the single-star model and binary star models independently, so that they are able

to be weighted correctly. To do so I write

$$\begin{aligned} p(D|E^{\rm Hot}_{B-V}, q, T_{\rm eff}, \tau) =& p(B)p(D|E^{\rm Hot}_{B-V}, q, T_{\rm eff}, \tau, B) \\ &+ p(S)p(D|E^{\rm Hot}_{B-V}, T_{\rm eff}, \tau, S) \end{aligned} \tag{5.6}$$

where $P(B)$ and $P(S)$ are the prior of the star being a binary or single star respectively. A flat prior was adopted for q ($0 \leq q \leq 1$), given that the mass-ratio distribution is consistent with being flat (Kraus et al. 2011; Raghavan et al. 2010). A flat prior was also adopted on τ as a Jeffreys prior is the simplest objective prior in log space. I then marginalised over q, and τ.

$$\begin{aligned} &p(D|E^{\rm Hot}_{B-V}, T_{\rm eff}) = \\ &\quad p(B) \int\int p(D|E^{\rm Hot}_{B-V}, q, T_{\rm eff}, \tau, B)p(q)P(\tau)\,{\rm d}q\,{\rm d}\tau \\ &\quad + p(S) \int p(D|E^{\rm Hot}_{B-V}, T_{\rm eff}, \tau, S)p(\tau){\rm d}\tau \end{aligned} \tag{5.7}$$

I thus obtained a likelihood for each combination of $E^{\rm Hot}_{B-V}$ and $T_{\rm eff}$. If one simply marginalised over $T_{\rm eff}$ this would then give the most likely $E^{\rm Hot}_{B-V}$. This is of limited use however, as remembering that $T_{\rm eff}$ can have a large impact on the derived extinction leads to the conclusion that without the $T_{\rm eff}$ information this cannot be accurately transformed to an A_λ. Instead for each $T_{\rm eff}$, $E^{\rm Hot}_{B-V}$ combination in the grid, the ($T_{\rm eff}$ dependent) extinction in the other filters, A_λ, was given by

$$A_\lambda = k(T_{\rm eff})E^{\rm Hot}_{B-V} \tag{5.8}$$

where $k(T_{\rm eff})$ is the temperature-dependent transformation factor. Given that $p(E^{\rm Hot}_{B-V}|D, T_{\rm eff})$ is a probability density function:

$$p(E^{\rm Hot}_{B-V}|D, T_{\rm eff}) = \frac{{\rm d}P}{{\rm d}E^{\rm Hot}_{B-V}} \tag{5.9}$$

where P is the cumulative distribution function. The likelihood in terms of A_λ is then

$$\begin{aligned} p(A_\lambda|D, T_{\rm eff}) &= \frac{{\rm d}P}{{\rm d}A_\lambda} \\ &= \frac{{\rm d}P}{{\rm d}E^{\rm Hot}_{B-V}} \frac{{\rm d}E^{\rm Hot}_{B-V}}{{\rm d}A_\lambda} \\ &= p(E^{\rm Hot}_{B-V}|D, T_{\rm eff}) \frac{{\rm d}E^{\rm Hot}_{B-V}}{{\rm d}A_\lambda}. \end{aligned} \tag{5.10}$$

The resultant A_λ was binned into 0.05 mag bins, and finally I marginalised along $T_{\rm eff}$,

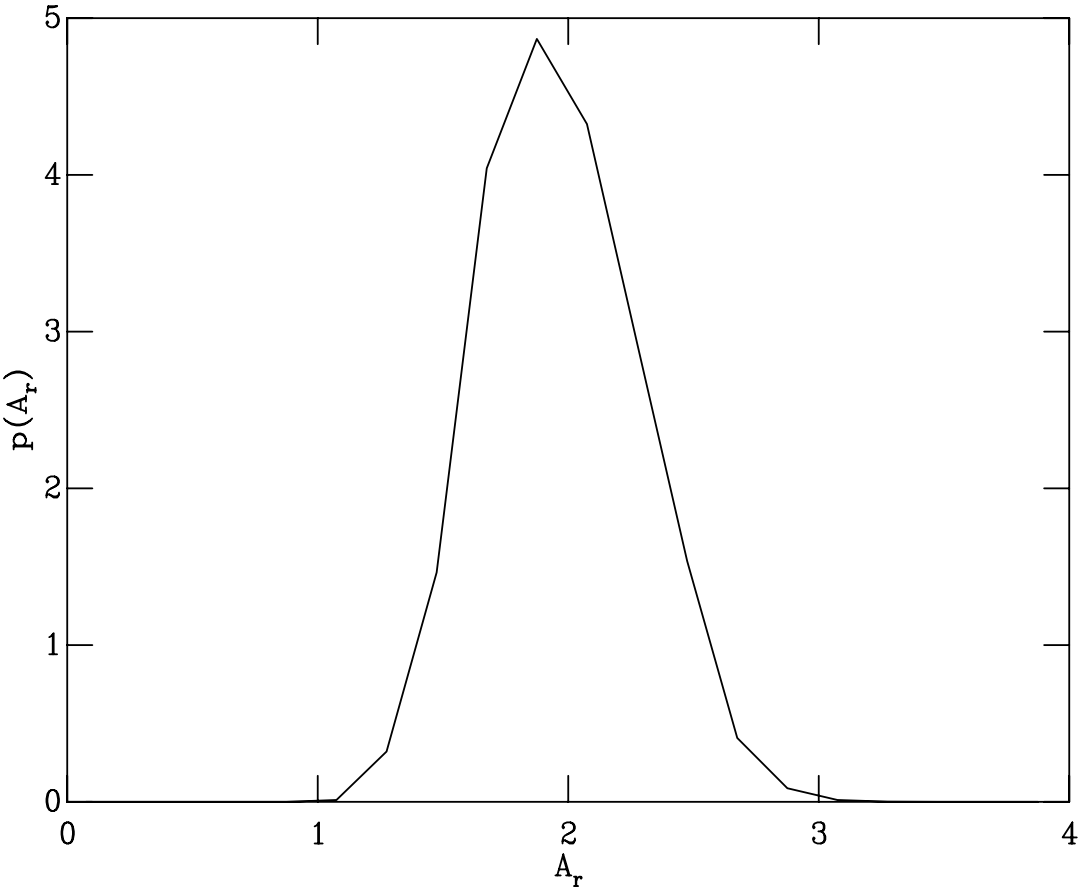

Figure 5.2: An example of the typical distribution of $p(A_r|D)$ values for the Taurus members.

adopting a flat $p(T_{\rm eff})$, giving a likelihood grid for the given colour or magnitude.

$$p(A_\lambda|D) = \int p(A_\lambda|D, T_{\rm eff})p(T_{\rm eff})\mathrm{d}T_{\rm eff} \tag{5.11}$$

The most likely value from this grid was adopted as the measured extinction for the given star, and the uncertainties were taken from the 68% confidence contour. A typical example of the $p(A_\lambda|D)$ is shown in Figure 5.2. The median uncertainty for our Taurus sample (Chapter 6) was $^{+0.3}_{-0.15}$ mag in A_r. This is similar to uncertainties in other studies, e.g. Herczeg & Hillenbrand (2014) state their uncertaintites are ≃0.2-0.3 mag in $A_{\rm V}$, and point to literature uncertainties of 0.2-1.0 mag. It will be shown in Section 6.4 that the use of the r, r-i CMD for age determination is relatively insensitive to uncertainties in extinction. It should be noted that an age is not adopted from this Bayesian fitting, because this method is built upon the $i - Z$, $J - H$ diagram and as was shown earlier the method is insensitive to age change. Thus the ages at this point will be poorly constrained.

5.1.4 The Bayesian method vs χ^2

Classically one might simply derive the χ^2 values for each point in the model grid and then adopt the single best fitting value. The result of fitting in this way may be different to fitting in the Bayesian method presented in Section 5.1.3. For example, if one imagines a 2D grid of $E^{\rm Hot}_{B-V}$ vs τ with a χ^2 value at each pixel, we can conceive of a situation in which a single pixel at a certain $E^{\rm Hot}_{B-V}/\tau$ combination has the lowest χ^2, surrounded by pixels with high χ^2, and at a different value of $E^{\rm Hot}_{B-V}$ a number of low χ^2 over multiple ages. From a statistical viewpoint the second $E^{\rm Hot}_{B-V}$ would be the more likely value, as it represents a good fit over multiple ages, as opposed to the first $E^{\rm Hot}_{B-V}$ which represents a good fit at only a single age.

The results from the Bayesian fitting process were compared to the best-fitting values from the χ^2 fitting and found that the results are largely consistent with each other. The median offset in A_r between the Bayesian value and the χ^2 value was 0.04 and 0.00 for the Class III and Class II sources in Taurus respectively. Thus although in practice the value from the Bayesian fitting process was adopted this does not significantly affect the outcome, but I have proven $T_{\rm eff}$, q, and age have little effect on the fitting.

5.1.5 Robustness

The focus for the fitting procedure has been the derivation of consistent extinction values, rather than attempting to determine stellar parameters. The accuracy of, for example, the derived best-fit $T_{\rm eff}$ and mass-ratio parameters are therefore of less concern. Instead the focus was on the robustness of the extinction fitting.

First I examined whether the extinctions derived in *iZJH* are consistent with those derived over a wider λ range by extending the fitting to redder bands. This can only be performed for objects without discs, and so I used the Class III objects in Taurus, and compared the results to the previous fit. The Class III objects were fitted over the $(riZ)_{\rm WFC}$ $(JHK)_{\rm 2MASS}$ and the four *Spitzer* IRAC bands and a more limited fit using *riZJH* and compared to the results obtained using *iZJH*. The derived extinction values differ only marginally between the three runs. When compared to the extinctions obtained from *iZJH* fitting, the extinctions from the *riZJH* fitting are larger, with a median difference of 0.05 and 0.08 in A_r for the Class II and Class III samples respectively. The extinctions obtained from fitting the *riZJHK* and *Spitzer* bands are larger than those obtained from *iZJH* fitting with a median difference of 0.08 for the Class III sample.

I also considered the effect of fitting over a range of mass-ratios. The concern here is the effect of fitting a single star with a binary model or vice-versa. I performed three runs of the fitting procedure on Taurus: one in which I fixed $q = 0$ (i.e single star only); one in which I fixed $q = 1$ (equal-mass binary) and one in which I allowed q to vary (regular fitting procedure). The resultant A_r, values from the three runs were then compared. The median difference between the single-star fit and free-fitting is 0.0. The median difference between the equal-mass binary fit and free-fitting is also 0.0. The mean differences are also small : the values obtained from the equal-mass binary fitting are smaller, with a mean difference of 0.05 (regular fit - binary fit). The values from the single-star fit are larger, with a mean difference of 0.10. It is clear therefore that the most likely value was again insensitive to the mass-ratio. Instead it was the best-fit age that changes between the three fits, moving to older ages to compensate for the increased luminosity arising from a companion object, which reinforces the decision to adopt only $E^{\rm Hot}_{B-V}$ values from the fitting process.

Finally, I considered the effect of adopting alternate reddening laws, which is especially important due to the switch in reddening laws in previous work (See Section 5.1.1).

The difference in $E(\lambda - V)/E(B - V)$ between the CCM and F99 laws can be seen in Figure 5.3. The laws are relatively consistent in g, and appear to be inconsistent as we move redwards (especially i and Z and redwards). However the key information for the reddening fitting is the relationship between $iZJH$. Both the F99 and CCM laws well reproduce the colour-ratios in JHK from Rieke & Lebofsky (1985) (i.e. $\frac{E(J-H)}{E(H-K)}$ is well matched between all three), and the colour ratios in i and Z are likewise similar between the F99 and CCM laws. Thus the reddening derived in these filters is consistent when switching reddening laws. Instead, the difference between the laws manifests in terms of $E^{\rm Hot}_{B-V}$. For a given $E^{\rm Hot}_{B-V}$, the derived values of A_J and A_H between the two extinction laws are different by a factor of 2-3. Conversely for a given reddening derived in $iZJH$, the associated $E^{\rm Hot}_{B-V}$ value will change depending on the reddening law used. This means that when extrapolating a derived reddening out to the shorter wavelengths, especially in g it varies greatly between the two laws. Consequently it was found that using an r, r-i diagram to derive ages gives consistent results for both reddening laws.

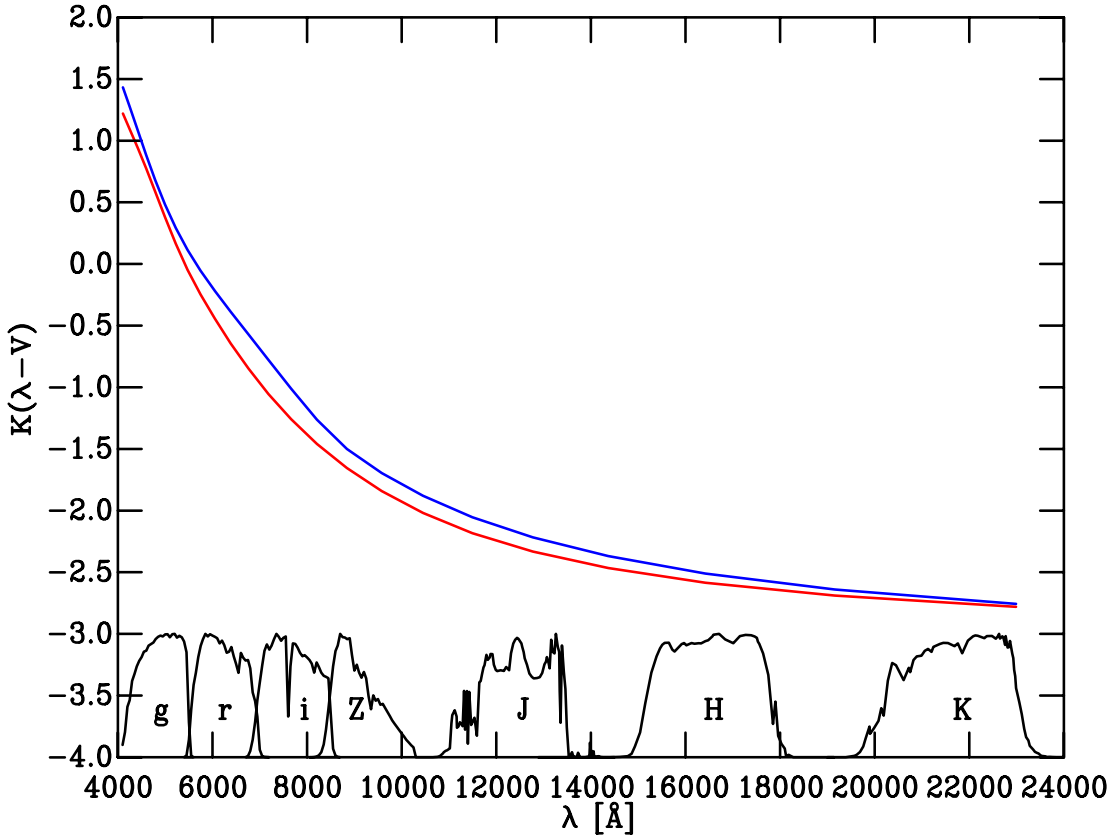

Figure 5.3: A comparison of the reddening laws from Fitzpatrick (1999) (red line) and Cardelli et al. (1989) (blue line). Also shown at the bottom of the plot are the filter responses for the WFC and 2MASS filter sets, with normalised and arbitrary y-values.

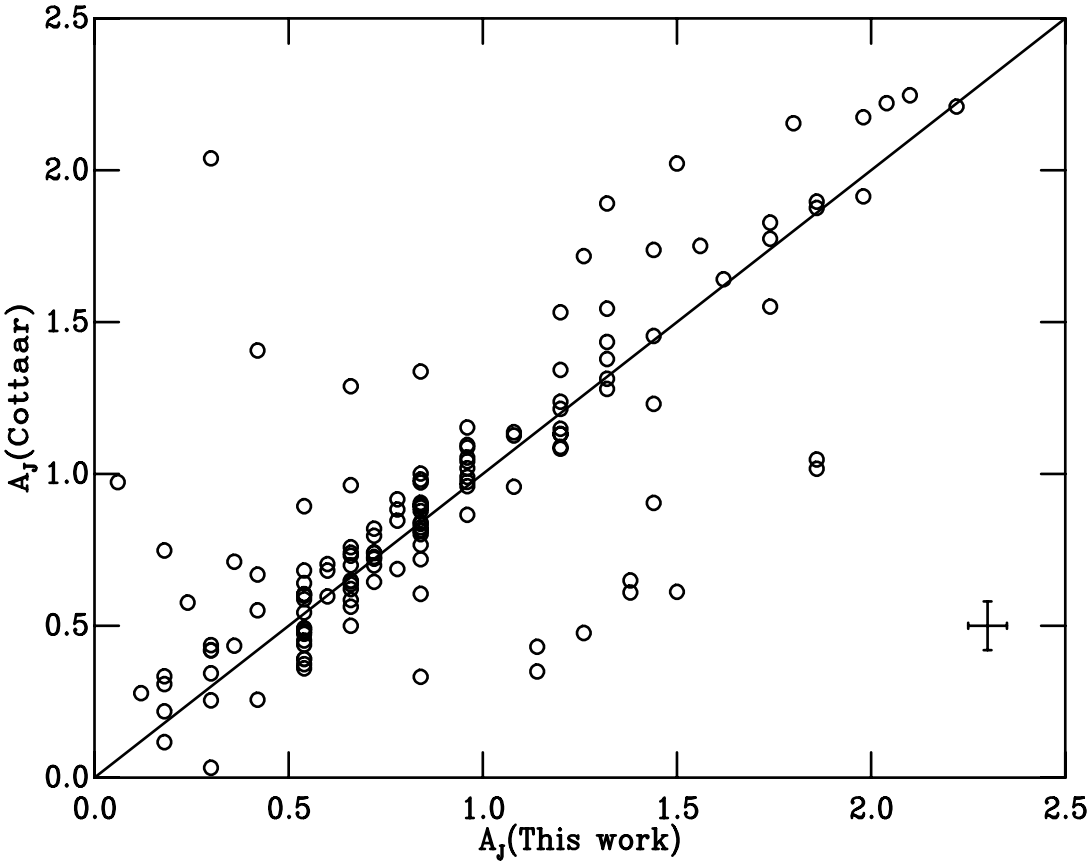

Figure 5.4: Comparison between the extinctions derived for IC348 in this work and literature values from Cottaar et al. (2014)

5.2 Testing Derived Reddenings Using IC348

In this work I have adopted a new scheme for determining the stellar reddenings, and also determined the nominal age based on the previously unused r, r-i CMD (Bell et al. 2013 used g vs g-i CMDs for age determinations). Therefore it is necessary to test for consistency between this result and the results from Bell et al. (2013). From the cluster sample in Bell et al. the best choice for such a purpose is IC348, as it is nearby (dm=6.98), and the reddening is highly variable across the field, as in Taurus. Bell et al. (2013) adopted a mean reddening determined from the upper-main sequence members using the Q-method. This method is obviously not ideal when dealing with differential reddening across the field. Here I adopt the same memberships as in Bell et al. (2013) (Herbig (1998); Luhman et al. (2003); Luhman et al. (2005a); Luhman et al. (2005b); Preibisch & Zinnecker (2002); Second ROSAT PSPC catalogue; Cohen et al. (2004); Littlefair et al. (2005)), and fit the IC348 members to determine individual extinctions using the dereddening procedure outlined in this chapter. Comparing the individual extinctions against those derived in Cottaar et al. (2014), who used near-infrared spectra to derive extinctions, (see Figure 5.4) it was clear that the extinctions derived from $iZJH$ were similar to the literature determinations. There is good agreement between the two estaimtes, with some scatter and some outlying points. The scatter in the values is likely due to the relatively large uncertainties in the extinction estimates ($\sim$ 0.16 mag for Cottaar et al., $\sim$ 0.1 mag for this work). There is also likely some effect due to small residual effects from the disks for Class II sources. Overall however, the dereddening technique here has been shown to yield results similar to those in the literature using other methods. Additionally the average extinction derived from $iZJH$ fitting was compared with that derived in Bell et al. (2013). My median value of E(B-V) is 0.75, which is similar to the median 0.69 found in Bell et al., despite the different techniques and populations probed.

6

The Age and Disc Fraction of Taurus

6.1 Motivation

To test whether circumstellar discs survive longer in low-density, low-mass regions requires a low stellar density T association with a well determined disc fraction, for which I will determine the age. Taurus is an ideal target. It is one of the best-studied star-forming regions in the sky, due to its proximity (d∼140 pc) and youth (typically quoted to be $\sim$ 1 Myr). Taurus is made up of a number of smaller sub-clouds and contains over 300 stars and brown dwarfs (Kenyon et al. 2008). With a stellar density of $\simeq$ 6 stars pc^{-3} (see e.g. Luhman et al. 2009) Taurus is an excellent laboratory for studying star-formation in a low density environment (compared to e.g. Trapezium with $n \sim 10^4$ pc^{-3} Hillenbrand et al. 2001). To apply the age derivation method used previously by Bell et al. (2013) to determine the age of Taurus requires (i) photometry of Taurus members in a well understood photometric system and (ii) model isochrones transformed into the same system to avoid the pitfalls of photometric transformations. In addition it requires a consistent treatment

of the spatially varying extinction in Taurus. In the massive regions studied in Bell et al. (2013) the extinction was largely uniform, and this is therefore a new concern.

In Section 6.2 I introduce and describe the data. In Section 6.3 the dereddening process discussed in Chapter 5 is applied to Taurus, and in Section 6.4 I fit for the age of Taurus and discuss the behaviour of Class II vs Class III sources. The implications of this derived age on both the mass function and disc lifetime are discussed in Section 6.5, and the conclusions are presented in Section 6.6.

6.2 New Data

The observations were obtained using the Wide Field Camera (WFC) on the 2.5m Isaac Newton Telescope (INT) on La Palma on the nights of December 3rd, 4th and 5th 2012. The data were reduced following the process in Chapter 2.

39 fields were observed in Taurus, focusing on the area that is not covered by the Sloan Digital Sky Survey (SDSS) (York et al. 2000). The INT-WFC data mainly cover the L1495, L1521 and L1529 clouds. Several fields in common with the SDSS were also covered, which allowed for members which are saturated in the SDSS data to be recovered. The observed fields can be seen in Fig. 6.1, which also shows the SDSS coverage, overlaid on an extinction map from Schlegel et al. (1998). The exposure times and filters used are given in Table A.3.

6.2.1 Membership and Distance for Taurus

To identify Taurus members the membership list of Luhman et al. (2010) was used (itself based on the review by Kenyon et al. 2008). The SED classifications from Luhman et al. (2010) were used to differentiate between Class I, II, and III objects in Taurus. For both the dereddening process and for plotting CMDs it is necessary to assume a distance. Distances were adopted based on parallax: D_m=5.60 for stars near the Lynds1495 complex (Torres et al. 2012), 5.84 for stars near T Tau (Loinard et al. 2007), 6.03 for the stars near the HP Tau complex (Torres et al. 2009) and 5.73 for all other objects.

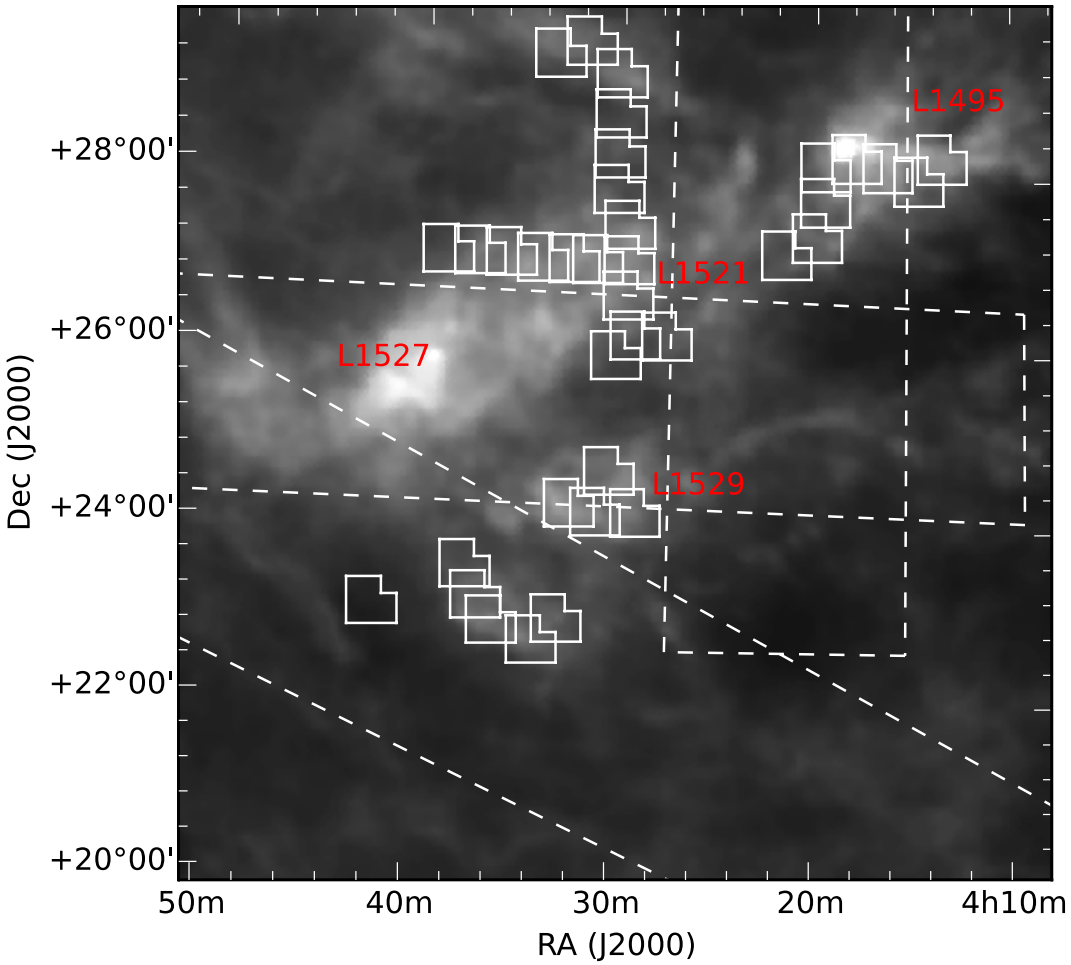

Figure 6.1: 36 of the 39 observed fields in Taurus overlayed on an extinction map from Schlegel et al. (1998). The solid white lines denote the observed INT-WFC fields and the dashed white lines show the SDSS coverage in this area. The labels in red denote the major clouds in Taurus. Note that the additional 3 fields (given in Table A.3) lie $\sim 4^{\circ}$ from those shown here.

6.3 Dereddedning the Taurus Members

The Taurus members were dereddened using the *iZJH* dereddening method described in Chapter 5. The model grid was constructed over an age range (6.0≤ τ ≤7.0), and a $T_{\rm eff}$ range down to the limit of the semi-empirical models. The binary fraction in Taurus is in the region 40-60% (see e.g. King et al. 2012; Daemgen et al. 2015) and is similar in the other young regions, so a binary fraction of 50% was assumed, and therefore $p(B) = p(S) = 0.5$.

6.3.1 Comparison with Literature Extinctions

Taurus has been well studied in the past, and there have been a number of previous estimates of the extinction, each using different techniques and covering different portions of the region. The extinctions derived from *iZJH* fitting were compared against a selection of literature sources which used photometry or spectroscopy in the optical or near-IR and which overlap with my Taurus sample. Furlan et al. (2011) used near infrared photometry and spectroscopy, Herczeg & Hillenbrand (2014) fit optical spectra and Luhman et al. (2009) use combinations of optical spectra, NIR spectra and 2MASS photometry. The comparisons are plotted in Figures 6.2, 6.3 and 6.4. It was found that my derived extinctions agree well with those in Furlan et al. (2011), i.e. the one calculation which uses just IR photometry, with a median ratio of 1.07. However when comparing my extinctions against the other sources it was found that the *iZJH*-derived extinction followed a similar trend, but were offset and scattered. The median ratio between the Herczeg extinctions and my own is 0.80 and 0.57 for the Luhman extinctions. Compared to these sources my derived extinctions appear systematically larger. Herczeg & Hillenbrand (2014) found a similar result, in that their derived extinctions agreed with those sources derived from optical data, but not with those derived from the infrared data. This is potentially an effect of differences in the extinction law used, which one would expect to have a larger effect when comparing between extinction estimates at larger wavelength separations (see Section 5.1.5). The agreement with the Furlan results, the only source in the sample derived entirely from infrared data, gave confidence in my derived extinction estimates. Caution is suggested however in adopting these extinction estimates for use in the blue optical bands (*g* and bluewards).

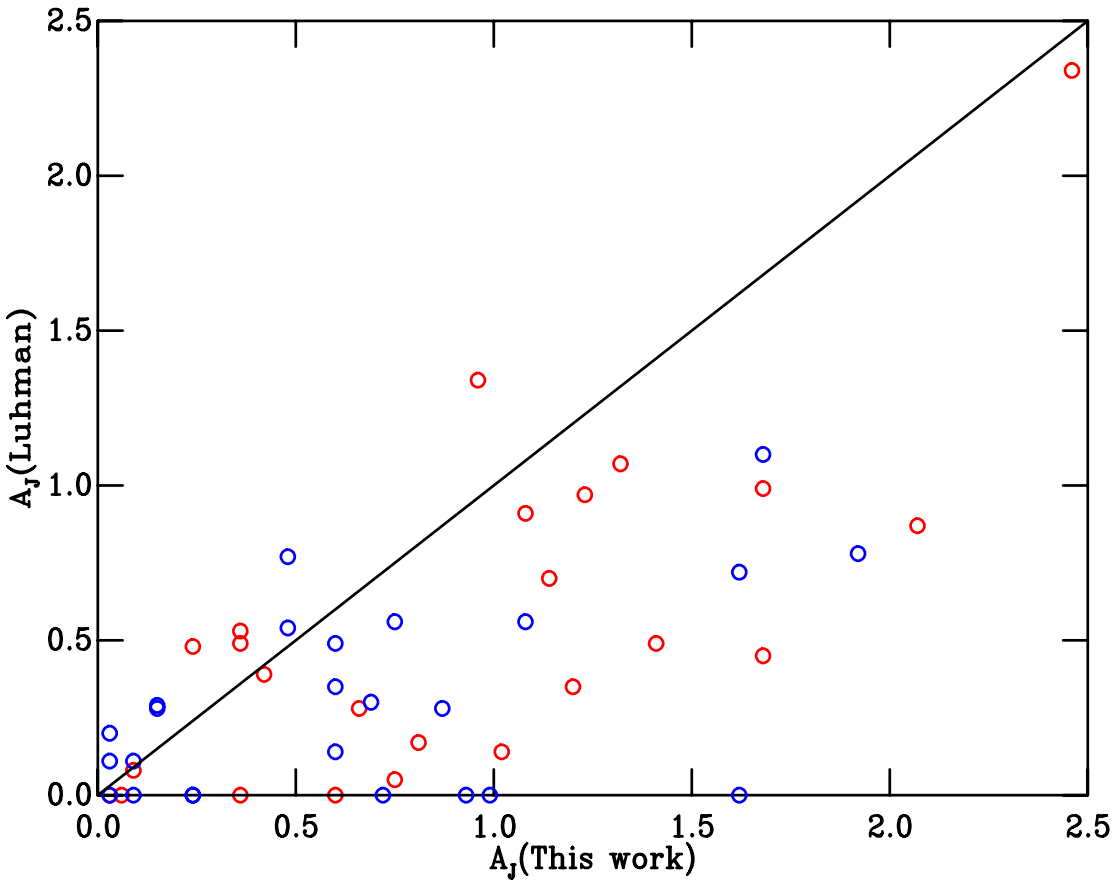

Figure 6.2: Comparison between extinctions derived from *iZJH* fitting and those in Luhman et al. (2009) for Taurus members. Red open circles are Class II sources, blue open circles are Class III sources. Equal extinction is indicated by the black line.

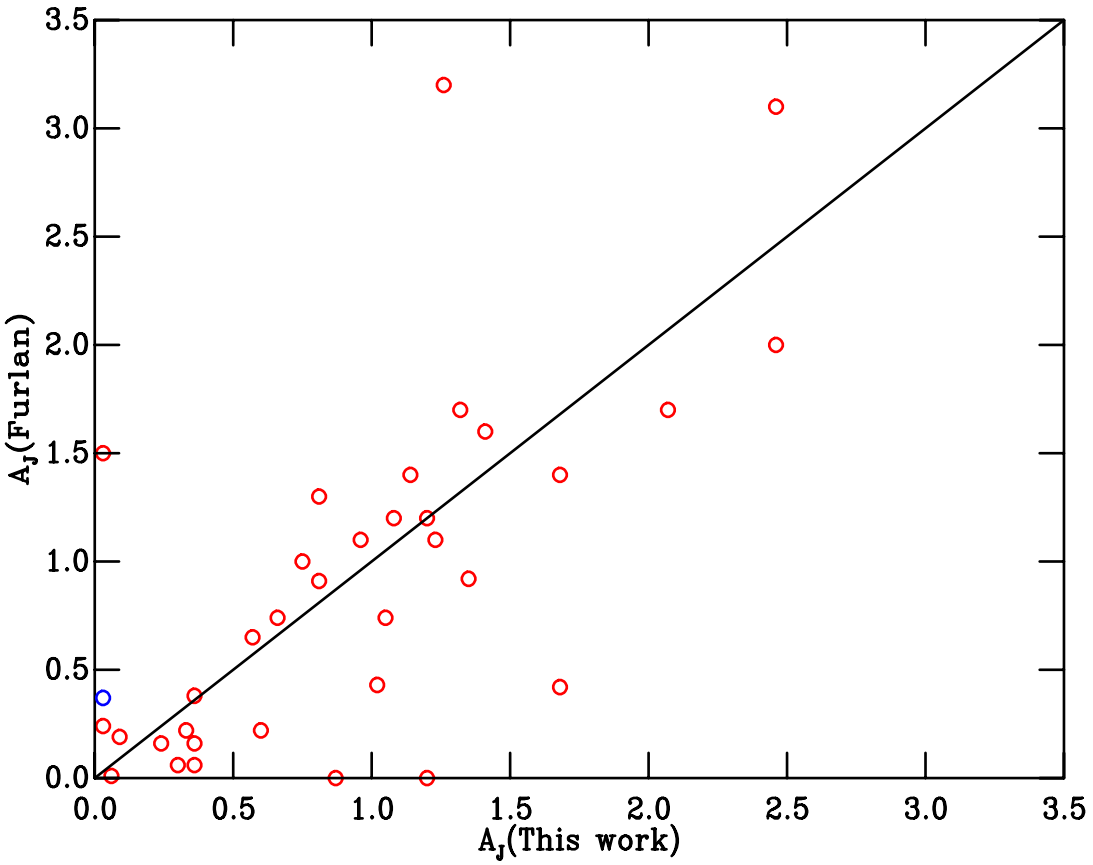

Figure 6.3: The same as Figure 6.2 but comparing against Furlan et al. (2011)

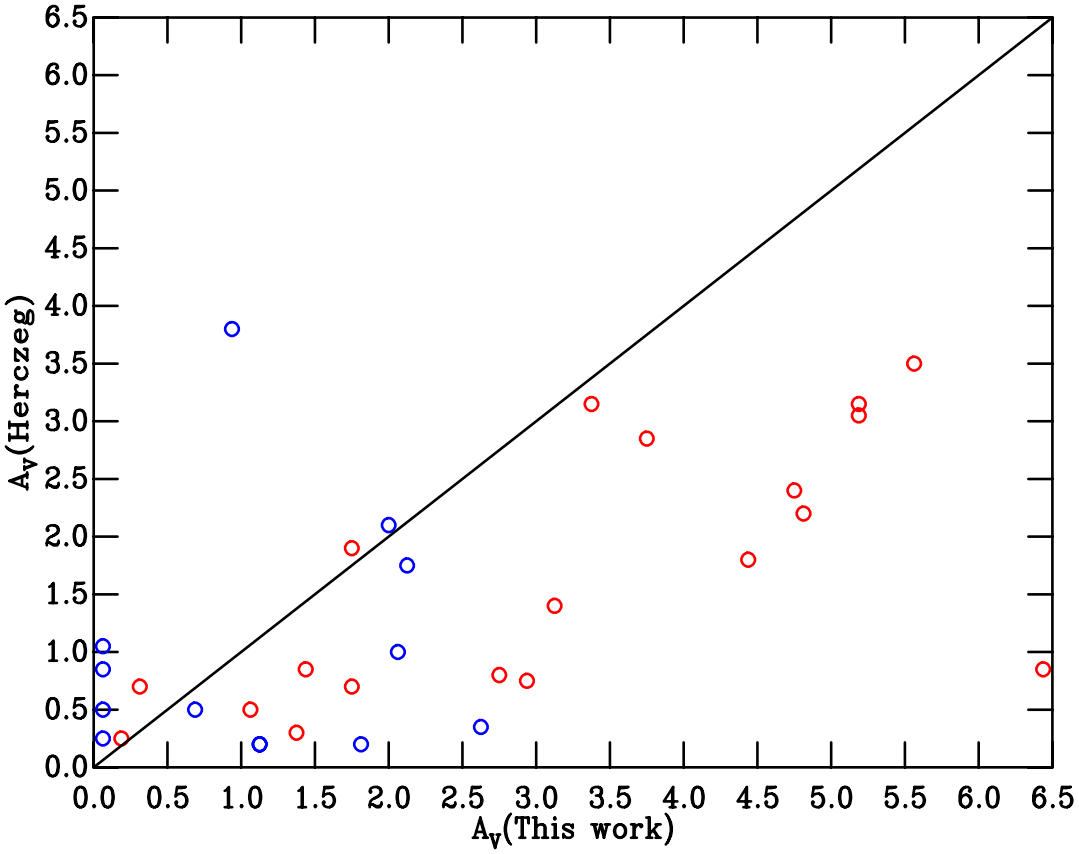

Figure 6.4: The same as Figure 6.2 but comparing against Herczeg & Hillenbrand (2014)

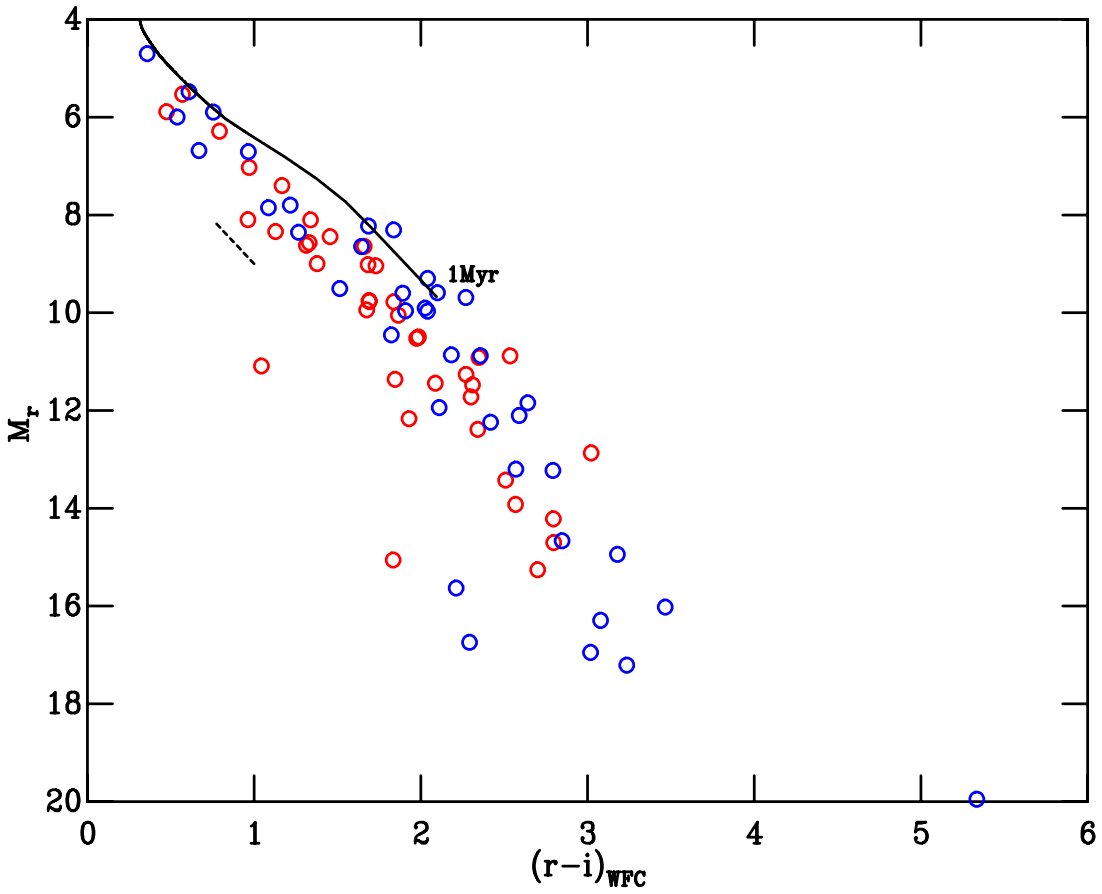

Figure 6.5: Taurus members plotted in an *r*, *r-i* CMD in the WFC system before dereddening was applied. Red points are those identified as Class IIs by Luhman et al. (2010), blue points are those identified as Class IIIs. Overplotted is a 1 Myr DCJ08 isochrone. The magnitudes have been converted to absolute magnitudes using the distances given in Section 6.3

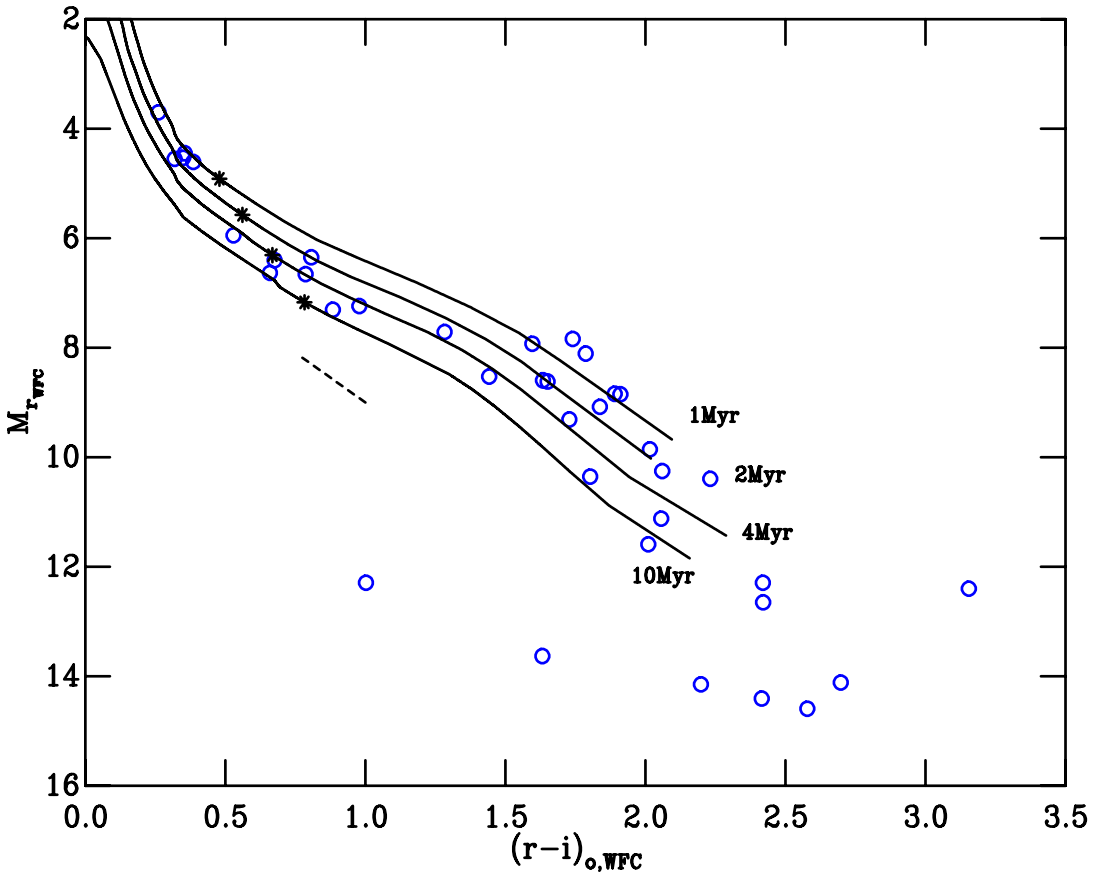

Figure 6.6: Taurus members plotted in an r, r-i CMD in the INT-WFC system. Blue open circles are those identified as Class IIIs by Luhman et al. (2010). Overplotted are DCJ08 isochrones with ages of 1Myr, 4Myr and 10Myr. On each isochrone the location of a $0.75 M_{\odot}$star is indicated with an asterisk.

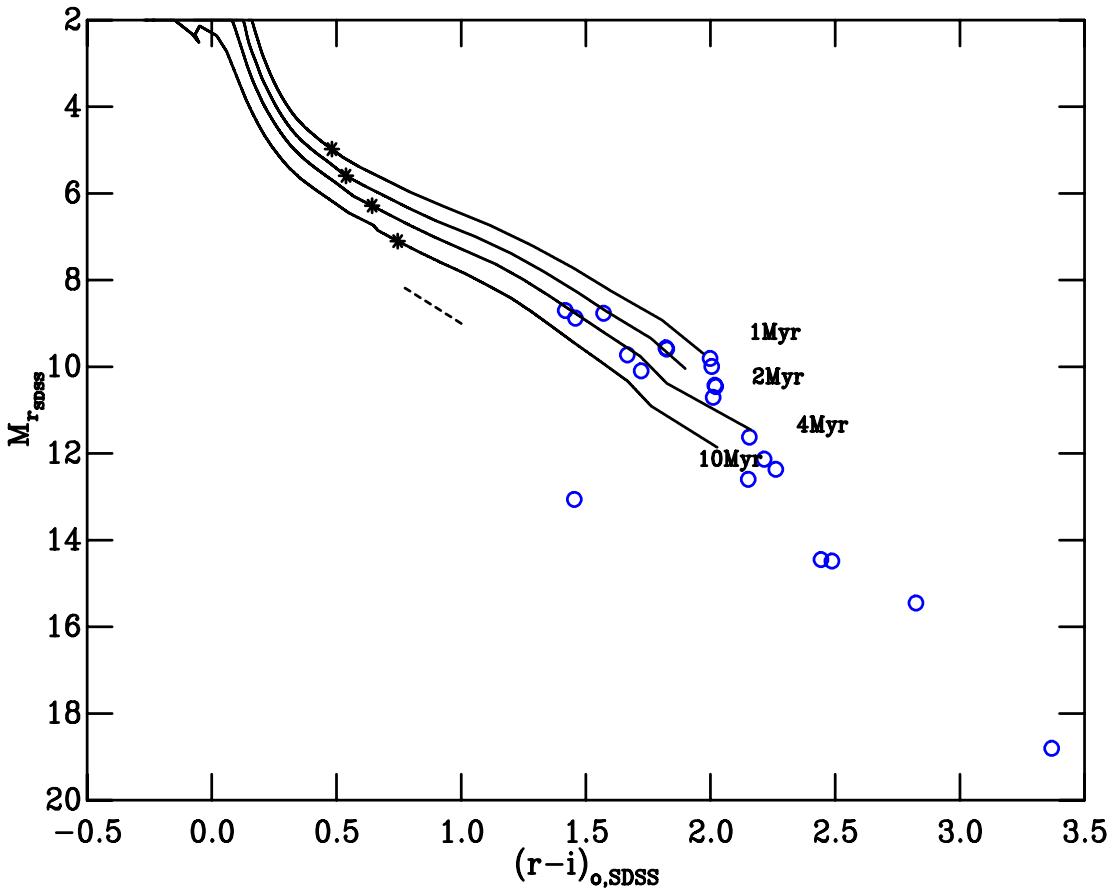

Figure 6.7: The same as Figure 6.6 but for the SDSS system.

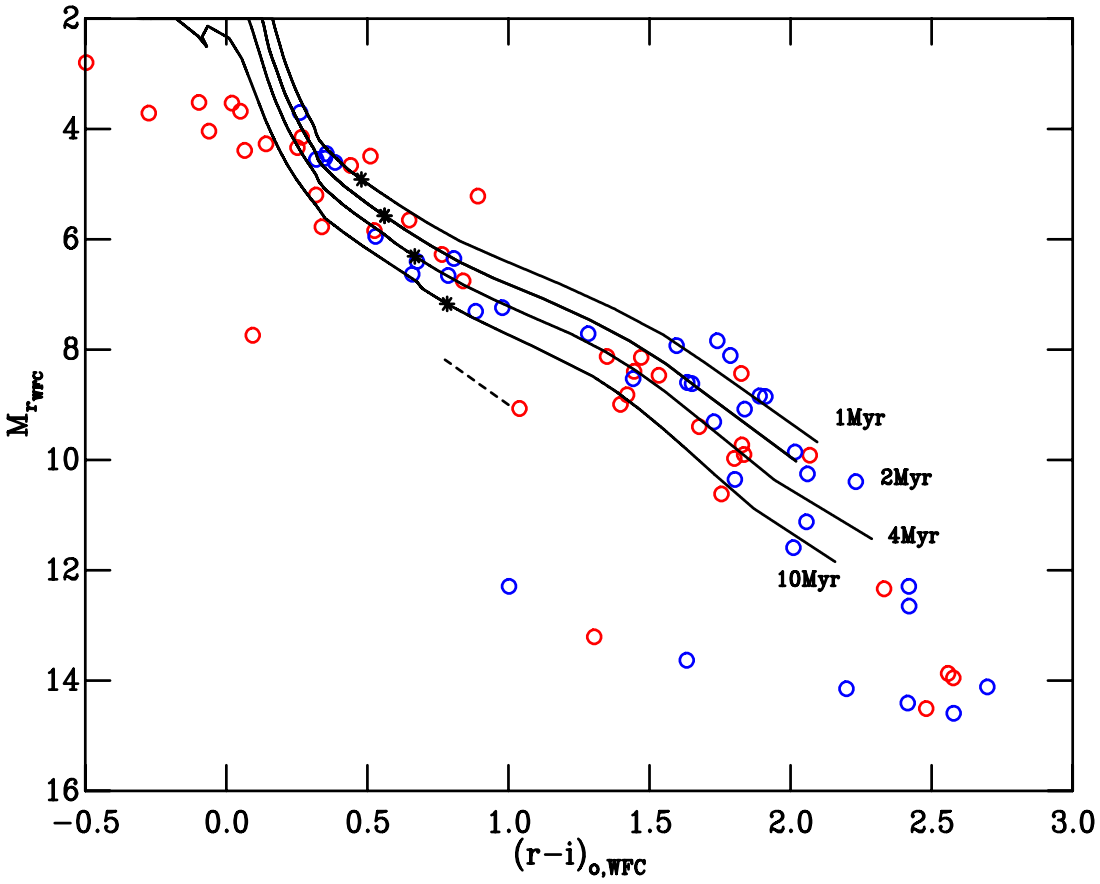

Figure 6.8: Taurus members plotted in an r, r-i CMD in the INT-WFC system. Red points are those identified as Class IIs by Luhman et al. (2010), blue points are those identified as Class IIIs. Overplotted are DCJ08 isochrones with ages of 1Myr, 4Myr and 10Myr. On each isochrone indicate the location of a $0.75 M_{\odot}$star is indicated with an asterisk.

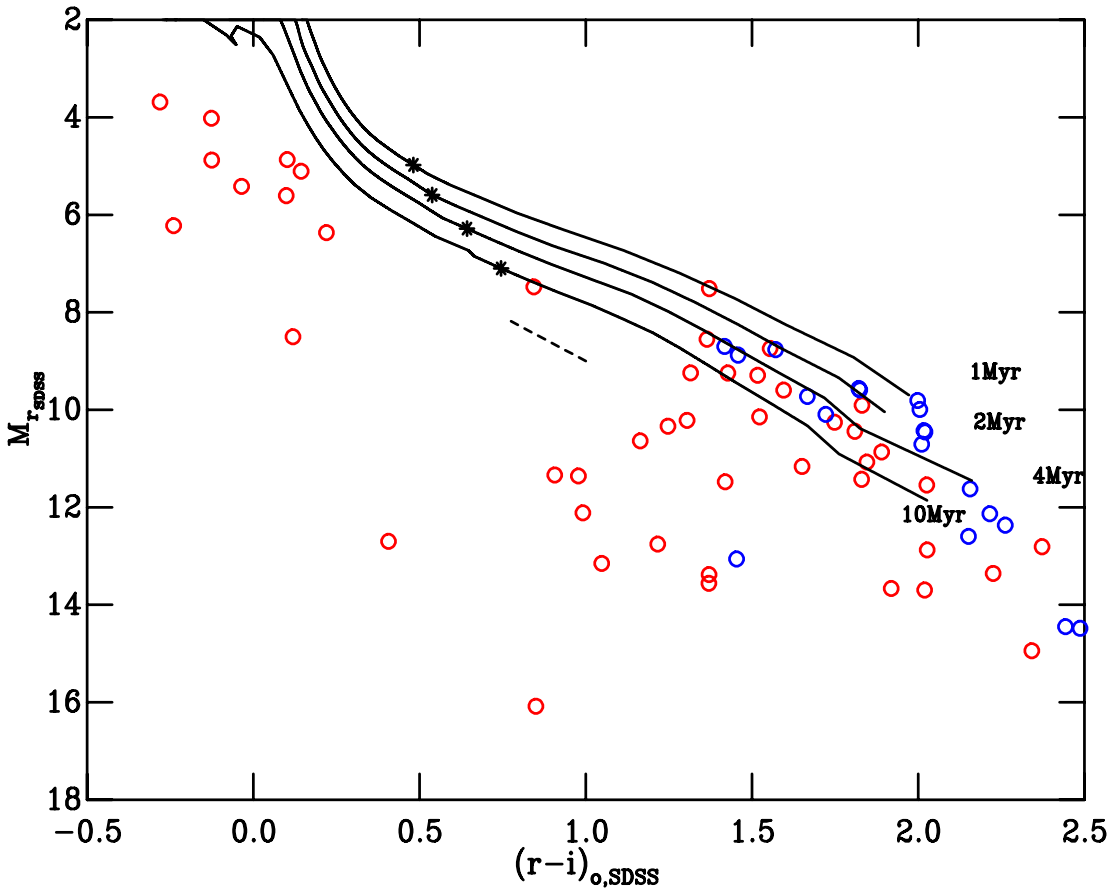

Figure 6.9: The same as Figure 6.8 but for the SDSS system.

6.4 Determining the Age of Taurus

The r, $r - i$ CMD for Taurus members, before dereddening, is shown in Figure 6.5. The derived reddenings and extinctions for the Taurus members were used to deredden the members. The age was determined in the same manner as in Bell et al. (2013). In Bell et al. (2013) ages were determined for older clusters via formal CMD fitting. For younger clusters (like Taurus) τ^2 fitting (Naylor & Jeffries 2006) cannot be used to fit for the age due to the large luminosity spreads exhibited by young clusters. Instead Bell et al. (2013) determined nominal ages by comparing the observed sequence, by eye, to single-star isochrones. To avoid biasing the answer due to the effect of probing different mass regimes based on a cluster's distance and reddening, the position of a theoretical star of 0.75 $M_{\odot}$was measured against the observed sequence. Bell et al. (2013) showed that this procedure yields age estimates that are still consistent with the results of τ^2 fitting.

Compared to the clusters in Bell et al. (2013) Taurus is much closer, and thus the data extend to lower masses. In this lower-mass regime a problem was encountered. Before dereddening, it was found that the Class II objects either lie coincident with the Class III objects, or lie significantly below the sequence (i.e. older). This is at odds with the typical assumption that the Class II objects are younger than the Class III objects, and they represent an evolutionary sequence. This cannot simply be a reddening effect, as the reddening vectors run almost parallel to the sequence.

This was found to be a larger issue with the SDSS data (which is of course a faint survey by design). Sergison et al. (in prep) see a similar effect in the Orion Nebula Cluster (ONC) and in Cepheus OB3b. In their ONC data in particular they are able to identify the source of these "old" Class II sources, as they have simultaneous photometry and spectroscopy observations. They find that these objects are much lower mass objects that are heavily accreting and being pushed to brighter/bluer magnitudes. This accretion luminosity appears to be broadband (i.e. not limited to e.g. Hα) and has a large effect on the $(r - i)$ colour.

Given the lack of accretion diagnostics in my Taurus data, and that including these low-mass heavy accretors would pull the derived age erroneously old there were two options. (1)Fit the entire sequence but only fit the Class III sources. This has the advantage of giving a longer sequence to fit, but could potentially bias the age estimate due to only including the Class III sources. (2)Alternatively fit only the higher-mass members where there is no difference in position between the classes, fitting both the Class II and Class III sources. This has the benefit of being consistent with the approach in Paper II, but only gives a short sequence to fit.

To begin with Method 1, the dereddened Taurus Class III members were plotted in an r, r-i CMD in both the WFC and SDSS systems (Figures 6.6 and 6.7). The distances were again adopted from parallax where possible to minimise the effect of any distance spread. When the model isochrones were overlaid on the CMDs it was clear that the typical 1 Myr age estimate for Taurus is inconsistent with the data. The 4Myr isochrones fit the sequence well, and a 6Myr isochrone (and older) begin to sit towards the bottom of the sequence. An age of 3-4Myr was therefore assigned for the Taurus members in the WFC sample. The SDSS sample is much more limited due to the saturation of bright members, but it is still inconsistent with an age of 1Myr.

Moving to Method 2, both the Class II and Class III sources were plotted in the r, $r-i$ CMD, but only the higher-mass sources were considered. Consistency was found with the previous result (see Figures 6.8 and 6.9). Again an age of 3-4 Myr appeared to provide a good fit to the WFC data. This consistency between the two regimes gave confidence in the age determination. An age of 3-4 Myr was therefore adopted as a mean age for Taurus, noting it should be on a consistent system with the ages presented in Bell et al. (2015), which looks at young moving groups within 100pc, as well as those presented in Bell et al. (2013). It should also be noted that previous studies have demonstrated consistency between upper main-sequence/lithium depletion boundary ages and ages derived using semi-empirical PMS isochrones as adopted here (see e.g Bell et al. 2013, Jeffries et al. 2013, and Bell et al. 2015).

6.4.1 Age variations across the field

Taurus is composed of a number of sub-clouds of varying density. It is conceivable that there would be age variations between the different sub-clouds, and if this were the case any age I quote for Taurus would instead represent an average age for the clouds covered. After dividing my sample according to position on the sky, I found no evidence of age differences between the clouds covered. Although there is a spread in the data which makes it difficult to comment on small-scale age differences, if an age gradient or variation of order 2 Myr existed between groups it should have been identifiable. However, the survey presented here was focussed on the densest portions of Taurus, to recover as many members as possible, and so it is still possible that the clouds outside of this sample have some age variation.

6.4.2 Consistency

In this Chapter I have adopted a new scheme for determining the stellar reddenings, and also determined the nominal age based on the r, $r-i$ CMD. Bell et al. (2013) used g vs $g-i$ CMDs for age determinations. Therefore it was necessary to test for consistency between the results presented in this Chapter and the results from Bell et al. (2013). I have already compared the extinctions determined for Taurus to others from the literature (see Section 6.3.1). The remaining concern then is the use of the untested r, $r-i$ CMD. For each of the young clusters in Bell et al. (2013) I adopted the extinction and distance estimates obtained from fitting the UMS and plotted the r, $r-i$ CMD for the PMS members. As we are adopting the extinctions determined in Bell et al. (2013), I reverted to using the CCM reddening law for this test. The ages derived from the r, $r-i$ CMD were consistent with those derived by Bell et al. from the g, $g-i$ CMD, with the exception of IC348, for which the r, $r-i$ CMD tentatively suggests a slightly older age ($\sim$8 Myr, c.f. 6 Myr). Note that this is likely merely an effect due to the extinction law. It was found that the high-extinction regions, (NGC6611, CepOB3b, IC348, IC5146) begin to show some discrepancies between the 2 CMDs in the positions of the stars compared to the isochrones. These are not enough to affect the age derived (with the exception of IC348), but again highlight the issues with the CCM extinction law.

6.5 Implications

Having derived the age of Taurus I now consider the implications of the new age.

6.5.1 Disc fraction

Bell et al. (2013) plotted the fraction of stars with discs against cluster age for a number of young clusters. This showed a strong correlation, as would be expected. The disc-fractions were adopted based on members with spectral types between K6 and early-M, to minimise the effect of probing different populations in different star forming regions due to distance and reddening. The majority of the clusters used in Bell et al. (2013) are high-density star forming regions, and thus very different to Taurus. Taurus offers an opportunity to test the disc-fraction/age relationship further. The disc-fraction in Taurus was studied in Luhman et al. (2010), using *Spitzer* data to look for infrared excess in Taurus members, finding a disc fraction of (69±4)% for spectral types ≥K6 and

≤M3.5. Early membership surveys of Taurus were based on searching for objects with infrared excess, and thus heavily biased towards objects with discs. To account for this one can look at the disc-fraction based on the fields observed as part of the XMM-Newton extended survey of the Taurus molecular cloud (XEST), (Güdel et al. 2007), as these fields have been well searched in multi-wavelength surveys, and thus should represent an unbiased and spatially complete sample of members (Luhman et al. 2009). The disc-fraction in the XEST fields for spectral types ≥K6 and ≤M3.5 is (71±5)%, consistent with that of the entirety of Taurus (Luhman et al. 2010).

This disc fraction could simply be adopted, however a point of concern with this result is the potential of bias in my Taurus sample. I have covered roughly 1/4 of the total members in Taurus in this survey, and used these to derive an age. However the disc fraction in Luhman et al. (2010) is based on the entirety of Taurus, and thus there exists the possibility that my sample is not representative of the sample from which this disc fraction is derived. Of the stars in my Taurus sample, a total of 19 Class II sources and 9 Class III sources fall between spectral types ≥K6 and ≤M3.5, yielding a disc fraction of 68^{+8}_{-9}% (Binomial statistical uncertainty only). This is consistent with the disc fraction derived from the entire area.

In Figure 6.10 Taurus is added to the disc plot from Bell et al. (2013), plotting both the age and disc fraction determined from my sample (i.e. fully consistent with each other). It can be seen that Taurus has the highest disc fraction of any cluster in the sample, and yet is clearly older than the youngest group of clusters. Based on this survey, the one-sided likelihood of the disc fraction being above 50% (i.e the disc fraction of the younger group) is 0.969. In fact, to bring Taurus into agreement with the observed decline of disc fraction with age would require a disc fraction of ∼ 40%. The likelihood of the disc fraction being greater than 40% is 0.998. This suggests that discs do survive longer in Taurus. It can be inferred that this may be an effect of the low-mass, low-density environment, but to test if this is actually the case requires further work (see Chapter 9

6.5.2 Mass function

Another potential effect of the older age for Taurus lies in the derived masses of stars. Stellar masses are typically determined by comparison with isochrones, and so the derived mass will depend on the age one uses. The mass function in Taurus has been measured in the past (Briceño et al. 2002; Luhman et al. 2003; Luhman et al. 2009) and has been noted to be inconsistent with

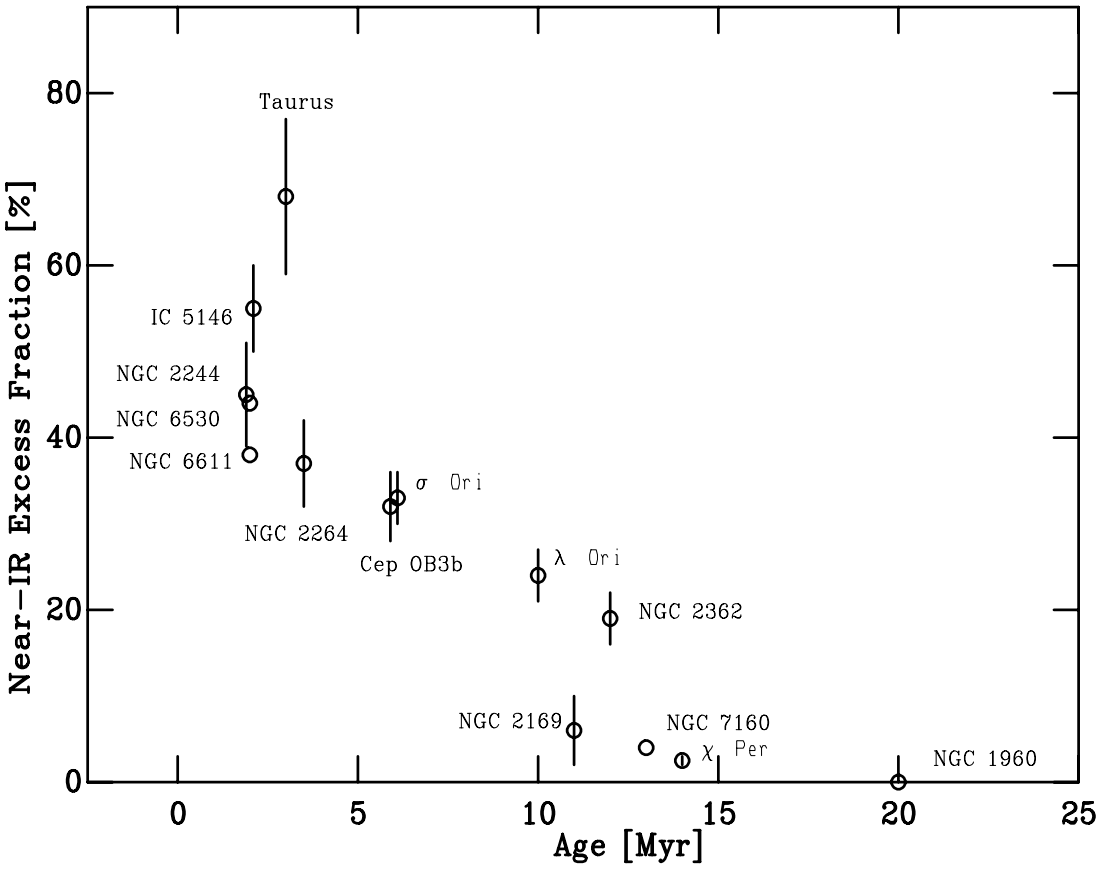

Figure 6.10: Fraction of stars with near-IR excess disc emission vs revised age (see Bell et al. 2013 for references). Note that the ages for IC5146, NGC2244, σ Ori, and CepOB3b have been shifted slightly to better display the uncertainties in the disc fractions. Taurus and NGC 2264 are taken from this thesis.

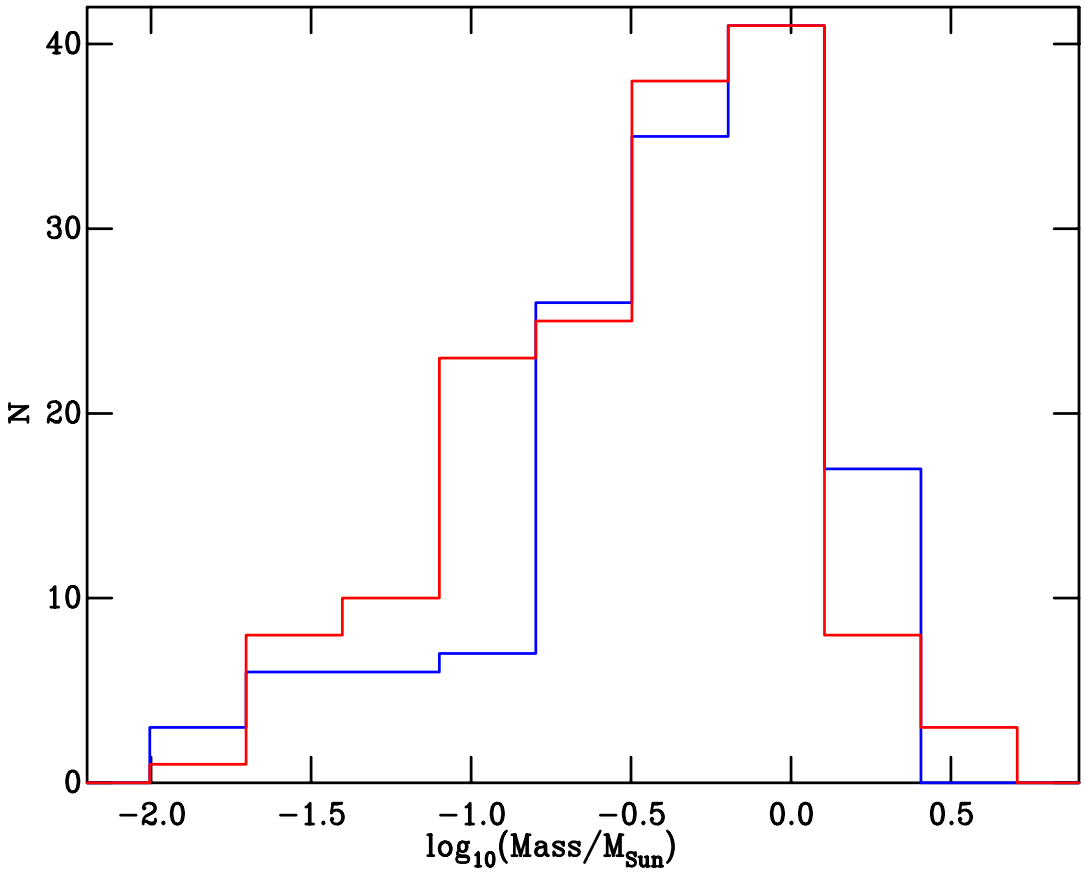

Figure 6.11: Mass function for Taurus members in Luhman et al. (2009). The blue histogram shows the MF assuming an age of 3.5 Myr for Taurus members. The red histogram is the MF from Luhman et al. (2009).

those of other young star forming regions, peaking at a larger mass than other regions. It was noted by Bastian et al. (2010) that Taurus remains the only region to show credible IMF variations. It is possible that the new age derived here for Taurus will impact on this mass function.

A complication arises when considering the observed luminosity spreads in young clusters. This is often interpreted as an age spread, and so often a series of isochrones of different ages are used to derive masses (see e.g Luhman et al. 2009). The source of the luminosity spread is not clear, but it is possibly a combination of multiple factors (see e.g Soderblom et al. 2014 for a review) and thus ascribing it entirely to an age spread is likely to affect the derived masses. Instead a single age of 3.5Myr was adopted, and the J-band magnitude was used to determine stellar masses. The J-band luminosities are well reproduced by the stellar models, with little empirical adjustment required and, unlike the K-band, should be relatively free of disc contamination.

My own sample of dereddened objects, though sufficient for deriving an age for Taurus, is not sufficiently complete to derive a robust mass function. Instead the data from Luhman et al. (2009), which built upon Briceño et al. (2002) and Luhman et al. (2003) were used. The data are based on the XEST fields, and so should be complete. Briceño et al. (2002) suggests a completeness limit of $0.02M_{\odot}$(based on an age of 1Myr, for all members with $A_V \leq 4$). This completeness limit is only marginally affected by the increase in age. A 3.5Myr old star with equal luminosity to a $0.02M_{\odot}$1Myr old star has a mass of $0.027M_{\odot}$. The reddenings were also adopted from these same papers, and distances were adopted as detailed in Section 6.2.1. The resulting mass function is shown in Figure 6.11. The mass function derived here shows a shift towards larger masses compared to the Luhman et al. (2009) mass function, exacerbating the discrepancy between Taurus and other regions. It can therefore be stated that adopting an age of 3.5Myr does not reconcile the mass function in Taurus with other young star forming regions.

6.6 Conclusions

Isochrone fitting in colour-magnitude diagrams was used to measure the age of the Taurus-Auriga T association. The crucial new steps made to obtain this age are as follows.

(i) I have used photometry in well-characterised photometric systems.

(ii) I have used empirically corrected isochrones which are known to be good fits to photometry of other young clusters, and extended them to the cooler temperatures needed for this association.

(iii) I have derived and used photometric reddenings. This has allowed me to correct for the highly variable extinction in this association by measuring individual extinctions to each object using a Bayesian method.

With these steps I have obtained a mean age of 3-4Myr for the association, which although much older than ages commonly quoted in literature, is in line with results for other young clusters measured with the same techniques. It is therefore also aligned with an age scale which matches the lithium depletion boundary and upper main sequence ages in other clusters and associations.

The revision of the age has significant implications.

(i) The fraction of stars with dust discs is significantly higher than would be expected for a denser cluster of similar age. This suggests that effects such as encounters or winds and UV radiation from high mass stars do significantly erode discs in higher density environments. This will be examined further in other regions in Chapter 9).

(ii) The revised age leads to a revised measurement of the mass function, which exacerbates the long-standing problem that the mass function in Taurus-Auriga peaks at a higher mass than in other regions.

7

Photometry in the Blanco DECam system

7.1 Motivation

In Chapter 2 the observations and data reduction process for the INT-WFC system was discussed. Some of the WFC data were used in Chapter 6 to show that the Taurus star-forming region has an excess of circumstellar discs compared to more massive dense clusters. To test the argument that this abundance of discs is due to the low-density environment requires observations of other low-density T-associations. The best targets for this are mostly southern-sky associations (see e.g. the list of star forming regions of Reipurth 2008a,b). The INT-WFC and SDSS are both northern hemisphere only, and thus an alternative solution is required to observe any southern targets. In this section the Blanco DECam instrument is introduced and the observations and data reduction process are discussed.

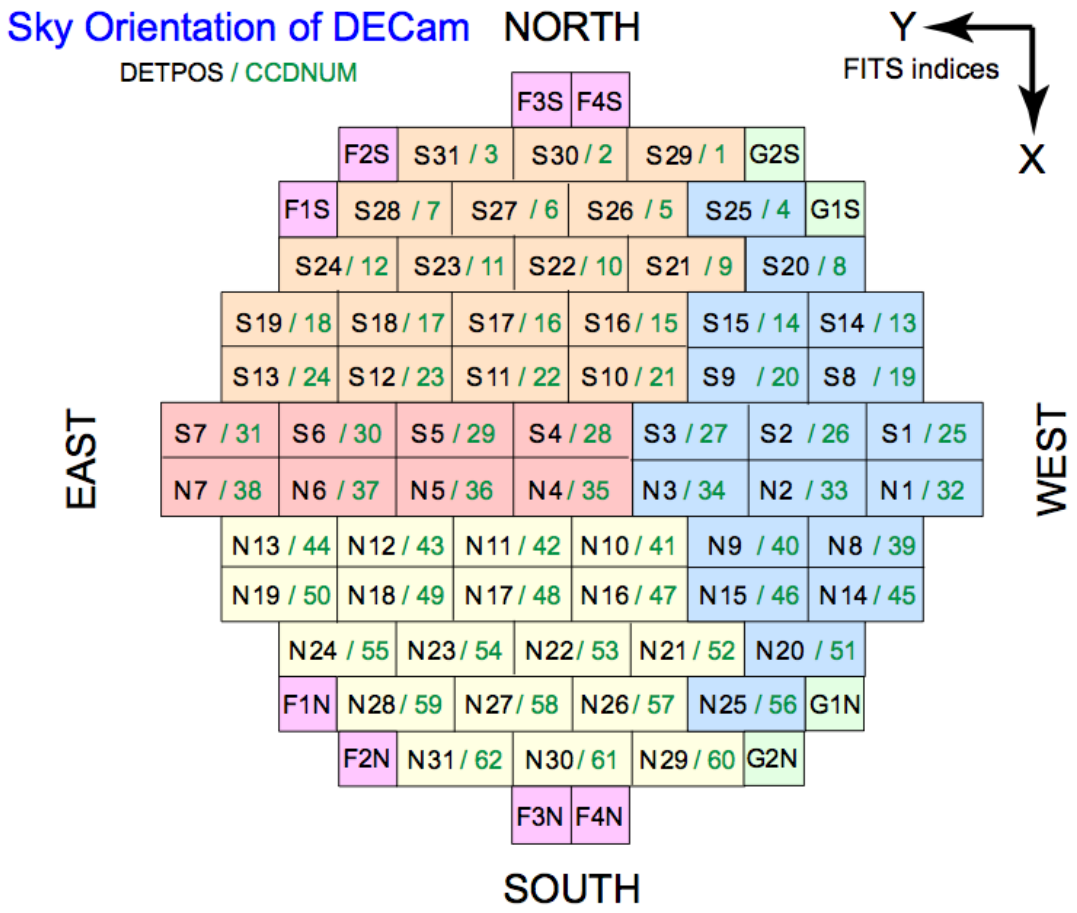

Figure 7.1: Layout of the Blanco DECam instrument showing the 62 science CCDs along with the 8 focussing and 4 guide CCDs. Credit:CTIO

7.2 Observations

The Dark Energy Camera (DECam) is a wide-field imager installed on the Blanco 4-m telescope, situated at the Cerro Tololo Inter-American Observatory (CTIO). DECam is made up of a mosaic of 62 2048x4096 pixel CCDs (see Figure 7.1) with a field-of-view of 3 square degrees. The large field-of-view makes DECam ideal for observations of T-associations, which are often spread over large areas on the sky and thus would require tiling many observations with other instruments. DECam is also equipped with *ugriz* filters (see Figure 7.2 for the responses), and thus offers a complementary observing system to that of the INT-WFC. Observations were obtained on the nights of 4th April and 30th August 2015, and both nights were photometric. The observations were obtained by David James, but the observing plan was my own. RASICAM, an independent infrared camera used to detect high level clouds that affect observing conditions, confirmed that

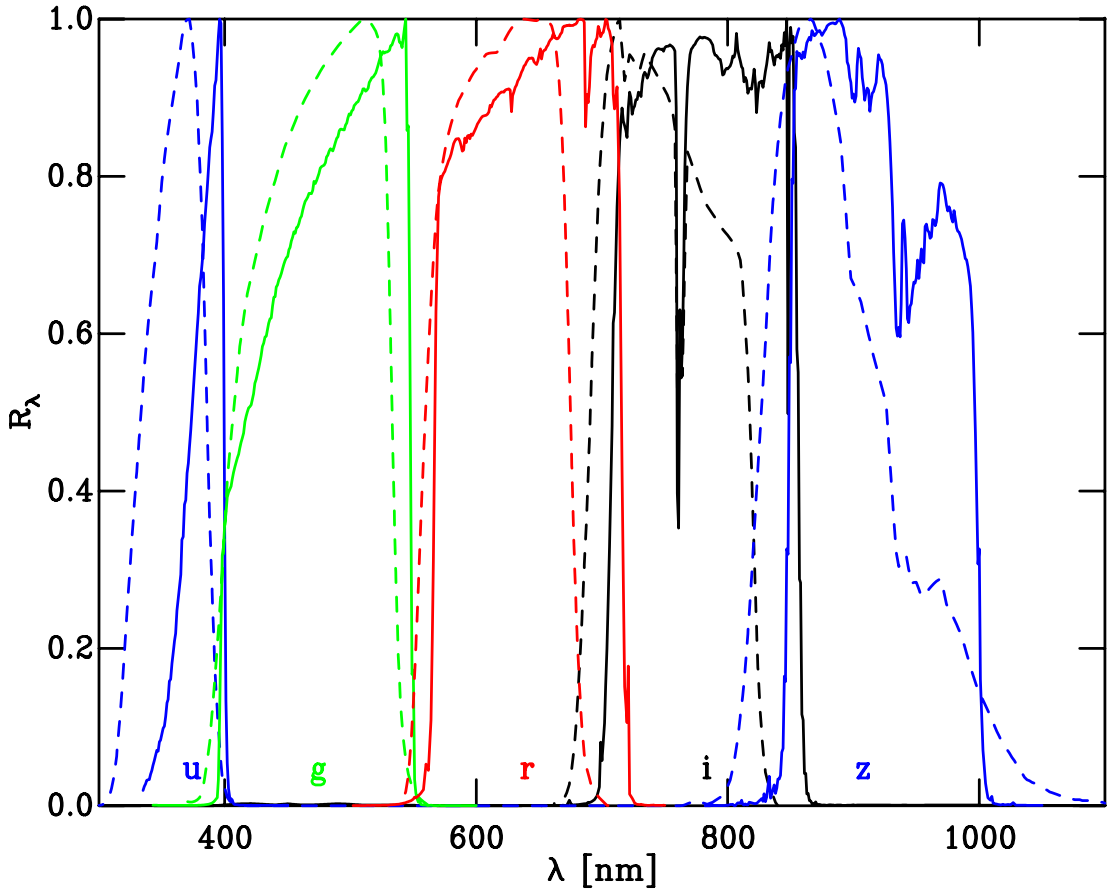

Figure 7.2: System response for the Blanco DECam (solid lines) and SDSS *ugriz* systems. The DECam responses were downloaded from the CTIO DECam site `http://www.ctio.noao.edu/noao/content/dark-energy-camera-decam`. Note the gap between the g_{DECam} and $r_{\rm DECam}$ filters, to avoid the 557.7 nm sky line. The filters have each been normalised to their peak response.

both nights remained free of clouds throughout[1]. The April data covered the Chamaeleon and ρ-Ophiuchus associations in the $(riz)_{\mathrm{DECam}}$ filters. The August data covered the open cluster Blanco 1 and included some short exposures in ρ-Ophiuchus to provide a second photometric solution. Chamaeleon however was too low in August to obtain a second set of observations. Table B.1 and Table B.2 list the fields and exposure times observed by DECam for the young clusters and standard star fields respectively.

7.3 Reduction Process

The reduction process for the DECam data is largely similar to that described for the INT-WFC data in Chapter 2. However the extreme wide-field nature of DECam requires some important differences in the reduction approach. DECam covers an area on the sky of 3 square degrees. For comparison the INT-WFC covers 0.25 square degrees. The observing strategy with the INT-WFC was to tile multiple fields together to cover large areas on the sky. Each field was then reduced individually, and overlapping regions between fields were used to normalise the photometric calibration across all fields. The DECam observations in comparison consist of a single pointing for each target. To fill in the inter-CCD gaps the telescope was nodded slightly between the repeat exposures. This nodding of the telescope effectively created several individual fields, offset from each other by a small amount. These cannot be reduced separately without sacrificing the deep coverage (i.e. the images need to be stacked together to detect the faintest objects). A new reduction algorithm was created to deal with this complication and is described below.

7.3.1 Bias, Flats and Fringing

The DECam pipeline[2] automatically applies a basic calibration to the raw data frames. This basic calibration includes bias subtraction, flatfielding, fringing correction for the red bands, linearity correction and saturated pixel flagging. An astrometric solution is also applied, based on comparing star positions to 2MASS. Bias frames and dome-flats are automatically taken during daytime operations. The data are debiased in a two step procedure. First the overscan regions are used to establish the bias level on a row-by-row basis which is then subtracted off of the data. A master bias frame is created by subtracting the overscan-determined values for each individual bias

[1] The RASICAM data is available to view on YouTube: `https://www.youtube.com/user/rasicam2`
[2] See the NOAO Data Handbook at `http://ast.noao.edu/data/docs`

frame, and then median combining the results. The master bias frame is then subtracted off of the data frames to account for higher order structure. Linearity correction is performed for each CCD using previously measured linearity coefficients. The individual dome-flats are median combined on a filter-by-filter basis to form a master flat for each filter. The data frames are then divided by these master flats to correct for inter-CCD sensitivity variations. Library fringe frames are subtracted from z and Y observations only, as fringing is not observed in the $ugri_{\mathrm{DECAM}}$ bands. These calibrated data frames (referred to as InstCal frames) were downloaded from the CTIO data archives along with their associated data quality masks. These data quality masks are files with quality flags for each pixel in the array, and are used to warn of saturated pixels or those pixels with known defects.

7.3.2 Searching for Objects

As with the INT-WFC reduction, in order to detect the faintest objects it is desirable to search for stars in a stacked image. A stacked mosaic image is created by the DECam pipeline, but the mosaic was noted to have a number of artefacts including bleed trails and noticeable artefacts at the location of chip edges. Although object detection could be performed on the individual images the source detection would not be as deep as in the stack. Instead a stacked image was created in a similar way to that used for the INT-WFC. There were some artefacts at chip edges in the x-direction on some CCDs and in these cases 40 pixels at the CCD edge were flagged (affecting CCDs 2, 3, 4, 6, 9, 10, 12, 17, 24, 31, 36, 37, 44, 46, 54, 57 and 58). In addition one half of CCD 30 was noted to be composed almost entirely of noise even in the long exposures, suggesting an amplifier issue (each CCD is read out using two amplifiers, one covering each half of the chip). The affected half of CCD 30 was flagged entirely. Simple x-y transformations were calculated between the long exposures in the i_{DECam}-band by comparing the positions of the stars detected in each image, and the images were then combined. The use of simple x-y transformations were only valid in this case because the offsets between frames were small. The sky value was calculated in the same manner as described in Section 2.3.4, and subtracted from each pixel. Source detection was performed as in Section 2.3.4. Each of the individual images has an astrometric solution pre-calculated by the CTIO pipeline, but the stack I created does not. The previously calculated x-y transformations were used to transform the x-y positions of sources detected in the stack to x-y positions in the positionally-central long exposure. The astrometric solution for the central frame

was then used to transform the x-y positions to RA-Dec coordinates.

The short and medium exposures were also searched to better constrain the position of any stars that were saturated in the stack. These were then transformed directly from x-y positions to RA-Dec using the astrometric solution of each frame. The resulting source lists were combined to create one master list of sources. Combining sources detected in the stack with those detected in the short and medium exposures introduced a number of repeat sources. These repeat sources were identified by position matching within $1''$ and a mean position (weighted by the uncertainty in the measured flux for each image) was calculated for each. If a source was flagged as saturated in the stack but was not saturated in a short or medium exposure the weighted-mean was calculated only using the unflagged values. The resulting master source catalogue contained a list of detected sources in RA-Dec coordinates.

7.3.3 Optimal Photometry

The optimal extraction method (see Section 2.3.5) was again used to perform photometry separately on each image. For each image the master source catalogue was transformed to x-y coordinates using the astrometric solution for that frame. A clipping radius of 2.0 pixels was adopted for the extraction mask. The profile corrections were derived in the same manner as for the INT-WFC reduction. Profile corrections were performed several times adopting different polynomials to define the corrections as a function of position. Figure 7.3 shows histograms of χ^2 values for the stars in a standard field, adopting different polynomials. Using a first-order polynomial in y eliminates a large number of the high-χ^2 objects and significantly improved the distribution. The best distribution of χ^2 was found for polynomials of order 1 and 2 for the x and y direction respectively (c.f. 3 and 5 for the INT-WFC). Increasing the order of the polynomials further beyond this did not lead to any improvement.

7.3.4 Photometric Calibration

The photometric calibration was also similar to that described in Section 2.3.6. Each image was corrected to the mean airmass of the group using the extinction coefficients derived from standard star observations. The relative transparency corrections were then applied to correct for the difference in transparency between the images. The magnitudes were combined to create colours. The colours and magnitudes were corrected to an airmass of 1.0, again using the extinction coefficients

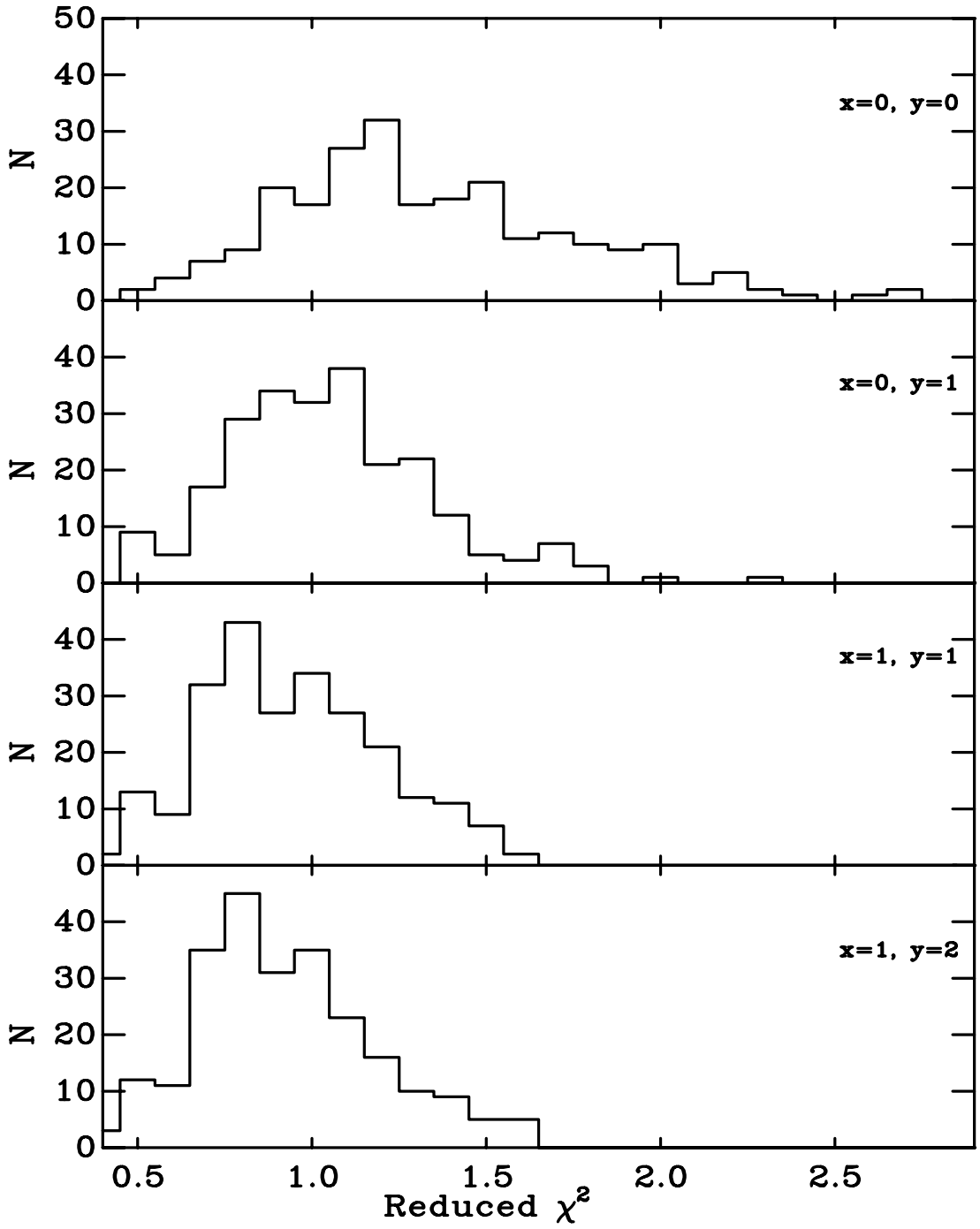

Figure 7.3: Histograms of Reduced-χ^2 values for stars in a standard field, after adopting different profile correction polynomials in the DECam system.

derived from the standard stars.

The standard star fields were a combination of the SDSS fields used for the INT-WFC reduction, other SDSS fields suggested by the DECam observing guide and the set of southern standard fields from Smith et al. (2007)[3]. The SDSS fields have the advantage of covering the full area of a DECam exposure, but as they are based on a northern hemisphere survey the fields are limited to low altitude, never rising above an elevation of 50° at the CTIO site. The southern standard fields in comparison were defined using older small CCD surveys, and so only cover small areas on the sky (roughly 1 DECam CCD), but reach high elevations. Thus a combination of the two was necessary to ensure a robust photometric calibration.

The DECam system responses are provided on the CTIO website. These responses are constructed using data from the DECam calibration system (DECal). DECal is a spectrophotometric calibration system that shines almost-monochromatic light (1nm bandwidth) onto the flatfield screen. This is then imaged by DECam and simultaneously measured by calibrated photodiodes. The signal measured by the photodiodes is directly proportional to the intensity of light illuminating the screen. The DECam images are compared with the photodiode output to determine the relative sensitivity of the DECam system. By imaging light at a succession of wavelengths covering the set of DECam filters, the system response can be characterised as a function of wavelength. Note that because this is a direct measurement of the response this includes the effect of the quantum efficiency of the CCD, reflectivity of the mirror and the effect of the glass elements making up the various corrector lenses. An estimate of the effect of atmospheric transmission at an airmass of 1.0 is also included with the system response. To photometrically calibrate the data it was first necessary to calculate the transformations between the DECam and SDSS photometric systems. The ZAMS interior model of Siess et al. (2000) was adopted, with a range of stellar masses between 0.1 - 7 $M_{\odot}$. The BT-Settl model atmospheres were folded through the responses for the DECam system to derive the BCs in this system. These calculated BCs were used to transform the ZAMS model to the CMD plane. The process was then repeated using the system responses for the SDSS photometric system from Doi et al. (2010). The difference between the ZAMS in the DECam and SDSS systems was then calculated in each filter and colour combination. The calculated transformation in the g and $(g - i)$ bands is shown in Figure 7.4. The calculated transformations were then used to transform standard star catalogues from the SDSS system to the DECam system. The

[3]See the southern standards page `http://www-star.fnal.gov/Southern_ugriz/New/index.html`

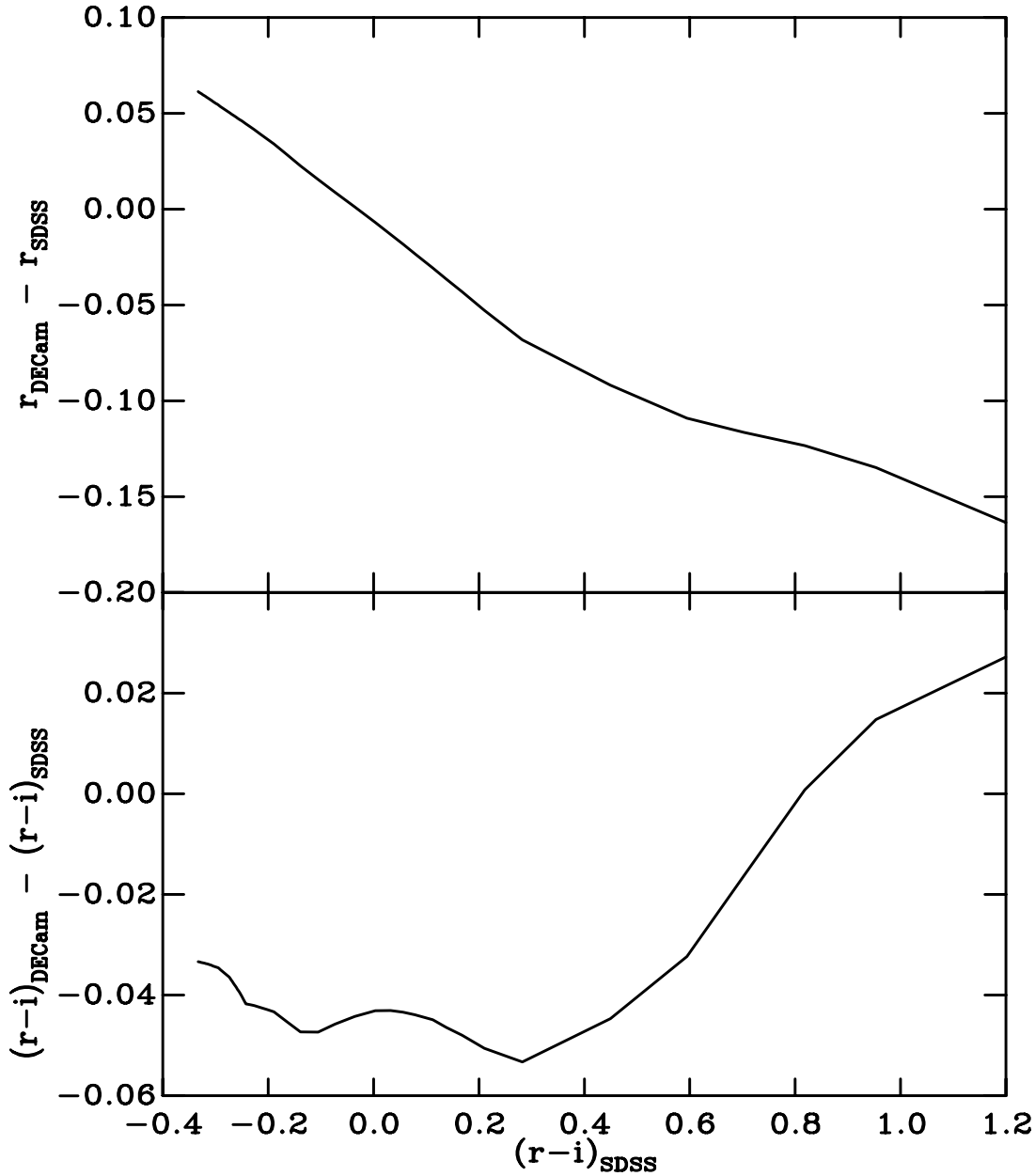

Figure 7.4: The calculated transformations between the DECam and SDSS photometric system for the r-band (top) and $(r - i)$-band (bottom) as a function of $(r - i)_{\mathrm{SDSS}}$. The transformations have been calculated using the ZAMS model of Siess et al. (2000).

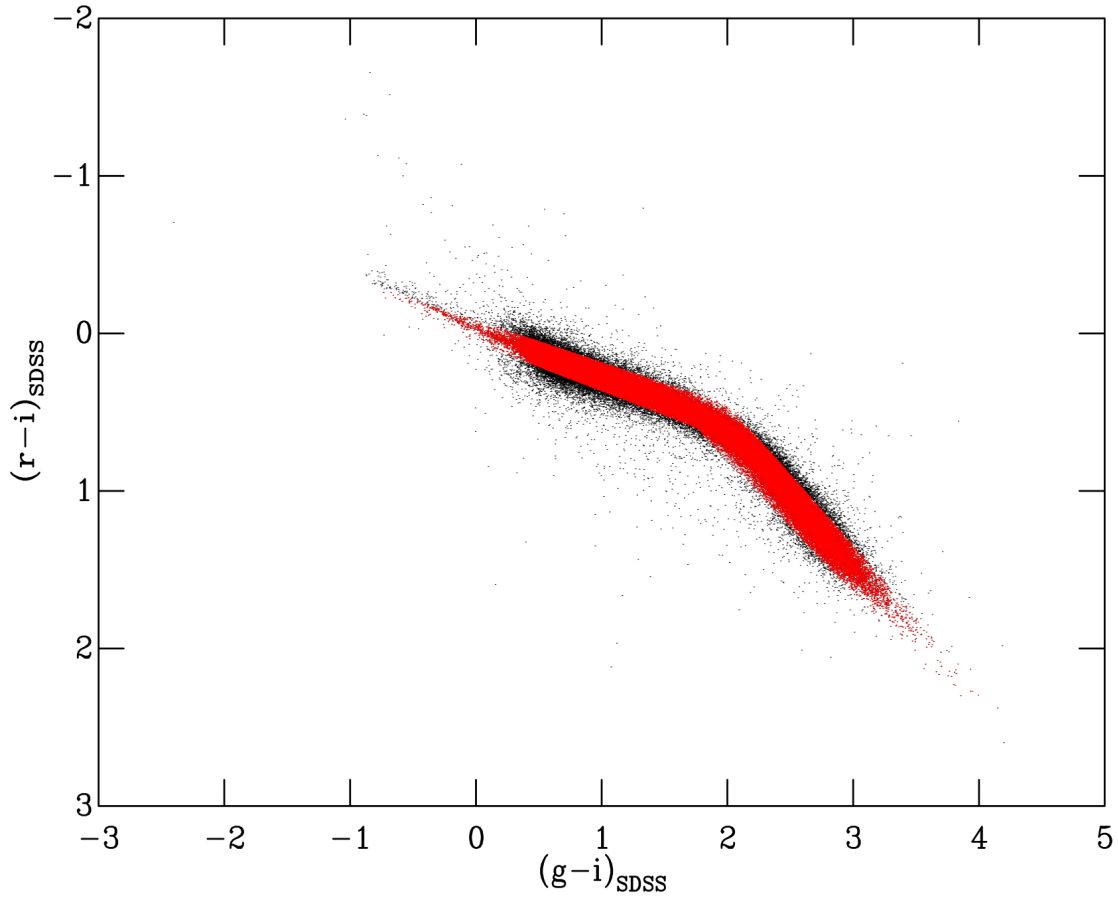

Figure 7.5: $(r - i)$, $(g - i)$ colour-colour diagram for one of the SDSS Stripe 82 fields (Sloan1). Black points show the full catalogue, red points show those stars isolated by the MS colour cuts.

transformations are only valid for MS stars, and so a series of photometric cuts were used in colour-colour diagrams to isolate the MS before the transformations were applied (see Figure 7.5). The SDSS magnitudes transformed to the DECam system will be denoted as $\mathrm{mag}_{\mathrm{calc}}$ and the observed DECam magnitudes as $\mathrm{mag}_{\mathrm{obs}}$. The transformed MS SDSS stars were then crossmatched with the DECam observations and used to derive the photometric zeropoints and atmospheric extinction terms for each night as was done previously in Section 2.3.6. As discussed in Section 2.3.6, the data must be left in the natural observational system, and so the zeropoint in a given band were derived from a small colour range ($0.0 \leq (g - i)_{\mathrm{DECam}} \leq 0.25$) to limit the effect of any residual colour term. For the INT-WFC reduction, these zeropoints were calculated on a CCD-by-CCD basis. However for this DECam data, because of the multiple pointings used to fill in inter-CCD gaps a given star can appear on multiple CCDs. It was thus not possible to assign each star to a unique CCD. The variation in the zeropoint between CCDs was small ($\lesssim$0.01 mags) and so instead

the calculated zeropoints were averaged over all 60 CCDs. The variation as a function of colour is useful for determining if the observation system is well characterised. The differences between the SDSS catalogue and the DECam observations were calculated for a standard star field. The difference between the two catalogues as a function of colour is shown in Figures 7.6, 7.7 and 7.8. Overlaid on these plots in green are the predicted differences based on the BT-Settl models folded through the system responses of the SDSS and DECam systems. If the observational system were perfectly characterised, and the stellar atmosphere models were without problems, the predicted differences should match the observations. The *i*-band predictions match very well, however there were noticeable differences in both the *r* and *z*-bands. The problem could be due to either the atmopshere models or due to an issue in the characterisation. In the past work with the INT-WFC the assumption was made that any issues with the stellar atmosphere models would cancel, to first order, as the filter set for the INT-WFC and SDSS are extremely similar. Figure 7.2 shows that this is not the case with the DECam and SDSS systems. Although they are similar, the *r*-band in particular is much wider in the DECam system compared to the SDSS system. If there is an issue with the atmosphere models in this region it could lead to the observed issue.

To test if the issue was with the system responses or the model atmospheres the spectral library of Pickles (1998) was adopted. This library includes fluxed spectra of main-sequence dwarfs, which were folded through both the SDSS and DECam system responses. If the issue lay with the system responses, the same problem should have been evident as with the BT-Settl models. If however the problem was due to the model atmospheres the (observational) Pickles spectra should represent an improvement. The calculated differences based on the Pickles spectra are also shown in Figures 7.6, 7.7 and 7.8. It can be seen that the observed spectra are better able to reproduce the observed differences between the DECam and SDSS systems. It seems therefore that the DECam system is well characterised and the problem lies largely with the model atmospheres. This is not a worrying proposition, because as discussed in Chapter 3, the empirical corrections that will be applied to the model isochrones will largely correct for this issue. Both the Pickles spectra and the BT-Settl models well reproduce the observations at neutral colour, which is the location at which the zeropoints are derived.

One final source of concern is the variation of filter response with position. Flaugher et al. (2015) note that the r_{DECam} filter cutoff wavelength has a radial dependence, with the inner radius ($< 0.3\ R_{\mathrm{max}}$) cutting off 25 Å longwards of the outer portion of the filter. The i_{DECam} filter

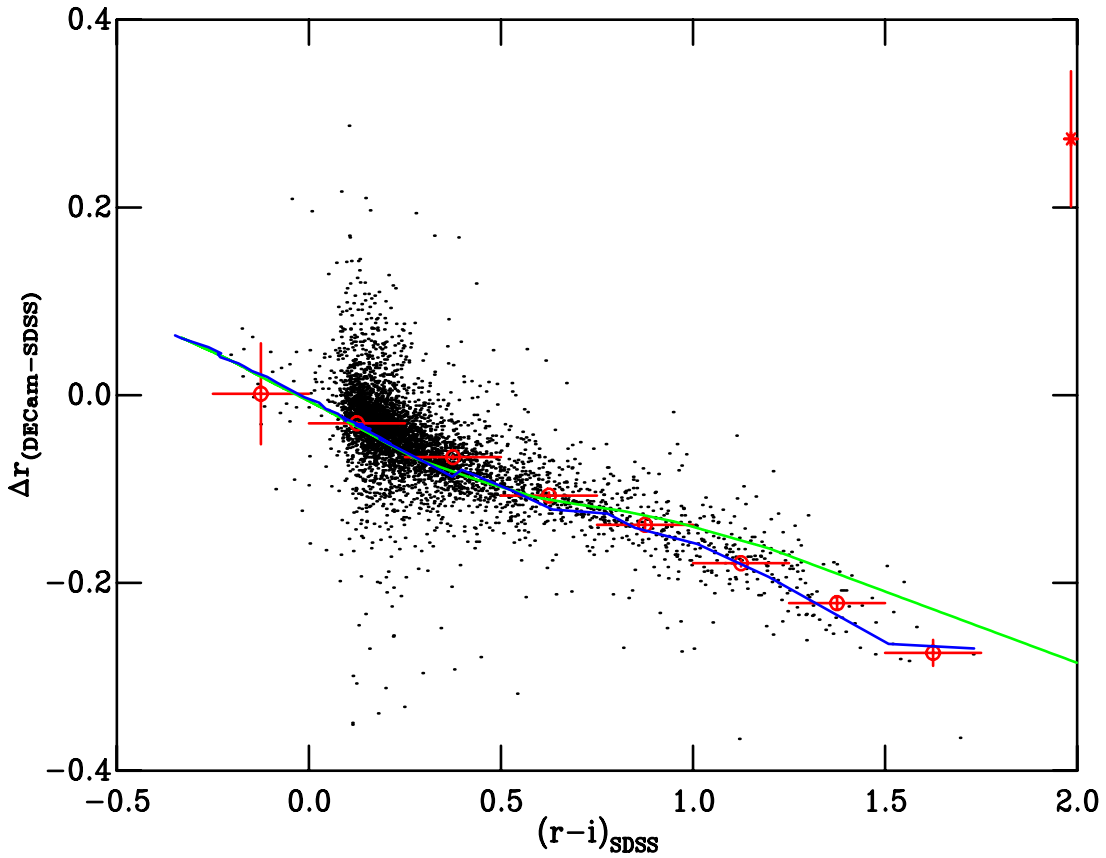

Figure 7.6: The difference between r_{DECam} and r_{SDSS} as a function of $(r-i)_{\mathrm{SDSS}}$ for a DECam standard field. The black points show the full catalogue and the red circles show the median difference for a bin of 0.25 mag in colour. The error bars on these points show the standard error about the median. Red asterisks represent individual points where the number of points in a given bin is less than five. The error bars on these points are simply the individual uncertainties. The green line shows the predicted difference calculated using the BT-Settl atmosphere models. The blue line shows the predicted difference based on the observed spectra of Pickles (1998).

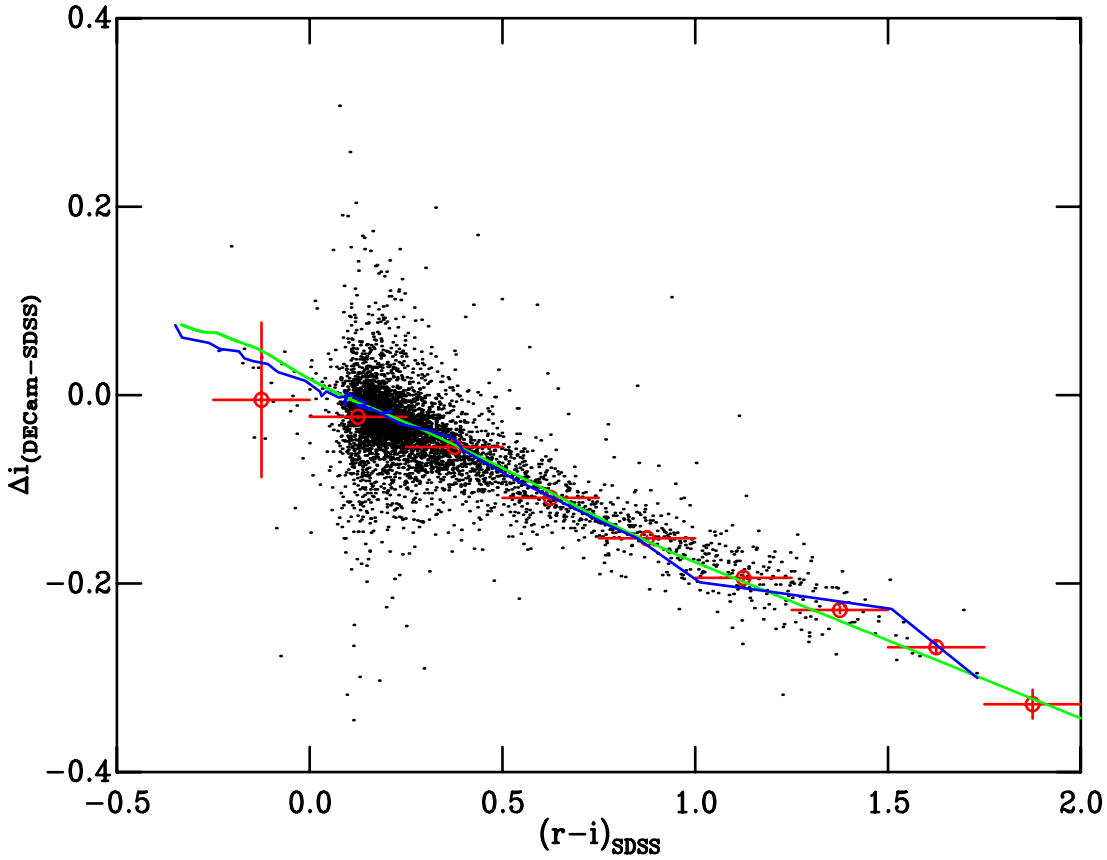

Figure 7.7: The same as Figure 7.6 but for the *i*-band

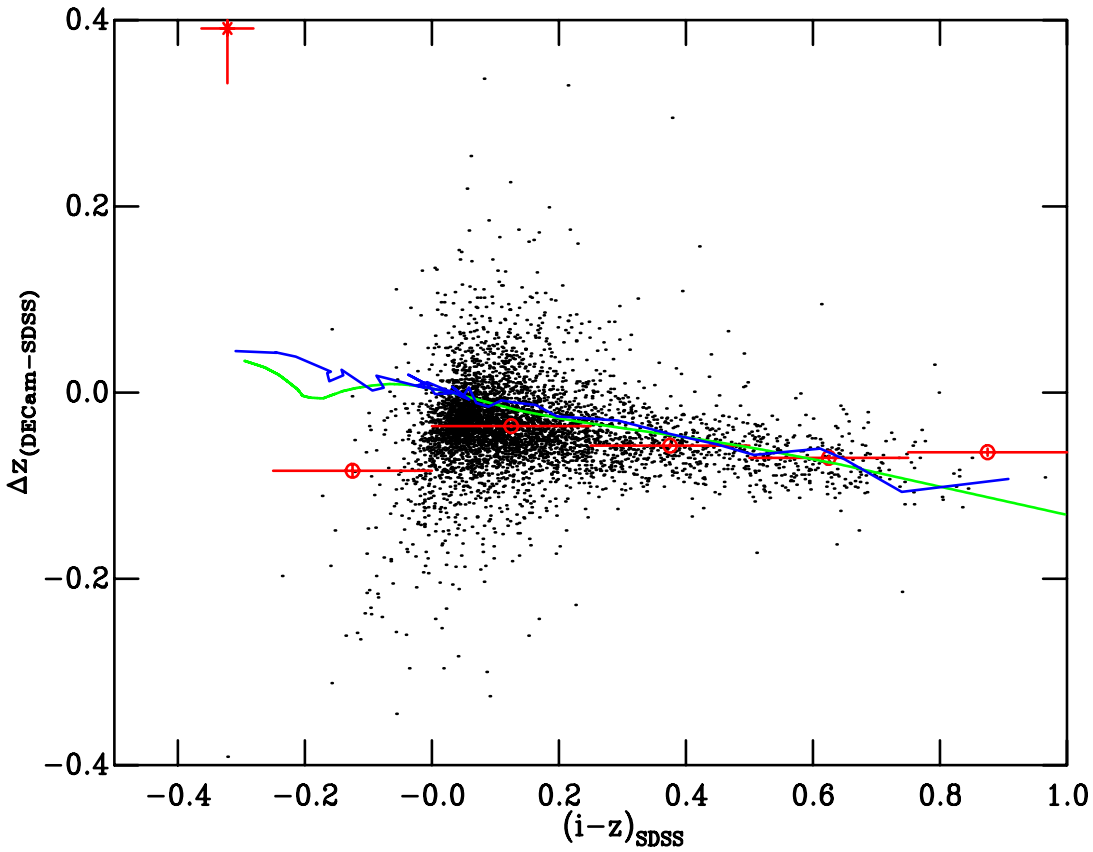

Figure 7.8: The same as Figure 7.6 but for the z-band as a function of $(i-z)_{\rm SDSS}$

cut-on has a radial dependence of 50 Å over the full radius of the filter (it should be noted that there is an error in Flaugher et al. in which the radial dependence is stated to be in nm instead of Å, W. Wester, priv. comm.). To determine how much the radial variation could potentially impact the photometry, the system responses were adjusted to represent the extremes of the potential variation. The BT-Settl models were folded through these modified responses and the bolometric corrections were compared to those derived from folding the models through the unmodified system responses. The differences were found to be small, at most ±1%. In principle the impact of this radial dependence could be mitigated using information from the DECal system, which is able to characterise the DECam system as a function of position, to derive a position-dependent correction which could be applied to the standard star fields. However the DECal data are not yet publicly released. Given the uncertainties typically associated with young cluster CMDs this level of potential uncertainty is comparatively small.

7.4 Summary

In this chapter the DECam system was introduced. The observations of a set of young clusters were discussed, and an updated reduction process was detailed. It was demonstrated that the DECam system is well characterised, and thus model isochrones can constructed in this system and used to determine the ages of the observed clusters. In the following chapters the creation of semi-empirical isochrones in the DECam system will be detailed, and the models will then be used to fit the young clusters.

8

Blanco 1 - The Southern Pleiades

8.1 Motivation

Chapter 7 introduced the DECam photometric system and the observations obtained in this system. Before the young clusters data could be analysed a set of semi-empirical model isochrones in the DECam system was required. In Chapter 3 the semi-empirical models were constructed using the Pleiades as a fiducial cluster, and in Chapter 4 Praesepe was introduced as an alternative fiducial. Due to the southern location of the Blanco telescope, neither of these clusters is an option for the observations in the DECam system. An alternative fiducial cluster was required, ideally a cluster with well constrained age and distance. In Section 8.2 the open cluster Blanco 1 is introduced, including the properties making it an ideal fiducial cluster. In Section 8.2.1 the age and distance of Blanco 1 are discussed and in Section 8.2.2 the membership catalogues are reviewed. In Section 8.3 the Blanco 1 cluster sequence is used to construct the semi-empirical models in the DECam system. In Chapter 9 these models will be used to fit the data to determine the age of two young

clusters.

8.2 Blanco 1

Blanco 1 (also called ζ Sculptoris) is an open cluster first discovered by Blanco (1949), who noticed an over-abundance of A-type stars in the region. Because it is well separated from the Galactic plane and both relatively nearby and young ($\simeq$ 130 Myr and 200 pc see e.g. Moraux et al. 2007; van Leeuwen 2009) Blanco 1 is an excellent target for studies of (relatively) young stars. Blanco 1 is near-solar metallicity (see e.g. Ford et al. 2005), and thus is very similar to the Pleiades in both age and metallicity. Given that it is a southern-hemisphere cluster, Blanco 1 offered excellent potential as a fiducial cluster.

8.2.1 The Age, Extinction and Distance of Blanco 1

For Blanco 1 to be useful as a fiducial cluster the age and distance must be well constrained. Fortunately the age and distance of Blanco 1 have been well studied and, like the Pleiades, it has a lithium depletion boundary age. The LDB in Blanco 1 was first identified by Cargile et al. (2010), and further refined by Juarez et al. (2014), who obtained a value of 126^{+13}_{-14} Myr. It was shown in Section 4.3.4 that the age for the Pleiades derived from fitting UMS members using the τ^2 statistic was in good agreement with the LDB age. Unfortunately unlike the Pleiades there are no high-quality published UBV data for Blanco 1, and so repeating the process from Section 4.3.4 was not possible. However, James et al. (in prep) have obtained their own UBV data in Blanco 1 and used τ^2 fitting to fit the UMS and determine the age of Blanco 1. James et al. found an age of 132^{+5}_{-8} Myr (priv. comm.), entirely consistent with the LDB age. For constructing the semi-empirical models in the DECam system the LDB age was adopted. The extinction to Blanco 1 is small, with a mean value of $E(B-V) = 0.016$ (see e.g. Appenzeller 1975; de Epstein & Epstein 1985; Juarez et al. 2014)

The distance to Blanco 1 has also been determined previously. Blanco 1 was among the open clusters targeted by the *Hipparcos* mission. Robichon et al. (1999) calculated *Hipparcos* distances to several open clusters deriving a distance of $262.5^{+34.3}_{-27.2}$ pc for Blanco 1. van Leeuwen (2009) presented a rereduction of the *Hipparcos* data and rederived the distances to open clusters, yielding a distance of 207.0±12.0 pc for Blanco 1. It was noted however that this distance for

Blanco 1 was not consistent with distances obtained from isochrone fitting (similar to the issue with the *Hipparcos* Pleiades distance).

The distance to Blanco 1 has also been measured by fitting photometric data. de Epstein & Epstein (1985) derived a distance of 240 pc by fitting the MS with a ZAMS model. Panagi et al. (1994), using previously published photometry, fit the ZAMS and found a distance of 246 pc. Perry et al. (1978) derived a value of 240 pc from ZAMS fitting. James et al. (in prep) obtained a distance of 251^{+4}_{-1} using τ^2 fitting (priv comm). It is clear therefore that, as with the Pleiades, the *Hipparcos* distance is discrepant compared to those derived from main-sequence fitting. Interestingly, the original *Hipparcos* distance was consistent with the photometric measurements, but the updated derivation based on the re-reduced data is not. Given that it was shown in Section 4.3.4 that the distance derived from τ^2 fitting is consistent with that derived from other measures, the τ^2-derived distance of James et al. was adopted.

8.2.2 Blanco 1 Memberships

In order to use the Blanco 1 observations to construct the semi-empirical models it was necessary to define the cluster sequence, for which a set of reliable cluster members was needed. A number literature sources are based on the study of de Epstein & Epstein (1985) (see e.g. Panagi et al. 1994; Micela et al. 1999; Pillitteri et al. 2004). This study was based on photographic plates and presented photometric measurements for roughly 1500 stars in the cluster area. Based on the CMD 150 of these stars were classified as members, but this likely includes a large degree of non-member contamination. Panagi et al. (1994) obtained and presented spectra for 81 targets in the Blanco area, largely made up of potential members from the de Epstein et al. list. Non-members were identified based on the spectra resembling giants, or large calculated stellar radii. Of the 81 stars presented, 3 were found to be non-members. Panagi & O'dell (1997) combined spectra with published photometry to revise memberships, giving a list of 210 members. Micela et al. (1999) presented ROSAT observations of Blanco 1 covering 83 of the 210 Panagi & O'dell (1997) members. Of these stars 42 were detected in X-rays. The ROSAT data also contained two sources identified with field stars and a further 88 X-ray sources that were uncatalogued sources (i.e. potentially young stars). Pillitteri et al. (2003) used a proper motion catalogue combined with photometric cuts to define memberships to lower masses than previous studies, yielding a catalogue of 93 stars (and an estimate of $\sim 10\%$ residual contamination from field stars). Moraux

et al. (2007) obtained deep Iz photometry and used photometric cuts to define a list of $\sim$ 900 potential members, but estimated the field star contamination to be at least 30%. Mermilliod et al. (2008) measured the radial velocities of 148 FGK stars, confirming 68 as members of Blanco 1 by combining the radial velocity measurements with a proper motion survey. Cargile et al. (2009) used a new proper motion survey (published later as Platais et al. 2011) to construct a membership catalogue down to $V \simeq 17$. Platais et al. (2011) presented two proper motion catalogues of the Blanco 1 area. The first catalogue was a high-accuracy catalogue (uncertainties of 0.30.5 mas yr^1) with objects down to $V \sim 18.5$, giving a total of 165 likely cluster members. The second catalogue included lower accuracy measurements from the Catalogue of Objects and Measured Parameters from All Sky Surveys (COMPASS) database, which extended the catalogue to $V \sim$ 21.0. However the confirmed "likely members" in the regular and deep catalogues only extend to a V mag of 14.5 and 18.0 respectively, due to the increased uncertainties on the proper motion at fainter magnitudes.

The most robust membership catalogues are the Pillitteri et al. (2003), Mermilliod et al. (2008), Cargile et al. (2009) and Platais et al. (2011) lists, as these catalogues do not rely on photometry or spectra alone. The Mermilliod et al. (2008) and Pillitteri et al. (2003) members are all included in the the Platais et al. (2011) catalogues, although not all are classified as members with the updated proper motion measurements. The Cargile et al. (2009) members were drawn from the Platais et al. (2011) catalogues, and so by definition are included. The Platais et al. (2011) memberships thus represented the best set of memberships for this work. To ensure that the membership catalogue extended to the faintest magnitudes possible the Platais et al. deep proper motion catalogue was used, adopting those members with a probability of membership $\geq$ 30%. The resulting membership catalogue includes a number of obvious field-star contaminants, and likely also includes further contamination that is less obvious because it is intermingled with the sequence. However the memberships were only used to help define the cluster sequence (see Figures 8.2, 8.3 and 8.4) and so the impact of field-star contamination was minimal. Further, the observed sequence extends to fainter magnitudes than the membership catalogue and so fainter than $i_{\rm DECam} \simeq 17$ the sequence was defined by eye. Fortunately the cluster sequence is well separated from the field by this point. It will be shown in Section 8.3.1 that the sequence defined by these members is well matched by models based on the INT-WFC tuning, which was independently tuned using the Pleiades. This gave confidence in the definition of the stellar sequence.

8.3 Constructing Semi-Empirical Models in the DECam System

The models were constructed in a similar manner to that used for the INT-WFC in Section 3.4, substituting Blanco 1 in place of the Pleiades as the fiducial cluster. K-band data were used to calibrate the colour-$T_{\rm eff}$ relationship, with the K-band data taken from 2MASS and, in place of UKIDSS for the deeper data, the VISTA Kilo-degree Infrared Galaxy (VIKING) survey. VIKING is a survey covering 1500 square degrees in $ZYJHK$ filters, with a limiting magnitude roughly 1 mag fainter than the UKIDSS GCS. A "clean" set of the VIKING data were selected by requiring the object to be classified as a star (based on the shape of the flux distribution) and the K-band "ppErrbits" value to be $\leq$256. "ppErrbits" is a flag value used by the VIKING database representing a combination of potential issues with the data, with a value above 256 indicating the possibility of major quality issues. Although this selection should nominally exclude saturated objects a number of obviously saturated objects remained in the CMD. Thus an additional magnitude cut was applied to exclude sources with K-band magnitudes brighter than 13. The VISTA system responses were created by combining the measured filter response, CCD quantum efficiency, reflectivity of the primary and secondary mirrors and a model of the absorption of the Earth's atmosphere assuming a precipitable water vapour content of 1 mm at an airmass of 1.0[1].

The DECam observations of Blanco 1 included deep (riz) observations but only a set of short g-band exposures. To ensure that the (riz) tuning extended to the lowest $T_{\rm eff}$ possible, the i-band ΔBCs were constructed using the K-band data as the reference in a $K, i-K$ CMD. The i-band ΔBCs were constructed using both the 2MASS data (which allowed the ΔBCs to be calculated down to 3300 K) and the VIKING data (ΔBCs down to 2300 K). The two sets of ΔBCs were extremely similar at 3400 K and so the two were combined at this point. The ΔBCs in other bands were then calculated with respect to the corrected i-band, as the sequence is easier to define in i, $r-i$ compared to K, $r-K$ for example. The various CMDs used to define the ΔBCs are shown in Figures 8.1, 8.2, 8.3 and 8.4.

8.3.1 The Blanco DECam System vs the INT-WFC System

After constructing the semi-empirical models in the DECam system the comparison could be made to the previously derived models in the INT-WFC system. Figures 8.5, 8.6, 8.7 and 8.8 show the

[1]Responses obtained from ESO pages at `http://www.eso.org/sci/facilities/paranal/instruments/vircam/inst.html`

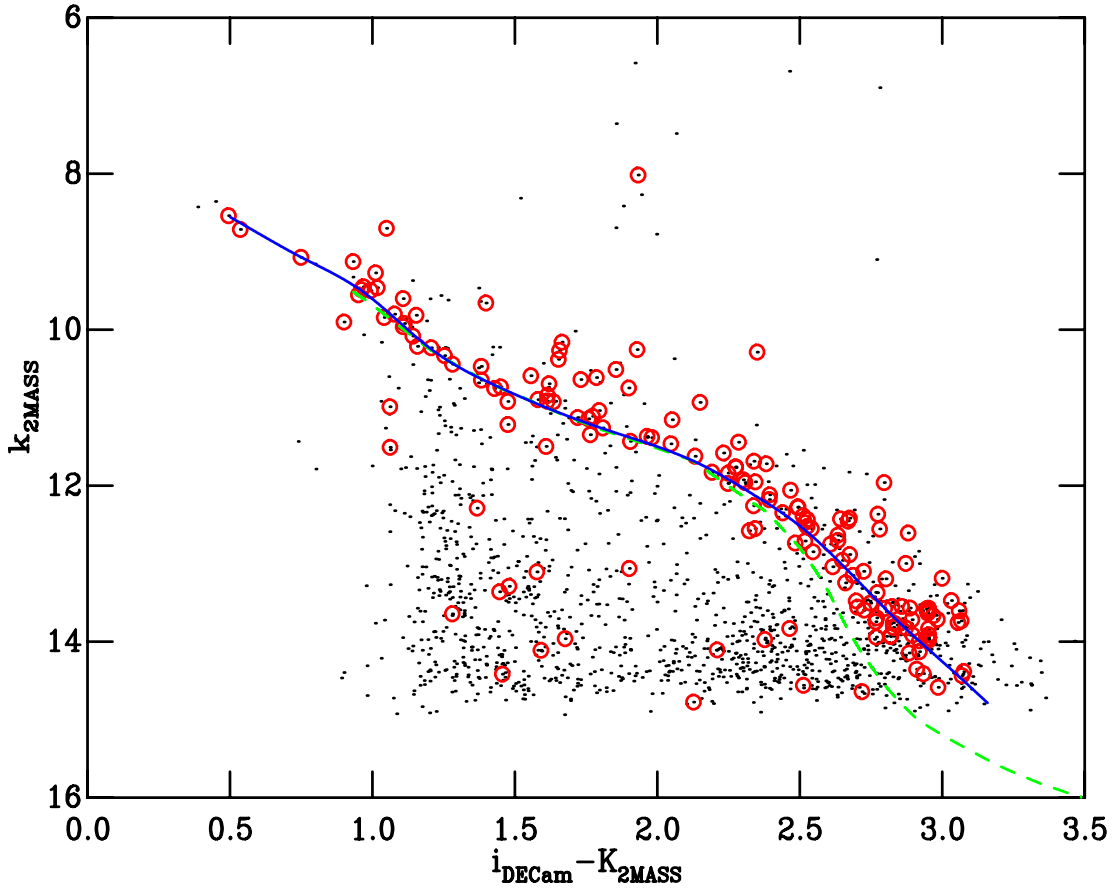

Figure 8.1: K, $i - K$ CMD for the Blanco 1 area. Black dots show the whole catalogue, red open circles indicate "members" based on the catalogues of Platais et al. (2011). Overlaid is a spline (fit by eye) showing the observed sequence (blue solid line). Also overlaid is a theoretical BCAH98 isochrone adopting an age of 120 Myr and dm = 7.0 (green dashed line).

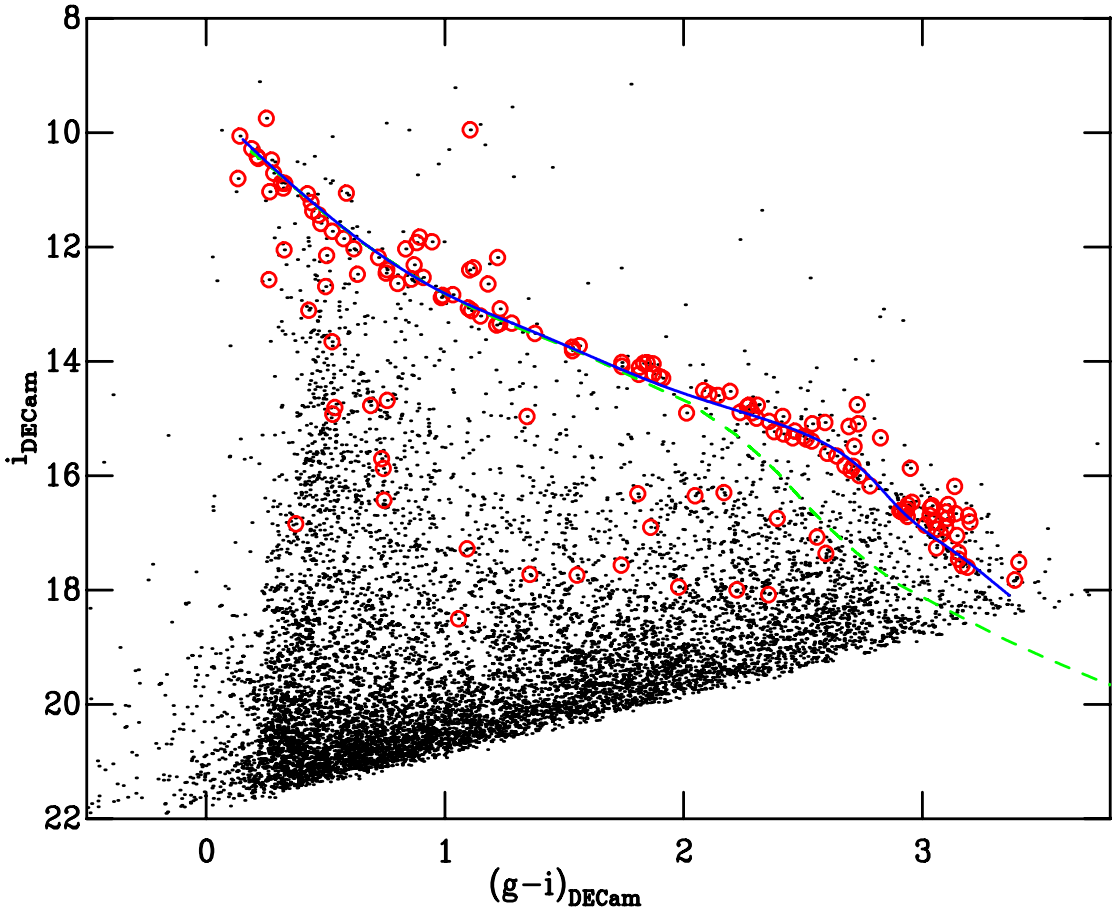

Figure 8.2: The same as Figure 8.1 but for the i, $g - i$ CMD

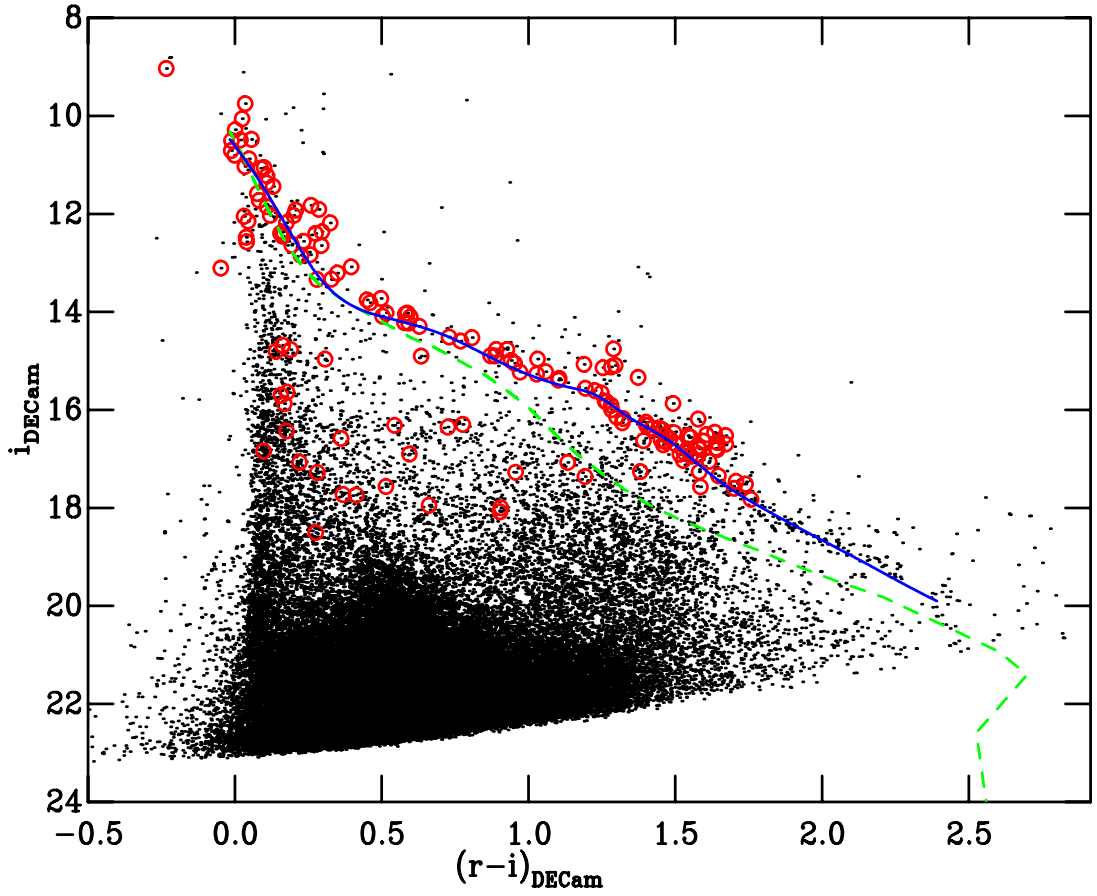

Figure 8.3: The same as Figure 8.1 but for the i, $r - i$ CMD

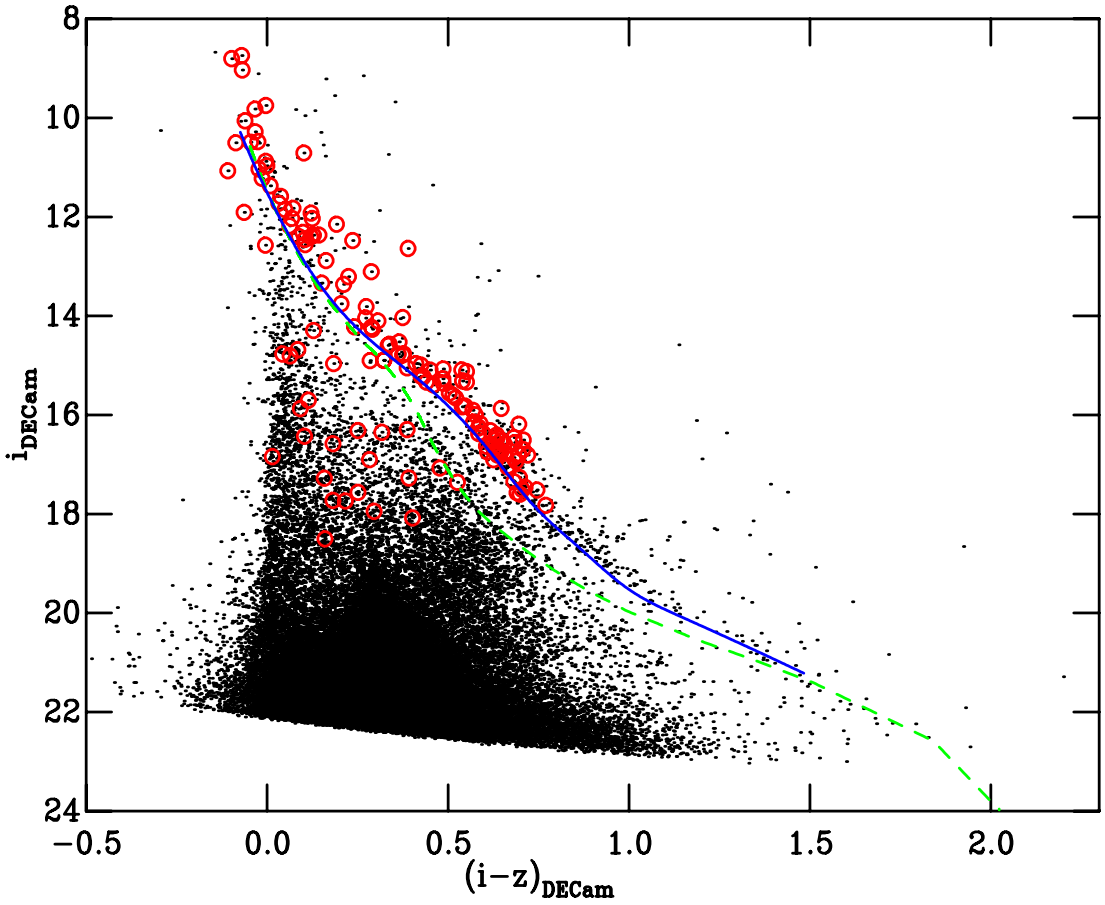

Figure 8.4: The same as Figure 8.1 but for the i, $i - z$ CMD

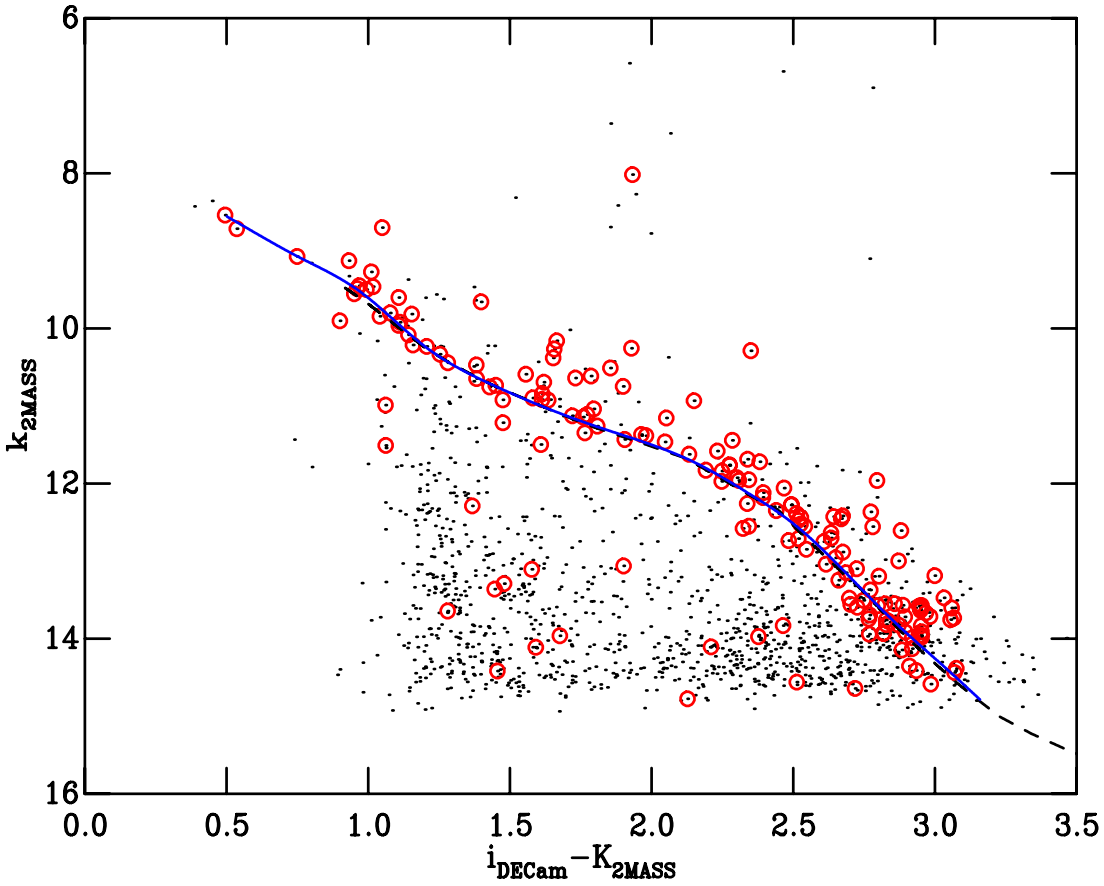

Figure 8.5: K, $i - K$ CMD for the Blanco 1 area. Black dots show the whole catalogue, red open circles indicate "members" based on the catalogues of Platais et al. (2011). Overlaid is the tuned isochrone constructed in this Chapter (blue solid line). Overlaid as a black dashed line is an isochrone constructed by adopting ΔBCs from the Pleiades-tuned INT-WFC system and applying them to the DECam theoretical isochrone. The excellent agreement between the two demonstrates that the DECam tuning is reliable.

Blanco 1 CMDs. Overlaid on these CMDs are the semi-empirical isochrones constructed in the previous section. Additionally overlaid are semi-empirical isochrones constructed by applying the ΔBCs calculated in the INT-WFC system (using the Pleiades) to the theoretical models in the DECam system. The two sets of models show excellent agreement along the sequence, demonstrating that the DECam tuning is consistent with that of the INT-WFC system.

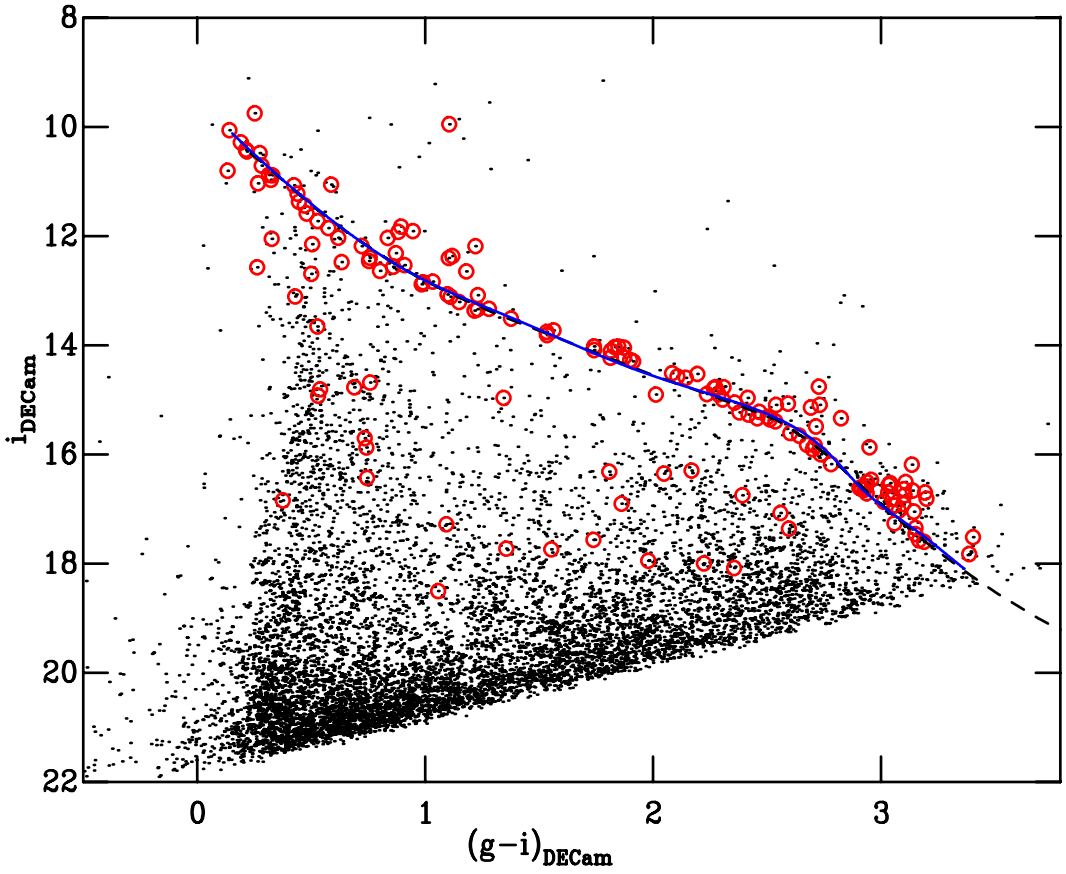

Figure 8.6: The same as Figure 8.5 but for the i, $g - i$ CMD

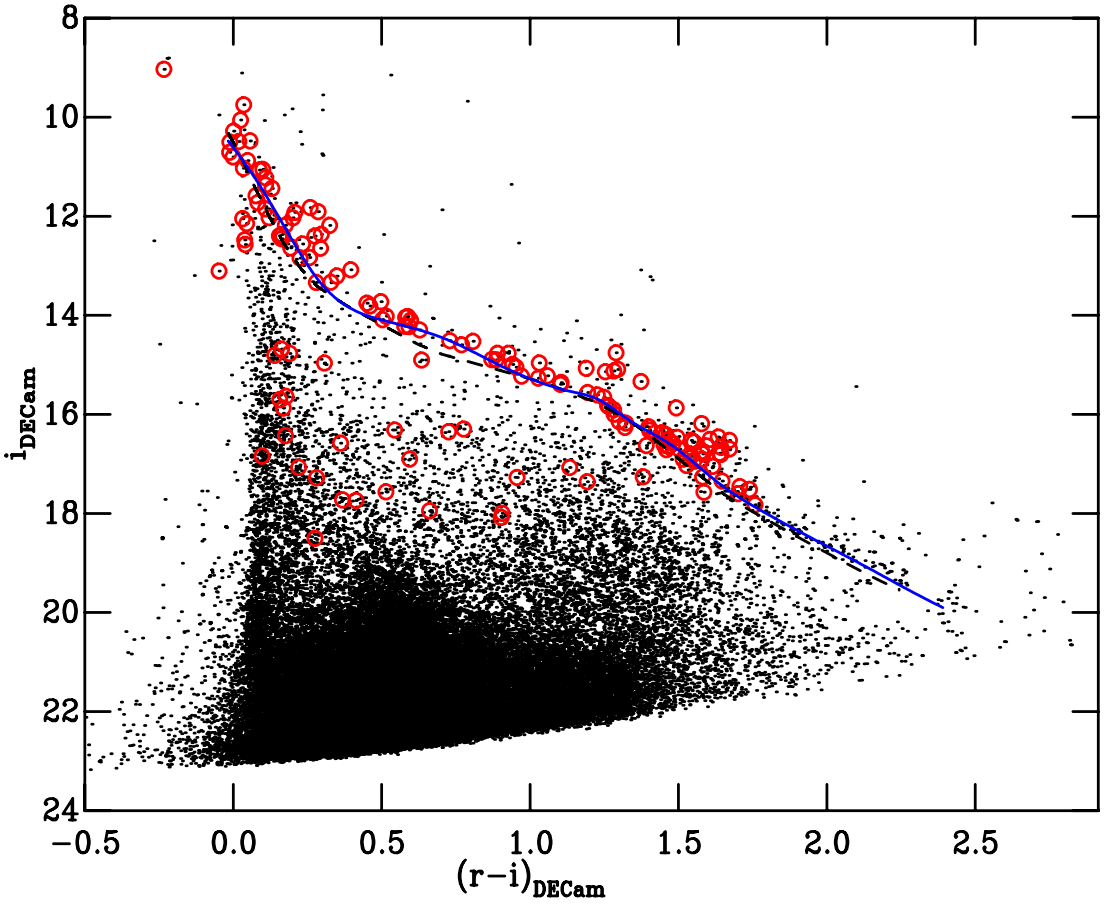

Figure 8.7: The same as Figure 8.5 but for the i, $r-i$ CMD

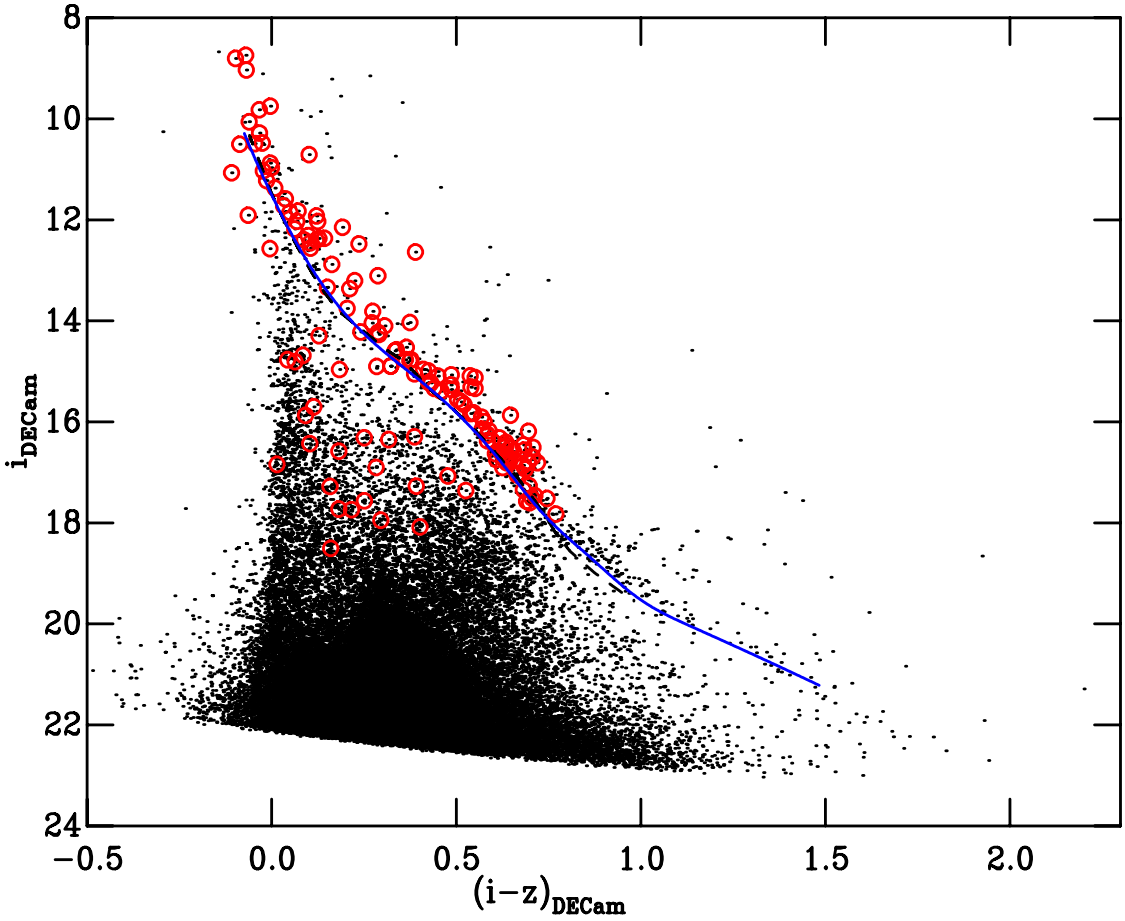

Figure 8.8: The same as Figure 8.5 but for the i, $i - z$ CMD

9

The Age and Disc Lifetimes in Chamaeleon I and ρ-Ophiuchus

9.1 Motivation

In Chapter 6 it was shown that the Taurus star-forming region shows an excess of discs compared to other regions. To establish if this is a result of environmental impact on discs it is necessary to consider other regions with similar environment to Taurus. Chamaeleon I is an ideal option. It is among the nearest star-forming regions, with a distance of $\simeq$ 160 pc (see e.g. Whittet et al. 1997; Wichmann et al. 1998; Bertout et al. 1999) and has relatively low extinction (typical $A_V \simeq 5$, see e.g. Luhman 2007, compared to a maximum of 50-100 for ρ-Ophiuchus). There are also sufficient members to provide a CMD adequate for age fitting (e.g. 196 members according to Luhman et al. 2008) and the stellar population has been well studied to low masses in a range of wavelength regimes, including spectral classification (see e.g. Comerón et al. 2004; Luhman 2004; Mohanty et al. 2005; Muzerolle et al. 2005; Luhman 2007; Luhman et al. 2008). Additionally, Chamaeleon

I is relatively isolated and thus confusion with other young clusters is not a problem. The disc population of Chamaeleon has also been well studied at near-, mid- and far-infrared wavelengths (e.g. Glass 1979; Persi et al. 2000; Kenyon & Gómez 2001; Gómez & Kenyon 2001; Luhman et al. 2008). In terms of environment Chamaeleon is low-stellar-density and low-mass region, similar to Taurus. The stellar density in Chamaeleon is estimated to be 5.7 stars pc^{-3} (King et al. 2012;c.f. 6.0 in Taurus). In terms of massive stars, there are no O stars, and two B stars in Chamaeleon, again similar to Taurus. Chamaeleon thus represents an ideal environment to test if the same excess of discs observed in Taurus exists in other low-density regions. Literature estimates for the age of Chamaeleon I are typically $\simeq$ 2 Myr (see e.g. Luhman et al. 2008, derived from HR diagram fitting).

ρ-Ophiuchus (ρ-Oph) is a low-mass region located $\simeq$ 130 pc away. Due to this small distance, it is possible to reach very low masses relatively easily and thus ρ-Oph has been well studied at a range of wavelengths. The large "wall" of extinction from the cloud itself also serves to eliminate background contamination, making member selection easier than in some other regions. ρ-Oph is typically assumed to have an age between 2-5 Myr (see e.g. Wilking et al. 2008; Mamajek 2008). Erickson et al. (2011) derived ages from HR diagram fitting, using the bolometric corrections of Bessell (1991) and assuming a $T_{\rm eff}$-spectral type relationship. The mean age of the association based on this work is 3.1 Myr. However recent work by James et al. (2016) suggests ρ-Oph may be slightly older, again using HR diagram fitting albeit covering a small number of members. Although ρ-Oph is low-mass, with a single A-star and no O- or B-type stars, it is a high-density region, with a stellar density estimated to be 236±27 star pc^{-3} (King et al. 2012). ρ-Oph thus offered an opportunity to test whether the excess of discs observed in Taurus persists in an environment that has only low-mass members but is not low-stellar-density, potentially highlighting the dominant source of disc dispersal in these regions.

9.2 The Data, Memberships and Distance

The DECam data covering Chamaeleon I and ρ-Oph were obtained on the 4th April 2015. As with the Blanco 1 data I created the observing plan, and the observing and final decisions on the night were performed by David James. The data were reduced in the manner discussed in Chapter 7. Although it is a low-stellar-density region, Chamaeleon is compact enough that a single pointing

with DECam is able to cover practically all of the currently known members. In practice several pointings were used in order to fill in the inter-CCD gaps. The focus of the ρ-Oph observations was the dense L1688 cloud, which makes up the majority of the cluster. As with the Chamaeleon data, several pointings were used to fill in inter-CCD gaps. The field centres and exposure times are given in Table B.1.

9.2.1 Chamaeleon I Membership and Distance

To determine the ages and disc fractions of the young clusters ideally required a sample with distinction between Class II and Class III sources as well as spectral classifications (to allow the disc fraction to be defined over a set spectral type range). Memberships for Chamaeleon I were taken from Luhman et al. (2008), which met these requirements with spectral types and SED classes for all members. The Luhman et al. (2008) catalogue is itself based on the membership list derived in Luhman (2007) using a combination of optical and infrared photometry together with spectroscopic follow-up. The completeness limit of the membership list is 0.01 $M_{\odot}$ according to Luhman (2007) and thus is well suited to the needs of this work. Additionally the *Spitzer*-based survey of discs in this region (Luhman et al. 2008) was performed in the same manner as that in Taurus (Luhman et al. 2010) ensuring that the comparison between the disc populations of the two regions is entirely consistent. Of the 196 members in the catalogue, 175 were detected in the DECam data. The remaining members largely fell outside of the area covered.

The distance of Chamaeleon I was determined to be 160±15 pc by Whittet et al. (1997), using the distribution of extinction as a function of distance for field stars seen in projection against the cloud. The field star distances were derived by measuring the spectral types and then adopting a spectral type-absolute magnitude relationship. Whittet et al. (1997) also obtained a distance of 152±18 pc for one of the B-stars in Chamaeleon (HD 97300) by assuming it had reached the ZAMS. Wichmann et al. (1998) used *Hipparcos* observations of 5 stars in Chamaeleon I to derive the mean cluster distance, finding it to be 160±17 pc. The excellent agreement between the extinction-derived distance and the *Hipparcos* distance as well as the (single star) ZAMS estimate suggests that 160 pc is a reliable estimate for the cluster distance.

9.2.2 ρ-Oph Membership and Distance

A census of ρ-Oph, including L1688, was compiled by Wilking et al. (2008) based on a combination of X-ray emission, strong Hα emission, lithium absorption, infrared excesses in *Spitzer* data, and position in CMDs. This census found 316 members, and after comparing the X-ray luminosity function of ρ-Oph to that of the ONC Wilking et al. (2008) argue that their census is complete for Class II and Class III sources, at least to the same limit as the ONC survey of Feigelson & Getman (2005). Erickson et al. (2011) later conducted a membership survey using spectra for 219 photometrically-selected stars, confirming 135 as members. Of these 135 members 80 were present in the census of Wilking et al. (2008) and 55 were new members. Combining the two catalogues yields 371 members, of which 205 are detected in my photometric catalogue. Of the non-detected members the majority lie in the very centre of the cloud where extinction and nebulosity are greatest. This membership catalogue is the best available in ρ-Oph but lacks the spectral type and SED class information for some members, which will be addressed further in Section 9.5.2.

The distance of ρ-Oph is still not well constrained, and is noticeably absent from the *Hipparcos* catalogues of Wichmann et al. (1998) and Bertout et al. (1999) due to the lack of bright stars. Estimates typically vary between 120 and 160 pc. Whittet (1974) used spectral types to determine the intrinsic luminosity for a selection of stars and estimated a distance of 166±8 pc. Chini (1981) measured the distance to be 165±20 using a combination of spectroscopy and photometry to derive absolute magnitudes. A number of more recent estimates have suggest that ρ-Oph may be closer. Makarov (2007) used proper motions for 58 members and derived a distance of 145 pc from the convergent point method. Mamajek (2008) estimated the distance of the L1688 cloud to be 135^{+8}_{-7} pc using a sample of seven members of reflection nebulae associated with ρ-Oph. Lombardi et al. (2008) used a combination of *Hipparcos* and *Tycho* data to derive a distanc of 119±6 pc. Loinard et al. (2008a) used VLBA data to measure the distance of two stars within ρ-Oph to be $120.0^{+4.5}_{-4.2}$ pc, however Loinard et al. (2008b) found a distance of 160 for other stars in the region. Combining several distance measurements, Wilking et al. (2008) adopted a mean distance of 130 pc for L1688, but noted that the true cluster distance was likely between 120 and 145 pc. The uncertainty in distance will be revisited in Section 9.4.2 when CMDs are used for age derivation.

9.3 Extinction Fitting for the DECam Clusters

The extinction fitting procedure described in Chapter 5 was applied to the Chamaeleon I and ρ-Oph members. Given the similarity in previous age derivations to that of Taurus the range of parameter space covered in the fitting process remained unchanged. A distance of 160 pc was adopted for all Chamaeleon members, and 130 pc or 165 pc was adopted for ρ-Oph (see Section 9.2.2).

9.3.1 Extinction Fitting in Chamaeleon I

The J- and H-band data used for the extinction fitting were taken from 2MASS. In total 91 stars in Chamaeleon have usable $izJH$ measurements. Luhman (2007) determined spectral types for these stars and derived their own measure of the extinction for each source. Figure 9.1 shows a comparison between the extinctions derived by Luhman (2007) and those derived here using the $izJH$ fitting. As with the Taurus extinctions, there is a large scatter evident in the comparison between the two extinction measures, but broad agreement. This lends further confidence to the extinction estimates derived here.

9.3.2 Extinction Fitting in ρ-Oph

The 205 members detected in the photometric catalogue were combined with the 2MASS data of the area. A total of 82 stars had clean photometry in the $izJH$ bands. Upon examining the quality flags for the DECam data, it was realised that a large quantity of the iz data was flagged as having been measured using aperture photometry in place of the optimal photometry, due to a lack of bright stars from which to derive profile corrections. Although these data would be noisier than those derived from optimal photometry, there was no other reason to exclude them and thus the sources with aperture photometry were included (maintaining the limit of a maximum uncertainty of 0.1 mag in each band). This expanded the sample of stars to 140 in total, which were then photometrically dereddened.

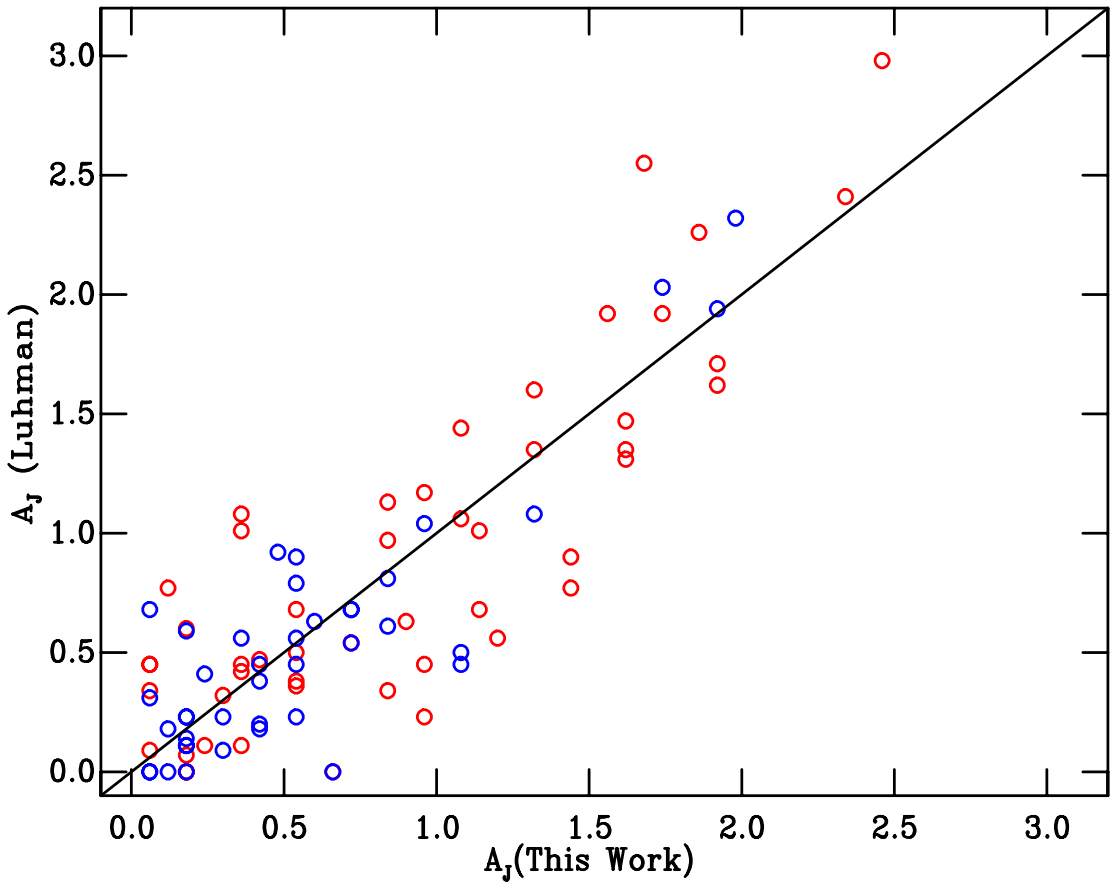

Figure 9.1: A comparison between the extinctions derived in this work and those derived by Luhman (2007) for Chamaeleon I members. Red open circles denote Class II sources, blue open circles denote Class III sources. The solid black line indicates equal extinction.

9.4 The Ages of the DECam Clusters

9.4.1 Determining the Age of Chamaeleon I

The dereddened r, $r - i$ CMDs with the tuned DCJ08 and Pisa isochrones overlaid is shown in Figure 9.2 and with the BCAH98 and BCAH15 isochrones overlaid in Figure 9.3. As with the Taurus data the canonical age isochrone (2 Myr in this case) sits above the data and is clearly not an acceptable fit. Comparing the location of the other isochrones to the observed sequence, Chamaeleon is clearly older than Taurus. The DCJ08 models showed a high cut-off $T_{\rm eff}$. This was due to the relatively high low-mass limit of the models (0.1 $M_{\odot}$) limiting the Blanco 1 tuning process to high $T_{\rm eff}$. The Pisa and DCJ08 models suggested a slightly younger age (4-8 Myr) than the BCAH98 or BCAH15 models (6-8 Myr). The age adopted here for Chamaeleon I (as a mean cluster age) was 6 Myr, for which the model isochrones traced the centre of the sequence well in all cases. This also held true when considering only the Class III objects (see Figures 9.4 and 9.5)

9.4.2 Determining the Age of ρ-Oph

The dereddened r, $r-i$ CMDs for ρ-Oph with the tuned BCAH98 and BCAH15 isochrones overlaid is shown in Figure 9.7 and with DCJ08 and Pisa isochrones overlaid in Figure 9.6, assuming a distance of 130 pc. The BCAH98 and BCAH15 models suggest a mean age of 20 Myr, and the DCJ08 and Pisa models suggest a younger age of 15 Myr. Such an old age would be surprising given the literature age derivations. Adopting a distance of 165 pc instead yielded the CMDs shown in Figures 9.9 (BCAH98 and BCAH15 isochrones overlaid) and 9.8 (DCJ08 and Pisa). This resulted in mean ages of 8-10 Myr. The ages derived assuming a distance of 165 pc are more consistent with previous age derivations, given the factor $\sim$ 2-3 increase in age derivations seen with other clusters in Bell et al. (2013). This is also in-line with the mean age of 11$\pm$1 Myr derived for Upper Sco by Pecaut et al. (2012), which is often suggested to have triggered star formation in ρ-Oph (see e.g. Mamajek 2008).

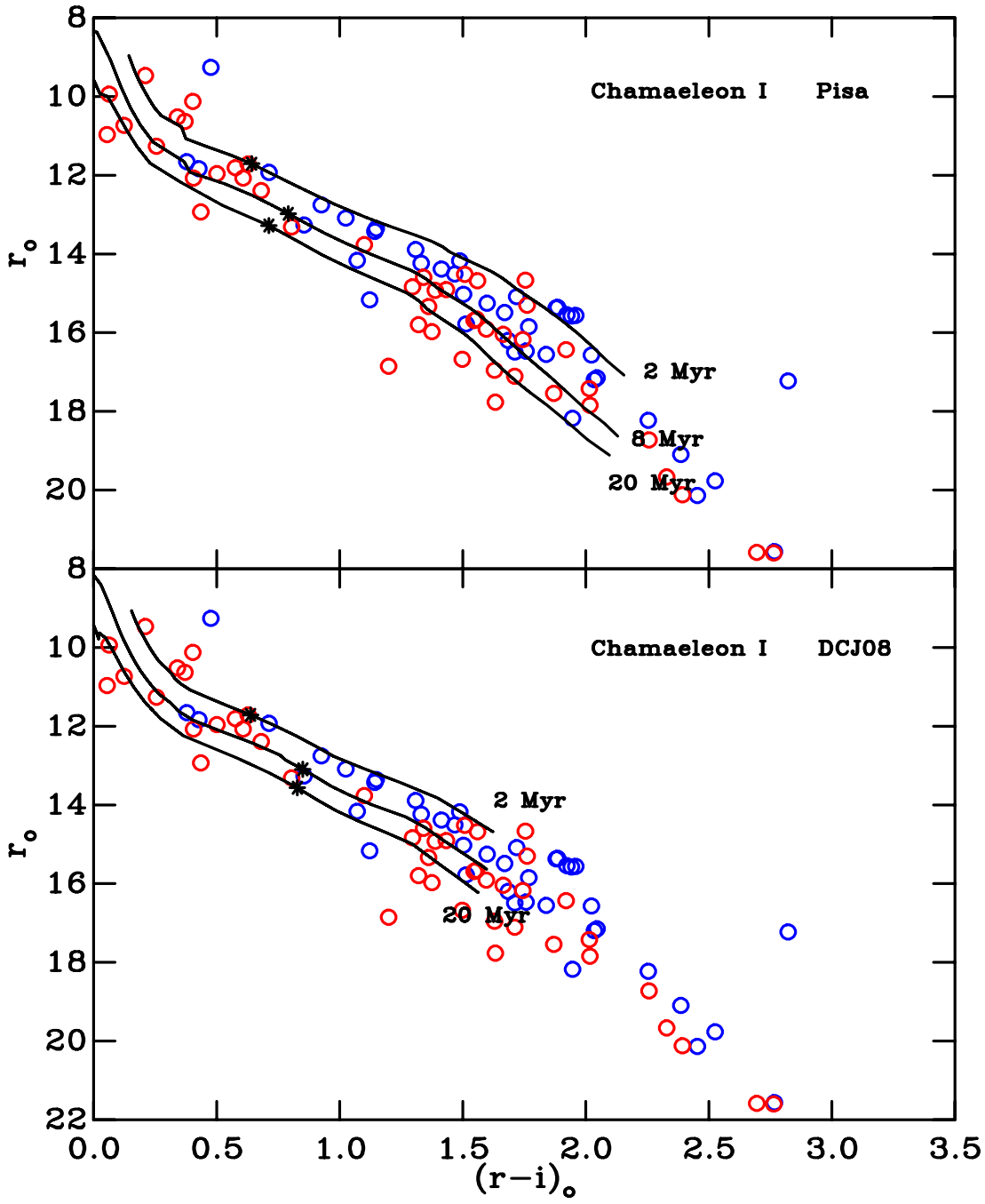

Figure 9.2: Dereddened r, $r-i$ CMDs for Chamaeleon I members. Red open circles denote Class II members according to the classifications of Luhman et al. (2008) and blue open circles denote Class III members. The data have been dereddened using the extinctions derived in Section 9.3.1 Overlaid are isochrones of 2, 8 and 20 Myr created using the interior models of DCJ08 (bottom) and Pisa (top). The models have been transformed into the observational plane using the semi-empirical BCs discussed in Chapter 8. The position of a theoretical 0.75 $M_{\odot}$ star is indicated on each model with an asterisk.

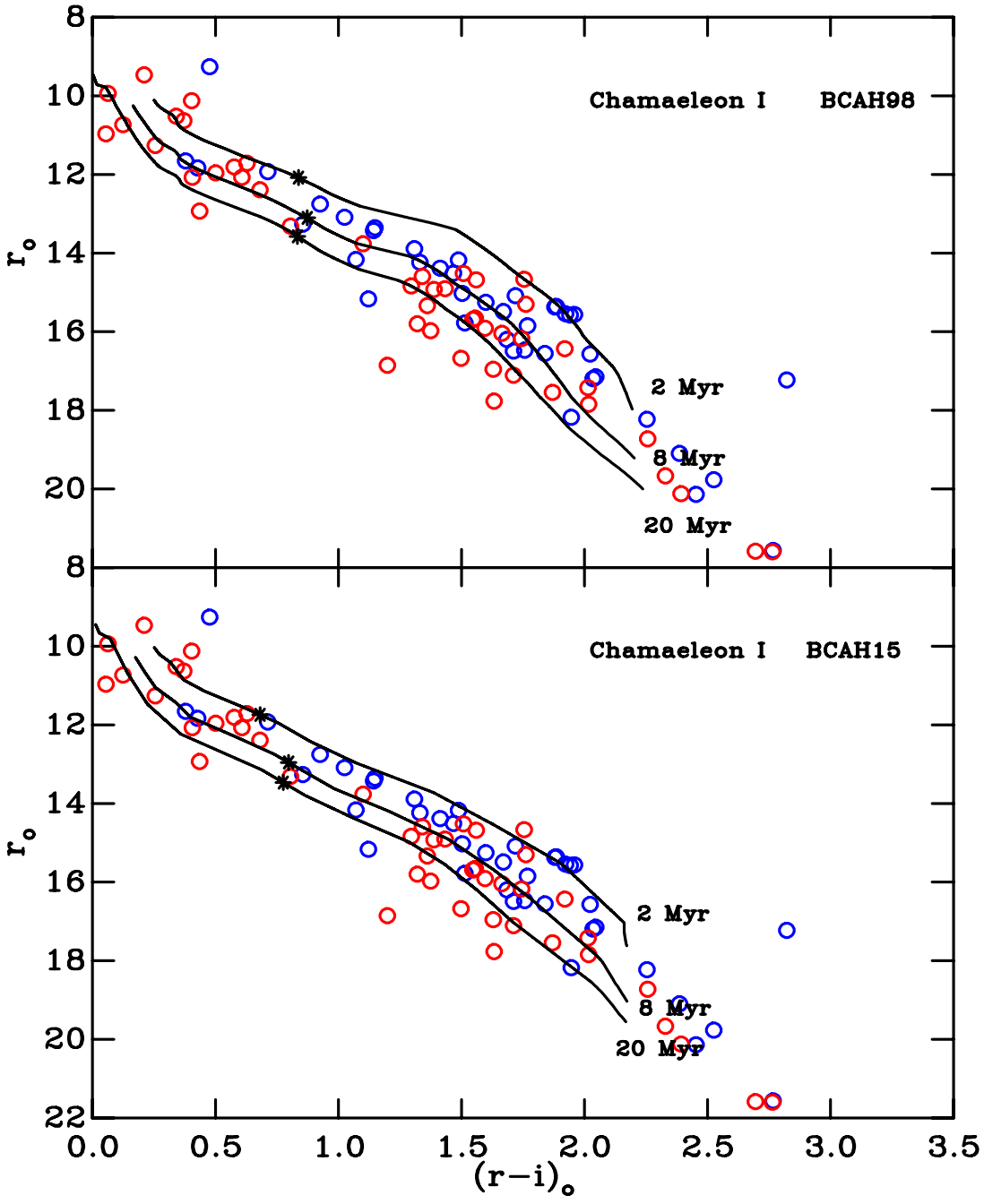

Figure 9.3: The same as Figure 9.2, but with the BCAH98 (top) and BCAH15 (bottom) models overlaid.

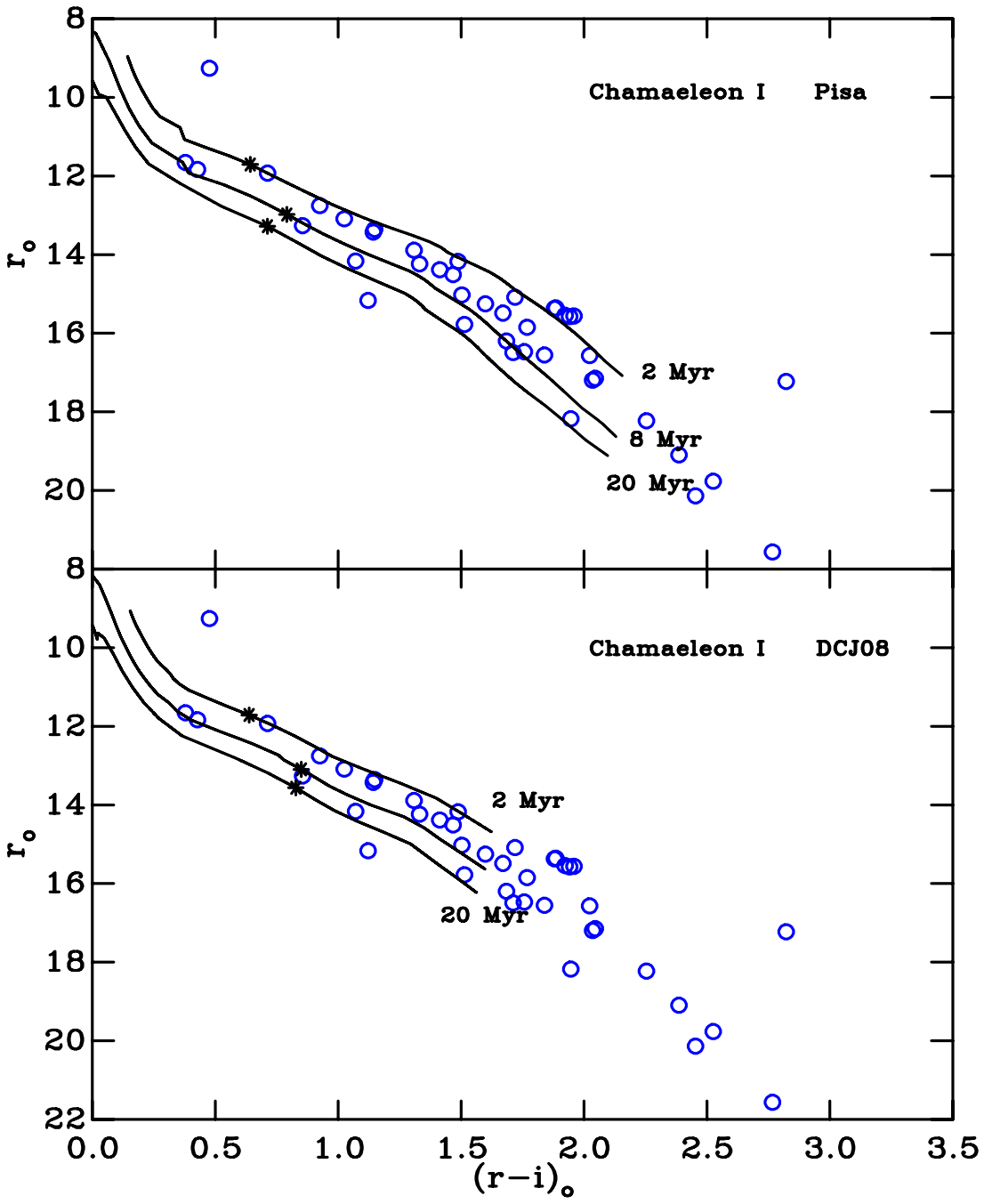

Figure 9.4: The same as Figure 9.2 but showing only the Class III objects.

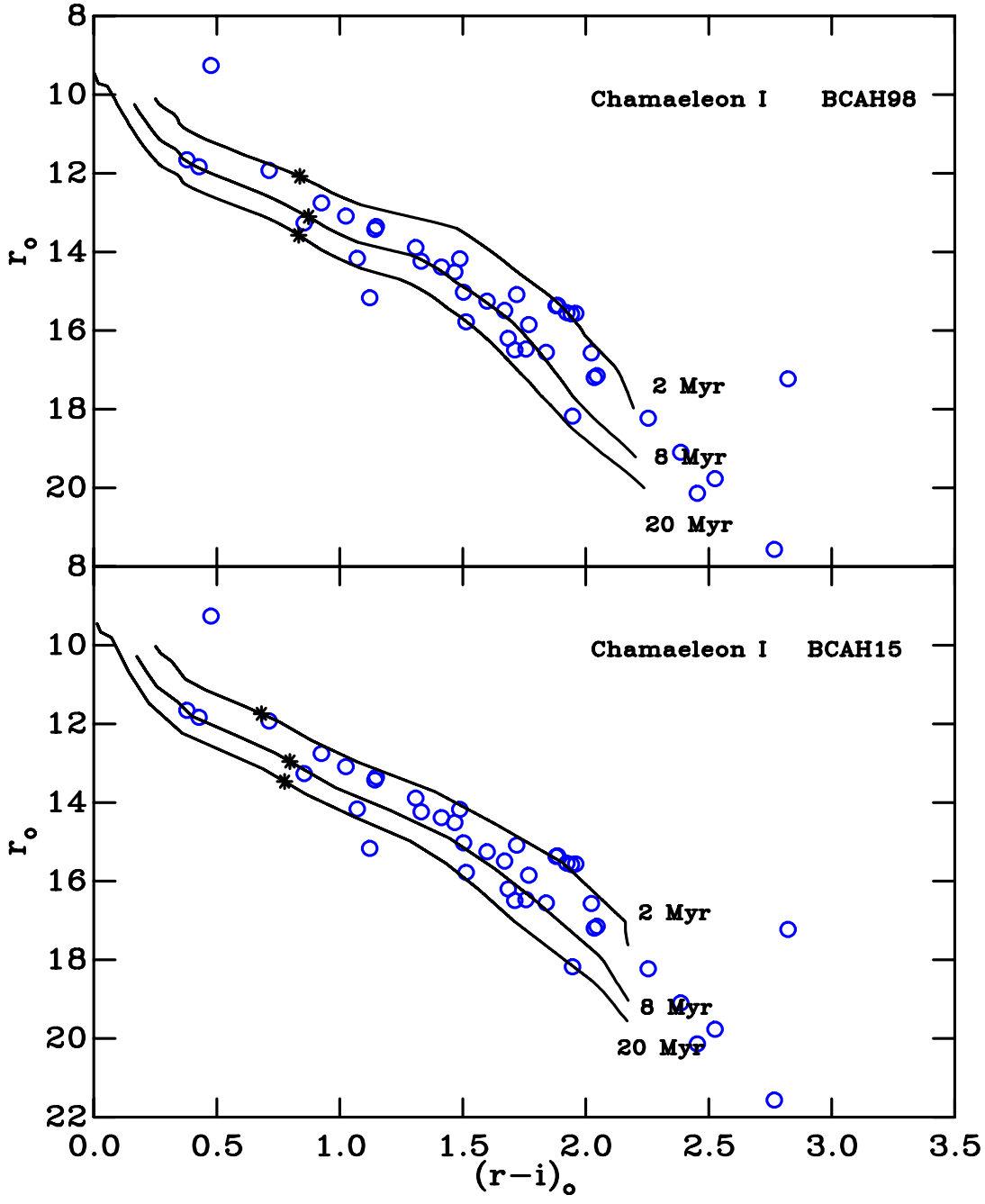

Figure 9.5: The same as Figure 9.4, but with BCAH98 (top) and BCAH15 (bottom) models overlaid.

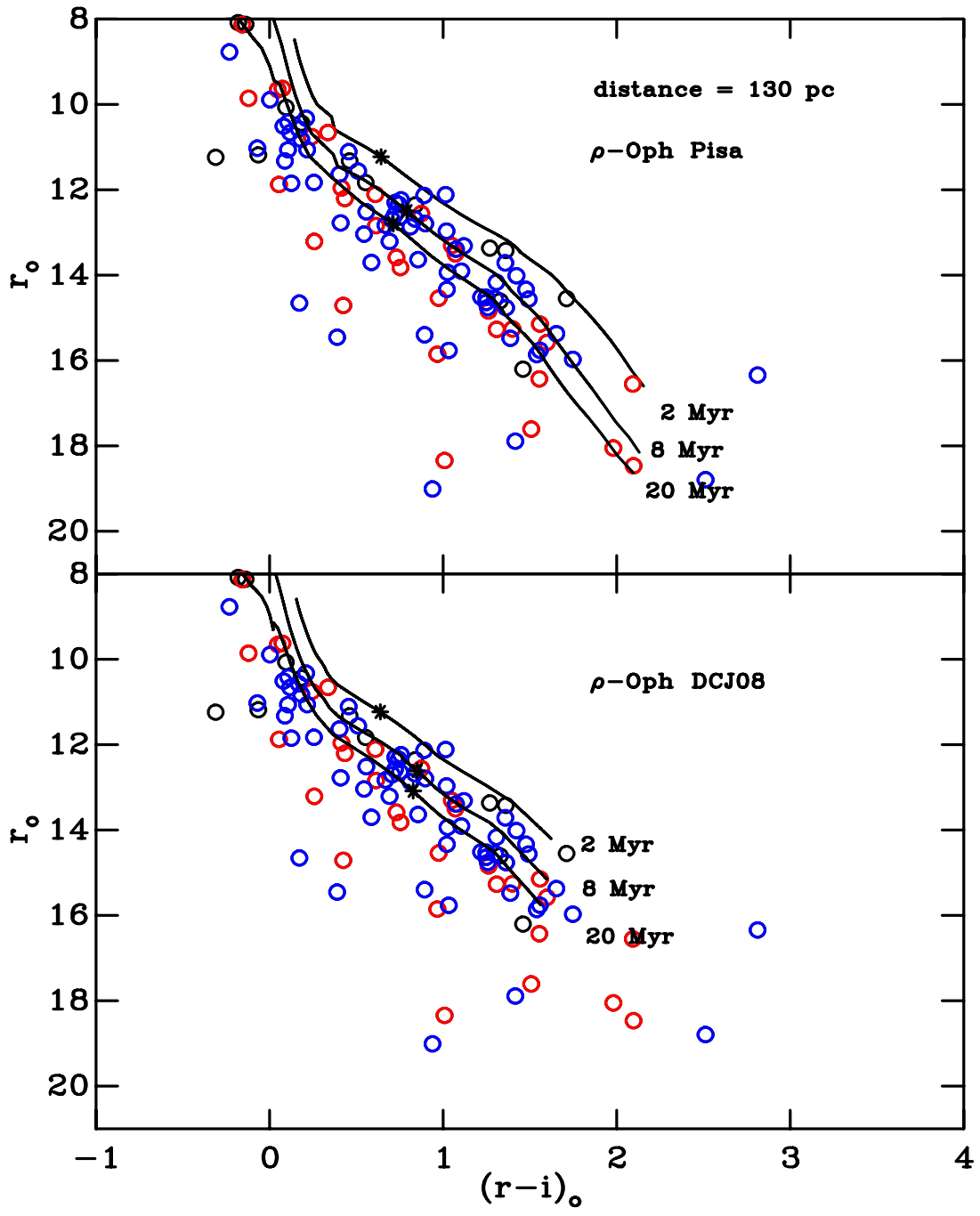

Figure 9.6: Dereddened r, $r - i$ CMDs for ρ-Oph members. Red open circles show the Class II sources and blue open circles show Class III sources, as derived in Section 9.5.2. Black open circles show the remaining members according to the combined catalogue of Wilking et al. (2008) and Erickson et al. (2011) that were unable to be classified. Overlaid are isochrones of 2, 8 and 20 Myr created using the interior models of DCJ08 (bottom) and Pisa (top) assuming a distance of 130 pc. The models have been transformed into the observational plane using the semi-empirical BCs discussed in Chapter 8. The position of a theoretical 0.75 $M_{\odot}$ star is indicated on each model with an asterisk.

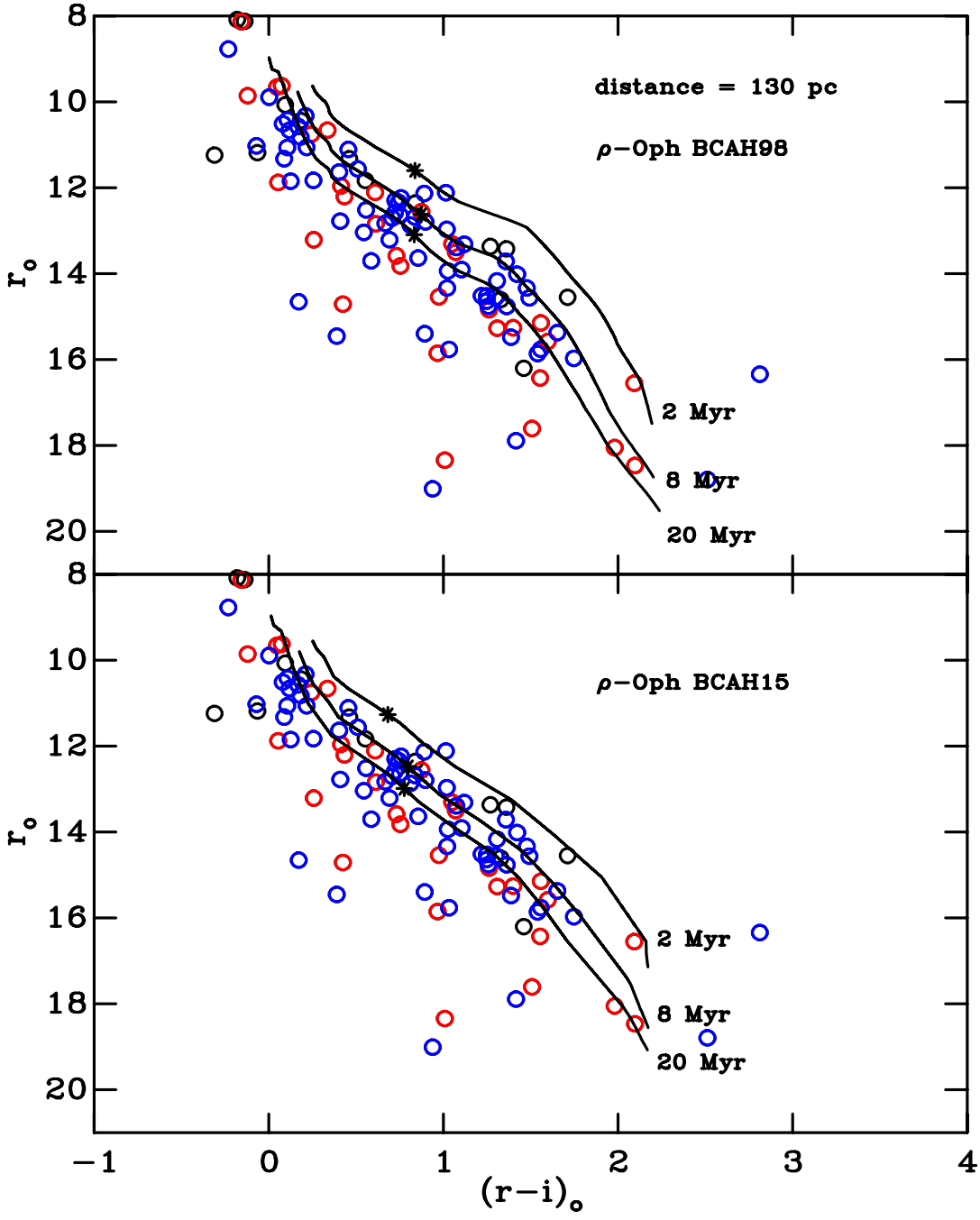

Figure 9.7: The same as Figure 9.6 but with BCAH98 (top) and BCAH15 (bottom) models overlaid.

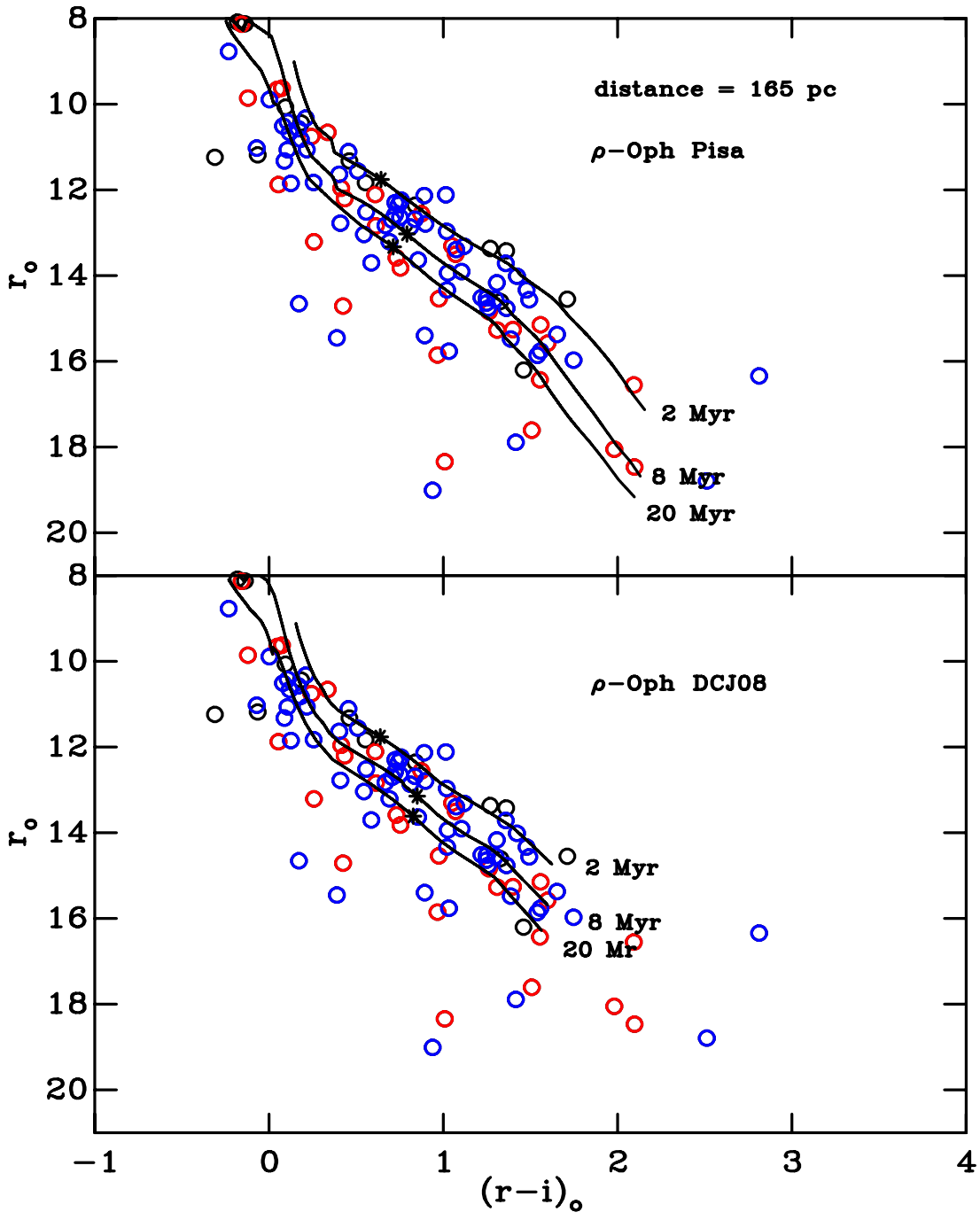

Figure 9.8: The same as Figure 9.6, but adopting a distance of 165 pc.

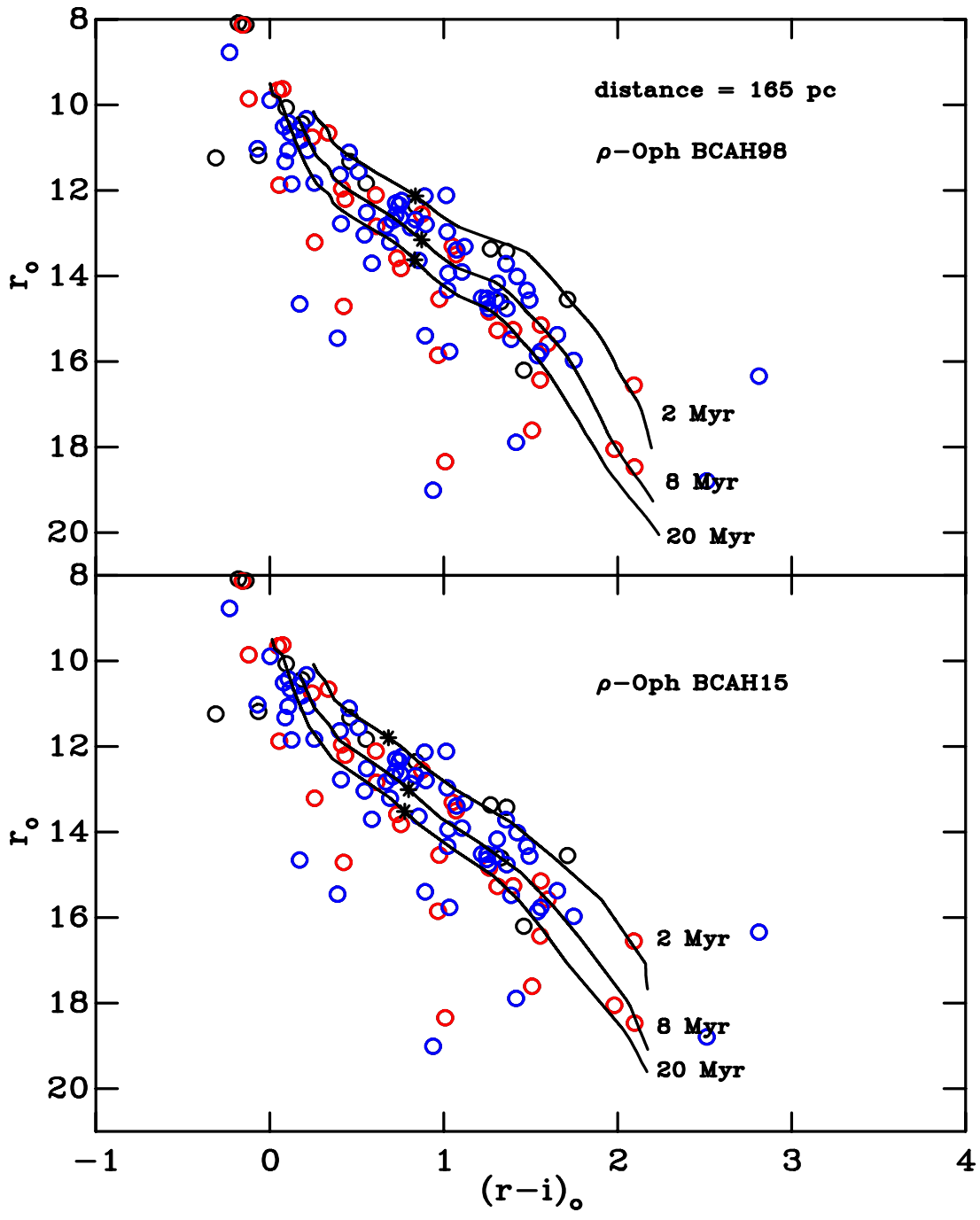

Figure 9.9: The same as Figure 9.8 but with BCAH98 (top) and BCAH15 (bottom) models overlaid.

9.5 Discs in the DECam Clusters

9.5.1 The Disc Fraction of Chamaeleon I

The disc fraction in Chamaeleon I is calculated in the same manner as for Taurus in Section 6.5.1. The classifications of Luhman et al. (2008) were used to determine Class II and Class III sources. The spectral types from Luhman (2007) were adopted and used to select only those members in the range K6 to M3.5 inclusive. In this spectral type range there are 14 Class II sources and 8 class Class III sources in the data presented here. This gave a disc fraction of (63±10)%. The disc fraction for the entirety of Chamaeleon I is (64±6)% and thus, as was the case in Taurus, the sample presented here was consistent with the overall disc properties in the cluster. This was particularly encouraging, as it confirms that the selection of cluster members in *izJH* (by requiring a clean detection in all bands) did not bias the sample.

9.5.2 The Disc Fraction of ρ-Oph

Compared to Chamaeleon, the disc fraction in ρ-Oph is less well constrained as a function of spectral type. Recent large studies include Erickson et al. (2011), who found a disc fraction of 27±5% making no distinction between different spectral types (c.f. 50% in Chamaeleon and 61% in Taurus), and Ribas et al. (2014) who found a disc fraction of 25±3% based on *Spitzer* IRAC excesses. However there are no large-scale surveys of the disc population in ρ-Oph as a function of spectral type. To derive the disc fraction for the same late-K to early-M bin as used in the other clusters, the spectral types given in Wilking et al. (2008) were combined with *Spitzer* data covering ρ-Oph. A total of 63 stars have a combination of clean photometry in *Spitzer* IRAC bands 1 and 3 and measured spectral types. To check for bias in this subsample of members compared to the members used for the age derivation in Section 9.4.2 the age was re-derived from this subsample of members, and remained unchanged.

The *Spitzer* zeropoint fluxes given in the IRAC handbook[1] were used to convert the IRAC magnitudes to fluxes. These fluxes were then used to calculate the spectral index α(3.6 - 5.8 μm) given by

$$\alpha(\lambda_1 - \lambda_2) = \frac{log_{10}(\lambda_1 F_{\lambda 1}) - log_{10}(\lambda_2 F_{\lambda 2})}{log_{10}(\lambda_1) - log_{10}(\lambda_2)}. \quad (9.1)$$

Sources with -1.6 < α(3.6 - 5.8 μm) < -0.3 were classified as Class II objects and those with .

[1] http://irsa.ipac.caltech.edu/data/SPITZER/docs/irac/iracinstrumenthandbook/17/

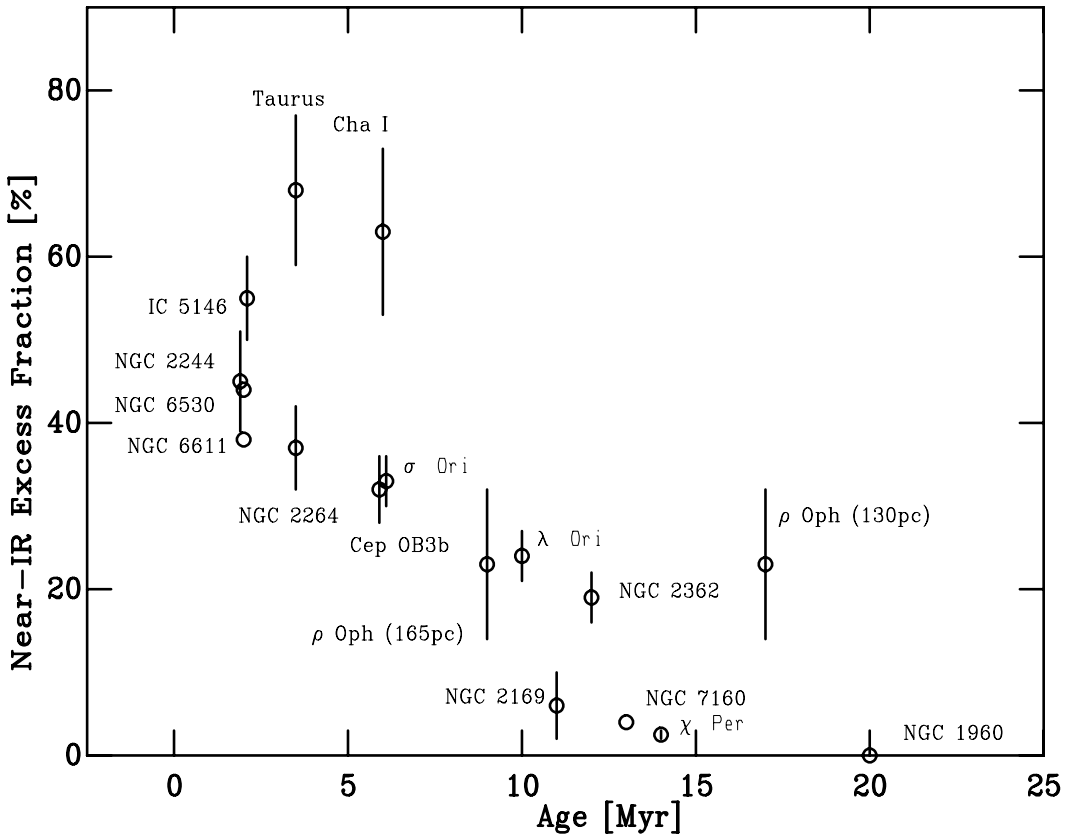

Figure 9.10: The fraction of stars with spectral types mid-K to early-M with near-IR excess disc emission as a function of (revised) age. Note that the ages for IC 5146, NGC 6530, σ Ori and CepOb3b have been shifted slightly to highlight the uncertainties in the disc fractions. Data for NGC 2264, Chamaeleon, ρ-Oph and Taurus are taken from this work, the data for the other clusters is taken from Bell et al. (2013) and references therein. ρ-Oph is plotted twice, to account for the dependence of the derived age on the assumed distance to the cluster (see Section 9.4.2

α(3.6 - 5.8 μm) $\lesssim$ -1.6 were classified as Class III objects. In the relevant spectral type range of K6 to M3.5 there were 5 Class II objects and 17 Class III objects, resulting in a disc fraction of 23^{+9}_{-8} %.

Using the ages derived in Sections 9.4.1 and 9.4.2, Chamaeleon I and ρ-Oph were added to the plot of disc fraction vs age (see Figure 9.10). The interpretation and implications of this result will be addressed in Chapter 10 to avoid repetition.

10

Conclusions and Future Work

10.1 Summary of Previous Chapters

This work has focussed on the derivation of ages for young stars, with the aim of determining the effect of local environment on circumstellar discs.

In Chapter 2 the data reduction process for the INT-WFC was detailed, and INT-WFC observations of the Pleiades, Praesepe and NGC 2264 were introduced. In Chapter 3 the Pleiades data were used in combination with sets of theoretical model isochrones to construct semi-empirical models that are able to reproduce the observed stellar sequences at low $T_{\rm eff}$. The deep $i-$ and $Z-$band observations of the Pleiades were used to create a set of semi-empirical models to lower $T_{\rm eff}$ than those presented in (Bell et al. 2012). These models were used to derive an age of 3-4 Myr for NGC 2264. Crucially, this newly derived age is on a scale consistent with the clusters studied in Bell et al. (2013). It was noted that with an age of 3-4 Myr the disc fraction in NGC 2264 is consistent with that expected from the other massive, dense regions studied in Bell et al. (2013).

In Chapter 4 semi-empirical models were constructed in the SDSS, 2MASS and UKIDSS photometric systems. The models in the UKIDSS system extended to lower $T_{\rm eff}$ than those in the 2MASS system, and the ΔBCs derived from low-$T_{\rm eff}$ UKIDSS data were applied to the models in the 2MASS system to extend them to lower $T_{\rm eff}$. The construction of the semi-empirical models in these widely used photometric systems allows the models to be applied to a wide range of data for a number of clusters, far beyond what was possible with the previous systems.

Chapter 5 detailed a method of photometric dereddening using *iZJH* data. The method was introduced in terms of dereddening in a colour-colour diagram, and was then extended to a Bayesian method of fitting to allow for the consideration of the effects of age and binarity. The dereddening procedure was tested against data for IC 348, and it was shown to reproduce consistent extinctions to literature values. This work provides a method of dereddening that is far less observationally intensive than similar spectroscopic methods.

In Chapter 6 the dereddening process was applied to INT-WFC and SDSS data for the Taurus star-forming region. The derived extinctions were compared to previous literature determinations and it was shown that they were consistent with other measures of infrared extinctions. The dereddened Taurus CMDs were used to derive a mean age for the region, finding it to be 3-4 Myr. This derived age is significantly older than the often quoted value of 1-2 Myr seen in the literature, but is entirely consistent with the factor ∼2-3 increase in cluster ages detailed by Bell et al. (2013). The implications of such an age for Taurus were discussed, and it was shown that the disc fraction of Taurus shows a clear excess of discs compared to massive, dense regions of a similar or younger age. This was interpreted as tentative evidence of longer-lived discs in the low-mass, low-density region of Taurus. The effect of an older age on the mass function in Taurus was also considered, and it was shown that this could not account for the discrepant mass function previously observed in Taurus.

In Chapter 7 a new data reduction process was described for data in the Blanco-DECam system. A set of observations was introduced covering Blanco 1, Chamaeleon I and ρ-Ophiuchus. The Blanco 1 data were used in Chapter 8 to construct semi-empirical models in the Blanco-DECam system. The resulting ΔBCs were compared to those from the INT-WFC photometric system, and it was shown that there was only slight variation between the two.

In Chapter 9 Chamaeleon I and ρ-Oph were discussed further. The dereddening process from Chapter 5 was applied to the DECam data for both regions and used to derive extinctions for

members. The semi-empirical models in the DECam system were then used to determine the mean ages of the two regions. Chamaeleon was found to have an age of 6 Myr. The age determination for ρ-Oph was complicated by the lack of a robust distance estimate for the region. Depending on the distance adopted the age was found to be between 8 and 20 Myr. The former age would be consistent with the scenario of ρ-Oph being the result of triggered star formation from the nearby Upper Sco region. *Spitzer* IRAC data were used to derive the disc fraction in ρ-Oph in a consistent manner as those adopted for the other regions in this study. The newly derived ages for Chamaeleon I and ρ-Oph were used to add both regions to the plot of disc fraction vs age (Figure 9.10).

10.2 Conclusions

Chamaeleon I shows a clear excess of discs compared to the dense, massive clusters. This strengthens the result from Chapter 6, in which it was shown that Taurus shows an excess of discs. The fact that both of the low-density, low-mass regions show an excess of discs is the first robust evidence that the local environment impacts disc lifetimes. An increased disc longevity in such environments has been predicted by theory, arising from either the lack of disc destruction by stellar encounters or by ablation from massive stars (see Section 1.1.3). Because ρ-Oph is a low-mass region yet has a high stellar density, it would be an ideal test to determine which is the dominant reason for this observed increased disc lifetime. If an excess of discs exists in ρ-Oph it would suggest that disc destruction by ablation is the dominant mechanism. Conversely if no such excess exists it would be evidence that stellar encounters dominates. However the evidence for a disc excess in ρ-Oph is dependent on the assumed distance. Adopting a distance of 130 pc ρ-Oph shows an excess of discs, but adopting a distance of 160 pc would bring the disc fraction in-line with the other dense regions. The upcoming *Gaia* parallax release will solve this issue. Thus there is evidence that low-mass, low-density regions can lead to a longer disc lifetime, but it is unclear whether the lack of massive stars or the low stellar density (and thus lack of stellar interactions) is the dominant mechanism.

Bell et al. (2013) noted that the revised age scale brought disc lifetimes into agreement with the theoretical timescales of planet formation. An increased disc lifetime in low-density regions potentially increases the time available for planet formation. There have been suggestions that

stellar mass may be determined by the length of the accretion phase (Bate & Bonnell 2005) and is thus also dependent on the longevity of the disc. This is a potential explanation for the skewed IMF seen in Taurus (see e.g. Bastian et al. 2010), but does not explain why the same is not then seen in Chamaeleon.

10.3 Further work

The work presented in Chapter 5 has the potential to be applied to other young clusters to derive extinctions without requiring intensive spectroscopy campaigns. There are a number of wide-area photometric surveys currently ongoing or nearing data releases (e.g. Pan-STARRS, APASS, DECaLS) which will give easy access to wide-area photometry for these purposes. The observations of fiducial clusters in each survey can also be used to construct semi-empirical models for each photometric system, which can then be used to study nearby young clusters.

The ongoing *Gaia* mission will provide astrometry and parallaxes for around a billion stars in the Milky Way. The parallax measurements will yield distances to the individual stars. These distances will allow the distance to ρ-Oph to be properly constrained, which can then be used to better constrain the age. This will then allow a determination of whether there is an excess of discs in ρ-Oph, which will further inform the mechanism behind the long-lived discs seen in the other associations. There is unlikely to be a large shift in the distances to most nearby young clusters, as previous distance measurements rely on well understood main-sequence fitting. However reducing the uncertainties in the distances to other young clusters may have an impact on the luminosity spreads we see in young nearby clusters. In Taurus for example there appears to be a $\simeq 0.4$ mag spread in the distance modulus to different clouds. Measuring distances of individual stars in other clusters will allow the contribution of distance to the luminosity spread in young clusters to be quantified. Combining the distance information with the astrometric data will allow for better determinations of membership of young, nearby clusters.

The Gaia-ESO survey is a project to obtain spectroscopic measurements of many of the stars which Gaia will observe. This will provide an excellent dataset for determinations of the metallicity of many young clusters and associations, which could potentially allow for the construction of semi-empirical pre-MS models for a range of metallicities. The effect of metallicity on the observed data-model discrepancies could also be used to help infer the source of the ex-

cess flux in the models. For example, if the problems with the models are largely due to missing opacity sources (e.g. TiO, VO) this would be expected to correlate strongly with metallicity. If the problems are due to other opacity sources (e.g. H^- opacity) or due to other issues the correlation with metallicity would be more complex.

The τ^2 technique for age determinations can be applied to other stellar populations, e.g. globular clusters. The low-metallicity populations seen in globular clusters will allow the evolutionary models to be tested in a new environment, and could also help to elucidate the source of the discrepancies between the models and observations. The evidence for the dependence of disc lifetimes on environment could also have implications for globular clusters, given the suggestions of e.g. Bastian et al. (2013) that accretion of enriched material into the discs of low-mass stars could explain the observed abundance variations.

A

INT-WFC Observed Fields and Exposure Times

Table A.1: The central coordinates for each field-of-view and $(UgriZ)_{\mathrm{WFC}}$ exposure times for the INT-WFC observations of the Pleiades and Praesepe.

Field	RA Dec. (J2000.0)	Filter	Exposure time (s)
Pleiades	$03^{\mathrm{h}}\,46^{\mathrm{m}}\,19.2^{\mathrm{s}}$	U_{WFC}	1, 10
Field A	$+23^{\circ}\,38'\,02.4''$	g_{WFC}	1, 10, 100(×2), 500(×2)
		r_{WFC}	1, 7, 50, 250, 500
		i_{WFC}	1, 10, 100(×2), 500(×7)
		Z_{WFC}	1, 7, 50, 250(×2), 500
Pleiades	$03^{\mathrm{h}}\,45^{\mathrm{m}}\,00.0^{\mathrm{s}}$	U_{WFC}	1, 10
Field B	$+23^{\circ}\,44'\,45.6''$	g_{WFC}	1, 10, 100, 500(×2)

continued on next page...

Table A.1: continued

Field	RA Dec. (J2000.0)	Filter	Exposure time (s)
		$r_{\rm WFC}$	1, 7, 50, 250
		$i_{\rm WFC}$	1, 10, 100(×2)
		$Z_{\rm WFC}$	1, 7, 50, 250
Pleiades	$03^{\rm h}\,43^{\rm m}\,44.4^{\rm s}$	$U_{\rm WFC}$	1, 10
Field C	+23° 58′ 08.4″	$g_{\rm WFC}$	1, 10, 100, 500(×2)
		$r_{\rm WFC}$	1, 7, 50, 250
		$i_{\rm WFC}$	1, 10, 100(×2)
		$Z_{\rm WFC}$	1, 7, 50, 250
Pleiades	$03^{\rm h}\,42^{\rm m}\,36.0^{\rm s}$	$U_{\rm WFC}$	1, 10
Field D	+23° 58′ 08.4″	$g_{\rm WFC}$	1, 10, 100, 500(×2)
		$r_{\rm WFC}$	1, 7, 50, 250
		$i_{\rm WFC}$	1, 10, 100(×2)
		$Z_{\rm WFC}$	1, 7, 50, 250
Pleiades	$03^{\rm h}\,43{\rm m}\,44.4^{\rm s}$	$U_{\rm WFC}$	1, 10
Field E	+24° 24′ 28.8″	$g_{\rm WFC}$	1, 10, 100, 500(×2)
		$r_{\rm WFC}$	1, 7, 50, 250
		$i_{\rm WFC}$	1, 10, 100(×2)
		$Z_{\rm WFC}$	1, 7, 50, 250
Pleiades	$03^{\rm h}\,43^{\rm m}\,44.4^{\rm s}$	$U_{\rm WFC}$	1, 10
Field F	+24° 25′ 39.5″	$g_{\rm WFC}$	1, 10, 100, 500(×2)
		$r_{\rm WFC}$	1, 7, 50, 250
		$i_{\rm WFC}$	1, 10, 100(×2)
		$Z_{\rm WFC}$	1, 7, 50, 250
Pleiades	$03^{\rm h}\,48^{\rm m}\,05.9^{\rm s}$	$U_{\rm WFC}$	1, 10
Field H	+23° 44′ 56.0″	$g_{\rm WFC}$	1, 10, 100
		$r_{\rm WFC}$	1, 7, 50
		$i_{\rm WFC}$	1, 10, 100

continued on next page...

Table A.1: continued

Field	RA Dec. (J2000.0)	Filter	Exposure time (s)
		$Z_{\rm WFC}$	1, 7, 50
Pleiades	$03^{\rm h}\,48^{\rm m}\,44.3^{\rm s}$	$U_{\rm WFC}$	1, 10
Field I	$+23^\circ\,31'\,44.0''$	$g_{\rm WFC}$	1, 10, 100
		$r_{\rm WFC}$	1, 7, 50
		$i_{\rm WFC}$	1, 10, 100
		$Z_{\rm WFC}$	1, 7, 50
Pleiades	$03^{\rm h}\,50^{\rm m}\,01.1^{\rm s}$	$U_{\rm WFC}$	1, 10
Field J	$+23^\circ\,54'\,32.0''$	$g_{\rm WFC}$	1, 10, 100
		$r_{\rm WFC}$	1, 7, 50
		$i_{\rm WFC}$	1, 10, 100
		$Z_{\rm WFC}$	1, 7, 50
Pleiades	$03^{\rm h}\,50^{\rm m}\,53.86^{\rm s}$	$U_{\rm WFC}$	1, 10
Field K	$+24^\circ\,15'\,32.0''$	$g_{\rm WFC}$	1, 10, 100
		$r_{\rm WFC}$	1, 7, 50
		$i_{\rm WFC}$	1, 10, 100, 500(×4)
		$Z_{\rm WFC}$	1, 7, 50, 250(×2)
Pleiades	$03^{\rm h}\,51^{\rm m}\,58.7^{\rm s}$	$U_{\rm WFC}$	1, 10
Field L	$+24^\circ\,41'\,56.0''$	$g_{\rm WFC}$	1, 10, 100
		$r_{\rm WFC}$	1, 7, 50
		$i_{\rm WFC}$	1, 10, 100
		$Z_{\rm WFC}$	1, 7, 50
Praesepe	$08^{\rm h}\,40^{\rm m}\,46.7^{\rm s}$	$g_{\rm WFC}$	1, 10(×3), 100
Field A	$+19^\circ\,32'\,56.0''$	$r_{\rm WFC}$	1, 10(×3)
		$i_{\rm WFC}$	1, 10(×3), 100
		$Z_{\rm WFC}$	1, 10
Praesepe	$08^{\rm h}\,40^{\rm m}\,22.7^{\rm s}$	$g_{\rm WFC}$	1, 10(×3)

continued on next page...

Table A.1: continued

Field	RA Dec. (J2000.0)	Filter	Exposure time (s)
Field B	+19° 59′ 56.0″	$r_{\rm WFC}$	1, 10(× 3)
		$i_{\rm WFC}$	1, 10(× 3)
		$Z_{\rm WFC}$	1, 10

Table A.2: The central coordinates for each field-of-view and $(UgriZ)_{\rm WFC}$ exposure times for the observations of the standard star fields with the INT-WFC

Field	RA Dec. (J2000.0)	Filter	Exposure time (s)
Sloan 1	$20^{\rm h}\,48^{\rm m}\,57.1^{\rm s}$	$U_{\rm WFC}$	5, 50
	−00° 53′ 47.6″	$g_{\rm WFC}$	5, 50
		$r_{\rm WFC}$	5, 50
		$i_{\rm WFC}$	5, 50
		$Z_{\rm WFC}$	5, 50
Sloan 2	$23^{\rm h}\,00^{\rm m}\,00.0^{\rm s}$	$U_{\rm WFC}$	5, 50
	+00° 00′ 00.0″	$g_{\rm WFC}$	5, 50
		$r_{\rm WFC}$	5, 50
		$i_{\rm WFC}$	5, 50
		$Z_{\rm WFC}$	5, 50
Sloan 3	$01^{\rm h}\,31^{\rm m}\,45.0^{\rm s}$	$U_{\rm WFC}$	5, 50
	−00° 40′ 00.0″	$g_{\rm WFC}$	5, 50
		$r_{\rm WFC}$	5, 50
		$i_{\rm WFC}$	5, 50
		$Z_{\rm WFC}$	5, 50
Sloan 4	$03^{\rm h}\,55^{\rm m}\,00.0^{\rm s}$	$U_{\rm WFC}$	5, 50
	+00° 00′ 00.0″	$g_{\rm WFC}$	5, 50
		$r_{\rm WFC}$	5, 50

continued on next page...

Table A.2: continued

Field	RA Dec. (J2000.0)	Filter	Exposure time (s)
		$i_{\rm WFC}$	5, 50
		$Z_{\rm WFC}$	5, 50
Sloan 6	$07^{\rm h}\,40^{\rm m}\,56.3^{\rm s}$	$U_{\rm WFC}$	5, 50
	$+29^\circ\,11'\,56.0''$	$g_{\rm WFC}$	5, 50
		$r_{\rm WFC}$	5, 50
		$i_{\rm WFC}$	5, 50
		$Z_{\rm WFC}$	5, 50

Table A.3: The central coordinates for each field-of-view and $(UgriZ)_{\rm WFC}$ exposure times for the INT-WFC observations of the young clusters Taurus and NGC2264.

Field	RA Dec. (J2000.0)	Filter	Exposure time (s)
Taurus	$04^{\rm h}\,39^{\rm m}\,58.6^{\rm s}$	$g_{\rm WFC}$	2, 20, 100, 170($\times$ 3)
Field 100	$+25^\circ\,54'\,00.0''$	$r_{\rm WFC}$	1, 10, 100
		$i_{\rm WFC}$	1, 10, 100
		$Z_{\rm WFC}$	1, 10, 100
Taurus	$04^{\rm h}\,23^{\rm m}\,36.0^{\rm s}$	$g_{\rm WFC}$	2, 20, 100
Field 101	$+25^\circ\,06'\,00.0''$	$r_{\rm WFC}$	1, 10, 100
		$i_{\rm WFC}$	1, 10, 100
		$Z_{\rm WFC}$	1, 10, 100
Taurus	$04^{\rm h}\,56^{\rm m}\,13.5^{\rm s}$	$g_{\rm WFC}$	2, 20
Field 102	$+30^\circ\,33'\,32.0''$	$r_{\rm WFC}$	1, 10
		$i_{\rm WFC}$	1, 10
		$Z_{\rm WFC}$	1, 10
Taurus	$04^{\rm h}\,52^{\rm m}\,22.7^{\rm s}$	$g_{\rm WFC}$	2, 20, 100
Field 103	$+30^\circ\,47'\,56.0''$	$r_{\rm WFC}$	1, 10, 100

continued on next page...

Table A.3: continued

Field	RA Dec. (J2000.0)	Filter	Exposure time (s)
		i_{WFC}	1, 10, 100
		Z_{WFC}	1, 10, 100
Taurus	$04^{\mathrm{h}}\,59^{\mathrm{m}}\,46.7^{\mathrm{s}}$	g_{WFC}	2, 20
Field 104	$+30^{\circ}\,05'\,56.0''$	r_{WFC}	1, 10
		i_{WFC}	1, 10
		Z_{WFC}	1, 10
Taurus	$04^{\mathrm{h}}\,33^{\mathrm{m}}\,34.7^{\mathrm{s}}$	g_{WFC}	2, 20, 100
Field 105	$+29^{\circ}\,20'\,56.0''$	r_{WFC}	1, 10, 100
		i_{WFC}	1, 10, 100
		Z_{WFC}	1, 10, 100
Taurus	$04^{\mathrm{h}}\,31^{\mathrm{m}}\,58.7^{\mathrm{s}}$	g_{WFC}	2, 20
Field 106	$+29^{\circ}\,29'\,56.0''$	r_{WFC}	1, 10
		i_{WFC}	1, 10
		Z_{WFC}	1, 10
Taurus	$04^{\mathrm{h}}\,30^{\mathrm{m}}\,22.7^{\mathrm{s}}$	g_{WFC}	2, 20
Field 107	$+29^{\circ}\,08'\,56.0''$	r_{WFC}	1, 10
		i_{WFC}	1, 10
		Z_{WFC}	1, 10
Taurus	$04^{\mathrm{h}}\,30^{\mathrm{m}}\,22.7^{\mathrm{s}}$	g_{WFC}	2, 20
Field 108	$+28^{\circ}\,41'\,56.0''$	r_{WFC}	1, 10
		i_{WFC}	1, 10
		Z_{WFC}	1, 10
Taurus	$04^{\mathrm{h}}\,30^{\mathrm{m}}\,22.7^{\mathrm{s}}$	g_{WFC}	2, 20
Field 109	$+28^{\circ}\,14'\,56.0''$	r_{WFC}	1, 10
		i_{WFC}	1, 10
		Z_{WFC}	1, 10

continued on next page...

Table A.3: continued

Field	RA Dec. (J2000.0)	Filter	Exposure time (s)
Taurus	$04^{h}\,30^{m}\,22.7^{s}$	g_{WFC}	2, 20
Field 110	$+27^{\circ}\,50'\,56.0''$	r_{WFC}	1, 10
		i_{WFC}	1, 10
		Z_{WFC}	1, 10
Taurus	$04^{h}\,29^{m}\,46.7^{s}$	g_{WFC}	2, 20
Field 111	$+27^{\circ}\,26'\,56.0''$	r_{WFC}	1, 10
		i_{WFC}	1, 10
		Z_{WFC}	1, 10
Taurus	$04^{h}\,29^{m}\,46.7^{s}$	g_{WFC}	2, 20
Field 112	$+27^{\circ}\,02'\,56.0''$	r_{WFC}	1, 10
		i_{WFC}	1, 10, 100
		Z_{WFC}	1, 10, 100
Taurus	$04^{h}\,29^{m}\,46.7^{s}$	g_{WFC}	2, 20
Field 113	$+26^{\circ}\,38'\,56.0''$	r_{WFC}	1, 10
		i_{WFC}	1, 10
		Z_{WFC}	1, 10
Taurus	$04^{h}\,31^{m}\,22.7^{s}$	g_{WFC}	2, 20
Field 114	$+27^{\circ}\,02'\,56.0''$	r_{WFC}	1, 10
		i_{WFC}	1, 10
		Z_{WFC}	1, 10
Taurus	$04^{h}\,32^{m}\,34.7^{s}$	g_{WFC}	2, 20
Field 115	$+27^{\circ}\,02'\,56.0''$	r_{WFC}	1, 10
		i_{WFC}	1, 10, 100
		Z_{WFC}	1, 10, 100
Taurus	$04^{h}\,35^{m}\,46.7^{s}$	g_{WFC}	2, 20
Field 116	$+27^{\circ}\,05'\,56.0''$	r_{WFC}	1, 10

continued on next page...

Table A.3: continued

Field	RA Dec. (J2000.0)	Filter	Exposure time (s)
		$i_{\rm WFC}$	1, 10
		$Z_{\rm WFC}$	1, 10
Taurus	$04^{\rm h}\,37^{\rm m}\,22.7^{\rm s}$	$g_{\rm WFC}$	2, 20
Field 117	$+27^\circ\,05'\,56.0''$	$r_{\rm WFC}$	1, 10
		$i_{\rm WFC}$	1, 10
		$Z_{\rm WFC}$	1, 10
Taurus	$04^{\rm h}\,38^{\rm m}\,58.7^{\rm s}$	$g_{\rm WFC}$	2, 20
Field 118	$+27^\circ\,05'\,56.0''$	$r_{\rm WFC}$	1, 10
		$i_{\rm WFC}$	1, 10
		$Z_{\rm WFC}$	1, 10
Taurus	$04^{\rm h}\,30^{\rm m}\,20.3^{\rm s}$	$g_{\rm WFC}$	2, 20, 100, 500
Field 119	$+25^\circ\,58'\,08.0''$	$r_{\rm WFC}$	1, 10, 100
		$i_{\rm WFC}$	1, 10, 100
		$Z_{\rm WFC}$	1, 10, 100
Taurus	$04^{\rm h}\,29^{\rm m}\,22.7^{\rm s}$	$g_{\rm WFC}$	2, 20
Field 120	$+26^\circ\,11'\,56.0''$	$r_{\rm WFC}$	1, 10
		$i_{\rm WFC}$	1, 10, 100
		$Z_{\rm WFC}$	1, 10, 100
Taurus	$04^{\rm h}\,27^{\rm m}\,46.7^{\rm s}$	$g_{\rm WFC}$	2, 20, 100
Field 121	$+26^\circ\,11'\,56.0''$	$r_{\rm WFC}$	1, 10, 100, 500($\times$ 2)
		$i_{\rm WFC}$	1, 10, 100
		$Z_{\rm WFC}$	1, 10, 100
Taurus	$04^{\rm h}\,32^{\rm m}\,29.9^{\rm s}$	$g_{\rm WFC}$	2, 20, 100
Field 122	$+24^\circ\,16'\,11.5''$	$r_{\rm WFC}$	1, 10, 100, 500
		$i_{\rm WFC}$	1, 10, 100
		$Z_{\rm WFC}$	1, 10, 100

continued on next page...

Table A.3: continued

Field	RA Dec. (J2000.0)	Filter	Exposure time (s)
Taurus	$04^{h}\,30^{m}\,32.3^{s}$	g_{WFC}	2, 20
Field 123	$+24^{\circ}\,38'\,56.0''$	r_{WFC}	1, 10
		i_{WFC}	1, 10
		Z_{WFC}	1, 10
Taurus	$04^{h}\,31^{m}\,10.7^{s}$	g_{WFC}	2, 20
Field 124	$+24^{\circ}\,10'\,44.0''$	r_{WFC}	1, 10
		i_{WFC}	1, 10, 100
		Z_{WFC}	1, 10, 100
Taurus	$04^{h}\,29^{m}\,10.7^{s}$	g_{WFC}	2, 20
Field 125	$+24^{\circ}\,10'\,44.0''$	r_{WFC}	1, 10
		i_{WFC}	1, 10
		Z_{WFC}	1, 10
Taurus	$04^{h}\,21^{m}\,44.3^{s}$	g_{WFC}	2, 20, 100
Field 126	$+27^{\circ}\,08'\,56.0''$	r_{WFC}	1, 10, 100, 500
		i_{WFC}	1, 10, 100
		Z_{WFC}	1, 10, 100
Taurus	$04^{h}\,20^{m}\,10.7^{s}$	g_{WFC}	2, 20
Field 127	$+27^{\circ}\,20'\,56.0''$	r_{WFC}	1, 10
		i_{WFC}	1, 10
		Z_{WFC}	1, 10
Taurus	$04^{h}\,19^{m}\,46.7^{s}$	g_{WFC}	2, 20
Field 128	$+28^{\circ}\,08'\,56.0''$	r_{WFC}	1, 10
		i_{WFC}	1, 10, 100
		Z_{WFC}	1, 10, 100
Taurus	$04^{h}\,18^{m}\,10.7^{s}$	g_{WFC}	2, 20
Field 129	$+28^{\circ}\,14'\,56.0''$	r_{WFC}	1, 10

continued on next page...

Table A.3: continued

Field	RA Dec. (J2000.0)	Filter	Exposure time (s)
		i_{WFC}	1, 10
		Z_{WFC}	1, 10
Taurus	$04^{\mathrm{h}}\,16^{\mathrm{m}}\,34.7^{\mathrm{s}}$	g_{WFC}	2, 20
Field 130	$+28^{\circ}\,08'\,56.0''$	r_{WFC}	1, 10
		i_{WFC}	1, 10
		Z_{WFC}	1, 10
Taurus	$04^{\mathrm{h}}\,14^{\mathrm{m}}\,58.7^{\mathrm{s}}$	g_{WFC}	2, 20
Field 131	$+27^{\circ}\,59'\,56.0''$	r_{WFC}	1, 10
		i_{WFC}	1, 10, 100
		Z_{WFC}	1, 10, 100
Taurus	$04^{\mathrm{h}}\,13^{\mathrm{m}}\,46.7^{\mathrm{s}}$	g_{WFC}	2, 20
Field 132	$+28^{\circ}\,14'\,56.0''$	r_{WFC}	1, 10
		i_{WFC}	1, 10
		Z_{WFC}	1, 10
Taurus	$04^{\mathrm{h}}\,42^{\mathrm{m}}\,06.6^{\mathrm{s}}$	g_{WFC}	2, 20
Field 133	$+23^{\circ}\,04'\,08.0''$	r_{WFC}	1, 10
		i_{WFC}	1, 10
		Z_{WFC}	1, 10
Taurus	$04^{\mathrm{h}}\,37^{\mathrm{m}}\,34.9^{\mathrm{s}}$	g_{WFC}	2, 20
Field 134	$+23^{\circ}\,32'\,20.0''$	r_{WFC}	1, 10
		i_{WFC}	1, 10
		Z_{WFC}	1, 10
Taurus	$04^{\mathrm{h}}\,37^{\mathrm{m}}\,00.1^{\mathrm{s}}$	g_{WFC}	2, 20
Field 135	$+23^{\circ}\,11'\,20.0''$	r_{WFC}	1, 10
		i_{WFC}	1, 10
		Z_{WFC}	1, 10

continued on next page...

Table A.3: continued

Field	RA Dec. (J2000.0)	Filter	Exposure time (s)
Taurus	$04^{h}\,36^{m}\,10.9^{s}$	$g_{\rm WFC}$	2, 20, 100, 500
Field 136	$+22^{\circ}\,54'\,42.0''$	$r_{\rm WFC}$	1, 10, 100, 500(×2)
		$i_{\rm WFC}$	1, 10, 100
		$Z_{\rm WFC}$	1, 10, 100
Taurus	$04^{h}\,34^{m}\,10.7^{s}$	$g_{\rm WFC}$	2, 20
Field 137	$+22^{\circ}\,41'\,56.0''$	$r_{\rm WFC}$	1, 10
		$i_{\rm WFC}$	1, 10
		$Z_{\rm WFC}$	1, 10
Taurus	$04^{h}\,32^{m}\,58.7^{s}$	$g_{\rm WFC}$	2, 20, 100, 500
Field 138	$+22^{\circ}\,56'\,56.0''$	$r_{\rm WFC}$	1, 10, 100
		$i_{\rm WFC}$	1, 10, 100
		$Z_{\rm WFC}$	1, 10, 100
Taurus	$04^{h}\,32^{m}\,58.7^{s}$	$g_{\rm WFC}$	2, 20
Field 139	$+17^{\circ}\,41'\,56.0''$	$r_{\rm WFC}$	1, 10
		$i_{\rm WFC}$	1, 10
		$Z_{\rm WFC}$	1, 10
Taurus	$04^{h}\,31^{m}\,58.7^{s}$	$g_{\rm WFC}$	2, 20, 100
Field 140	$+17^{\circ}\,59'\,56.0''$	$r_{\rm WFC}$	1, 10, 100
		$i_{\rm WFC}$	1, 10, 100
		$Z_{\rm WFC}$	1, 10, 100
NGC 2264	$06^{h}\,39^{m}\,47.1^{s}$	$U_{\rm WFC}$	1, 10, 100
Field A	$+09^{\circ}\,26'\,33.0''$	$g_{\rm WFC}$	1, 10, 100, 500
		$r_{\rm WFC}$	1, 10, 100, 500
		$i_{\rm WFC}$	1, 10, 100, 500
		$Z_{\rm WFC}$	1, 10, 100, 500
NGC 2264	$06^{h}\,41^{m}\,51.2^{s}$	$U_{\rm WFC}$	1, 10, 100

continued on next page...

Table A.3: continued

Field	RA Dec. (J2000.0)	Filter	Exposure time (s)
Field B	+09° 26′ 32.9″	$g_{\rm WFC}$	1, 10, 100, 500
		$r_{\rm WFC}$	1, 10, 100, 500
		$i_{\rm WFC}$	1, 10, 100, 500
		$Z_{\rm WFC}$	1, 10, 100, 500
NGC 2264	$06^{\rm h}\,39^{\rm m}\,47.1^{\rm s}$	$U_{\rm WFC}$	1, 10, 100
Field C	+09° 53′ 36.8″	$g_{\rm WFC}$	1, 10, 100, 500
		$r_{\rm WFC}$	1, 10, 100, 500
		$i_{\rm WFC}$	1, 10, 100
		$Z_{\rm WFC}$	1, 10, 100, 500
NGC 2264	$06^{\rm h}\,41^{\rm m}\,51.2^{\rm s}$	$U_{\rm WFC}$	1, 10, 100
Field D	+09° 53′ 36.8″	$g_{\rm WFC}$	1, 10, 100, 500
		$r_{\rm WFC}$	1, 10, 100, 500
		$i_{\rm WFC}$	1, 10, 100, 500
		$Z_{\rm WFC}$	1, 10, 100, 200, 500
NGC 2264	$06^{\rm h}\,40^{\rm m}\,49.1^{\rm s}$	$U_{\rm WFC}$	1, 10, 100
Field E	+09° 40′ 04.9″	$g_{\rm WFC}$	1, 10, 100
		$r_{\rm WFC}$	1, 10, 100
		$i_{\rm WFC}$	1, 10, 100
		$Z_{\rm WFC}$	1, 10, 100

B

Blanco DECam Observed Fields and Exposure Times

Table B.1: The central coordinates for each field-of-view and $(griz)_{\mathrm{DECam}}$ exposure times for the Blanco-DECam observations of Blanco 1, rho Ophiuchus and Chamaeleon.

Field	RA Dec. (J2000.0)	Filter	Exposure time (s)
Blanco 1	$00^{\mathrm{h}}\,04^{\mathrm{m}}\,24.0^{\mathrm{s}}$		
	$-29^{\circ}\,56'\,24.0''$	g_{DECam}	1, 20, 200
		r_{DECam}	0.1, 2, 30, 220(×13)
		i_{DECam}	0.1, 1, 12, 240(×9)
		Z_{DECam}	0.1, 3, 80(×5)

continued on next page...

Table B.1: continued

Field	RA Dec. (J2000.0)	Filter	Exposure time (s)
ρ-Ophiuchus	$16^{h}\,26^{m}\,48.0^{s}$		
	$-24^{\circ}\,26'\,48.0''$	$g_{\rm DECam}$	1, 20
		$r_{\rm DECam}$	$0.1(\times 3)$, $2(\times 3)$, $30(\times 3)$, $150(\times 5)$
		$i_{\rm DECam}$	$0.1(\times 3)$, $2(\times 3)$, $35(\times 3)$
		$Z_{\rm DECam}$	$0.1(\times 3)$, $3(\times 3)$, $20(\times 3)$
Chamaeleon I	$11^{h}\,08^{m}\,20.0^{s}$		
	$-77^{\circ}\,00'\,00.0''$		
		$r_{\rm DECam}$	$0.1(\times 3)$, $2(\times 3)$, $30(\times 3)$, $150(\times 3)$, $300(\times 8)$
		$i_{\rm DECam}$	$0.1(\times 3)$, $1(\times 3)$, $12(\times 3)$, $130(\times 3))$
		$Z_{\rm DECam}$	$0.1(\times 3)$, $3(\times 3)$, $70(\times 3)$

Table B.2: The central coordinates for each field-of-view and $(griz)_{\rm DECam}$ exposure times for the Blanco-DECam observations of the standard star fields.

Field	RA Dec. (J2000.0)	Filter	Exposure time (s)
SDSSJ0200-0000	$02^{h}\,00^{m}\,00.0^{s}$		
	$+00^{\circ}\,00'\,00.0''$	$g_{\rm DECam}$	$15(\times 2)$
		$r_{\rm DECam}$	$15(\times 2)$
		$i_{\rm DECam}$	$15(\times 2)$
		$Z_{\rm DECam}$	$15(\times 2)$
SDSSJ1048-0000	$10^{h}\,48^{m}\,00.0^{s}$		
	$+00^{\circ}\,00'\,00.0''$		
		$r_{\rm DECam}$	$15(\times 2)$
		$i_{\rm DECam}$	$15(\times 2)$
		$Z_{\rm DECam}$	$15(\times 2)$
SDSSJ1227-0000	$12^{h}\,27^{m}\,00.0^{s}$		

continued on next page...

Table B.2: continued

Field	RA Dec. (J2000.0)	Filter	Exposure time (s)
	$+00^\circ\,00'\,00.0''$		
		r_{DECam}	$15(\times 2)$
		i_{DECam}	$15(\times 2)$
		Z_{DECam}	$15(\times 2)$
SDSSJ1442-0000	$14^{\mathrm{h}}\,42^{\mathrm{m}}\,00.0^{\mathrm{s}}$		
	$+00^\circ\,00'\,00.0''$		
		r_{DECam}	$15(\times 2)$
		i_{DECam}	$15(\times 2)$
		Z_{DECam}	$15(\times 2)$
SDSSJ2140-0000	$21^{\mathrm{h}}\,40^{\mathrm{m}}\,00.0^{\mathrm{s}}$		
	$+00^\circ\,00'\,00.0''$	g_{DECam}	$15(\times 2)$
		r_{DECam}	$15(\times 2)$
		i_{DECam}	$15(\times 2)$
		Z_{DECam}	$15(\times 2)$
E5-A	$12^{\mathrm{h}}\,04^{\mathrm{m}}\,11.0^{\mathrm{s}}$		
	$-45^\circ\,24'\,02.0''$	g_{DECam}	3
		r_{DECam}	3
		i_{DECam}	3
		Z_{DECam}	3
E6-A	$14^{\mathrm{h}}\,45^{\mathrm{m}}\,33.0^{\mathrm{s}}$		
	$-45^\circ\,15'\,33.0''$	g_{DECam}	3
		r_{DECam}	3
		i_{DECam}	3
		Z_{DECam}	3
E8-A	$20^{\mathrm{h}}\,07^{\mathrm{m}}\,22.0^{\mathrm{s}}$		
	$-44^\circ\,37'\,00.0''$	g_{DECam}	3
		r_{DECam}	3

continued on next page...

Table B.2: continued

Field	RA Dec. (J2000.0)	Filter	Exposure time (s)
		i_{DECam}	3
		Z_{DECam}	3
E9-A	$22^{\mathrm{h}}\,45^{\mathrm{m}}\,37.0^{\mathrm{s}}$		
	$-44^{\circ}\,27'\,47.0''$	g_{DECam}	3
		r_{DECam}	3
		i_{DECam}	3
		Z_{DECam}	3

Bibliography

Ahn, C. P., Alexandroff, R., Allende Prieto, C., et al. 2012, ApJS, 203, 21

Alexander, D. R. & Ferguson, J. W. 1994, ApJ, 437, 879

Alexander, R. D., Clarke, C. J., & Pringle, J. E. 2006, MNRAS, 369, 229

Allard, F. & Hauschildt, P. H. 1995, ApJ, 445, 433

Allard, F., Homeier, D., & Freytag, B. 2011, in Astronomical Society of the Pacific Conference Series, Vol. 448, 16th Cambridge Workshop on Cool Stars, Stellar Systems, and the Sun, ed. C. Johns-Krull, M. K. Browning, & A. A. West, 91

Allen, L. E., Calvet, N., D'Alessio, P., et al. 2004, ApJS, 154, 363

An, D., Terndrup, D. M., & Pinsonneault, M. H. 2007, ApJ, 671, 1640

Andre, P., Ward-Thompson, D., & Barsony, M. 1993, ApJ, 406, 122

Andre, P., Ward-Thompson, D., & Barsony, M. 2000, Protostars and Planets IV, 59

Appenzeller, I. 1975, A&A, 38, 313

Appenzeller, I. & Mundt, R. 1989, A&A Rev., 1, 291

Asplund, M., Grevesse, N., Sauval, A. J., & Scott, P. 2009, ARA&A, 47, 481

Ayliffe, B. A. & Bate, M. R. 2009, MNRAS, 393, 49

Ballesteros-Paredes, J., Klessen, R. S., Mac Low, M.-M., & Vazquez-Semadeni, E. 2007, Protostars and Planets V, 63

Baraffe, I., Chabrier, G., Allard, F., & Hauschildt, P. H. 1998, A&A, 337, 403

Baraffe, I., Homeier, D., Allard, F., & Chabrier, G. 2015, A&A, 577, A42

Barber, R. J., Tennyson, J., Harris, G. J., & Tolchenov, R. N. 2006, MNRAS, 368, 1087

Barentsen, G., Vink, J. S., Drew, J. E., et al. 2011, MNRAS, 415, 103

Barrado y Navascués, D., Stauffer, J. R., & Jayawardhana, R. 2004, ApJ, 614, 386

Bastian, N., Covey, K. R., & Meyer, M. R. 2010, ARA&A, 48, 339

Bastian, N., Lamers, H. J. G. L. M., de Mink, S. E., et al. 2013, MNRAS, 436, 2398

Bate, M. R. 1998, ApJL, 508, L95

Bate, M. R. & Bonnell, I. A. 2005, MNRAS, 356, 1201

Bate, M. R., Bonnell, I. A., & Bromm, V. 2003, MNRAS, 339, 577

Bell, C. P. M., Mamajek, E. E., & Naylor, T. 2015, MNRAS, 454, 593

Bell, C. P. M., Naylor, T., Mayne, N. J., Jeffries, R. D., & Littlefair, S. P. 2012, MNRAS, 424, 3178

Bell, C. P. M., Naylor, T., Mayne, N. J., Jeffries, R. D., & Littlefair, S. P. 2013, MNRAS, 434, 806

Bell, C. P. M., Rees, J. M., Naylor, T., et al. 2014, MNRAS, 445, 3496

Bertout, C., Basri, G., & Bouvier, J. 1988, ApJ, 330, 350

Bertout, C., Robichon, N., & Arenou, F. 1999, A&A, 352, 574

Bessell, M. & Murphy, S. 2012, PASP, 124, 140

Bessell, M. S. 1991, AJ, 101, 662

Bessell, M. S., Castelli, F., & Plez, B. 1998, A&A, 333, 231

Binks, A. S. & Jeffries, R. D. 2014, MNRAS, 438, L11

Blanco, V. M. 1949, PASP, 61, 183

Boesgaard, A. M., Roper, B. W., & Lum, M. G. 2013, ApJ, 775, 58

Boudreault, S., Lodieu, N., Deacon, N. R., & Hambly, N. C. 2012, MNRAS, 426, 3419

Brandt, T. D. & Huang, C. X. 2015, ArXiv e-prints

Briceño, C., Luhman, K. L., Hartmann, L., Stauffer, J. R., & Kirkpatrick, J. D. 2002, ApJ, 580, 317

Brott, I. & Hauschildt, P. H. 2005, in ESA Special Publication, Vol. 576, The Three-Dimensional Universe with Gaia, ed. C. Turon, K. S. O'Flaherty, & M. A. C. Perryman, 565

Buckle, J. V. & Richer, J. S. 2015, MNRAS, 453, 2006

Burke, C. J., Pinsonneault, M. H., & Sills, A. 2004, ApJ, 604, 272

Burningham, B., Naylor, T., Littlefair, S. P., & Jeffries, R. D. 2005, MNRAS, 363, 1389

Calvet, N., Basri, G., & Kuhi, L. V. 1984, ApJ, 277, 725

Cardelli, J. A., Clayton, G. C., & Mathis, J. S. 1989, in IAU Symposium, Vol. 135, Interstellar Dust, ed. L. J. Allamandola & A. G. G. M. Tielens, 5P

Cargile, P. A., James, D. J., & Jeffries, R. D. 2010, ApJL, 725, L111

Cargile, P. A., James, D. J., & Platais, I. 2009, AJ, 137, 3230

Castelli, F. & Kurucz, R. L. 2004, ArXiv Astrophysics e-prints

Chaboyer, B. & Kim, Y.-C. 1995, ApJ, 454, 767

Chabrier, G. & Baraffe, I. 1997, A&A, 327, 1039

Chabrier, G., Baraffe, I., Allard, F., & Hauschildt, P. 2000, ApJ, 542, 464

Chini, R. 1981, A&A, 99, 346

Chini, R., Hoffmeister, V. H., Nasseri, A., Stahl, O., & Zinnecker, H. 2012, MNRAS, 424, 1925

Clarke, C. J. & Pringle, J. E. 1993, MNRAS, 261, 190

Clayton, D. D. 1983, Principles of stellar evolution and nucleosynthesis

Cohen, M. & Kuhi, L. V. 1979, ApJS, 41, 743

Cohen, M., Wheaton, W. A., & Megeath, S. T. 2003, AJ, 126, 1090

Cohen, R. E., Herbst, W., & Williams, E. C. 2004, AJ, 127, 1602

Comerón, F., Reipurth, B., Henry, A., & Fernández, M. 2004, A&A, 417, 583

Copenhagen University, O., Institute, A. O., Cambridge, Uk, & Real Instituto Y Observatorio de La Armada, F. E. S. 2006, VizieR Online Data Catalog, 1304, 0

Cottaar, M., Covey, K. R., Meyer, M. R., et al. 2014, ApJ, 794, 125

Cox, D. P. 2005, ARA&A, 43, 337

Crutcher, R. M., Hakobian, N., & Troland, T. H. 2009, ApJ, 692, 844

Curtis, J. L., Wolfgang, A., Wright, J. T., Brewer, J. M., & Johnson, J. A. 2013, AJ, 145, 134

Cutri, R. M., Skrutskie, M. F., van Dyk, S., et al. 2003, 2MASS All Sky Catalog of point sources.

Cutri, R. M., Skrutskie, M. F., van Dyk, S., et al. 2012, VizieR Online Data Catalog, 2281

Da Rio, N., Gouliermis, D. A., & Gennaro, M. 2010, ApJ, 723, 166

Daemgen, S., Bonavita, M., Jayawardhana, R., Lafrenière, D., & Janson, M. 2015, ApJ, 799, 155

Dahm, S. E. 2008, The Young Cluster and Star Forming Region NGC 2264, ed. B. Reipurth, 966

Dalton, G., Trager, S. C., Abrams, D. C., et al. 2012, in Proc. SPIE, Vol. 8446, Ground-based and Airborne Instrumentation for Astronomy IV, 84460P

D'Antona, F. & Mazzitelli, I. 1994, ApJS, 90, 467

de Epstein, A. E. A. & Epstein, I. 1985, AJ, 90, 1211

de Zeeuw, P. T., Hoogerwerf, R., de Bruijne, J. H. J., Brown, A. G. A., & Blaauw, A. 1999, AJ, 117, 354

Deacon, N. R., Groot, P. J., Drew, J. E., et al. 2009, MNRAS, 397, 1685

Dias, W. S., Alessi, B. S., Moitinho, A., & Lépine, J. R. D. 2002, A&A, 389, 871

Dobbie, P. D., Lodieu, N., & Sharp, R. G. 2010, MNRAS, 409, 1002

Doi, M., Tanaka, M., Fukugita, M., et al. 2010, AJ, 139, 1628

Dotter, A., Chaboyer, B., Jevremović, D., et al. 2008, ApJS, 178, 89

Erickson, K. L., Wilking, B. A., Meyer, M. R., Robinson, J. G., & Stephenson, L. N. 2011, AJ, 142, 140

Evans, II, N. J., Dunham, M. M., Jørgensen, J. K., et al. 2009, ApJS, 181, 321

Feiden, G. A. 2016, ArXiv e-prints

Feigelson, E. D. 1984, in Lecture Notes in Physics, Berlin Springer Verlag, Vol. 193, Cool Stars, Stellar Systems, and the Sun, ed. S. L. Baliunas & L. Hartmann, 27

Feigelson, E. D., Gaffney, III, J. A., Garmire, G., Hillenbrand, L. A., & Townsley, L. 2003, ApJ, 584, 911

Feigelson, E. D. & Getman, K. V. 2005, in Bulletin of the American Astronomical Society, Vol. 37, American Astronomical Society Meeting Abstracts, 1404

Ferguson, J. W., Alexander, D. R., Allard, F., et al. 2005, ApJ, 623, 585

Ferrière, K. M. 2001, Reviews of Modern Physics, 73, 1031

Fitzpatrick, E. L. 1999, PASP, 111, 63

Flaugher, B., Diehl, H. T., Honscheid, K., et al. 2015, AJ, 150, 150

Ford, A., Jeffries, R. D., & Smalley, B. 2005, MNRAS, 364, 272

Fossati, L., Bagnulo, S., Landstreet, J., et al. 2008, A&A, 483, 891

Freytag, B., Allard, F., Ludwig, H.-G., Homeier, D., & Steffen, M. 2010, A&A, 513, A19

Furlan, E., Luhman, K. L., Espaillat, C., et al. 2011, ApJS, 195, 3

Gagné, J., Faherty, J. K., Cruz, K. L., et al. 2015, ApJS, 219, 33

Gagne, M., Caillault, J.-P., & Stauffer, J. R. 1995, ApJ, 450, 217

Galli, P. A. B., Bertout, C., Teixeira, R., & Ducourant, C. 2015, A&A, 580, A26

Gatewood, G. & de Jonge, J. K. 1994, ApJ, 428, 166

Gatewood, G., de Jonge, J. K., & Han, I. 2000, ApJ, 533, 938

Genzel, R. & Stutzki, J. 1989, ARA&A, 27, 41

Geroux, C., Baraffe, I., Viallet, M., et al. 2016, A&A, 588, A85

Glass, I. S. 1979, MNRAS, 187, 305

Gómez, M. & Kenyon, S. J. 2001, AJ, 121, 974

González-Solares, E. A., Walton, N. A., Greimel, R., et al. 2008, MNRAS, 388, 89

Gorti, U. & Hollenbach, D. 2009, ApJ, 690, 1539

Greene, T. P. & Lada, C. J. 2000, AJ, 120, 430

Greene, T. P., Wilking, B. A., Andre, P., Young, E. T., & Lada, C. J. 1994, ApJ, 434, 614

Grevesse, N., Noels, A., & Sauval, A. J. 1993, A&A, 271, 587

Grevesse, N. & Sauval, A. J. 1998, Space Sci. Rev., 85, 161

Güdel, M., Briggs, K. R., Arzner, K., et al. 2007, A&A, 468, 353

Guzik, J. A. 2011, Ap&SS, 336, 95

Haisch, Jr., K. E., Lada, E. A., & Lada, C. J. 2001, ApJL, 553, L153

Hartigan, P., Kenyon, S. J., Hartmann, L., et al. 1991, ApJ, 382, 617

Hartmann, L. 2001, AJ, 121, 1030

Hatchell, J., Fuller, G. A., Richer, J. S., Harries, T. J., & Ladd, E. F. 2007, A&A, 468, 1009

Hauschildt, P. H., Allard, F., & Baron, E. 1999, ApJ, 512, 377

Hayashi, C. 1961, PASJ, 13

Henyey, L. G., Lelevier, R., & Levée, R. D. 1955, PASP, 67, 154

Herbig, G. H. 1962, Advances in Astronomy and Astrophysics, 1, 47

Herbig, G. H. 1998, ApJ, 497, 736

Herczeg, G. J. & Hillenbrand, L. A. 2014, ApJ, 786, 97

Herczeg, G. J. & Hillenbrand, L. A. 2015, ArXiv e-prints

Hernández, J., Calvet, N., Briceño, C., et al. 2007, ApJ, 671, 1784

Hertzsprung, E. 1911, Publikationen des Astrophysikalischen Observatoriums zu Potsdam, 63

Hillenbrand, L. A. 1997, AJ, 113, 1733

Hillenbrand, L. A. 2005, ArXiv Astrophysics e-prints

Hillenbrand, L. A., Carpenter, J. M., & Feigelson, E. D. 2001, in Astronomical Society of the Pacific Conference Series, Vol. 243, From Darkness to Light: Origin and Evolution of Young Stellar Clusters, ed. T. Montmerle & P. André, 439

Hillenbrand, L. A., Strom, S. E., Calvet, N., et al. 1998, AJ, 116, 1816

Høg, E., Fabricius, C., Makarov, V. V., et al. 2000, A&A, 355, L27

Homeier, D., Hauschildt, P. H., & Allard, F. 2003, in Astronomical Society of the Pacific Conference Series, Vol. 288, Stellar Atmosphere Modeling, ed. I. Hubeny, D. Mihalas, & K. Werner, 357

Howell, S. B. 2012, PASP, 124, 263

Hunter, C. 1962, ApJ, 136, 594

Iglesias, C. A. & Rogers, F. J. 1996, ApJ, 464, 943

Irwin, A. W. 2012, FreeEOS: Equation of State for stellar interiors calculations, Astrophysics Source Code Library

Irwin, M. J. 1997, Detectors and data analysis techniques for wide field optical imaging., ed. J. M. Rodríguez Espinosa, A. Herrero, & F. Sánchez, 35–74

Jackson, R. J., Jeffries, R. D., Randich, S., et al. 2016, A&A, 586, A52

James, D. J., Aarnio, A. N., Richert, A. J. W., et al. 2016, MNRAS, 459, 1363

Jeffries, R. D. 2006, Pre-Main-Sequence Lithium Depletion, ed. S. Randich & L. Pasquini, 163

Jeffries, R. D. 2012, Astrophysics and Space Science Proceedings, 29, 163

Jeffries, R. D., Jackson, R. J., James, D. J., & Cargile, P. A. 2009, MNRAS, 400, 317

Jeffries, R. D., Littlefair, S. P., Naylor, T., & Mayne, N. J. 2011, MNRAS, 418, 1948

Jeffries, R. D., Naylor, T., Mayne, N. J., Bell, C. P. M., & Littlefair, S. P. 2013, MNRAS, 434, 2438

Jeffries, R. D. & Oliveira, J. M. 2005, MNRAS, 358, 13

Jeffries, R. D., Oliveira, J. M., Naylor, T., Mayne, N. J., & Littlefair, S. P. 2007, MNRAS, 376, 580

Johnson, H. L. 1952, ApJ, 116, 640

Johnson, H. L. 1957, ApJ, 126, 121

Johnson, H. L. & Morgan, W. W. 1953, ApJ, 117, 313

Johnstone, D., Hollenbach, D., & Bally, J. 1998, ApJ, 499, 758

Joshi, H., Kumar, B., Singh, K. P., et al. 2008, MNRAS, 391, 1279

Joy, A. H. 1945, ApJ, 102, 168

Juarez, A. J., Cargile, P. A., James, D. J., & Stassun, K. G. 2014, ApJ, 795, 143

Kamai, B. L., Vrba, F. J., Stauffer, J. R., & Stassun, K. G. 2014, AJ, 148, 30

Kamezaki, T., Imura, K., Omodaka, T., et al. 2014, ApJS, 211, 18

Kennedy, G. M. & Kenyon, S. J. 2009, ApJ, 695, 1210

Kenyon, M. J., Jeffries, R. D., Naylor, T., Oliveira, J. M., & Maxted, P. F. L. 2005, MNRAS, 356, 89

Kenyon, S. J. & Gómez, M. 2001, AJ, 121, 2673

Kenyon, S. J., Gómez, M., & Whitney, B. A. 2008, Low Mass Star Formation in the Taurus-Auriga Clouds, ed. B. Reipurth No. 1915, 405

Kenyon, S. J. & Hartmann, L. 1995, ApJS, 101, 117

King, R. R., Naylor, T., Broos, P. S., Getman, K. V., & Feigelson, E. D. 2013, ApJS, 209, 28

King, R. R., Parker, R. J., Patience, J., & Goodwin, S. P. 2012, MNRAS, 421, 2025

Klessen, R. S., Heitsch, F., & Mac Low, M.-M. 2000, ApJ, 535, 887

Kotoneva, E., Flynn, C., & Jimenez, R. 2002, MNRAS, 335, 1147

Kraus, A. L. & Hillenbrand, L. A. 2007, AJ, 134, 2340

Kraus, A. L., Ireland, M. J., Martinache, F., & Hillenbrand, L. A. 2011, ApJ, 731, 8

Kroupa, P. 2001, MNRAS, 322, 231

Kurucz, R. L. 1979, ApJS, 40, 1

Kurucz, R. L. 1992, in IAU Symposium, Vol. 149, The Stellar Populations of Galaxies, ed. B. Barbuy & A. Renzini, 225

Lada, C. J. 1987, in IAU Symposium, Vol. 115, Star Forming Regions, ed. M. Peimbert & J. Jugaku, 1–17

Lada, C. J. & Adams, F. C. 1992, ApJ, 393, 278

Lada, C. J. & Wilking, B. A. 1984, ApJ, 287, 610

Larson, R. B. 1969, MNRAS, 145, 271

Larson, R. B. 2002, MNRAS, 332, 155

Lawrence, A., Warren, S. J., Almaini, O., et al. 2007, MNRAS, 379, 1599

Lejeune, T. & Schaerer, D. 2001, A&A, 366, 538

Lesser, M. P. 1990, in Astronomical Society of the Pacific Conference Series, Vol. 8, CCDs in astronomy, ed. G. H. Jacoby, 65–75

Levi, M., Bebek, C., Beers, T., et al. 2013, ArXiv e-prints

Littlefair, S. P., Naylor, T., Burningham, B., & Jeffries, R. D. 2005, MNRAS, 358, 341

Lodieu, N., Deacon, N. R., & Hambly, N. C. 2012, MNRAS, 422, 1495

Loinard, L., Torres, R. M., Mioduszewski, A. J., & Rodríguez, L. F. 2008a, ApJL, 675, L29

Loinard, L., Torres, R. M., Mioduszewski, A. J., & Rodríguez, L. F. 2008b, in IAU Symposium, Vol. 248, A Giant Step: from Milli- to Micro-arcsecond Astrometry, ed. W. J. Jin, I. Platais, & M. A. C. Perryman, 186–189

Loinard, L., Torres, R. M., Mioduszewski, A. J., et al. 2007, ApJ, 671, 546

Lombardi, M., Lada, C. J., & Alves, J. 2008, A&A, 480, 785

Lucas, P. W., Hoare, M. G., Longmore, A., et al. 2008, MNRAS, 391, 136

Luhman, K. L. 2004, ApJ, 602, 816

Luhman, K. L. 2007, ApJS, 173, 104

Luhman, K. L., Allen, L. E., Allen, P. R., et al. 2008, ApJ, 675, 1375

Luhman, K. L., Allen, P. R., Espaillat, C., Hartmann, L., & Calvet, N. 2010, ApJS, 186, 111

Luhman, K. L., Lada, E. A., Muench, A. A., & Elston, R. J. 2005a, ApJ, 618, 810

Luhman, K. L., Mamajek, E. E., Allen, P. R., & Cruz, K. L. 2009, ApJ, 703, 399

Luhman, K. L., McLeod, K. K., & Goldenson, N. 2005b, ApJ, 623, 1141

Luhman, K. L., Stauffer, J. R., Muench, A. A., et al. 2003, ApJ, 593, 1093

Maddalena, R. J., Morris, M., Moscowitz, J., & Thaddeus, P. 1986, ApJ, 303, 375

Makarov, V. V. 2007, ApJ, 670, 1225

Mamajek, E. E. 2008, Astronomische Nachrichten, 329, 10

Manzi, S., Randich, S., de Wit, W. J., & Palla, F. 2008, A&A, 479, 141

Margulis, M., Lada, C. J., & Young, E. T. 1989, ApJ, 345, 906

Matsuyama, I., Johnstone, D., & Hartmann, L. 2003, ApJ, 582, 893

Mayne, N. J. & Naylor, T. 2008, MNRAS, 386, 261

McKee, C. F. & Ostriker, J. P. 1977, ApJ, 218, 148

Mermilliod, J.-C., Platais, I., James, D. J., Grenon, M., & Cargile, P. A. 2008, A&A, 485, 95

Micela, G., Sciortino, S., Favata, F., Pallavicini, R., & Pye, J. 1999, A&A, 344, 83

Mohanty, S., Jayawardhana, R., & Basri, G. 2005, ApJ, 626, 498

Montmerle, T., Koch-Miramond, L., Falgarone, E., & Grindlay, J. E. 1983, ApJ, 269, 182

Moraux, E., Bouvier, J., Stauffer, J. R., Barrado y Navascués, D., & Cuillandre, J.-C. 2007, A&A, 471, 499

Muzerolle, J., Luhman, K. L., Briceño, C., Hartmann, L., & Calvet, N. 2005, ApJ, 625, 906

Myers, P. C., Fuller, G. A., Mathieu, R. D., et al. 1987, ApJ, 319, 340

Nakajima, Y., Tamura, M., Oasa, Y., & Nakajima, T. 2000, AJ, 119, 873

Naylor, T. 1998, MNRAS, 296, 339

Naylor, T. 2009, MNRAS, 399, 432

Naylor, T. & Fabian, A. C. 1999, MNRAS, 302, 714

Naylor, T. & Jeffries, R. D. 2006, MNRAS, 373, 1251

Naylor, T., Totten, E. J., Jeffries, R. D., et al. 2002, MNRAS, 335, 291

Olczak, C., Pfalzner, S., & Eckart, A. 2010, A&A, 509, A63

Olczak, C., Pfalzner, S., & Spurzem, R. 2006, ApJ, 642, 1140

Palla, F. & Stahler, S. W. 1990, ApJL, 360, L47

Pan, X., Shao, M., & Kulkarni, S. R. 2004, Nature, 427, 326

Panagi, P. M. & O'dell, M. A. 1997, A&AS, 121

Panagi, P. M., O'dell, M. A., Collier Cameron, A., & Robinson, R. D. 1994, A&A, 292, 439

Pecaut, M. J. & Mamajek, E. E. 2013, ApJS, 208, 9

Pecaut, M. J., Mamajek, E. E., & Bubar, E. J. 2012, ApJ, 746, 154

Perry, C. L., Walter, D. K., & Crawford, D. L. 1978, PASP, 90, 81

Perryman, M. A. C., Lindegren, L., Kovalevsky, J., et al. 1997, A&A, 323

Persi, P., Marenzi, A. R., Olofsson, G., et al. 2000, A&A, 357, 219

Pfalzner, S., Steinhausen, M., & Menten, K. 2014, ApJL, 793, L34

Pickles, A. J. 1998, PASP, 110, 863

Pillitteri, I., Micela, G., Sciortino, S., Damiani, F., & Harnden, Jr., F. R. 2004, A&A, 421, 175

Pillitteri, I., Micela, G., Sciortino, S., & Favata, F. 2003, A&A, 399, 919

Pinsonneault, M. H., Stauffer, J., Soderblom, D. R., King, J. R., & Hanson, R. B. 1998, ApJ, 504, 170

Platais, I., Girard, T. M., Vieira, K., et al. 2011, MNRAS, 413, 1024

Pratt, J., Baraffe, I., Goffrey, T., et al. 2016, ArXiv e-prints

Preibisch, T. & Feigelson, E. D. 2005, ApJS, 160, 390

Preibisch, T., Guenther, E., Zinnecker, H., et al. 1998, A&A, 333, 619

Preibisch, T., Kim, Y.-C., Favata, F., et al. 2005, ApJS, 160, 401

Preibisch, T. & Zinnecker, H. 2002, in Astronomical Society of the Pacific Conference Series, Vol. 277, Stellar Coronae in the Chandra and XMM-NEWTON Era, ed. F. Favata & J. J. Drake, 185

Raghavan, D., McAlister, H. A., Henry, T. J., et al. 2010, ApJS, 190, 1

Rebull, L. M., Makidon, R. B., Strom, S. E., et al. 2002, AJ, 123, 1528

Reipurth, B. 2008a, Handbook of Star Forming Regions, Volume I: The Northern Sky

Reipurth, B. 2008b, Handbook of Star Forming Regions, Volume II: The Southern Sky

Ribas, Á., Merín, B., Bouy, H., & Maud, L. T. 2014, A&A, 561, A54

Rieke, G. H. & Lebofsky, M. J. 1985, ApJ, 288, 618

Robichon, N., Arenou, F., Mermilliod, J.-C., & Turon, C. 1999, A&A, 345, 471

Robitaille, T. P. & Whitney, B. A. 2010, ApJL, 710, L11

Robitaille, T. P., Whitney, B. A., Indebetouw, R., Wood, K., & Denzmore, P. 2006, ApJS, 167, 256

Roeser, S., Demleitner, M., & Schilbach, E. 2010, AJ, 139, 2440

Rogers, F. J. & Nayfonov, A. 2002, ApJ, 576, 1064

Rosotti, G. P., Dale, J. E., de Juan Ovelar, M., et al. 2014, MNRAS, 441, 2094

Russell, H. N. 1910, AJ, 26, 147

Salaris, M., Weiss, A., & Percival, S. M. 2004, A&A, 414, 163

Sato, F., Hasegawa, T., Whiteoak, J. B., & Miyawaki, R. 2000, ApJ, 535, 857

Saumon, D., Chabrier, G., & van Horn, H. M. 1995, ApJS, 99, 713

Scandariato, G., Da Rio, N., Robberto, M., Pagano, I., & Stassun, K. 2012, A&A, 545, A19

Schaller, G., Schaerer, D., Meynet, G., & Maeder, A. 1992, A&AS, 96, 269

Schlegel, D. J., Finkbeiner, D. P., & Davis, M. 1998, ApJ, 500, 525

Siess, L., Dufour, E., & Forestini, M. 2000, A&A, 358, 593

Skrutskie, M. F., Cutri, R. M., Stiening, R., et al. 2006, AJ, 131, 1163

Slesnick, C. L., Hillenbrand, L. A., & Carpenter, J. M. 2008, ApJ, 688, 377

Smith, J. A., Allam, S. S., Tucker, D. L., & Fornal, B. 2007, in Bulletin of the American Astronomical Society, Vol. 39, American Astronomical Society Meeting Abstracts, 964

Soderblom, D. R., Hillenbrand, L. A., Jeffries, R. D., Mamajek, E. E., & Naylor, T. 2014, Protostars and Planets VI, 219

Soderblom, D. R., Laskar, T., Valenti, J. A., Stauffer, J. R., & Rebull, L. M. 2009, AJ, 138, 1292

Soderblom, D. R., Nelan, E., Benedict, G. F., et al. 2005, AJ, 129, 1616

Spezzi, L., Alcalá, J. M., Covino, E., et al. 2008, ApJ, 680, 1295

Stassun, K. G., Ardila, D. R., Barsony, M., Basri, G., & Mathieu, R. D. 2004, AJ, 127, 3537

Stassun, K. G., van den Berg, M., Feigelson, E., & Flaccomio, E. 2006, ApJ, 649, 914

Stauffer, J., Cody, A. M., Rebull, L., et al. 2016, AJ, 151, 60

Stauffer, J. R., Hartmann, L. W., Fazio, G. G., et al. 2007, ApJS, 172, 663

Stauffer, J. R., Jones, B. F., Backman, D., et al. 2003, AJ, 126, 833

Stauffer, J. R., Navascués, D. B. y., Bouvier, J., et al. 1999, ApJ, 527, 219

Stauffer, J. R., Schild, R., Barrado y Navascués, D., et al. 1998, ApJ, 504, 805

Störzer, H. & Hollenbach, D. 1999, ApJ, 515, 669

Strassmeier, K. G. 2009, A&A Rev., 17, 251

Strom, K. M., Strom, S. E., Edwards, S., Cabrit, S., & Skrutskie, M. F. 1989, AJ, 97, 1451

Sung, H. & Bessell, M. S. 2000, PASA, 17, 244

Sung, H., Bessell, M. S., & Chun, M.-Y. 2004, AJ, 128, 1684

Sung, H., Bessell, M. S., Chun, M.-Y., Karimov, R., & Ibrahimov, M. 2008, AJ, 135, 441

Sung, H., Bessell, M. S., & Lee, S.-W. 1997, AJ, 114, 2644

Sung, H., Stauffer, J. R., & Bessell, M. S. 2009, AJ, 138, 1116

Taylor, B. J. 2006, AJ, 132, 2453

Tognelli, E., Prada Moroni, P. G., & Degl'Innocenti, S. 2011, A&A, 533, A109

Torres, R. M., Loinard, L., Mioduszewski, A. J., et al. 2012, ApJ, 747, 18

Torres, R. M., Loinard, L., Mioduszewski, A. J., & Rodríguez, L. F. 2007, ApJ, 671, 1813

Torres, R. M., Loinard, L., Mioduszewski, A. J., & Rodríguez, L. F. 2009, ApJ, 698, 242

Turner, D. G. 2012, Astronomische Nachrichten, 333, 174

van Leeuwen, F. 2009, A&A, 497, 209

VandenBerg, D. A., Bergbusch, P. A., & Dowler, P. D. 2006, ApJS, 162, 375

Vanhala, H. A. T. & Cameron, A. G. W. 1998, ApJ, 508, 291

Vincke, K., Breslau, A., & Pfalzner, S. 2015, A&A, 577, A115

Walker, M. F. 1956, ApJS, 2, 365

Walter, F. M., Brown, A., Mathieu, R. D., Myers, P. C., & Vrba, F. J. 1988, AJ, 96, 297

White, R. J., Greene, T. P., Doppmann, G. W., Covey, K. R., & Hillenbrand, L. A. 2007, Protostars and Planets V, 117

Whittet, D. C. B. 1974, MNRAS, 168, 371

Whittet, D. C. B., Prusti, T., Franco, G. A. P., et al. 1997, A&A, 327, 1194

Wichmann, R., Bastian, U., Krautter, J., Jankovics, I., & Rucinski, S. M. 1998, MNRAS, 301, 39L

Wilking, B. A., Gagné, M., & Allen, L. E. 2008, Star Formation in the ρ Ophiuchi Molecular Cloud, ed. B. Reipurth, 351

Williams, J. P., Blitz, L., & McKee, C. F. 2000, Protostars and Planets IV, 97

Williams, J. P. & Cieza, L. A. 2011, ARA&A, 49, 67

Wilson, T. 2013, Master's thesis, University of Exeter

York, D. G., Adelman, J., Anderson, J. E., et al. 2000, AJ, 120, 1579

Yorke, H. W., Bodenheimer, P., & Laughlin, G. 1993, ApJ, 411, 274

Zinnecker, H. 1984, MNRAS, 210, 43

Zuckerman, B., Forveille, T., & Kastner, J. H. 1995, Nature, 373, 494